

EFFECT OF CONFIGURATION AND DIMENSIONS ON THE THERMO-MECHANICAL  
PERFORMANCE OF SPARK PLASMA SINTERED BISMUTH TELLURIDE ANNULAR  
THERMOELECTRIC GENERATOR (TEG) MODULES

EFFECT OF CONFIGURATION AND DIMENSIONS ON THE THERMO-MECHANICAL  
PERFORMANCE OF SPARK PLASMA SINTERED BISMUTH TELLURIDE ANNULAR  
THERMOELECTRIC GENERATOR (TEG) MODULES

By AHMED A. ABDELNABI, B.Eng. (Honours)

A Thesis Submitted to the School of Graduate Studies in Partial Fulfilment of the Requirements  
for the Degree Doctor of Philosophy in Mechanical Engineering

McMaster University © Copyright by Ahmed A. Abdelnabi, October 2020

McMaster University Ph.D. (2020) Hamilton, Ontario (Mechanical Engineering)

TITLE: EFFECT OF CONFIGURATION AND DIMENSIONS ON THE  
THERMO-MECHANICAL PERFORMANCE OF SPARK  
PLASMA SINTERED BISMUTH TELLURIDE ANNULAR  
THERMOELECTRIC GENERATOR (TEG) MODULES

AUTHOR: Ahmed A. Abdelnabi, B.Eng.

SUPERVISOR: Dr. James S. Cotton, Professor, Dept. of Mechanical Engineering

NUMBER OF PAGES: xiv, 188

## **Abstract**

Thermoelectric generators (TEG) are re-emerging technology that can be used to recover heat waste from commercial and industrial processes to generate electricity, enhancing fuel utilization and lowering greenhouse gas emissions. TEG modules are solid state heat engines that produce no noise or vibration during operation. Notably, TEG modules are also able to operate at low-temperature differences, which makes them ideal for a wide range of heat waste recovery applications. Annular thermoelectric generator (ATEG) modules are optimal in applications where either the heat source or sink are round in shape.  $\text{Bi}_2\text{Te}_3$  solution-based compounds are of significant interest in the application of thermoelectric materials (TE) used in low-temperature cooling and power generation applications.

The main objective of the current work is to design a mechanically reliable ring-shaped ATEG module with a predictable performance using spark plasma sintered  $\text{Bi}_2\text{Te}_3$  TE material for low temperature waste heat recovery applications. In terms of structure, this work is divided into two parts. The first part investigates how the use of a powder pre-treatment technique affects the mechanical and thermoelectric properties of P- and N-type  $\text{Bi}_2\text{Te}_3$ . In addition, part one also presents the measurements of these materials' mechanical and thermoelectric properties, which serve as inputs for the finite element models used to design thermoelectric modules with parallel and perpendicular configurations vis-a-vis the sintering pressing direction. The second part evaluates the thermoelectric performance and thermal stresses of a ring-shaped ATEG couple that has been integrated between hot-side and cold-side heat exchangers. To this end, two

configurations are compared with respect to their heat/electrical current flow paths: one that allows for radial flow (radial configuration), and one that allows for axial flow (axial configuration).

The P- and N-type  $\text{Bi}_2\text{Te}_3$  powder was treated using a mechanically agitated fluidized powder reduction facility that was built in-house. The characteristic uniaxial tensile strength of the P-type  $\text{Bi}_{0.4}\text{Sb}_{1.6}\text{Te}_3$  increased from 13.9 MPa to 26.3 MPa parallel to the sintering pressure, and from 16.3 MPa to 30.6 MPa perpendicular to the sintering pressure following oxide reduction using 5%  $\text{H}_2$  - 95% Ar at 380 °C for 24 h. The figure of merit, ZT, increased from 0.35 to 0.80 and from 0.42 to 1.13 at room temperature (25 °C) in the parallel and the perpendicular directions, respectively, after the surface oxide reduction treatment. On the other hand, the annealing effects of the oxide reduction pre-treatment of the N-type  $(\text{Bi}_{0.95}\text{Sb}_{0.05})_2(\text{Se}_{0.05}\text{Te}_{0.95})_3$  using 5%  $\text{H}_2$  - 95% Ar at 380 °C for 24 h were found to be responsible for the majority of the mechanical properties and ZT enhancement. Additionally, the characteristic uniaxial tensile strengths for this material increased from 30.4 to 34.1 MPa and from 30.8 to 38 MPa in the parallel and the perpendicular directions, respectively. The  $ZT_{\text{max}}$  (150 °C) increased from 0.54 to 0.63 in both the parallel and perpendicular directions due to oxide reduction, while annealing led to an increase to 0.58 and 0.62 in the parallel and the perpendicular directions, respectively.

An analytical model was constructed to compare the thermoelectric performance of the two configurations under three different hot-side thermal resistances, and a 3D coupled finite element ANSYS model was constructed to study and compare the thermal stresses of the two configurations at different dimensions. The two models were then used to create 2D maps in order to investigate the effects of ATEG couple configuration and dimensions, as well as the hot-side thermal

resistance, with the goal of identifying the optimum design. The optimization of module geometry requires a trade-off between performance and mechanical reliability. The results of these investigations showed that increases in the temperature difference across the ATEG couple ( $\Delta T$ ) led to increases in both power and thermal stresses in both configurations. When both configurations were generating the same power at  $\Delta T = 105\text{ }^{\circ}\text{C}$ , the thermal stresses in the radial configuration were as much as 67 MPa higher than those in the axial configuration due to the formation of additional tensile hoop stresses. The lowest thermal stress obtained for the axial couple configuration was 67.8 MPa, which was achieved when the couple had an outer diameter of 16 mm, an axial thickness of 1 mm, a  $\Delta T$  of  $14.8\text{ }^{\circ}\text{C}$ , and power generation of 10.4 mW per couple. The maximum thermal stress values were located at the corners of the interface between the solder and the TE rings due to the mismatched coefficient of thermal expansion.

This thesis makes a novel contribution to the state-of-the-art literature in ring-shaped ATEG modules, as it details a well-characterised spark plasma sintered  $\text{Bi}_2\text{Te}_3$  TE material and a methodology for designing a ring-shaped ATEG module with reliable, robust, and predictable thermoelectric and mechanical performance. The details of the contribution made by this work have been disseminated in the form of three journal publications, which have been integrated into this sandwich Ph.D. thesis.

## **Acknowledgments**

In the name of Allah, the Most Gracious and the Most Merciful, all praises to Allah for blessing me with patience, knowledge, and strength to complete this work.

I would like to give thanks to my supervisor and my supervisory committee, Dr. Cotton, Dr. McDermid and Dr. Ching, who were and still guiding me and supporting me all the time. You made my Ph.D. experience special; I would have never accomplished this without your mentorship.

Special thanks to Dr. Sadek for your support and believing in me. Thank you TMRL, an amazing team of people who kept me company. I will forever be a part of you, and I look forward to seeing the many more accomplishments and Selfies.

Thank you to the Mechanical Engineering technicians. Ron, John, Mike, Mark, Justin, Rob, and Dan (you will never be forgotten) as well as Jim Garrett, you were amazing every step along the way, and I couldn't have done it without you.

Thank you to the Mechanical Engineering former and present administration. Vania, Florence, Nicole, Leslie and Lily you always make everything easy. I really enjoyed our little chats every time I visit your office.

Thank you, Vick, for being a good friend. Thank you for supporting me through this challenging Ph.D. journey the many design conversations, blowing glass, gym and Costco trips.

Thanks to my Irish sister, Sarah, and my Egyptian brothers Abdalla, Fathallah, Helal, Yasser, Hossam, Zizo, and 7oda.

I would like to thank my mother and father, Abla and Ali, who raised me, loved me, and supported me overseas to achieve this. I will always owe you everything.

Thanks to my siblings, Mariam, and Mahmoud, you were always there specially the last two years of my Ph.D. journey and I'm looking forward to seeing you succeed and reach all your goals and dreams.

Thanks to my brother and best friend, Mohamed, you are the only person I can candidly talk to, my lifeboat when I am drowning, and my springboard when I'm on my way up. I count on you to be my rock.

Last, and most importantly, thanks to my beautiful wife Maryam for taking care of me, supporting me, and keeping me grounded. I owe a large part of this Ph.D. to you. I love you.

## Table of Contents

Table of Contents .....	viii
Chapter 1: Introduction .....	1
1.1 Introduction .....	1
1.2 Summary.....	10
1.3 Objective and Contributions.....	11
1.4 Thesis Organization.....	13
1.5 References .....	15
Chapter 2: Enhancement of mechanical properties and thermoelectric performance of spark plasma sintered P-type Bismuth Telluride by powder surface oxide reduction.....	27
2.1. Introduction .....	30
2.2. Experimental Methods.....	32
2.2.1 Sample Preparation .....	32
2.2.2 Sample Analysis:.....	34
2.4. Results and Discussion .....	35
2.4.1 Powder Chemistry and Powder Particle Size Distribution.....	35
2.4.2 Sintered Microstructures .....	37
2.4.3 As-Sintered Relative Density .....	38
2.4.4 Coefficient of Thermal Expansion and Density of SPS Bodies.....	38
2.4.5 Mechanical Properties .....	40
2.4.6 Thermoelectric Properties .....	42
2.5. Conclusions .....	46
2.6. Appendix .....	48
2.7. Figures and Tables:.....	50
2.8. References: .....	66
Chapter 3: The effect of powder pre-treatment on the mechanical and thermoelectric properties of spark plasma sintered N-type bismuth telluride .....	79
3.1. Introduction .....	82
3.2. Experimental methodology.....	84



3.2.1.	Sample Preparation .....	84
3.2.2.	Sample Analyses .....	85
3.3.	Results and Discussion .....	87
3.3.1.	Powder Chemistry and Powder Particle Distribution .....	87
3.3.2.	Sintered Microstructures .....	88
3.3.3.	As-sintered Relative Density .....	90
3.3.4.	Coefficient of Thermal Expansion and Density of SPS Bodies .....	90
3.3.5.	Mechanical Properties .....	91
3.3.6.	Thermoelectric Properties .....	93
3.4.	Conclusion .....	97
3.5.	Appendix .....	98
3.6.	Figures and Tables: .....	100
3.7.	References .....	114
Chapter 4: A parametric study aimed at selecting dimensions for a new annular TEG module design that will yield maximum power density and minimum thermal stress .....		120
4.1.	Introduction .....	123
4.2.	Geometric model description .....	128
4.3.	Analytical model .....	130
4.3.1.	Thermoelectric governing equations .....	130
4.3.2.	Material properties and boundary conditions .....	133
4.4.	Finite element model .....	134
4.4.1.	Thermoelectric analysis' governing equations .....	135
4.4.2.	Thermal stress analysis' governing equations .....	136
4.4.3.	Material properties .....	137
4.4.4.	Computational procedure .....	138
4.4.5.	Boundary conditions .....	139
4.4.6.	Model verification .....	140
4.5.	Results and discussion .....	140
4.5.1.	The effect of the ATEG couple configuration on performance .....	141

4.5.2. The effect of hot-side thermal resistance on the performance of the two couple configurations .....	143
4.5.3. Thermal stresses vs performance: .....	144
4.6. Conclusion .....	147
4.7. Appendix A. – Analytical and finite element models details .....	149
4.8. Figures and Tables .....	152
4.9. References .....	170
Chapter 5: Conclusions and Future Work .....	178
5.1. Conclusions .....	178
5.2. Recommendations for Future Work .....	182
Appendix: .....	184

## Nomenclature

D	Diameter, [mm]
t	Axial thickness, [mm]
T	Absolute temperature, [K]
ZT	Figure of merit, [-]
R <sub>L</sub>	Electrical load, [ $\Omega$ ]
R	Thermal/Electrical resistance, [ $\text{Km}^2/\text{W}$ ]/[ $\Omega$ ]
r	Internal electrical resistance, [ $\Omega$ ]
P	Electrical power, [W]

Q	Heat flow, [W]
I	Electrical current, [A]
V	Voltage, [V]
k	Thermal conductivity, [W/m K]
h	Convective coefficient, [W/m <sup>2</sup> K]
$\eta$	Thermal efficiency, [-]
$\alpha$	Seebeck coefficient, [ $\mu$ V/K]
$\rho$	Density, [kg/m <sup>3</sup> ]
$\rho_{ele}$	Electrical resistivity, [ $\Omega$ m <sup>2</sup> ]
$\sigma$	Stress, [MPa]

### **Subscripts**

g	Exhaust gas
w	Cooling water
h,H	Hot
c,C	Cold
o	Outer

i	Inner
th	Thermal
ele	Electrical
cont	Contact
A	Axial
R	Radial

### **Abbreviations and Symbols**

TE	Thermoelectric
TEG	Thermoelectric generator
ATEG	Annular thermoelectric generator
FTEG	Flat thermoelectric generator
TIM	Thermal interface material
CTE	Coefficient of thermal expansion
CPM	Constant property model

## Co-Authorship

This thesis was arranged corresponding to the standard sandwich thesis format and includes multi-authored papers with their academic contribution details. The majority of the contributions to the presented papers were based on the first author's work. The following depicts the contributions of each author as well as demonstrates the contributions of Ahmed A. Abdelnabi the author of this thesis:

**Paper I:** Ahmed A. Abdelnabi, Vickram Lakhian, Joseph R. McDermid, Yu-Chih Tseng, James S. Cotton, " Enhancement of mechanical properties and thermoelectric performance of spark plasma sintered P-type Bismuth Telluride by powder surface oxide reduction," Journal of Alloys and Compounds, (Submitted).

Ahmed A. Abdelnabi: Conceptualization; Data curation; Formal analysis; Investigation; Methodology; Validation; Visualization; Writing - original draft; Vickram Lakhian: Investigation; Methodology; Writing - review & editing. Joseph R. McDermid: Methodology; Writing - review & editing, Yu-Chih Tseng: Data curation; Formal analysis, James S. Cotton: Conceptualization; Funding acquisition; Project administration; Resources; Supervision; Writing - review & editing.

**Paper II:** Ahmed A. Abdelnabi, Vickram Lakhian, Joseph R. McDermid, James S. Cotton, " The effect of powder pre-treatment on the mechanical and thermoelectric properties of spark plasma sintered N-type bismuth telluride," targeted Journal of Alloys and Compounds, (Ready for submission).

Ahmed A. Abdelnabi: Conceptualization; Data curation; Formal analysis; Investigation; Methodology; Validation; Visualization; Writing - original draft; Vickram Lakhian: Investigation;

Methodology; Writing - review & editing. Joseph R. McDermid: Methodology; Writing - review & editing, James S. Cotton: Conceptualization; Funding acquisition; Project administration; Resources; Supervision; Writing - review & editing.

**Paper III:** Ahmed A. Abdelnabi, Joseph R. McDermid, James S. Cotton, " A parametric study aimed at selecting dimensions for a new annular TEG module design that will yield maximum power density and minimum thermal stress," targeted Applied Energy, (Ready for submission).

Ahmed A. Abdelnabi: Conceptualization; Analytical formulations; Modeling; Data curation; Formal analysis; Investigation; Methodology; Validation; Visualization; Writing - original draft; Joseph R. McDermid: Methodology; Writing - review & editing, James S. Cotton: Conceptualization; Deliberating the results; Funding acquisition; Project administration; Resources; Supervision; Writing - review & editing.

## Chapter 1: Introduction

### 1.1 Introduction

Around 72% of the world's energy is lost as heat waste from residential, commercial and industrial processes and power plants [1]. Thermoelectric generators (TEG) are one technology that can be used to recover some of this heat waste, thereby enhancing fuel efficiency and lowering greenhouse gas emissions [2]. TEG modules are solid-state heat engines that are connected to a heat source and a heat sink; the module functions as heat flows through it, which allows it to generate electricity commensurate with its efficiency. The building block of a TEG module is a TEG couple. Typically, each TEG module consists of multiple TEG couples, which are connected electrically in series and thermally in parallel. Since TEG couples contain no moving parts, TEG modules produce no noise or vibration during operation. Notably, TEG modules are also able to operate at low-temperature differences, which makes them ideal for a wide range of heat waste recovery applications, such as in automobile [3–5] and commercial pizza oven energy recovery systems [6].

The efficiency and the electrical power of the TEG module could be obtained from Ioffe's constant property model (CPM) [48]. In the proposed analytical model, the coupling between Peltier heat, thermal conductance, and joule heating was modelled using constant temperature-average thermoelectric properties, an approach which inherently neglects the Thomson effect [28]. The thermal conductance through the couple is represented as  $((T_h - T_c)/R_{TEG th})$ , the Peltier heat is represented as  $(\alpha I T_h)$  for the hot side and  $(\alpha I T_c)$  for the cold side, and the joule heating  $(I^2 r_{TEG})$  is split equally between the hot and cold sides [24]. The  $Q_H$  is calculated as,

$$Q_H = K_{TEG}(T_h - T_c) + \alpha I T_h - \frac{1}{2} I^2 r_{TEG} \quad (1)$$

where  $I$  is the electrical current,  $T_c$  is the TEG module cold-side temperature, and  $R_{TEG\ th}$  is the total thermal resistance of the TEG module. The thermal conductance of the P- and N-type legs in parallel,  $K_{TEG} = \frac{1}{R_{TEG\ th}} = \frac{1}{R_P} + \frac{1}{R_N} = \frac{A_P k_P}{l_P} + \frac{A_N k_N}{l_N}$ , where  $k$  is the thermal conductivity of each leg and  $A$  and  $l$  are the cross section area and the length of each leg, respectively.  $\alpha = |\alpha_P| + |\alpha_N|$ , give the TEG module's total Seebeck coefficient, which is also the P- and N-type legs' absolute Seebeck coefficient values.  $r_{TEG} = r_P + r_N = \frac{l_P \rho_{eP}}{A_P} + \frac{l_N \rho_{eN}}{A_N}$  is the total module electrical resistance, where  $\rho$  is the electrical resistivity of each leg.  $Q_C$  is calculated as:

$$Q_C = K_{TEG}(T_h - T_c) + \alpha I T_c + \frac{1}{2} I^2 r_{TEG} \quad (2)$$

As electrical power produced from the TEG module  $P$  is the difference between the  $Q_H$  and  $Q_C$  values,

$$P = \alpha I (T_h - T_c) - I^2 r_{TEG} \quad (3)$$

For the external electrical load,  $R_L$ , which is powered by the TEG module,  $P$  is also calculated as:

$$P = I^2 R_L \quad (4)$$

The current flowing through the  $R_L$  is:

$$I = \frac{\alpha (T_h - T_c)}{R_L + r_{TEG}} \quad (5)$$

The load ratio is defined as:

$$\frac{R_L}{r_{TEG}} = m \quad (6)$$

By substituting Eq. (5) and (6) into Eq. (4), the power could be presented in the following form:



$$P = \frac{\alpha^2}{r_{TEG}} (T_h - T_c)^2 \frac{m}{(m + 1)^2} \quad (7)$$

In which the term  $\frac{\alpha^2}{r_{TEG}}$  resembles the power factor of the TEG module as the power factor of a single TE leg is  $\frac{\alpha^2}{\rho_e}$ . The thermal efficiency is calculated as follows:

$$\eta = \frac{P}{Q_H} \quad (8)$$

By substituting Eq. (1), (3), (5) and (6) into Eq. (8), the module thermal efficiency could be presented in the following form:

$$\eta = \frac{T_h - T_c}{T_h} \times \frac{\frac{m}{m + 1}}{\frac{K_{TEG} r_{TEG}}{\alpha^2} \times \frac{m + 1}{T_h} - \frac{1}{2} (T_h - T_c) \times \frac{1}{m + 1} + 1} \quad (9)$$

The module thermal efficiency consists of two main parts which are the Carnot thermal efficiency of a heat engine ( $\frac{T_h - T_c}{T_h}$ ) and the other is the TE materials efficiency part which contains the material properties represented in the term  $\frac{K_{TEG} r_{TEG}}{\alpha^2}$  that is denoted by  $1/Z$ . The figure of merit  $Z$  is a measure of the TE material efficiency. The dimensionless form of the figure of merit of a TE material could be written as:

$$ZT = \frac{\alpha^2 T}{\rho_e k} \quad (10)$$

where  $\alpha$  is the Seebeck coefficient,  $T$  is the temperature in Kelvins,  $\rho_e$  is the electrical resistivity, and  $k$  is the thermal conductivity.

$\text{Bi}_2\text{Te}_3$  solution-based compounds are of significant interest in the application of thermoelectric materials (TE) used in low-temperature cooling and power generation applications

[7]. Although P- and N-type  $\text{Bi}_2\text{Te}_3$  TE materials created using spark plasma sintering (SPS) have been found to show enhanced thermoelectric properties, the powder must be stored and handled in an inert environment to avoid the formation of an external oxide layer [8], [8]. The presence of the oxides in the  $\text{Bi}_2\text{Te}_3$  powder affects the thermoelectric properties, where performing a reduction step using  $\text{H}_2$  on the powder results in improved thermoelectric properties of the SPS processed samples [9–11] [9,12–16]. Oxide removal was found to increase the carrier concentration and decreases the mobility. The increase in the carrier concentration was the main reason for the Seebeck coefficient increase and the thermal conductivity decrease. The electrical resistivity was found to increase despite the decrease in carrier mobility as the increase in the carrier concentration was the dominant factor. Lim et al. [9] and Seo et al. [13], studied the effect of  $\text{H}_2$  reduction on an oxidized P-type  $\text{Bi}_{0.5}\text{Sb}_{1.5}\text{Te}_3$  powder. The reduction procedure reduced the oxygen content to 1580 and 2000 ppm in the powder and increased the sintered part  $ZT_{\text{max}}$  to 0.92 and 1.05, respectively, due to an increase in the carrier concentration. Rimal et al. [11] found that oxide removal in N-type  $\text{Bi}_2\text{Se}_{0.3}\text{Te}_{2.7}$  using  $\text{H}_2$  at 360 °C for 4 h enhanced the maximum power factor at 30 °C from  $9.5 \times 10^{-5}$  to  $11.5 \times 10^{-5}$  W/(K<sup>2</sup> m).

Unidirectional crystal growth such as zone melting and Bridgman technique [17,18] are used to prepare  $\text{Bi}_2\text{Te}_3$  alloys. Even though Single crystals have high thermoelectric properties, they suffer from poor mechanical properties due to the weak Van der Waals bond between Te-Te layers which forms cleavage plans between unit crystals [19,20]. Pan et al [21] found that the strength of a SPS P and N type  $\text{Bi}_2\text{Te}_3$  increased by around 3 times over the ingot and the hardness was increased by 65% and 69% for P and N type  $\text{Bi}_2\text{Te}_3$ , respectively. Jun Jiang et al studied the effect of SPS on the bending strength of both N-type  $\text{Bi}_2(\text{Te}, \text{Se})_3$  and P-type  $(\text{Bi}, \text{Sb})_2\text{Te}_3$  which increased by around 8 times over that of a zone-melted ingot [22,23]. Zhao et al [24] studied the

hot forging using SPS of  $Bi_2Te_3$  disk samples sintered from mechanically alloyed powder using SPS. The hot forging was made by using a graphite die with a larger diameter. It is found that the bending strength of the hot forged at 460°C increased from 62 MPa for the sample without hot forging to 120 MPa in the hot forged sample. In this study, the grain boundaries were oriented perpendicular to the pressing direction. It was reported that the bending strength of both N and P type  $Bi_2Te_3$  sintered using SPS increased to a maximum of 60 MPa which is 250% larger in value than of the zone-melted ingots for the same composition [25]. The Vickers micro-hardness of P-type 25%  $Bi_2Te_3$ -75%  $Sb_2Te_3$  sintered using SPS reached maximum value of 112.7 Hv, which is double the value of the zone-melted single crystal [26].

Studies into the impact of SPS on the thermoelectric properties of  $Bi_2Te_3$  have shown mixed results. In a related study by Pan et al, The ZT of the P-type  $Bi_{0.5}Sb_{1.5}Te_3$  increased compared to a Bridgeman formed ingot sample all over the temperature range, but it decreased in the case of the N-type  $Bi_2Te_{2.7}Se_{0.3}$  in the temperature range of 25°C to 150°C [21]. Jiang et al, also reported that the ZT in case of using SPS with and P-type  $(Bi, Sb)_2Te_3$  has increased to 115% of the zone-melted ingot, but decreased to 90% for N-type  $Bi_2(Te, Se)_3$  of the zone-melted ingot [22,23]. Also, the ZT of the hot forged samples at 460°C increased by 33% over the unforged samples [24]. Fan et al, studied the effect of sintering temperature on the thermoelectric properties of N-type  $Bi_2Te_{2.85}Se_{0.15}$  sintered using SPS. Different samples were sintered at 320, 350, 380, 410 and 440 °C for 15 mins and 30 MPa in which the maximum figure of merit (Z) was archived through sintering at 410 °C [27].

Table 1 shows the effect of sintering techniques on the thermoelectric and mechanical properties of  $Bi_2Te_3$ . The SPS found to produce P- and N-type  $Bi_2Te_3$  with high bending strength when compared to zone-melted ingots, hot extrusion, and hot pressing.

Table 1

The effect of sintering technique on the thermoelectric and mechanical properties of Bi<sub>2</sub>Te<sub>3</sub>:

Author	TE material type	Sintering technique	ZT	Bending strength	Tensile strength
Park et al [28]	P-type Bi <sub>0.5</sub> Sb <sub>1.5</sub> Te <sub>3</sub>	Hot extrusion	0.83 @ 25 °C	61.2MPa	NA
Jiang et al [29]	P-type Bi <sub>0.4</sub> Sb <sub>1.6</sub> Te <sub>3</sub>	Zone-melted ingot	1.00 @ 77 °C	10 MPa	NA
Jiang et al [29]	N-type Bi <sub>0.4</sub> Sb <sub>1.6</sub> Te <sub>3</sub>	SPS	1.15 @ 77 °C	80 MPa	NA
Jiang et al [30]	N-type Bi <sub>2</sub> Te <sub>2.8</sub> Se <sub>0.2</sub>	Zone-melted ingot	0.8 @ 77 °C	10 MPa	NA
Jiang et al [30]	N-type Bi <sub>2</sub> Te <sub>2.8</sub> Se <sub>0.2</sub>	SPS	0.7 @ 127 °C	80 MPa	NA
Xu et al [31]	P-type Bi <sub>0.5</sub> Sb <sub>1.5</sub> Te <sub>3</sub>	Zone-melted ingot	0.80 @ 127 °C	27-30 MPa	NA
Xu et al [31]	P-type Bi <sub>0.5</sub> Sb <sub>1.5</sub> Te <sub>3</sub>	Hot pressing	1.36 @ 127 °C	62-68 MPa	NA

There are two main approaches to improving the performance of a TEG module. The first approach involves improving the thermoelectric properties of the thermoelectric TE materials used in the module, which is achieved by improving the ZT, as well as its mechanical properties. Researchers have attempted to increase ZT by increasing the Seebeck coefficient and decreasing

the electrical resistivity and thermal conductivity via ball milling and powder sintering techniques [13,21,22,32–34]. The mechanical strength of the TE material is also an important determinant of TE module performance. Consequently, researchers have explored a number of approaches for improving the strength of TE materials, including additives [35,36], sintering [21], and hot forging [24]. Determining and improving the mechanical properties of the  $\text{Bi}_2\text{Te}_3$  particularly the tensile strength is important for designing a mechanically reliable TEG module. Thermal stresses finite element simulations showed that the highest values of thermal stresses are tensile stresses regardless the TEG module geometry. The high tensile thermal stresses in the TE legs are due to two main reasons [37–40]. The first is the large temperature gradient along the TE legs of the TEG couple. The second is due to the mismatch in the coefficient of thermal expansion between the TE legs material and the solder where the maximum tensile thermal stresses are located [41,42]. The literature in Table 1 shows that the tensile strength of  $\text{Bi}_2\text{Te}_3$  TE material is not found to be measured.

Knowledge of the mechanical properties of  $\text{Bi}_2\text{Te}_3$  TE materials, particularly the tensile strength, as well as the thermoelectric properties are essential for designing reliable, high-quality low temperature thermoelectric modules. However, it is challenging for researchers to find fully characterized  $\text{Bi}_2\text{Te}_3$  TE materials that have the well-documented mechanical and thermoelectric properties needed as an input to finite element models for designing thermoelectric modules. Accordingly, the required properties have tended to be obtained from different sources or to be assumed, which often do not represent the actual material simulated and can lead to unreliable, low quality thermoelectric modules as shown in Table 2.

Table 2

Sources of mechanical and thermoelectric properties used in TEG module finite element design simulation:

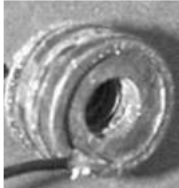

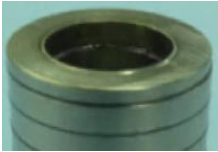


Author	Density	Young's modulus and Poisson ratio	CTE	Thermoelectric properties	Thermal conductivity	Tensile strength
Clin et al [37]	Measured	Measured	Measured	Measured	Measured	NA
Gao et al [43]	[37]	[37]	[37]	[37]	[37]	NA
Al-Merbati et al [44]	[24]	[45]	[45]	[24]	[24]	[45]
Chen et al [46]	[37]	[37]	[37]	[37]	[37]	NA
Erturun et al [47]	[37]	[37]	[37]	[37]	[37]	NA
Yilbas et al [39]	No reference	No reference	No reference	No reference	No reference	No reference
Fan and Gao [48]	[37]	[37]	[37]	Thermonamic.com	Thermonamic.com	NA
Shittu et al [49]	[50]	[50]	[50]	[50]	[50]	No reference

Flat TEG (FTEG) modules require flat interfaces to be integrated into power generation systems. In contrast, ATEG modules are optimal in applications where either the heat source or sink are round in shape. Min et al. [51] fabricated a novel ring-shaped ATEG module made up of two couples that was able to produce 33 mW at a temperature difference of 70 K. Min et al.'s [18] ring-shaped ATEG module offers comparable performance to an FTEG, with the added advantage of a geometry that can be used in applications with radial heat flow. In this ATEG design, the P- and N-type legs were arranged axially in an alternating pattern, so as to fully surround the inside

tube and were linked by metallic connectors. Despite these advantages, subsequent research on ring-shaped ATEGs has revealed a number of challenges, such as high contact resistance due to assembly [52,53] and the cracking of ring-shaped TE legs during manufacturing and testing [54,55]. The successfully manufactured modules were tested at temperature difference of  $<100^{\circ}\text{C}$ , as this temperature range is thought to mitigate the chance of failure during operation due to excessive thermal stresses [51,53] as shown in Table 3.

Table 3

Comparison between different manufactured ATEG modules:

Parameters	Min and Row [51]	Schmitz et al [52]	Sakai et al [53]	Mansouri et al [56]	Morsy [57]
TE Material	$Bi_2Te_3$	$PbTe$	$Bi_2Te_3$	Skutterudite	$Bi_2Te_3$
Geometry					
Module mechanical integrity	No cracks	Cracks during sintering	No cracks	Cracks during sintering	Cracks after sintering and after testing.
Tested parameters	Power output	Electrical resistance	Power output & Efficiency	N/A	Open circuit voltage
Temperature range	$\Delta T = 70^{\circ}\text{C}$	$T = 25^{\circ}\text{C}$	$T_h = 95^{\circ}\text{C}$ , $T_c = 10^{\circ}\text{C}$	N/A	$T_h = 200^{\circ}\text{C}$ , $T_c = 30^{\circ}\text{C}$

Mansouri et al. [54] have made several attempts to manufacture a ring-shaped P-type module by sintering skutterudite directly between two titanium rings to act as metallic conductors. Finite element analysis revealed the possibility of cracking due to thermal stresses caused by the mismatch between the P-type skutterudite and the titanium rings. They were able to eliminate this problem by using multiple legs between brass rings in place of the previous full ring-shaped approach. Morsy [55] was also unable to obtain reproducible performance results for his ring-shaped ATEG modules, which were manufactured using bismuth telluride ( $\text{Bi}_2\text{Te}_3$ ) for both P- and N-type rings, as the rings cracks after each test at a temperature difference of 160 K.

## 1.2 Summary

Designing a high performance and reliable ring-shaped ATEG modules for low temperature applications is challenging giving the available mechanical properties of  $\text{Bi}_2\text{Te}_3$  TE material, particularly the tensile strength. Also, the optimization of module geometry requires a trade-off between performance and mechanical reliability. The literature review also exposed key research gaps, which will be addressed by the current work. 1) There is a knowledge gap in the literature regarding the effect of the oxide removal on mechanical properties of the spark plasma sintered P- and N-type  $\text{Bi}_2\text{Te}_3$  TE material. 2) It is challenging for researchers to find well-documented and fully characterized mechanical and thermoelectric properties for finite element TEG modeling of the spark plasma sintered P- and N-type  $\text{Bi}_2\text{Te}_3$  TE material. 3) To the best of our knowledge, no prior research has examined the mechanical reliability of ATEG couples with ring-shaped legs. 4) Prior studies have only considered the heat and electric current flows in the ATEG in the radial direction. And 5) prior ATEG thermal stress analyses have neglected to consider the effects of the hot-side and cold-side heat exchangers; rather, these effects have only been considered in performance studies.



### 1.3 Objective and Contributions

The main objective of the current work is to design a reliable, robust, and predictable thermoelectric and mechanical performance ring-shaped ATEG module. The presented work add together to form a methodology to powder pre-treatment and full thermoelectric and mechanical properties characterization of spark plasma sintered P- and N-type  $\text{Bi}_2\text{Te}_3$  as well as, analytical and 3D coupled modeling of the thermoelectric performance and thermal stresses of ring-shaped ATEG module. The contributions of this Ph.D. work, which are fully documented in the three journal publications presented in this thesis, can be summarized into the following:

- A TE materials powder pre-treatment methodology that uses mechanically agitated facility built in-house in which vibration and gas flow are utilized in powder particles fluidization aiming to enhance mixing and increases the gas-powder contact time.
- The development of a direct uniaxial tensile measurement method for small brittle TE samples. An special in-house built fixture capable of measuring the tensile strength of The methodology was adopted from following the same methodology found in the ASTM C1468-13 [58] standard to ensure uniaxial tensile failure, a special in-house fixture was made.
- A constant property model (CPM) analytical model was constructed to assess the thermoelectric performance of the ring-shaped ATEG couple and investigate the effect of couple configuration and dimensions on the performance.
- A 3D coupled finite element ANSYS model was constructed to investigate both the thermoelectric performance and the thermal stress fields of the ring-shaped ATEG couple and investigate the effect of changing the couple configuration and dimensions.

Below is a brief description of the main contributions of each publication.

Paper I: The paper titled “Enhancement of mechanical properties and thermoelectric performance of spark plasma sintered P-type Bismuth Telluride by powder surface oxide reduction” focuses on determining the effect of powder preparation technique including annealing and surface oxide removal using H<sub>2</sub> on the mechanical and thermoelectric properties of SPS sintered P-type (Bi,Sb)<sub>2</sub>Te<sub>3</sub> TE materials.

The novelty of this investigation is the precise measurement of key mechanical design parameters and the thermoelectric performance of spark plasma sintered P-type Bi<sub>0.4</sub>Sb<sub>1.6</sub>Te<sub>3</sub> material. The effect of the powder preparation technique on the powder surface oxide layer as well as both the mechanical and thermoelectric properties were determined on identically prepared sintered samples in both parallel and perpendicular direction to the sintering pressure.

Paper II: In the paper titled “The effect of powder pre-treatment on the mechanical and thermoelectric properties of spark plasma sintered N-type bismuth telluride” the effect of N-type (Bi<sub>0.95</sub> Sb<sub>0.05</sub>)<sub>2</sub>(Se<sub>0.05</sub> Te<sub>0.95</sub>)<sub>3</sub> powder particles pre-treatments, including annealing and surface oxides reduction, was determined in terms of both the mechanical and thermoelectric properties for bodies fabricated using SPS.

The novelty of this investigation is the precise measurement of key mechanical design parameters and the thermoelectric performance of spark plasma sintering N-type (Bi<sub>0.95</sub> Sb<sub>0.05</sub>)<sub>2</sub>(Se<sub>0.05</sub> Te<sub>0.95</sub>)<sub>3</sub> material. The effect of the powder pre-treatment technique on both the mechanical and thermoelectric properties were determined on identically prepared sintered samples in both parallel and perpendicular direction to the sintering pressure.

Paper III: The paper titled “A parametric study aimed at selecting dimensions for a new annular TEG module design that will yield maximum power density and minimum thermal stress”

investigated how heat flow/electrical current paths and dimensions affect the performance and thermal stress fields in ring-shaped ATEG couples.

The contribution from this paper is the development of an analytical and a 3D coupled finite element models that investigate the effect of TE rings dimensions and heat flow/electrical current paths in ring-shaped ATEG couple on the thermoelectric performance and thermal stresses field. To this end, two ring-shaped ATEG couple configurations integrated between hot-side and cold-side heat exchangers are compared with respect to their heat/electrical current flow paths: one that allow for radial flow (radial configuration), and one that allows for axial flow (axial configuration). The model accounted for the additional electrical contact resistance of the solder between the P and N legs, as well as the thermal contact resistance between the annular TEG couple and both the hot-side and cold-side heat exchangers. The model was extended to capture the effect of the hot-side and the cold-side heat exchangers in order to establish constant hot gases ( $T_g$ ) and constant cooling water ( $T_w$ ) temperatures as the thermal boundary conditions.

#### **1.4 Thesis Organization**

This thesis is organized into 5 chapters:

**Chapter 1** introduces the thesis with a critical literature review that highlights the core focus of this study and the key research gaps in the field. Also, it provides a background for the publications presented in this thesis. This chapter highlights the contributions of this academic work to the state-of-the-art literature in the field of annular thermoelectric generators and summarizes the organization of this thesis.

**Chapter 2** presents the first paper titled: “Enhancement of mechanical properties and thermoelectric performance of spark plasma sintered P-type Bismuth Telluride by powder surface oxide reduction”

**Chapter 3** presents the second paper titled: “The effect of powder pre-treatment on the mechanical and thermoelectric properties of spark plasma sintered N-type bismuth telluride”

**Chapter 4** presents the third paper titled: “A parametric study aimed at selecting dimensions for a new annular TEG module design that will yield maximum power density and minimum thermal stress”

**Chapter 5** concludes the thesis and recommends future work on the subject matter.

## 1.5 References

- [1] C. Forman, I.K. Muritala, R. Pardemann, B. Meyer, Estimating the global waste heat potential, *Renew. Sustain. Energy Rev.* 57 (2016) 1568–1579.  
<https://doi.org/10.1016/j.rser.2015.12.192>.
- [2] D.M. Rowe, *CRC Handbook of THERMOELECTRICS*, CRC press LLC, 1995.
- [3] A. Massaguer, E. Massaguer, M. Comamala, T. Pujol, J.R. González, M.D. Cardenas, D. Carbonell, A.J. Bueno, A method to assess the fuel economy of automotive thermoelectric generators, *Appl. Energy.* 222 (2018) 42–58.  
<https://doi.org/10.1016/j.apenergy.2018.03.169>.
- [4] Y. Wang, S. Li, X. Xie, Y. Deng, X. Liu, C. Su, Performance evaluation of an automotive thermoelectric generator with inserted fins or dimpled-surface hot heat exchanger, *Appl. Energy.* 218 (2018) 391–401. <https://doi.org/10.1016/j.apenergy.2018.02.176>.
- [5] B. Li, K. Huang, Y. Yan, Y. Li, S. Twaha, J. Zhu, Heat transfer enhancement of a modularised thermoelectric power generator for passenger vehicles, *Appl. Energy.* 205 (2017) 868–879. <https://doi.org/10.1016/j.apenergy.2017.08.092>.
- [6] M.H. Zaher, M.Y. Abdelsalam, J.S. Cotton, Study of the effects of axial conduction on the performance of thermoelectric generators integrated in a heat exchanger for waste heat recovery applications, *Appl. Energy.* 261 (2020) 114434.  
<https://doi.org/10.1016/j.apenergy.2019.114434>.
- [7] E.D.M. Rowe, D. Ph, D. Sc, F. Group, *Thermoelectric Handbook - Macro to Nano*, CRC Press Taylor & Francis Group, 2006.
- [8] H. Bando, K. Koizumi, Y. Oikawa, K. Daikohara, V. a. Kulbachinskii, H. Ozaki, The time-dependent process of oxidation of the surface of Bi<sub>2</sub>Te<sub>3</sub> studied by X-ray

- photoelectron spectroscopy, *J. Phys. Condens. Matter.* 12 (2000) 5607.  
<https://doi.org/10.1088/0953-8984/12/26/307>.
- [9] C.H. Lim, D.C. Cho, Y.S. Lee, C.H. Lee, Effects of Hydrogen Reduction on the Thermoelectric Properties of Spark-Plasma-Sintered Bi<sub>2</sub>Te<sub>3</sub>-Based Compounds, 46 (2005) 995–1000.
- [10] Y. Horio, A. Inoue, Effect of Oxygen Content on Thermoelectric Properties of n-Type (Bi,Sb)<sub>2</sub>(Te,Se)<sub>3</sub> Alloys Prepared by Rapid Solidification and Hot-Pressing Techniques, *Mater. Trans.* 47 (2006) 1412–1416. <https://doi.org/10.2320/matertrans.47.1412>.
- [11] P. Rimal, S.-M. Yoon, E.-B. Kim, C.-H. Lee, S.-J. Hong, Effects of Hydrogen Reduction in Microstructure, Mechanical and Thermoelectric Properties of Gas Atomized n-type Bi<sub>2</sub>Te<sub>2.7</sub>Se<sub>0.3</sub> Material, *J. Korean Powder Metall. Inst.* 23 (2016) 126–131.  
<https://doi.org/10.4150/KPMI.2016.23.2.126>.
- [12] J. Seo, K. Park, D. Lee, C. Lee, Characteristics of p-type Bi<sub>0.5</sub>Sb<sub>1.5</sub>Te<sub>3</sub> compounds doped with Te, *Mater. Lett.* 35 (1998) 4–9. [https://doi.org/10.1016/S0167-577X\(97\)00217-6](https://doi.org/10.1016/S0167-577X(97)00217-6).
- [13] S. Seo, Y. Jeong, M.W. Oh, B. Yoo, Effect of hydrogen annealing of ball-milled Bi<sub>0.5</sub>Sb<sub>1.5</sub>Te<sub>3</sub> powders on thermoelectric properties, *J. Alloys Compd.* 706 (2017) 576–583. <https://doi.org/10.1016/j.jallcom.2017.02.181>.
- [14] H.S. Shin, H.P. Ha, D. Bin Hyun, J.D. Shim, D.H. Lee, Thermoelectric properties of 25%Bi<sub>2</sub>Te<sub>3</sub>-75%Sb<sub>2</sub>Te<sub>3</sub> solid solution prepared by hot-pressing method, *J. Phys. Chem. Solids.* 58 (1997) 671–678. [https://doi.org/10.1016/S0022-3697\(96\)00049-2](https://doi.org/10.1016/S0022-3697(96)00049-2).
- [15] K. Park, J.H. Seo, D.C. Cho, B.H. Choi, C.H. Lee, Thermoelectric properties of p-type Te doped Bi<sub>0.5</sub>Sb<sub>1.5</sub>Te<sub>3</sub> fabricated by powder extrusion, *Mater. Sci. Eng. B Solid-State Mater. Adv. Technol.* 88 (2002) 103–106. [https://doi.org/10.1016/S0921-5107\(01\)00912-](https://doi.org/10.1016/S0921-5107(01)00912-)

6.

- [16] S. Yoon, C. Nagarjuna, D. Shin, C. Lee, B. Madavali, S. Hong, K. Lee, Influence of milling atmosphere on thermoelectric properties of p-type Bi-Sb-Te based alloys by mechanical alloying, *J. Korean Powder Metall. Inst.* 24 (2017) 357–363.  
<https://doi.org/10.4150/KPMI.2017.24.5.357>.
- [17] O.B. Sokolov, S.Y. Skipidarov, N.I. Duvankov, The variation of the equilibrium of chemical reactions in the process of (Bi<sub>2</sub>Te<sub>3</sub>)(Sb<sub>2</sub>Te<sub>3</sub>)(Sb<sub>2</sub>Se<sub>3</sub>) crystal growth, *J. Cryst. Growth.* 236 (2002) 181–190. [https://doi.org/10.1016/S0022-0248\(01\)01808-5](https://doi.org/10.1016/S0022-0248(01)01808-5).
- [18] O. Yamashita, S. Tomiyoshi, K. Makita, Bismuth telluride compounds with high thermoelectric figures of merit, *J. Appl. Phys.* 93 (2003) 368–374.  
<https://doi.org/10.1063/1.1525400>.
- [19] G. Kavei, Improving Hardness and Thermoelectric Performance in Pseudo-ternary Thermoelectric Alloys (Bi<sub>2</sub>Te<sub>3</sub>)(Bi<sub>2</sub>Se<sub>3</sub>)(Nd<sub>2</sub>Te<sub>3</sub>), *Jpn. J. Appl. Phys.* 45 (2006) 7032–7035. <https://doi.org/10.1143/JJAP.45.7032>.
- [20] J.P. Fleurial, L. Gailliard, R. Triboulet, H. Scherrer, S. Scherrer, Thermal properties of high quality single crystals of bismuth telluride—Part I: Experimental characterization, *J. Phys. Chem. Solids.* 49 (1988) 1237–1247. [https://doi.org/10.1016/0022-3697\(88\)90182-5](https://doi.org/10.1016/0022-3697(88)90182-5).
- [21] Y. Pan, T.-R. Wei, Q. Cao, J.-F. Li, Mechanically enhanced p- and n-type Bi<sub>2</sub>Te<sub>3</sub>-based thermoelectric materials reprocessed from commercial ingots by ball milling and spark plasma sintering, *Mater. Sci. Eng. B.* 197 (2015) 75–81.  
<https://doi.org/10.1016/j.mseb.2015.03.011>.
- [22] J. Jiang, L. Chen, S. Bai, Q. Yao, Thermoelectric performance of p-type Bi-Sb-Te

- materials prepared by spark plasma sintering, *J. Alloys Compd.* 390 (2005) 208–211.  
<https://doi.org/10.1016/j.jallcom.2004.07.056>.
- [23] J. Jiang, L. Chen, S. Bai, Q. Yao, Q. Wang, Fabrication and thermoelectric performance of textured n-type  $\text{Bi}_2(\text{Te,Se})_3$  by spark plasma sintering, *Mater. Sci. Eng. B.* 117 (2005) 334–338. <https://doi.org/10.1016/j.mseb.2005.01.002>.
- [24] L.D. Zhao, B.P. Zhang, J.F. Li, H.L. Zhang, W.S. Liu, Enhanced thermoelectric and mechanical properties in textured n-type  $\text{Bi}_2\text{Te}_3$  prepared by spark plasma sintering, *Solid State Sci.* 10 (2008) 651–658. <https://doi.org/10.1016/j.solidstatesciences.2007.10.022>.
- [25] X. a Fan, J.Y. Yang, W. Zhu, S.Q. Bao, X.K. Duan, C.J. Xiao, Q.Q. Zhang, Z. Xie, Effect of nominal  $\text{Sb}_2\text{Te}_3$  content on thermoelectric properties of p-type  $(\text{Bi}_2\text{Te}_3)_x(\text{Sb}_2\text{Te}_3)_{1-x}$  alloys by MA–HP, *J. Phys. D. Appl. Phys.* 39 (2006) 5069–5073.  
<https://doi.org/10.1088/0022-3727/39/23/025>.
- [26] X. a Fan, J.Y. Yang, R.G. Chen, H.S. Yun, W. Zhu, S.Q. Bao, X.K. Duan, Characterization and thermoelectric properties of p-type  $25\%\text{Bi}_2\text{Te}_3-75\%\text{Sb}_2\text{Te}_3$  prepared via mechanical alloying and plasma activated sintering, *J. Phys. D. Appl. Phys.* 39 (2006) 740–745. <https://doi.org/10.1088/0022-3727/39/4/021>.
- [27] J. Yang, R. Chen, X. Fan, W. Zhu, S. Bao, X. Duan, Microstructure control and thermoelectric properties improvement to n-type bismuth telluride based materials by hot extrusion, *J. Alloys Compd.* 429 (2007) 156–162.  
<https://doi.org/10.1016/j.jallcom.2006.04.030>.
- [28] K. Park, J.H. Seo, D.C. Cho, B.H. Choi, C.H. Lee, Thermoelectric properties of p-type Te doped  $\text{Bi}_{0.5}\text{Sb}_{1.5}\text{Te}_3$  fabricated by powder extrusion, 88 (2001) 103–106.
- [29] J. Jiang, L. Chen, S. Bai, Q. Yao, Thermoelectric performance of p-type Bi-Sb-Te



- materials prepared by spark plasma sintering, *J. Alloys Compd.* 390 (2005) 208–211.  
<https://doi.org/10.1016/j.jallcom.2004.07.056>.
- [30] J. Jiang, L. Chen, S. Bai, Q. Yao, Q. Wang, Fabrication and thermoelectric performance of textured n-type  $\text{Bi}_2(\text{Te,Se})_3$  by spark plasma sintering, *Mater. Sci. Eng. B Solid-State Mater. Adv. Technol.* 117 (2005) 334–338. <https://doi.org/10.1016/j.mseb.2005.01.002>.
- [31] Z.J. Xu, L.P. Hu, P.J. Ying, X.B. Zhao, T.J. Zhu, Enhanced thermoelectric and mechanical properties of zone melted p-type  $(\text{Bi,Sb})_2\text{Te}_3$  thermoelectric materials by hot deformation, *Acta Mater.* 84 (2015) 385–392. <https://doi.org/10.1016/j.actamat.2014.10.062>.
- [32] J.H. Son, M.W. Oh, B.S. Kim, S.D. Park, B.K. Min, M.H. Kim, H.W. Lee, Effect of ball milling time on the thermoelectric properties of p-type  $(\text{Bi,Sb})_2\text{Te}_3$ , *J. Alloys Compd.* 566 (2013) 168–174. <https://doi.org/10.1016/j.jallcom.2013.03.062>.
- [33] J. Jiang, L. Chen, Q. Yao, Q. Wang, Preparation and Properties of p-Type  $(\text{Bi}_2\text{Te}_3)_x(\text{Sb}_2\text{Te}_3)_{1-x}$  Thermoelectric Materials, 46 (2005) 959–962.
- [34] C.H. Lim, K.T. Kim, Y.H. Kim, Y.S. Lee, C.H. Lee, D.C. Cho, C.H. Lee, Effect of powder mixing on thermoelectric properties in  $\text{Bi}_2\text{Te}_3$ -based sintered compounds, *Intermetallics.* 14 (2006) 1370–1374. <https://doi.org/10.1016/j.intermet.2005.10.018>.
- [35] D.W. Liu, J.F. Li, C. Chen, B.P. Zhang, Effects of SiC nanodispersion on the thermoelectric properties of p-type and n-Type  $\text{Bi}_2\text{Te}_3$ -based alloys, *J. Electron. Mater.* 40 (2011) 992–998. <https://doi.org/10.1007/s11664-010-1476-x>.
- [36] L.D. Zhao, B.P. Zhang, J.F. Li, M. Zhou, W.S. Liu, J. Liu, Thermoelectric and mechanical properties of nano-SiC-dispersed  $\text{Bi}_2\text{Te}_3$  fabricated by mechanical alloying and spark plasma sintering, *J. Alloys Compd.* 455 (2008) 259–264.  
<https://doi.org/10.1016/j.jallcom.2007.01.015>.

- [37] T. Clin, S. Turenne, D. Vasilevskiy, R.A. Masut, Numerical simulation of the thermomechanical behavior of extruded bismuth telluride alloy module, *J. Electron. Mater.* 38 (2009) 994–1001. <https://doi.org/10.1007/s11664-009-0756-9>.
- [38] A.S. Al-Merbaty, B.S. Yilbas, A.Z. Sahin, Thermodynamics and thermal stress analysis of thermoelectric power generator: Influence of pin geometry on device performance, *Appl. Therm. Eng.* 50 (2013) 683–692. <https://doi.org/10.1016/j.applthermaleng.2012.07.021>.
- [39] B.S. Yilbas, S.S. Akhtar, A.Z. Sahin, Thermal and stress analyses in thermoelectric generator with tapered and rectangular pin configurations, *Energy*. 114 (2016) 52–63. <https://doi.org/10.1016/j.energy.2016.07.168>.
- [40] S. Shittu, G. Li, X. Zhao, X. Ma, Y.G. Akhlaghi, E. Ayodele, High performance and thermal stress analysis of a segmented annular thermoelectric generator, *Energy Convers. Manag.* 184 (2019) 180–193. <https://doi.org/10.1016/j.enconman.2019.01.064>.
- [41] M. Picard, S. Turenne, D. Vasilevskiy, R.A. Masut, Numerical simulation of performance and thermomechanical behavior of thermoelectric modules with segmented bismuth-telluride-based legs, *J. Electron. Mater.* 42 (2013) 2343–2349. <https://doi.org/10.1007/s11664-012-2435-5>.
- [42] S. Turenne, T. Clin, D. Vasilevskiy, R.A. Masut, Finite element thermomechanical modeling of large area thermoelectric generators based on bismuth telluride alloys, *J. Electron. Mater.* 39 (2010) 1926–1933. <https://doi.org/10.1007/s11664-009-1049-z>.
- [43] J.L. Gao, Q.G. Du, X.D. Zhang, X.Q. Jiang, Thermal Stress Analysis and Structure Parameter Selection for a Bi<sub>2</sub>Te<sub>3</sub>-Based Thermoelectric Module, *J. Electron. Mater.* 40 (2011) 884–888. <https://doi.org/10.1007/S11664-011-1611-3>.
- [44] A.S. Al-Merbaty, B.S. Yilbas, A.Z. Sahin, Thermodynamics and thermal stress analysis of

- thermoelectric power generator: Influence of pin geometry on device performance, *Appl. Therm. Eng.* 50 (2013) 683–692. <https://doi.org/10.1016/j.applthermaleng.2012.07.021>.
- [45] Y. Tong, F. Yi, L. Liu, P. Zhai, Q. Zhang, Molecular dynamics study on thermo-mechanical properties of bismuth telluride bulk, *Comput. Mater. Sci.* 48 (2010) 343–348. <https://doi.org/10.1016/j.commatsci.2010.01.019>.
- [46] G. Chen, Y. Mu, P. Zhai, G. Li, Q. Zhang, An investigation on the coupled thermal-mechanical-electrical response of automobile thermoelectric materials and devices, *J. Electron. Mater.* 42 (2013) 1762–1770. <https://doi.org/10.1007/s11664-012-2422-x>.
- [47] U. Erturun, K. Erermis, K. Mossi, Effect of various leg geometries on thermo-mechanical and power generation performance of thermoelectric devices, *Appl. Therm. Eng.* 73 (2014) 128–141. <https://doi.org/10.1016/j.applthermaleng.2014.07.027>.
- [48] S. Fan, Y. Gao, Numerical simulation on thermoelectric and mechanical performance of annular thermoelectric generator, *Energy.* 150 (2018) 38–48. <https://doi.org/10.1016/j.energy.2018.02.124>.
- [49] S. Shittu, G. Li, X. Zhao, X. Ma, Y.G. Akhlaghi, E. Ayodele, High performance and thermal stress analysis of a segmented annular thermoelectric generator, *Energy Convers. Manag.* 184 (2019) 180–193. <https://doi.org/10.1016/j.enconman.2019.01.064>.
- [50] Z.G. Shen, X. Liu, S. Chen, S.Y. Wu, L. Xiao, Z.X. Chen, Theoretical analysis on a segmented annular thermoelectric generator, *Energy.* 157 (2018) 297–313. <https://doi.org/10.1016/j.energy.2018.05.163>.
- [51] G. Min, D.M. Rowe, Ring-structured thermoelectric module, *Semicond. Sci. Technol.* 22 (2007) 880–883. <https://doi.org/10.1088/0268-1242/22/8/009>.
- [52] A. Schmitz, C. Stiewe, E. Müller, Preparation of ring-shaped thermoelectric legs from

- PbTe powders for tubular thermoelectric modules, *J. Electron. Mater.* 42 (2013) 1702–1706. <https://doi.org/10.1007/s11664-012-2402-1>.
- [53] A. Sakai, T. Kanno, K. Takahashi, H. Tamaki, Y. Yamada, Power Generation and Peltier Refrigeration by a Tubular Pi-Type Thermoelectric Module, *J. Electron. Mater.* 44 (2015) 4510–4515. <https://doi.org/10.1007/s11664-015-4017-9>.
- [54] N. Mansouri, E.J. Timm, H.J. Schock, D. Sahoo, A. Kotrba, Development of a Circular Thermoelectric Skutterudite Couple Using Compression Technology, *J. Energy Resour. Technol.* 138 (2016) 052003. <https://doi.org/10.1115/1.4032619>.
- [55] M. Morsy, Manufacturing and Characterization of Annular Thermoelectric Generators and Verification of a Novel Design, McMaster University, Hamilton, Canada, 2015.
- [56] N. Mansouri, E.J. Timm, H.J. Schock, D. Sahoo, A. Kotrba, Development of a Circular Thermoelectric Skutterudite Couple Using Compression Technology, *J. Energy Resour. Technol.* 138 (2016) 052003. <https://doi.org/10.1115/1.4032619>.
- [57] M. Morsy, Manufacturing and Characterization of Annular Thermoelectric Generators and Verification of a Novel Design, (2015).
- [58] A.U. Tensile, C.A. Force, Standard Test Method for Transthickness Tensile Strength of Continuous Fiber- Reinforced Advanced Ceramics at Ambient Temperature 1, i (2012) 1–16. <https://doi.org/10.1520/C1468-06.2>.
- [59] J.M. Simard, D. Vasilevskiy, S. Turenne, Influence of composition and texture on the thermoelectric and mechanical properties of extruded  $(\text{Bi}_{1-x}\text{Sbx})_2(\text{Te}_{1-y}\text{Sey})_3$  alloys, *Int. Conf. Thermoelectr. ICT, Proc. 2003-Janua* (2003) 13–18. <https://doi.org/10.1109/ICT.2003.1287438>.
- [60] O. Yamashita, S. Tomiyoshi, Effect of annealing on thermoelectric properties of bismuth

telluride compounds, *Jpn. J. Appl. Phys.* 42 (2003) 492–500.

<https://doi.org/10.1143/JJAP.42.492>.

- [61] J.-L. Gao, Q.-G. Du, X.-D. Zhang, X.-Q. Jiang, Thermal Stress Analysis and Structure Parameter Selection for a Bi<sub>2</sub>Te<sub>3</sub>-Based Thermoelectric Module, *J. Electron. Mater.* 40 (2011) 884–888. <https://doi.org/10.1007/s11664-011-1611-3>.
- [62] X. Jia, Y. Gao, Estimation of thermoelectric and mechanical performances of segmented thermoelectric generators under optimal operating conditions, *Appl. Therm. Eng.* 73 (2014) 333–340. <https://doi.org/10.1016/j.applthermaleng.2014.07.069>.
- [63] S. Fan, Y. Gao, Numerical simulation on thermoelectric and mechanical performance of annular thermoelectric generator, *Energy*. 150 (2018) 38–48. <https://doi.org/10.1016/j.energy.2018.02.124>.
- [64] S. St-Laurent, S. Chen, H. Li, Low melting point metal or alloy powders atomization manufacturing processes, US 20190193164 A1, 2018.
- [65] M.M. Stasova, N.H. Abrikosov, *Izv. Akad. Nauk SSSR, Neorg. Mater.*, 6, 1090, 1970.
- [66] V.B. Chernogorenko, K.A. Lynchak, Z.A. Klimak, R.A. Morozova, Kinetics of antimony trioxide reduction by hydrogen. Effect of atomic hydrogen, *Sov. Powder Metall. Met. Ceram.* 17 (1978) 419–421. <https://doi.org/10.1007/BF00795791>.
- [67] Standard Test Methods for Determining Average Grain Size, *ASTM Stand.* (2020) 1–28. <https://doi.org/10.1520/E0112-13.1.4>.
- [68] Z. Zhang, P.A. Sharma, E.J. Lavernia, N. Yang, Thermoelectric and transport properties of nanostructured Bi<sub>2</sub>Te<sub>3</sub> by spark plasma sintering, *J. Mater. Res.* 26 (2011) 475–484. <https://doi.org/10.1557/jmr.2010.67>.
- [69] H.S. B. Eisenmann, *LANDOLT-BORNSTEIN Numerical Data and Functional*

Relationships in Science and Technology, 1985.

- [70] L.M. Pavlova, Y.I. Shtern, R.E. Mironov, Thermal expansion of bismuth telluride, *High Temp.* 49 (2011) 369–379. <https://doi.org/10.1134/S0018151X1103014X>.
- [71] G.D. Quinn, B.T. Sparenberg, P. Koshy, L.K. Ives, S. Jahanmir, D.D. Arola, Flexural Strength of Ceramic and Glass Rods, 37 (2009) 1–23.
- [72] Y. Zheng, H. Xie, S. Shu, Y. Yan, H. Li, X. Tang, High-temperature mechanical and thermoelectric properties of p-type Bi<sub>0.5</sub>Sb<sub>1.5</sub>Te<sub>3</sub> commercial zone melting ingots, *J. Electron. Mater.* 43 (2014) 2017–2022. <https://doi.org/10.1007/s11664-013-2938-8>.
- [73] L. Ćurković, A. Bakić, J. Kodvanj, T. Haramina, Flexural strength of alumina ceramics: Weibull analysis, *Trans. Famena.* 34 (2010) 13–18.
- [74] Astm, Standard Practice for Reporting Uniaxial Strength Data and Estimating Weibull Distribution Parameters for Advanced Ceramics, *Astm. i* (2000) 1–17. <https://doi.org/10.1520/C1239-13.Scope>.
- [75] D.R.L. Ed, CRC Handbook of Chemistry and Physics, 84th Edition, 2003-2004, (n.d.).
- [76] T.A.C. Society-discussions, Effect of Porosity on Young's, 45 (n.d.) 94–95.
- [77] K.K. Phani, S.K. Niyogi, Young's modulus of porous brittle solids, *J. Mater. Sci.* 22 (1987) 257–263. <https://doi.org/10.1007/BF01160581>.
- [78] J. Luo, R. Stevens, Porosity-dependence of elastic moduli and hardness of 3Y-TZP ceramics, 25 (1999).
- [79] M. Asmani, C. Kermel, A. Leriche, M. Ourak, Influence of porosity on Young's modulus and poisson's ratio in alumina ceramics, *J. Eur. Ceram. Soc.* 21 (2001) 1081–1086. [https://doi.org/10.1016/S0955-2219\(00\)00314-9](https://doi.org/10.1016/S0955-2219(00)00314-9).
- [80] ASTM, Standard Practice for Measuring Ultrasonic Velocity in Materials, 2015.

<https://doi.org/10.1520/E0494-15>.

- [81] M.L. Lwin, P. Dharmiah, B. Madavali, C.H. Lee, D. won Shin, G. Song, K.H. Lee, S.J. Hong, Oxide formation mechanism and its effect on the microstructure and thermoelectric properties of p-type Bi<sub>0.5</sub>Sb<sub>1.5</sub>Te<sub>3</sub> alloys, *Intermetallics*. 103 (2018) 23–32.  
<https://doi.org/10.1016/j.intermet.2018.09.015>.
- [82] J.M. Schultz, J.P. McHugh, W.A. Tiller, Effects of heavy deformation and annealing on the electrical properties of Bi<sub>2</sub>Te<sub>3</sub>, *J. Appl. Phys.* 33 (1962) 2443–2450.  
<https://doi.org/10.1063/1.1728990>.
- [83] J. Horák, K. Čermák, L. Koudelka, Energy formation of antisite defects in doped Sb<sub>2</sub>Te<sub>3</sub> and Bi<sub>2</sub>Te<sub>3</sub> crystals, *J. Phys. Chem. Solids*. 47 (1986) 805–809.  
[https://doi.org/10.1016/0022-3697\(86\)90010-7](https://doi.org/10.1016/0022-3697(86)90010-7).
- [84] Z. Starý, J. Horák, M. Stordeur, M. Stölzer, Antisite defects in Sb<sub>2-x</sub>Bi<sub>x</sub>Te<sub>3</sub> mixed crystals, *J. Phys. Chem. Solids*. 49 (1988) 29–34. [https://doi.org/10.1016/0022-3697\(88\)90130-8](https://doi.org/10.1016/0022-3697(88)90130-8).
- [85] P. Dharmiah, H.S. Kim, C.H. Lee, S.J. Hong, Influence of powder size on thermoelectric properties of p-type 25%Bi<sub>2</sub>Te<sub>3</sub>-75%Sb<sub>2</sub>Te<sub>3</sub> alloys fabricated using gas-atomization and spark-plasma sintering, *J. Alloys Compd.* 686 (2016) 1–8.  
<https://doi.org/10.1016/j.jallcom.2016.05.340>.
- [86] D.M. Lee, C.H. Lim, S.Y. Shin, D.C. Cho, C.H. Lee, Thermoelectric properties of p-type Bi<sub>0.5</sub>Sb<sub>1.5</sub>Te<sub>3</sub> compounds fabricated by spark plasma sintering, *J. Electroceramics*. 17 (2006) 879–883. <https://doi.org/10.1007/s10832-006-6807-1>.
- [87] D. Hyun, J. Hwang, J. Shim, Thermoelectric properties of (Bi<sub>0.25</sub>Sb<sub>0.75</sub>)<sub>2</sub>Te<sub>3</sub> alloys fabricated by hot-pressing method, *J. Mater. Sci.* 36 (2001) 1285–1291.

<https://doi.org/10.1023/A:1004862700211>.

- [88] M. Cutler, J.F. Leavy, R.L. Fitzpatrick, Electronic transport in semimetallic cerium sulfide, *Phys. Rev.* 133 (1964). <https://doi.org/10.1103/PhysRev.133.A1143>.
- [89] M. Cutler, R.L. Fitzpatrick, J.F. Leavy, The conduction band of cerium sulfide  $Ce_{3-x}S_4$ , *J. Phys. Chem. Solids.* 24 (1963) 319–327. [https://doi.org/10.1016/0022-3697\(63\)90136-7](https://doi.org/10.1016/0022-3697(63)90136-7).
- [90] G.A.O. Yuanwen, H.E. Yuezhou, Z.H.U. Linli, Impact of grain size on the Seebeck coefficient of bulk polycrystalline thermoelectric materials, (2010). <https://doi.org/10.1007/s11434-009-0705-2>.
- [91] P. Eaksuwanchai, S. Tanusilp, P. Jood, M. Ohta, K. Kurosaki, Increased Seebeck Coefficient and Decreased Lattice Thermal Conductivity in Grain-Size-Controlled p - Type PbTe – MgTe System, (2018). <https://doi.org/10.1021/acsaem.8b01491>.
- [92] D.H. Kim, C. Kim, S.H. Heo, H. Kim, Influence of powder morphology on thermoelectric anisotropy of spark-plasma-sintered Bi-Te-based thermoelectric materials, *Acta Mater.* 59 (2011) 405–411. <https://doi.org/10.1016/j.actamat.2010.09.054>.
- [93] R.J. Moffat, Describing the uncertainties in experimental results, *Exp. Therm. Fluid Sci.* 1 (1988) 3–17. [https://doi.org/10.1016/0894-1777\(88\)90043-X](https://doi.org/10.1016/0894-1777(88)90043-X).
- [94] J. Mackey, F. Dynys, A. Sehirlioglu, Uncertainty analysis for common Seebeck and electrical resistivity measurement systems, *Rev. Sci. Instrum.* 85 (2014). <https://doi.org/10.1063/1.4893652>.



**Chapter 2: Enhancement of mechanical properties and thermoelectric performance of spark plasma sintered P-type Bismuth Telluride by powder surface oxide reduction**

*Journal paper*

## Enhancement of mechanical properties and thermoelectric performance of spark plasma sintered P-type Bismuth Telluride by powder surface oxide reduction

Ahmed A. Abdelnabi <sup>a</sup>, Vickram Lakhian <sup>a</sup>, Joseph R. McDermid<sup>b</sup>, Yu-Chih Tseng<sup>c</sup> James S. Cotton <sup>a, \*</sup>

<sup>a</sup> Department of Mechanical Engineering, McMaster University, Hamilton, ON, Canada

<sup>b</sup> Department of Materials Science and Engineering, McMaster University, Hamilton, ON, Canada

<sup>c</sup> CanmetMATERIALS, Natural Resources Canada, Hamilton, ON, Canada

\*Corresponding author. Department of Mechanical Engineering, McMaster University, Hamilton, ON, Canada

Email address: cottonjs@mcmaster.ca (James S. Cotton).

### **Highlights:**

- Powder pre-treatment enhanced both mechanical and thermoelectric properties.
- Powder surface oxide reduction increased the tensile strength by 89%.
- The figure of merit (ZT) increased by up to 170% at room temperature (25°C).
- An anisotropy in the tensile strength and ZT was observed.
- Superior performance in the direction perpendicular to the sintering pressure.

**Keywords:**

Thermoelectric materials;  $\text{Bi}_{0.4}\text{Sb}_{1.6}\text{Te}_3$ ; Spark plasma sintering (SPS); Surface oxides; Mechanical properties; Uniaxial tensile strength

**Abstract:**

In the present investigation, key mechanical design parameters and the thermoelectric performance of powder ball milled spark plasma sintered P-type  $\text{Bi}_{0.4}\text{Sb}_{1.6}\text{Te}_3$  material was determined. In particular, the effect of the powder preparation technique on the powder surface oxide layer as well as both the mechanical and thermoelectric properties were determined. All measurements were performed on identically prepared sintered samples in both parallel and perpendicular to the applied sintering pressure. The mechanical properties determined included relative density, uniaxial tensile strength, coefficient of thermal expansion, Young's modulus, Poisson's ratio, and shear modulus. The thermoelectric properties measured included the Seebeck coefficient, electrical resistivity, and thermal conductivity. A mechanically agitated reduction facility built in-house was used to reduce the powder surface oxide at 380 °C for 24 h using dry 5%  $\text{H}_2$  - 95% Ar. To separate between the annealing and the reduction effects, the P-type  $(\text{Bi}, \text{Sb})_2\text{Te}_3$  powder was annealed using highly purified Ar at the same temperature and time as the reduction process. The oxygen content in the sintered P-type samples was then measured using the inert gas fusion technique. The oxygen content was found to be decreased by 35 wt% after 24 h of reduction but did not change significantly after annealing with Ar only relative to the dried powders. The reduction of the surface oxides increased the relative density of the sintered parts from 97% to 99%. Consequently, the characteristic uniaxial tensile strength increased from 13.9 MPa to 26.3 MPa and from 16.3 MPa to 30.6 MPa in the parallel and the perpendicular directions to the sintering pressure, respectively, for the sintered bodies from the reduced powder. Both the Young's

modulus and the shear modulus increased from 44.3 GPa to 48.7 GPa and 17.8 GPa to 19.5 GPa in the parallel direction, respectively, after the reduction treatment and sintering. The figure of merit,  $ZT$ , increased from 0.35 to 0.80 and from 0.42 to 1.13 at room temperature (25 °C) in the parallel and the perpendicular directions, respectively, after the surface oxide reduction treatment.

## 2.1. Introduction

Bismuth Telluride ( $\text{Bi}_2\text{Te}_3$ ) is one of the most common low temperature thermoelectric (TE) compounds, used in a wide range of applications including low-temperature waste heat recovery, sensors and refrigeration [7]. The performance of the thermoelectric generator is defined by the thermoelectric material figure of merit ( $ZT$ ):

$$ZT = \alpha^2 T / \rho_e k \quad (1)$$

where  $\alpha$  is the Seebeck coefficient,  $\rho_e$  the electrical resistivity,  $T$  the absolute temperature in Kelvins and  $k$  the thermal conductivity. P-type  $(\text{Bi,Sb})_2\text{Te}_3$  includes Antimony (Sb) as the primary dopant to change the charge carrier concentration such that the thermoelectric behaviour of the material is significantly enhanced [59]. Typically, unidirectional crystal growth techniques, such as the Bridgman technique and zone melting, are used to prepare commercial P-type  $(\text{Bi,Sb})_2\text{Te}_3$  compounds [17,60]. These methods result in single crystals which have high thermoelectric properties along the crystal growth direction; however, they suffer from poor mechanical properties because of the weak Van der Waals forces bonding the  $\text{Te}(1) - \text{Te}(1)$  layers, forming cleavage planes between unit cells [19,20].

Spark plasma sintering (SPS) is a promising technique for TE materials fabrication, based upon powder metallurgy, as opposed to single crystal growth. SPS is of particular interest due to its relatively short sintering time and lower manufacturing temperature requirements resulting in reduced manufacturing costs and energy requirements, but has also been found to increase both

mechanical and thermoelectric properties [13,22,33,34]. Jiang et al. [22] and Pan et al. [21] found that P-type  $(\text{Bi,Sb})_2\text{Te}_3$  samples sintered using SPS demonstrated an increase in bending strength from 10 to 80 MPa and from 17 to 59 MPa for the modified small punch test strength, respectively, compared to crystalline ingots. In the same study, Jiang et al. [22] also reported that the presence of particle boundaries and the increased hole concentration decreased the thermal conductivity, resulting in an increase in the  $ZT_{\text{max}}$  from 1 to 1.15. Son et al. [32] reported that the decrease in the carrier concentration due to ball milling for 10 hours pre-sintering using SPS resulted in a ZT of 1.14 at 310 K, which was 10% higher than the ingot P-type  $(\text{Bi,Sb})_2\text{Te}_3$ .

Although P-type  $(\text{Bi,Sb})_2\text{Te}_3$  TE materials created using SPS have been found to show enhanced thermoelectric properties, the powder must be stored and handled in an inert atmosphere in order to avoid the formation of an external oxide layer [8]. It has also been reported that P-type  $(\text{Bi,Sb})_2\text{Te}_3$  powder preparation should be performed in an inert atmosphere and, should be powder be exposed to ambient atmosphere at any point, it should be reduced using  $\text{H}_2$  [9,12–16]. Lim et al. [9] and Seo et al. [13], studied the effect of  $\text{H}_2$  reduction on an oxidized P-type  $\text{Bi}_{0.5}\text{Sb}_{1.5}\text{Te}_3$  powder. The reduction procedure reduced the powder oxygen contents to 1580 and 2000 ppm and increased the sintered part  $ZT_{\text{max}}$  to 0.92 and 1.05, respectively, due to an increase in the carrier concentration. However, neither Lim et al. [9] nor Seo et al. [13] studied the effect of this reduction on the mechanical properties. Yoon et al. [16] found that the Vicker's hardness decreased from 117 to 113 Hv for SPS sintered P-type  $(\text{Bi,Sb})_2\text{Te}_3$  samples with 25% less oxygen content when Ar was used in ball milling the powder instead of air. Their study showed an increase in relative density for the samples with lower oxygen content but a decrease in the hardness. However, previous studies did not investigate the effect of the surface oxide on other mechanical properties, especially the uniaxial tensile strength.

Knowledge of the mechanical properties of P-type  $(\text{Bi,Sb})_2\text{Te}_3$  TE materials, particularly the tensile strength, as well as the thermoelectric properties are essential for designing reliable, high-quality low temperature thermoelectric modules. However, it is challenging for researchers to find fully characterized P-type  $(\text{Bi,Sb})_2\text{Te}_3$  TE materials that have the well-documented mechanical and thermoelectric properties needed as an input to finite element models for designing thermoelectric modules [47,61,62]. Accordingly, the required properties have tended to be obtained from different sources or to be assumed, which often do not represent the actual material simulated and can lead to unreliable, low quality thermoelectric modules [38–40,63].

The focus of this study is on determining the effect of the powder preparation technique, including annealing and surface oxide removal using  $\text{H}_2$ , on the mechanical and thermoelectric properties of SPS sintered P-type  $(\text{Bi,Sb})_2\text{Te}_3$  TE materials. This study aims to accomplish this by considering the uniaxial tensile strength, Young's modulus, Poisson's ratio, shear modulus, relative density and coefficient of thermal expansion (CTE) as they provide a complete picture of the effect of annealing and oxygen content on the mechanical behaviour of the material. The thermoelectric properties measured (e.g. the Seebeck coefficient, the electrical resistivity, and the thermal conductivity) are then used to calculate  $ZT$  (equation (1)) as a measure of the performance of the material. Curve fitted relations as a function of temperature for all the measured thermoelectric properties as well as the TE material thermal diffusivity and specific heat capacity are provided in the Appendix.

## **2.2.Experimental Methods**

### **2.2.1 Sample Preparation**

Commercial p-type  $\text{Bi}_{0.4}\text{Sb}_{1.6}\text{Te}_3$  powder (5N Plus Inc., Montréal (Québec), Canada) was used as the starting material for the current work [64]. The powder was sieved to a particle size fraction

of  $\leq 20 \mu\text{m}$  and was then subjected to a sedimentation process in ethanol to remove all the particles less than  $1 \mu\text{m}$ , leaving a particle size fraction of 1 to  $20 \mu\text{m}$ . The particle size distribution was verified using a laser diffraction particle size analyzer (Mastersizer 2000, Malvern Panalytical Ltd). The powder was divided and tested under three different processing atmosphere treatment conditions: dried, annealed and oxide reduced. The dried fraction was dried under vacuum at  $100 \text{ }^\circ\text{C}$  for 24 h to eliminate the effect of absorbed moisture within the powder. The reduced powder was annealed under high purity ( $\geq 99.9999\%$ N purity using a molecular sieve) 5%  $\text{H}_2$  - 95% Ar at  $380 \text{ }^\circ\text{C}$  for 24 h to reduce the powder surface oxides. The annealed powder was heat treated in high purity ( $\geq 99.9999\%$ N purity using a molecular sieve) Ar at  $380 \text{ }^\circ\text{C}$  for 24 h to isolate the effect of raising the temperature (annealing) from surface oxide removal (reduction) on the resultant material properties. All powder processing was carried out in an in-house built fluidized bed facility which mechanically agitated the powder during processing to increase the powder-gas contact time. After treatment, the powder was transferred to a room temperature nitrogen ( $\text{N}_2$ ) filled glove box in a sealed treatment vessel to prevent exposure to ambient atmosphere. The powder was prepared for sintering by loading 5 g of powder into graphite dies inside the glovebox, which were then transferred under ambient atmosphere within 300 s (5 min.) to be sintered using a Spark Plasma Sintering facility ( SPS, SPS-211LX, FUJI Electronic Industrial Co., LTD). Powders were heated from room temperature ( $25 \text{ }^\circ\text{C}$ ) at  $8.3 \text{ }^\circ\text{C/s}$  ( $50 \text{ }^\circ\text{C/min.}$ ) to  $420 \text{ }^\circ\text{C}$  and were held under a uniaxial pressure of 50 MPa for 600 s to form discs of dimensions  $\text{Ø}12.7 \text{ mm} \times 5.5 \text{ mm}$  and  $\text{Ø}12 \text{ mm} \times 4 \text{ mm}$ .

### 2.2.2 Sample Analysis:

The oxygen content of the sintered samples as a function of process atmosphere was measured for the sintered samples as bar-shaped solid samples using a nitrogen/oxygen analyser (TCH600 - Leco) in which three samples of  $5.5 \times 4.5 \times 4.5$  mm (equivalent to  $\sim 1$  g each) were used to assess each process atmosphere condition. The phases present in the sintered samples were determined using X-ray Diffraction (XRD, PANalytical X'Pert) using Cu- $K_{\alpha 1}$  radiation ( $\lambda = 1.5406$  Å). Sample cross-sections were prepared for microstructural examination using standard metallographic techniques with the final polishing step employing  $0.25\mu\text{m}$  colloidal silica (OP-S). Microstructural examination was carried out using a Scanning Electron Microscope (SEM, JEOL JSM-6610LV) in backscattered electrons (BSE) mode using an acceleration voltage of 15 keV and a working distance of 8 mm.

The Archimedes method was used to measure the density of the as-sintered samples before cutting, in which at least ten samples were measured per process atmosphere condition. The Coefficient of Thermal Expansion (CTE) was measured using a quench dilatometer (L78 RITA Dilatometer, LINSEIS) on  $5.5 \times 2.3 \times 2.3$  mm samples. The measurement was made in a temperature range from  $35$  °C to  $250$ °C at a heating rate of  $6.7$  °C/s ( $40$  °C/min). The characteristic uniaxial tensile strength ( $\sigma_T$ ) was measured using a conventional tensile frame (AGS-X, Shimadzu Autograph) equipped with a 500 N load cell. The tensile strength was measured both parallel to ( $\sigma_{T\parallel}$ ) and perpendicular to ( $\sigma_{T\perp}$ ) the pressing direction for twenty bar-shaped samples of dimensions  $5.5 \times 2.3 \times 2.3$  mm per process atmosphere per direction following the methodology specified in ASTM C1468-13 [58]. To ensure uniaxial tensile failure, a special in-house fixture was made, as shown in Fig. 1. The samples were glued with commercial high strength epoxy that is at least double the nominal strength of the sintered samples to two 6.35 mm (1/4 in.) threaded steel rods with flat ends



perpendicular to the tensile direction. Young's modulus, Poisson ratio and shear modulus were calculated by measuring both longitudinal and shear ultrasonic waves using a Pulser/Receiver module (5072PR, OLYMPUS) at 2 kHz pulse repetition frequency (PRF), 104  $\mu$  J pulse energy, 500  $\Omega$  damping, a 1 MHz high-pass filter and +5 dB gain, and an 100 MHz digital oscilloscope (DSO-X2014A, Agilent Technologies).

The  $\text{\O}12.7$  mm sintered samples were cut into bars of  $5.5 \times 2.3 \times 2.3$  mm both parallel ( $\parallel$ ) and perpendicular ( $\perp$ ) to the pressing direction for measuring the Seebeck coefficient, the electrical resistivity and coefficient of thermal expansion. The electrical resistivity and the Seebeck coefficient were measured using an ULVAC ZEM3 system. The average values of the electrical resistivity and the Seebeck coefficient were calculated from four values through two heating/cooling cycles at 25  $^{\circ}\text{C}$  increments for temperatures from 25 to 250  $^{\circ}\text{C}$  using 5  $^{\circ}\text{C}/\text{min}$  heating and the cooling rates. The  $\text{\O}12$  mm sintered discs were sliced into thin 1 mm solid disks for thermal diffusivity and specific heat capacity measurements. The thermal diffusivity and the specific heat capacity were measured using the laser flash method (DLF-1200, TA Instruments) and then the thermal conductivity was calculated by the machine software after the density values were entered. The Hall coefficient was measured on room temperature  $\text{\O}12.7$  mm  $\times$  0.6 mm thickness samples with 200 nm gold-sputtered contacts.

## **2.4. Results and Discussion**

### **2.4.1 Powder Chemistry and Powder Particle Size Distribution**

The XRD patterns for the dried, annealed and reduced P-type  $\text{Bi}_{0.4}\text{Sb}_{1.6}\text{Te}_3$  powders are shown in Fig. 2 with comparison to a standard P-type  $\text{Bi}_{0.4}\text{Sb}_{1.6}\text{Te}_3$  spectrum [65]. As shown in Fig. 2, there was no significant difference between the spectra for the various processing routes and,

furthermore, all the spectra matched that of the P-type  $\text{Bi}_{0.4}\text{Sb}_{1.6}\text{Te}_3$  standard with no additional phases detected.

Table 1 contains the powder oxygen analysis as a function of processing atmosphere (dry, annealed and reduced) for P-type  $\text{Bi}_{0.4}\text{Sb}_{1.6}\text{Te}_3$ . The dried powder had an oxygen concentration of  $0.67 \pm 0.02$  wt.%, whilst the annealed powder had an oxygen concentration of  $0.71 \pm 0.02$  wt.%, an increase of 0.039 wt.%. The reduced powder had the lowest oxygen concentration, as expected, of  $0.48 \pm 0.01$  wt.%. The uncertainty values in Table 1 were calculated according to the sample precision error based on six samples per powder pre-treatment and show that the effects of processing atmosphere on powder oxygen content are statistically significant. The increase in oxygen concentration in the annealed samples is believed to have been caused by the oxygen concentration still (1 ppb) in the purified Ar, which is the lower limit of the molecular sieve. The oxygen content of the as-sintered reduced pre-treatment body could be due to the following: i) internal oxides could have been introduced during ball milling and were not subsequently reduced during the reduction treatment; ii) oxygen could have been re-introduced to the sample for a brief period of time during the sintering process through material loading and evacuating the sintering chamber, a current limitation of the SPS system and iii) as the powder being used is P-Type  $\text{Bi}_{0.4}\text{Sb}_{1.6}\text{Te}_3$ , one of the possible oxides being produced is  $\text{Sb}_2\text{O}_3$ , which is more difficult to reduce versus  $\text{Bi}_2\text{O}_3$  or  $\text{TeO}_2$  since it has the lowest negative value of  $\Delta G^\circ$  amongst the three oxides [9]. To reduce  $\text{Sb}_2\text{O}_3$ , a reduction temperature above  $575^\circ\text{C}$  is needed, which is higher than the melting point of P-type  $\text{Bi}_{0.4}\text{Sb}_{1.6}\text{Te}_3$  [66].

The powder particle size distribution of the as-received (dried) powder, as determined using the laser diffraction technique, is presented in Fig. 3. Examination of Fig. 3 will show that the particle size distribution is distinctly non-Gaussian, with the particle size distribution spanning

approximately 0.9 to 50  $\mu\text{m}$  and the majority of the powder particles being less than 10  $\mu\text{m}$ . Further analysis of the powder size distribution revealed that the surface and volume weighted average of the powder particle sizes were 5.2 and 9.7  $\mu\text{m}$ , respectively. The width of the particle size distribution indicates that there were likely significant populations of agglomerated fine particles prior to the powders being subjected to further processing.

### 2.4.2 Sintered Microstructures

Fig. 4 and Fig. 5 show low and high magnification SEM cross-section micrographs, respectively, for the dried, annealed and reduced powder P-Type  $\text{Bi}_{0.4}\text{Sb}_{1.6}\text{Te}_3$  SPS bodies. The vertical direction of the micrographs is parallel to the pressing direction during sintering in all cases. An examination of Fig. 4 will reveal that the sintered bodies comprised large grains or agglomerates of 5 – 20  $\mu\text{m}$  with regions consisting of finer powder particles between the larger grains – as is most apparent in Fig. 4(a) – and voids. However, the finer scale examination of the sintered bodies documented in Fig. 5 reveals that these larger grains consist of a large number of sintered smaller grains, where the linear intercept method (ASTM E112-13 [67]) determined that the average particle size for the SPS bodies was approximately 1  $\mu\text{m}$  (Table 2). The seeming disagreement between the laser diffractometer average particle size of 5 – 9  $\mu\text{m}$  (Fig. 3) and the particle size documented in Table 2 can be explained by the effect of agglomeration in the as-received powders carrying through to the SPS bodies, as is clearly documented in Fig. 4 and Fig. 5.

Further examination of the data in Table 2 reveals that there was significant anisotropy in the grain size in the parallel versus perpendicular directions (Table 2), with the plate-like particles (Fig. 5) being significantly larger in the perpendicular direction (Table 2). This particle morphology is likely a consequence of the relatively weak van der Waals' binding between the  $\text{Te}_{(1)} - \text{Te}_{(2)}$  layers in the P-type  $\text{Bi}_{0.4}\text{Sb}_{1.6}\text{Te}_3$  crystal resulting in the milled powder having a higher aspect ratio plate-

like shape. During sintering, this particle morphology would orient itself such the flat surface was perpendicular to the applied sintering pressure in order to more easily accommodate the shape change occurring during sintering (Fig. 5). This finding is consistent with that of Zhang et al. [68], who found that the plate-like morphology of the anisotropic Bi<sub>2</sub>Te crystal resulted in the sintered grains rotating perpendicular to the pressing direction. As will be discussed below, this anisotropy in the particle shape influences both the uniaxial tensile strength and the electrical resistivity.

### **2.4.3 As-Sintered Relative Density**

The relative density of the sintered bodies arising from the three powder processing routes is shown in Table 1. The theoretical density of P-Type Bi<sub>0.4</sub>Sb<sub>1.6</sub>Te<sub>3</sub> was calculated using the formula reported in Landolt-Börnstein [69]. The dried powder attained a low relative density of  $97.1 \pm 0.3\%$  whereas employing powder reduction increased the relative density of the sintered samples to  $99.2 \pm 0.1\%$  while the annealing treatment increased it to  $98.7 \pm 0.1\%$  (Table 1). It is believed that the reducing heat treatment decreased the particle surface oxides, thereby enhancing the diffusional bonding between the particles during sintering, leading to a higher density than both the dried and the annealed samples, as can be seen in Fig. 4 and Fig.5.

### **2.4.4 Coefficient of Thermal Expansion and Density of SPS Bodies**

The temperature averaged linear Coefficient of Thermal Expansion ( $CTE_{ave}$ ) over 35 to 250 °C for the three powder pre-treatments was measured parallel ( $CTE_{ave\parallel}$ ) and perpendicular to ( $CTE_{ave\perp}$ ) the pressing direction during SPS. Table 3 shows that there was a measurable difference between the  $CTE_{ave\parallel}$  and  $CTE_{ave\perp}$  values, in which the  $CTE_{ave\parallel}$  has a value of  $18.2 \pm 0.2 \times 10^{-6}$  m/m K for both the dry and annealed powder samples, while the  $CTE_{ave\perp}$  is  $17.5 \pm 0.2 \times 10^{-6}$  m/ m K for both the dry and annealed powder samples. This suggests that annealing did not affect the values of

$CTE_{ave}$  in both directions. Samples made from the reduced powder demonstrated  $CTE_{ave\parallel}$  and  $CTE_{ave\perp}$  values of  $18.4 \pm 0.2 \times 10^{-6}$  and  $17.9 \pm 0.2 \times 10^{-6}$  m/m K, respectively. However, these values were not outside the measurement uncertainty for the dry and annealed samples and, therefore, are insignificantly different from those of the dried and annealed powder SPS bodies. These findings closely resemble those of Pavlova et al.'s  $CTE_{ave}$  in both directions of  $17.1 \times 10^{-6}$  m/m K [70]. Per the microstructures shown in Fig.5, the CTE anisotropy is undoubtedly a consequence of the preferentially oriented grains in the SPS bodies.

Fig. 6 shows the density values for the three powder processing treatments as a function of temperature, calculated using the  $CTE_{ave}$  values from Table 3 in both direction and the following equation:

$$\rho(T) = \rho_0 \left( 1 - 3 * \frac{(CTE_{ave\parallel} + CTE_{ave\perp})}{2} * (T - T_0) \right) \quad (2)$$

where  $T_0$  is room temperature (25 °C) and  $\rho_0$  is the measured density for each powder treatment at room temperature [70], as documented in Table 1. The  $CTE_{ave}$  values at room temperature were assumed to be the same value as at 35 °C due to limitations in the measurement. As can be seen in Fig. 6 the values of density with temperature for the three powder processing treatments varied linearly, so they maintained the same difference over the entire temperature testing range. From Fig.6, it is clear that the annealing and reducing powder treatments significantly increased the sintered body densities, with the reduced powders showing a higher density than the annealed powders. This finding correlates well with the microstructural analysis documented in Fig. 4 and Fig. 5.

### 2.4.5 Mechanical Properties

Weibull analysis is used to analyze brittle material mechanical properties since they fail from flaws over a variety of length scales and tend to give scattered results [71–73]. The characteristic uniaxial tensile strength ( $\sigma_T$ ) and the Weibull modulus for the different powder treatments both parallel ( $\sigma_{T\parallel}$ ) and perpendicular ( $\sigma_{T\perp}$ ) to the pressing direction during sintering are listed in Table 4. Fig. 7 shows a force vs. displacement curve for one of the reduced powder pre-treatment SPS sample, where this curve is typical of all the samples tested in that they showed the same brittle material behavior with no plastic region. The first part of the curve is not linear since it is the region where alignment takes place. The characteristic uniaxial tensile strength for the three powder treatments measured parallel and perpendicular to the sintering pressure direction is shown in Fig. 8. The increasing trend in tensile strength in both directions with powder annealing and reduction can be seen. The upper and the lower bounds for both the tensile strength and the Weibull modulus (Table 4) were calculated for 90% confidence according to the number of samples tested for each powder treatment per ASTM C1239-13 [74]. Using the dry processed powder SPS samples as the baseline, the  $\sigma_{T\parallel}$  and the  $\sigma_{T\perp}$  increased from 13.9 (15.5, 12.6) MPa to 26.3 (28.6, 24.5) MPa and 16.3 (18.3, 14.6) to 30.6 (34.6, 27.2) MPa (i.e. an 89% increase for both) after powder reduction, respectively (Table 4). This anisotropic behaviour in the  $\sigma_T$  of the reduced powder sintered bodies is almost certainly due to the preferential orientation of the sintered particles perpendicular to the sintering pressuring direction and the stronger crystallographic bonds in that direction within the particles (Fig. 5(c)).

The large increase in strength due to the powder reduction process performed before sintering may be explained according to the following hypothesis. In this case, removal of the oxide layer around the powder particles by  $H_2$  reduction (Table 1) enhances green compact consolidation and

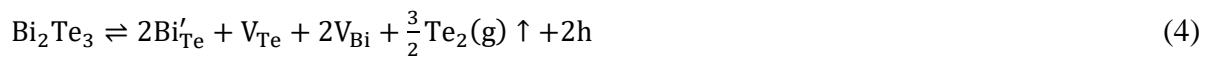
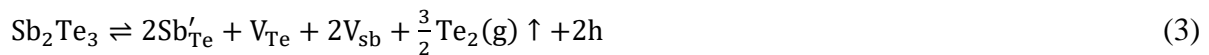
densification during the sintering process, consistent with the sintered body density increase observed in Fig. 6. This oxide layer consists of the different metal oxides in the P-type compound, namely bismuth oxide ( $\text{Bi}_2\text{O}_3$ ), antimony oxide ( $\text{Sb}_2\text{O}_3$ ) and tellurium dioxide ( $\text{TeO}_2$ ) [8]. These compounds have a higher melting point than the P-type  $\text{Bi}_{0.4}\text{Sb}_{1.6}\text{Te}_3$  parent material, so partially removing this oxide layer makes it possible to increase the number of diffusional weld sites between the powder particles during sintering, which in turn increases both the density (Fig. 6) and tensile strength in the samples (Table 4) [75]. In addition, the surface oxides are not affected by the low sintering temperature of the base material, and subsequently act as flaws in the bulk material. Increasing the flaws in a brittle material such as P-type  $\text{Bi}_{0.4}\text{Sb}_{1.6}\text{Te}_3$  increases the probability of the material failure at low stresses which explains the low characteristic uniaxial tensile strength of the sintered bodies produced using the dry process atmosphere.

In ceramics, as the porosity decreases the Young's modulus and the Poisson ratio tend to increase [76–79]. The Young's modulus, the shear modulus, and the Poisson ratio for the sintered bodies as a function of the powder processing route are presented in Table 5. The properties documented in Table 5 were calculated by measuring both the ultrasonic longitudinal and shear waves using the relations found in ASTM E 494-95 [80]. The powder reduction and annealing pre-treatments increased the Young's modulus to  $48.7 \pm 0.1$  GPa and  $48.1 \pm 0.2$  GPa, respectively, compared to  $44.3 \pm 0.2$  GPa for the dry atmosphere processed powder. Powder reduction and annealing had the same relative effect on the shear modulus, where it increased to  $19.5 \pm 0.1$  GPa and  $19.3 \pm 0.1$  GPa, respectively, compared to  $17.8 \pm 0.1$  GPa for the dry atmosphere processed powder. The annealing and reduction powder pre-treatment did not show any significant effect on the Poisson's ratio. The values of both moduli depend on both the longitudinal and shear wave velocities and the density, which increased mostly due to the annealing effect more than the oxide reduction effect (Table 1).

This explains the large difference between the dry and both the annealed and reduced powder processed compacts and the small difference between the annealed and the reduced powders for both moduli (Table 5). Poisson's ratio depends on only the ratio of the two wave velocities and that ratio was not affected by either the powder annealing or reduction treatments.

#### 2.4.6 Thermoelectric Properties

The annealing and reduction powder pre-treatments have been found to significantly affect the thermoelectric properties of P-type  $\text{Bi}_{0.4}\text{Sb}_{1.6}\text{Te}_3$  by previous researchers [9,13,22,81,82]. Table 6 shows that both the room temperature carrier concentration ( $n$ ) and mobility ( $\mu$ ) were increased with powders processed by annealing and reduction powder pre-treatments relative to the dry atmosphere processed powder. Chemical composition and lattice structure are known to greatly affect the carrier concentration and mobility, which directly affects the thermoelectric properties, especially the electrical resistivity [13,82]. The P-type  $\text{Bi}_{0.4}\text{Sb}_{1.6}\text{Te}_3$  structure is formed from repeated unit cells of  $\text{Te}_{(1)}\text{-Bi(or Sb)}_{(1)}\text{-Te}_{(2)}\text{-Bi (or Sb)}_{(1)}\text{-Te}_{(1)}$ . The weak Van der Waals bonds between the cells makes  $\text{Te}_{(1)}$  easier to volatilize during powder pre-treatment annealing at 380 °C for 24 h in both the annealed and reduced samples prior the SPS process. Due to the small electronegativity difference between Bi, Sb and Te ( $\chi_{\text{Bi}} = 1.8$ ,  $\chi_{\text{Sb}} = 1.9$ ,  $\chi_{\text{Te}} = 2.1$ ), Bi or Sb could occupy the  $\text{Te}_{(1)}$  vacancy created by the volatilization event [83]. This atomic replacement causes anti-site defects and increases the carrier concentration because of hole production, as given by [84]:





where  $h$  is the produced hole and  $\uparrow$  refers to the volatilization of  $Te_{(1)}$ . Equations (3) and (4) show that the volatilization of  $Te_{(1)}$  during the powder annealing treatment, which is then replaced by either Bi or Sb atoms, results in hole production and a consequent increase in carrier concentration. This accounts for the significant increase in  $n$  and  $\mu$  observed between the dry and annealed powder SPS bodies (Table 6). Oxide removal during the reduction treatment likely reduced the thickness of any external oxide films present on the as-processed powder. In the as sintered bodies this will result in the reduced powder having thinner oxide films between the sintered powder particles and result in barriers to carrier flow being lessened. In addition, the removal of the external oxide film resulted in a higher density (Fig. 6) and a consequence increase in the number of continuous paths for carrier flow (Fig. 4 and Fig. 5). The additional diffusional bonding associated with the reduced powders can be seen in Fig. 4(c) and Fig. 5(c) as the particle boundaries are more tightly packed and the void fraction is reduced for the reduced pre-treatment SPS body. These factors combined to lessened barriers for carrier flow and the observed enhanced properties for the SPS processed powder (Fig. 13).

Fig.9 shows that the electrical resistivity of the SPS bodies is generally decreased by the powder annealing and reduction pre-treatments in both the parallel and perpendicular directions versus the dry powder sintered bodies in the same direction. Fundamentally, electrical resistivity ( $\rho_e$ ) is a strong function of both the carrier density ( $n$ ) and carrier mobility ( $\mu$ ) through the following relation [9]:

$$\rho_e = \frac{1}{ne\mu} \quad (5)$$

where  $e$  is the electron charge. The powder reduction treatment decreased the electrical resistivity by 25% while annealing decreased it by 15% compared to the dried samples in both the parallel

and perpendicular directions through out the temperature range examined (Fig. 9). Fig.9 also shows the electrical resistivity values for a powder particle size of  $\leq 30 \mu\text{m}$  from Dharmaiah et al. [85] (referred to “Literature [85]” in the text and Fig. 9 – Fig. 13), who studied the effect of gas-atomized powder particle size for spark plasma sintered P-type  $\text{Bi}_{0.5}\text{Sb}_{1.5}\text{Te}_3$ . The measurements carried out by Dharmaiah et al. [85] were perpendicular to the sintering pressing direction. The trends observed for the reduced  $\perp$  samples are close to those of Dharmaiah et al. [85]. However, the values in [49] are significantly lower than those of the present study at lower temperatures (Fig. 9). This difference is thought to be due to the smaller powder particle size used in the current work, which leads to an increase in the number of grain boundaries the carriers must cross per unit length, thereby decreasing the carrier mobility and, therefore, results in an increase in the electrical resistivity [14,22,82,85–87].

On the other hand, powder annealing was found to have no significant effect on the Seebeck coefficient both parallel and perpendicular, however oxide reduction increased it slightly, as shown in Fig. 10. The Seebeck coefficient ( $\alpha$ ) can be expressed as follows [88]:

$$\alpha = \left( \frac{\pi^2 k^2 T}{3e} \right) \left( \frac{8m^*}{h^2} \right) \left( \frac{\pi}{3n} \right)^{\frac{2}{3}} \left( 1 + \left( \frac{d \ln \lambda_s}{d \ln E} \right)_{E_f} \right) \quad (6)$$

where  $n$  is the carrier concentration,  $T$  the absolute temperature,  $k$  the Boltzmann constant,  $e$  the electron charge,  $m^*$  the effective mass,  $\lambda_s$  the scattering distance,  $h$  Plank’s constant and  $E$  the average electron energy. At room temperature, the Seebeck coefficient value is proportional to  $n^{(-2/3)}$  [89]. Despite the significant increase in carrier concentration due to the powder annealing and reduction pre-treatments (Table 6), the Seebeck coefficient was only slightly increased due to powder reduction pre-treatment (Fig. 10), where the maximum  $\alpha$  value is  $332 \mu\text{V/K}$  at room temperature for the reduced sample in the parallel direction.

Energy filtering is a potential barrier mechanism that could be introduced by particle powder boundaries. The potential barrier mechanism is responsible for the strong scattering of carriers with energies lower than that of the barrier [90,91]. The deviation of the carrier energy distribution is the reason behind the matched values and trend of the reduced  $\perp$  sample Seebeck coefficient to the small powder particle size sintered sample of Dharmaih et al. [85], as shown in Fig. 10.

Fig. 9 shows an anisotropy in the electrical resistivity for the three powder processing routes, where the resistivity in the perpendicular direction is lower than that in the parallel direction by 20% for both the dry and annealed powder samples whilst it is 30% lower for the reduced powder samples. This anisotropy in the electrical resistivity is thought to be due to the particle orientation shown in Fig. 5. The higher number of boundaries per unit length due to the size in the parallel direction is thought to decrease the carrier mobility  $\mu$ , which in turn increases the electrical resistivity in the parallel direction compared to that in the perpendicular direction [92], per Equation (5). In the same study, Kim et al. [92] reported that the Seebeck coefficient is isotropic and was not affected by particle shape anisotropy. This correlates well with the findings seen in Fig. 10, in which the Seebeck coefficient for the three powder processing routes is seen to be isotropic.

The significant decrease of the electrical resistivity arising from the reduced powder processing route increased the power factor by approximately 115% at room temperature in the perpendicular direction vs. the dry processed powder, with a value of  $2.32 \times 10^{-3} \text{ W/m.K}^2$ , as shown in Fig. 11. The power factor values converge to approximately the same value for all the powder processing routes and sintered body directions by increasing the temperature to 250 °C (Fig. 11). The deviation in the power factor values between the reduced  $\perp$  sample and the literature values [85] is mainly due to the deviation in the electrical resistivity values, even though the trends are identical, as shown in Fig. 11.

Thermal conductivity is a relatively weak function of carrier concentration [2]. As shown in Fig. 12, the annealing powder treatment showed no significant effect on the thermal conductivity versus the dry processed powder save for the slightly higher values observed for temperatures above 150 °C. However, the sintered compact thermal conductivity decreased by an average of 15% over the tested temperature range when the powder was subjected to the reduction treatment, as shown in Fig. 12. The reduced  $\perp$  sample thermal conductivity trend over the tested temperature range (25 to 250 °C) is identical to the Dharmaih et al. [85] (Fig. 12). However, the lower values of the reduced  $\perp$  sample are thought to be due to the smaller powder particle size versus Dharmaih et al., which increased phonon scattering and decreased the mobility due to the higher number of grain boundary barriers per unit length.

Accordingly, the figure of merit (ZT) for the reduced powder SPS bodies was enhanced by 170 % vs. the dry processed powder at room temperature in the perpendicular direction, reaching a value of 1.1, and a value of 0.8 in the parallel direction, as shown in Fig. 13. The observed anisotropy in the ZT is a result of the anisotropy in the electrical resistivity, leading to a higher thermoelectric performance in the perpendicular direction by 40 %. The ZT trend over the tested temperature range (25 to 250 °C) of the reduced  $\perp$  sample are very close to that of Dharmaih et al. [85] with an insignificantly different  $ZT_{\max}$  value at 25 °C and at higher temperatures, as shown in Fig. 13.

## 2.5. Conclusions

This research sought to determine the effect of several powder pre-treatment process atmospheres – namely vacuum drying at 100 °C, annealing at 380 °C using high purity Ar and an oxide reduction treatment at 380 °C using high purity Ar + 5% $H_2$  – on the thermoelectric and mechanical properties of a spark plasma sintered (SPS) P-type  $Bi_{0.4}Sb_{1.6}Te_3$  thermoelectric ceramic. In summary, the oxide

reduction process using Ar + 5% H<sub>2</sub> enhanced both the mechanical and thermoelectric properties of the spark plasma sintered P-type Bi<sub>0.4</sub>Sb<sub>1.6</sub>Te<sub>3</sub> thermoelectric material. The main findings of the current research can be summarized as follows:

- 1- It is recommended that P-type Bi<sub>0.4</sub>Sb<sub>1.6</sub>Te<sub>3</sub> powders be subjected to a surface oxides reduction treatment using a Ar + 5% H<sub>2</sub> process atmosphere at 380 °C for 24 h prior to spark plasma sintering as it had a significant enhancement effect on both the mechanical and thermoelectric properties.
- 2- The increase in the relative density using the oxide reduction treatment is key to increasing the characteristic uniaxial tensile strength, in which it increased to 26.3 (28.6, 24.5) MPa and 30.6 (34.6, 27.2) MPa parallel to and perpendicular to the sintering pressure directions, respectively, or an increase of 89 % relative to the strengths of the SPS material derived from the baseline drying treatment.
- 3- When using the powder reduction treatment, the ZT value increased by approximately 170 % for the perpendicular direction samples and approximately 126 % for the parallel direction SPS bodies relative to the dried bodies, reaching values of 1.1 and 0.8, respectively, at room temperature.
- 4- The increase in the ZT for the SPS bodies derived from the reduced powders is mainly a result of the significant decrease in both the electrical resistivity and the thermal conductivity of the reduced powders.
- 5- The powder reduction treatment increased both the carrier concentration and mobility, decreasing the electrical resistivity, while the Seebeck coefficient was not affected.

## Acknowledgement

This work was supported by the Natural Sciences and Engineering Research Council of Canada (NSERC CREATE 432242-13, NSERC CRD473500-14) and the Ontario Centre of Excellence (OCE22261).

## 2.6. Appendix

The thermoelectric properties vs. temperature for the spark plasma sintered P-type  $\text{Bi}_{0.4}\text{Sb}_{1.6}\text{Te}_3$  in the temperature range of 35 °C to 250 °C were curve-fitted and are presented in the following relationships:

a) In the parallel direction:

$$\alpha_{\parallel} = 0.00082635 T^2 - 1.19253647 T - 361.38672353 \text{ } [\mu\text{V/K}] \quad (7)$$

$$\rho_{e\parallel} = 0.01145339 T^3 - 0.23843639 T^2 + 1.16237225 T + 5.76676682 \text{ } [\Omega \text{ m} * 10^{-5}] \quad (8)$$

$$k_{\parallel} = 0.00000532 T^2 - 0.00196080 T + 0.55932397 \text{ } [\text{W/m.K}] \quad (9)$$

$$ZT_{\parallel} = -0.00000007 T^3 + 0.00004123 T^2 - 0.00961974 T + 1.01092481 \text{ } [-] \quad (10)$$

$$\alpha_{d\parallel} = 0.00000004 T^2 - 0.00001057 T + 0.00424340 \text{ } [\text{cm}^2/\text{s}] \quad (11)$$

$$C_{p\parallel} = 0.00026803 T^2 + 0.05044616 T + 202.31639660 \text{ } [\text{J/kg.K}] \quad (12)$$

b) In the perpendicular direction:

$$\alpha_{\perp} = 0.00115230 T^2 - 1.33136475 T - 360.96732450 \text{ } [\mu\text{V/K}] \quad (13)$$

$$\rho_{e\perp} = 0.00783850 T^3 - 0.16657315 T^2 + 0.83857866 T + 3.97280280 \text{ } [\Omega \text{ m} * 10^{-5}] \quad (14)$$

$$ZT_{\perp} = -0.00000011 T^3 + 0.00006392 T^2 - 0.01475014 T + 1.44932850 \text{ } [-] \quad (15)$$

where  $T$  is the temperature in  $^{\circ}\text{C}$ . The average uncertainty for the temperature range for the Seebeck coefficient is  $\pm 10.3\%$ , the electrical resistivity is  $\pm 4.5\%$ , the thermal conductivity is  $\pm 4.9\%$ , the  $ZT$  is  $\pm 22\%$ , the thermal diffusivity is  $\pm 1.1\%$  and the specific heat capacity is  $\pm 2.5\%$ .

2.7. Figures and Tables:

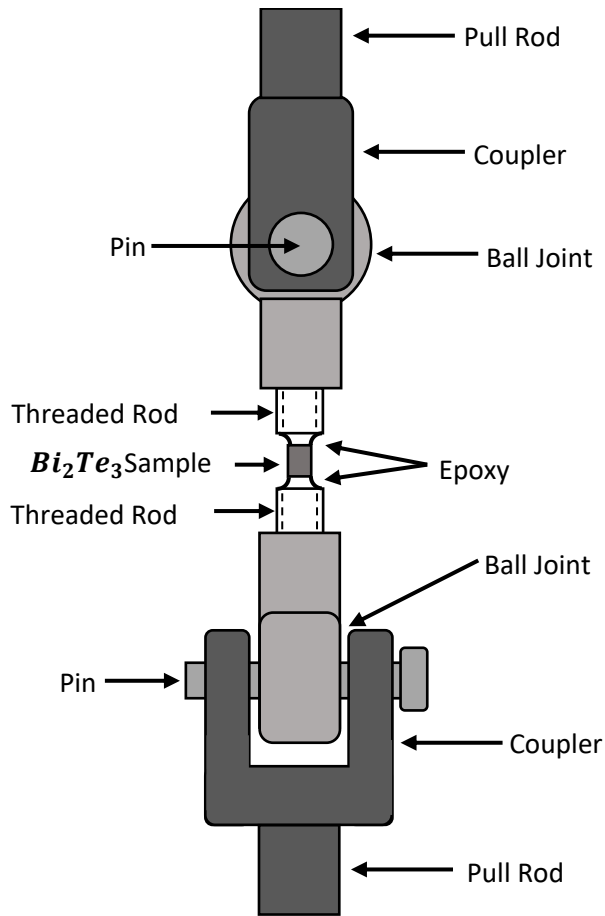


Fig. 1. A schematic diagram for the arrangement used to perform the uniaxial tensile test on the P-type  $\text{Bi}_{0.4}\text{Sb}_{1.6}\text{Te}_3$  bar-shaped samples. The sample is glued to two threaded rods at the ends which are attached to two skewed ball joints and couplers for alignment purposes.



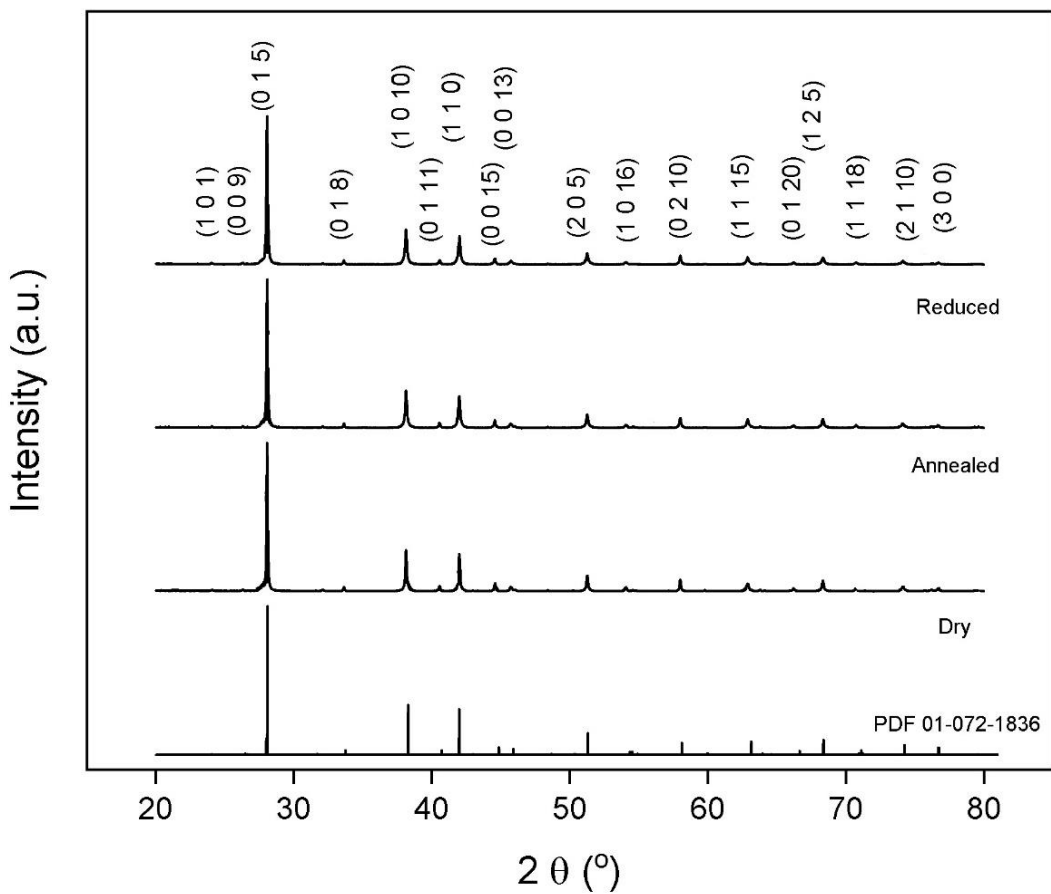


Fig. 2. XRD patterns of P-type  $\text{Bi}_{0.4}\text{Sb}_{1.6}\text{Te}_3$  (PDF 01-072-1836) [28] as a function of powder processing treatment.

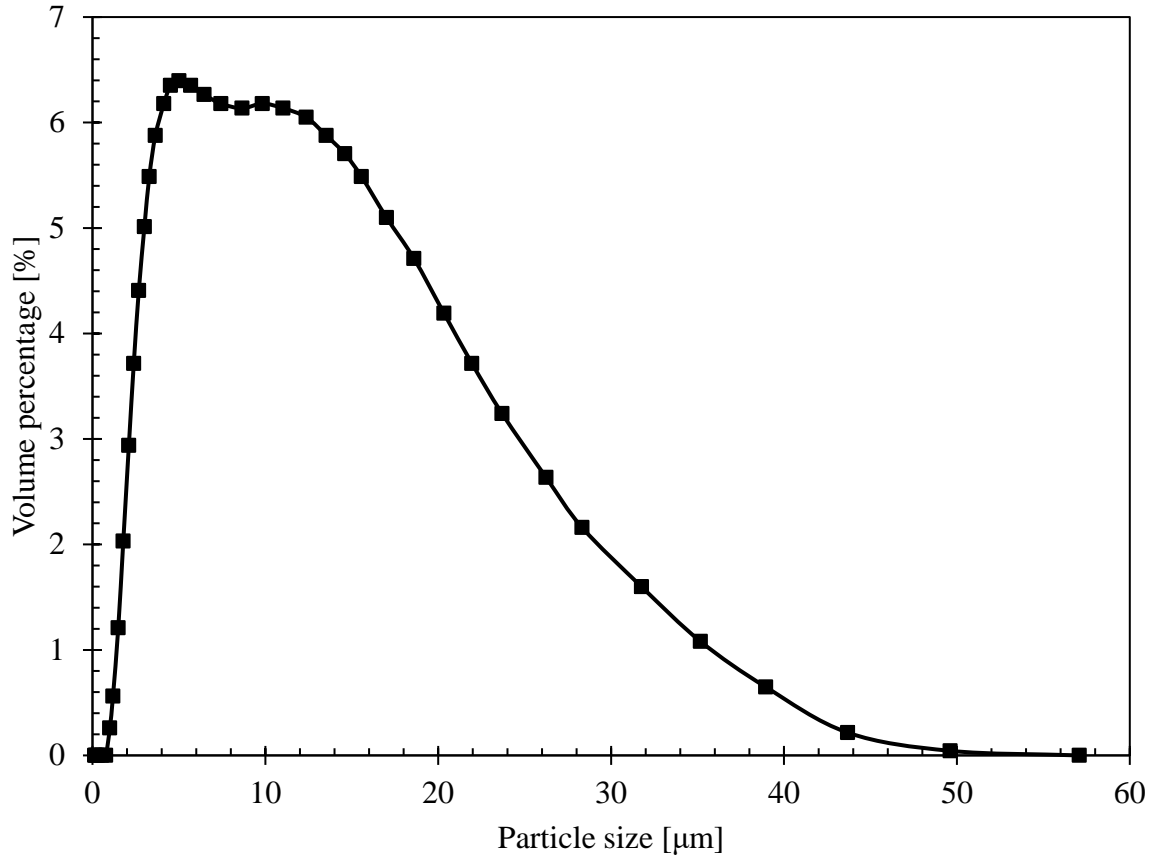


Fig. 3. Particle size distribution of the starting powder after sieving and the ethanol sedimentation process and prior any powder pre-treatment of P-type  $\text{Bi}_{0.4}\text{Sb}_{1.6}\text{Te}_3$  produced using laser diffraction particle size analyzer.

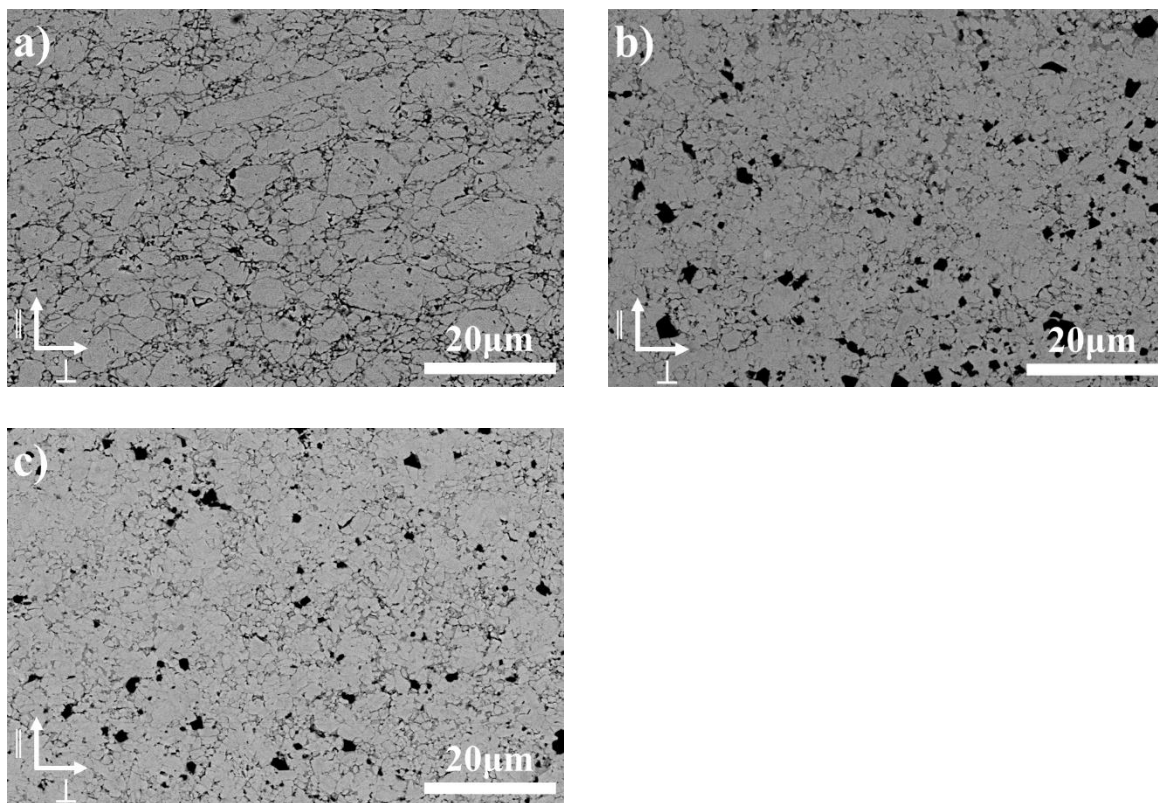


Fig.4. Low magnification SEM cross-sectional microstructures after sintering for the three powder processing routes. a) dry, b) annealed and c) reduced. The vertical side of the images is parallel to the pressing direction during sintering.

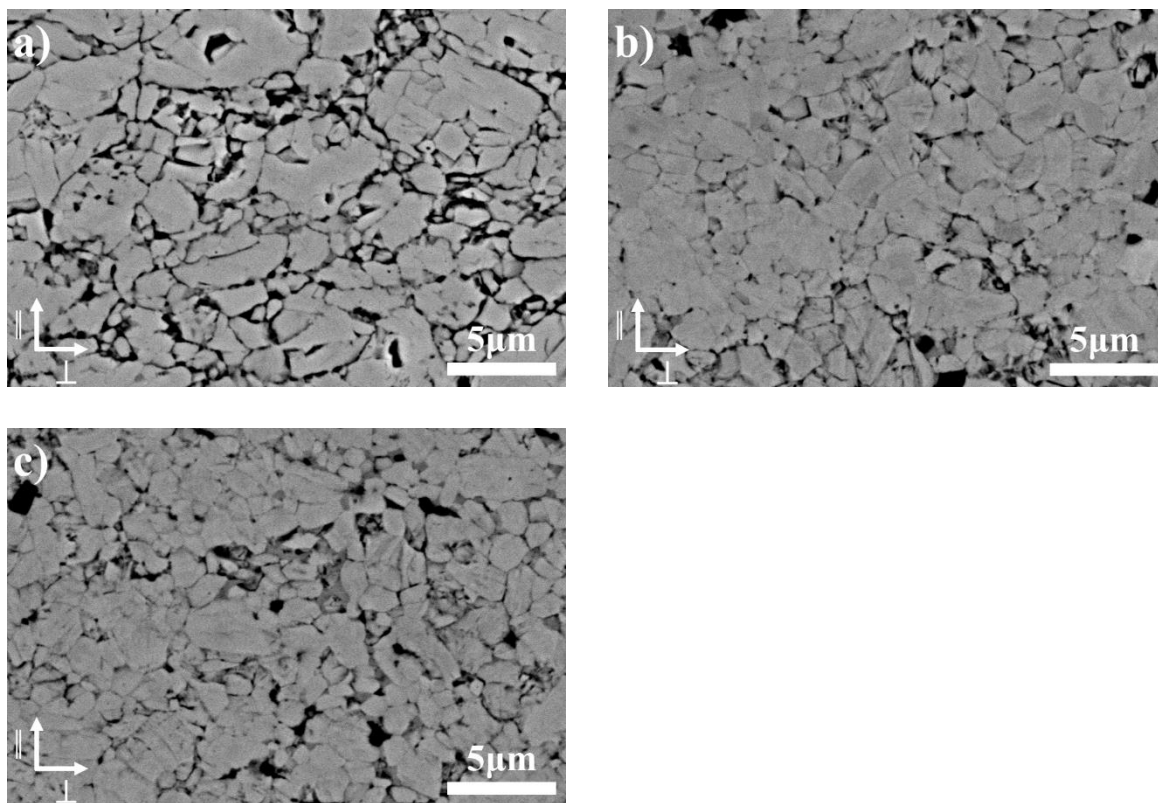


Fig.5. High magnification SEM cross-sectional microstructures after sintering for the three powder processing routes. a) dry, b) annealed and c) reduced. The vertical side of the images is parallel to the pressing direction during sintering.

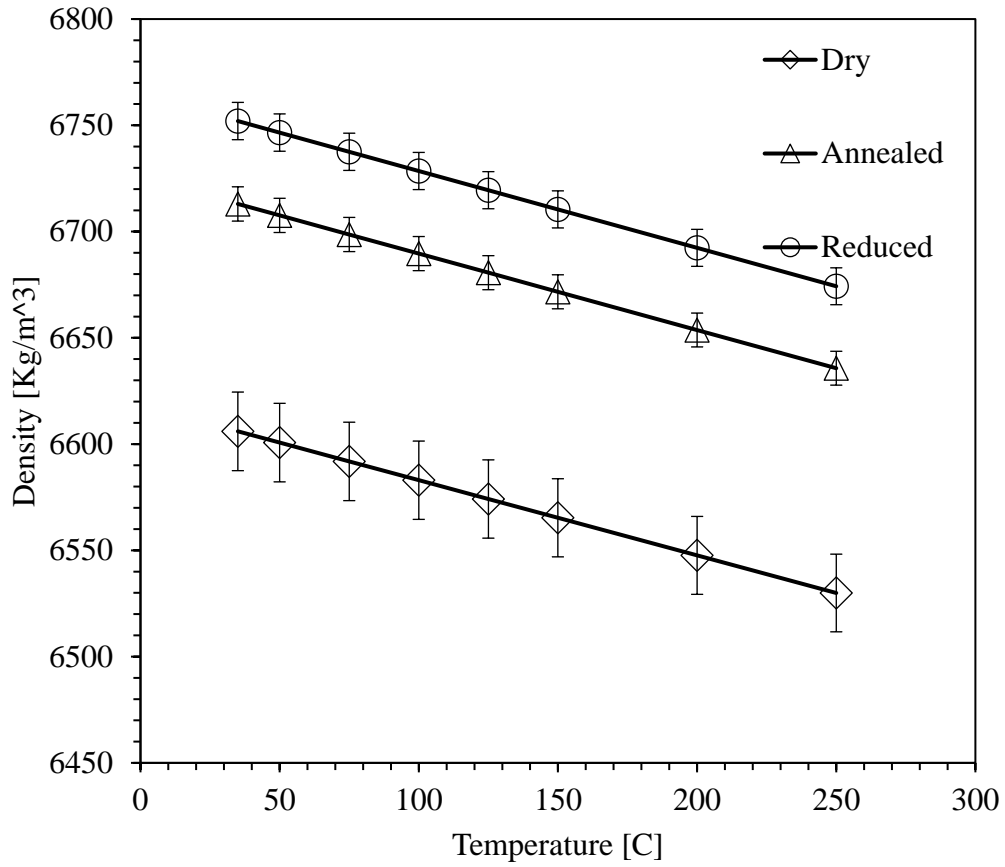


Fig.6. Density as a function of temperature for the powder treatments corrected using the average CTE.

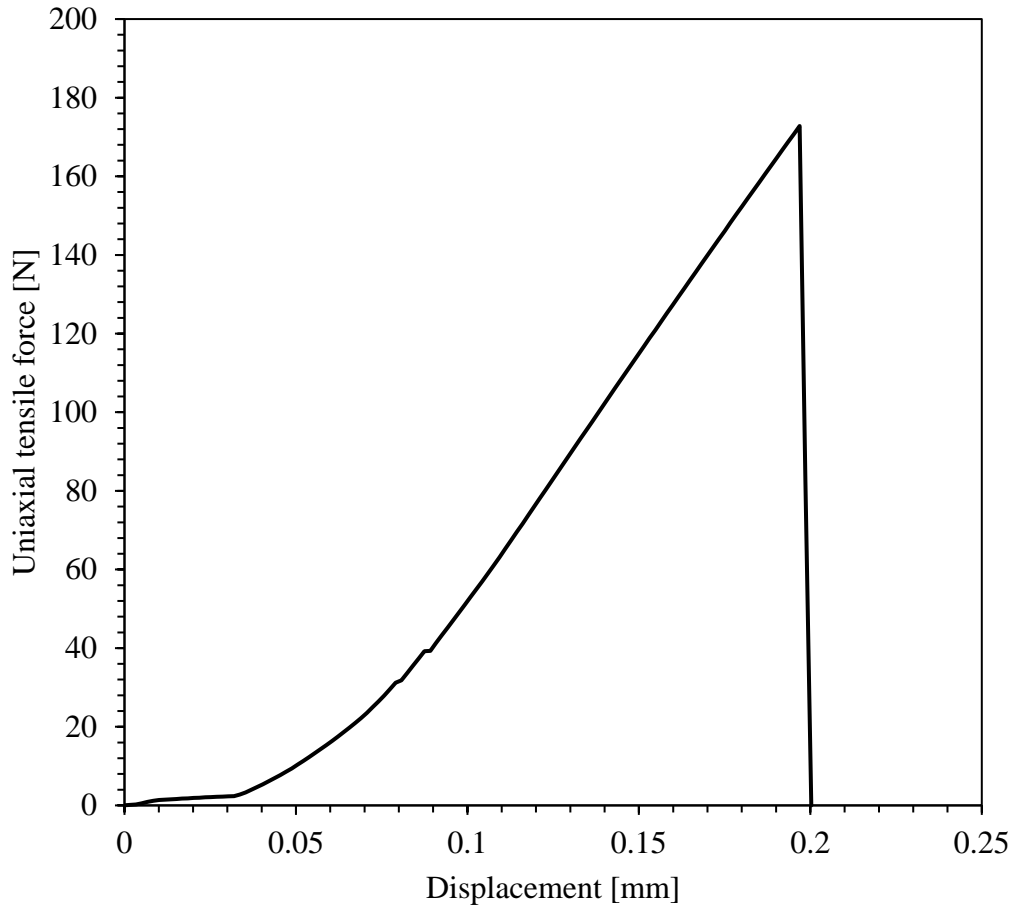


Fig.7. Uniaxial tensile test force vs. displacement curve for a reduced powder SPS sample.

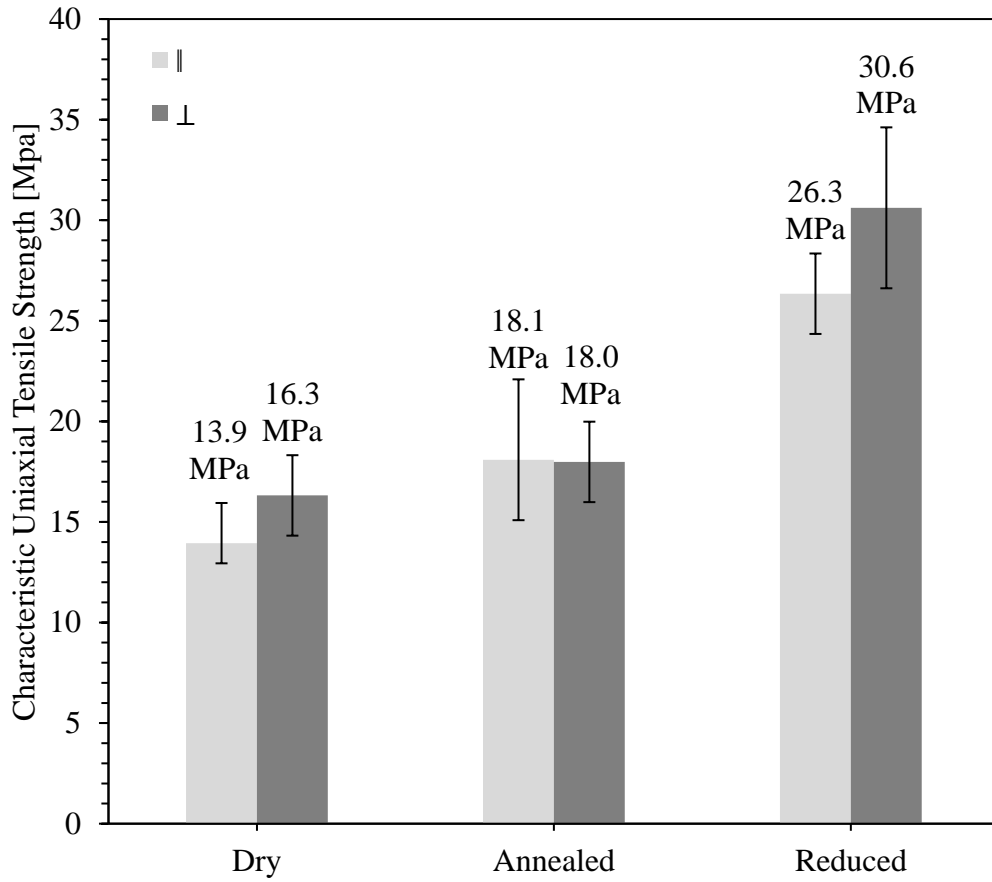


Fig.8. The characteristic uniaxial tensile strength for the three powder treatments measured in the parallel and the perpendicular direction to the applied pressure during sintering.

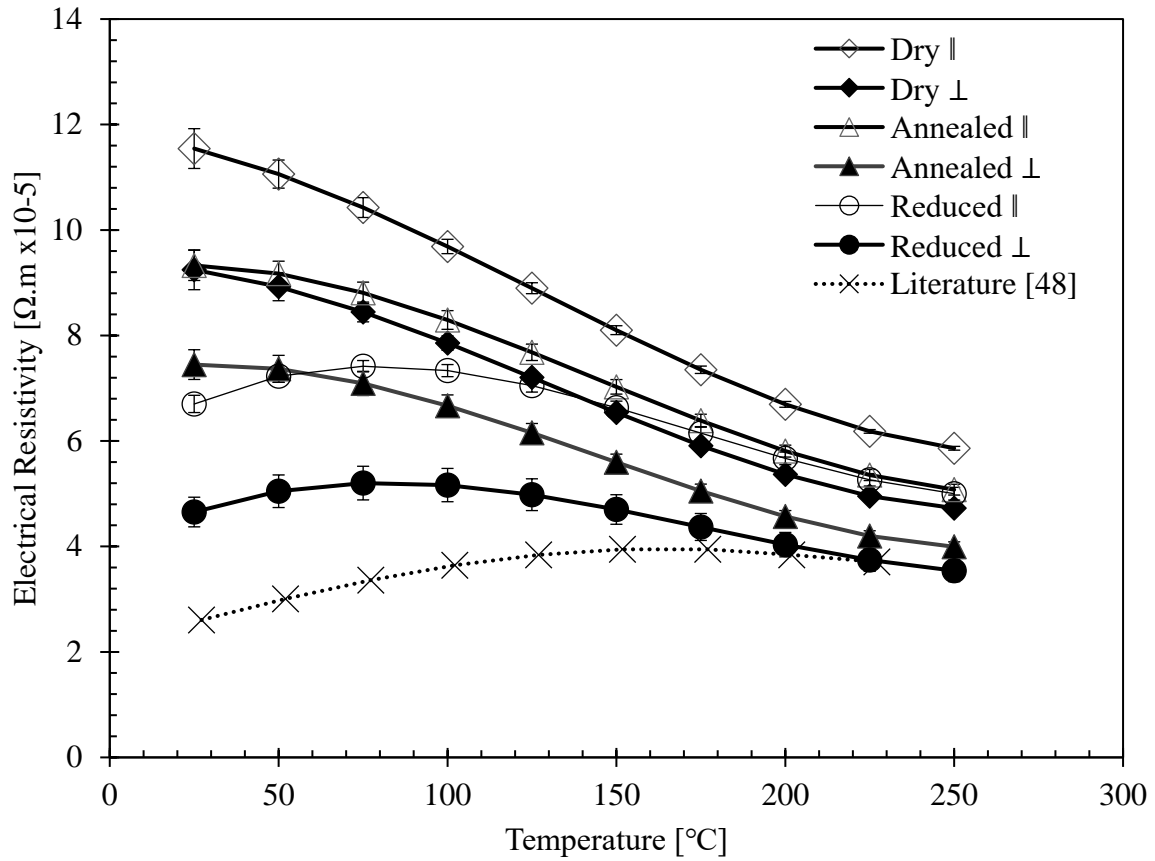


Fig.9. Electrical resistivity  $\rho_e$  vs. temperature for the three powder treatments in the parallel and the perpendicular directions, and Dharmaiah et al. (Literature [48]) with a powder particle size  $< 30 \mu m$ .



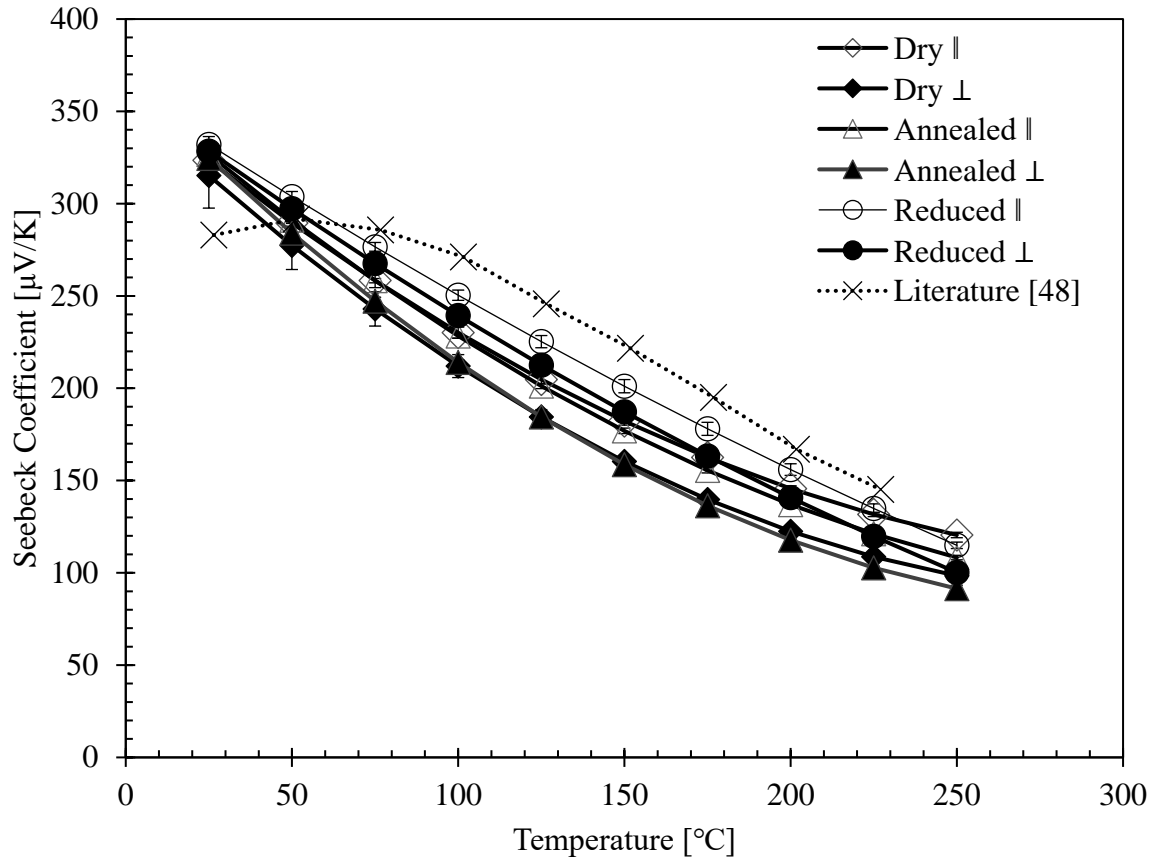


Fig.10. Seebeck Coefficient ( $\alpha$ ) vs. temperature for the three powder treatments in both the parallel and the perpendicular directions, and Dharmaiah et al. (Literature [48]) with a powder particle size  $< 30 \mu\text{m}$ .

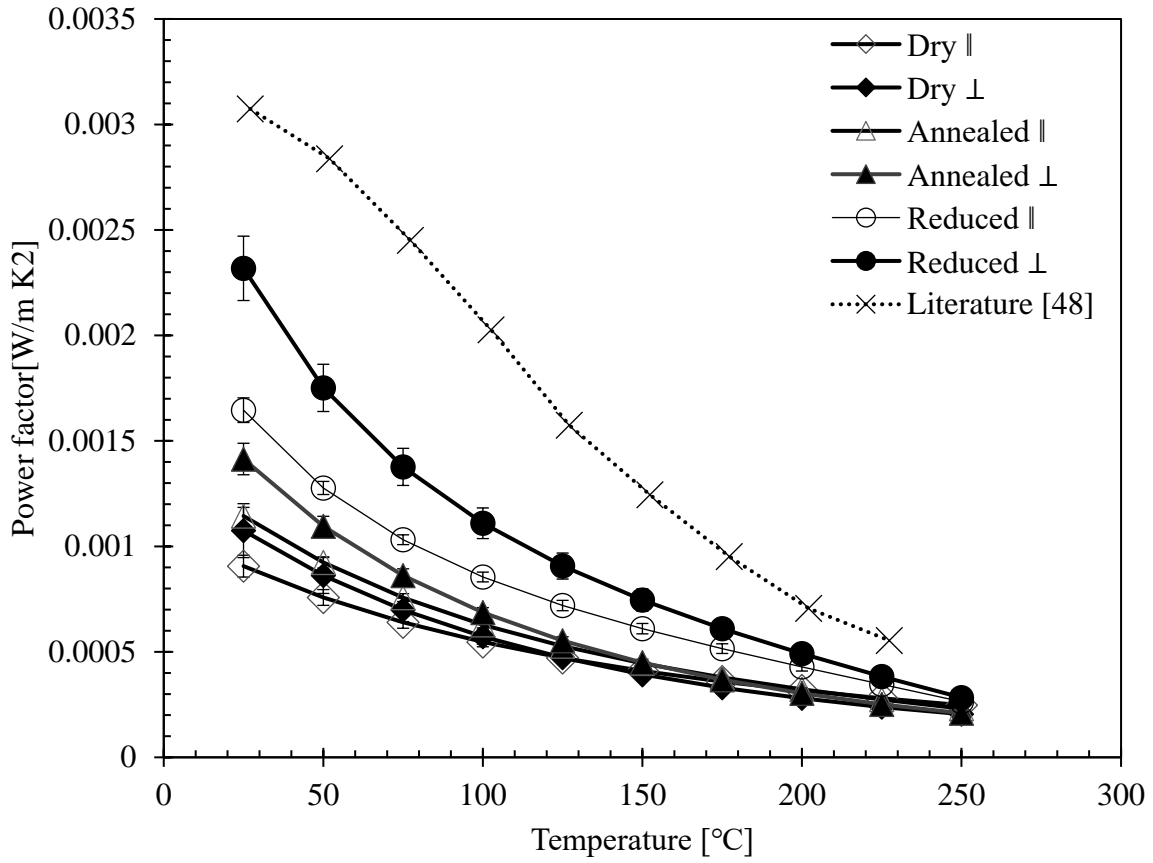


Fig.11. Power factor vs. temperature for the three powder treatments in both the parallel and the perpendicular directions, and Dharmiah et al. (Literature [48]) with a powder particle size  $< 30 \mu\text{m}$ .

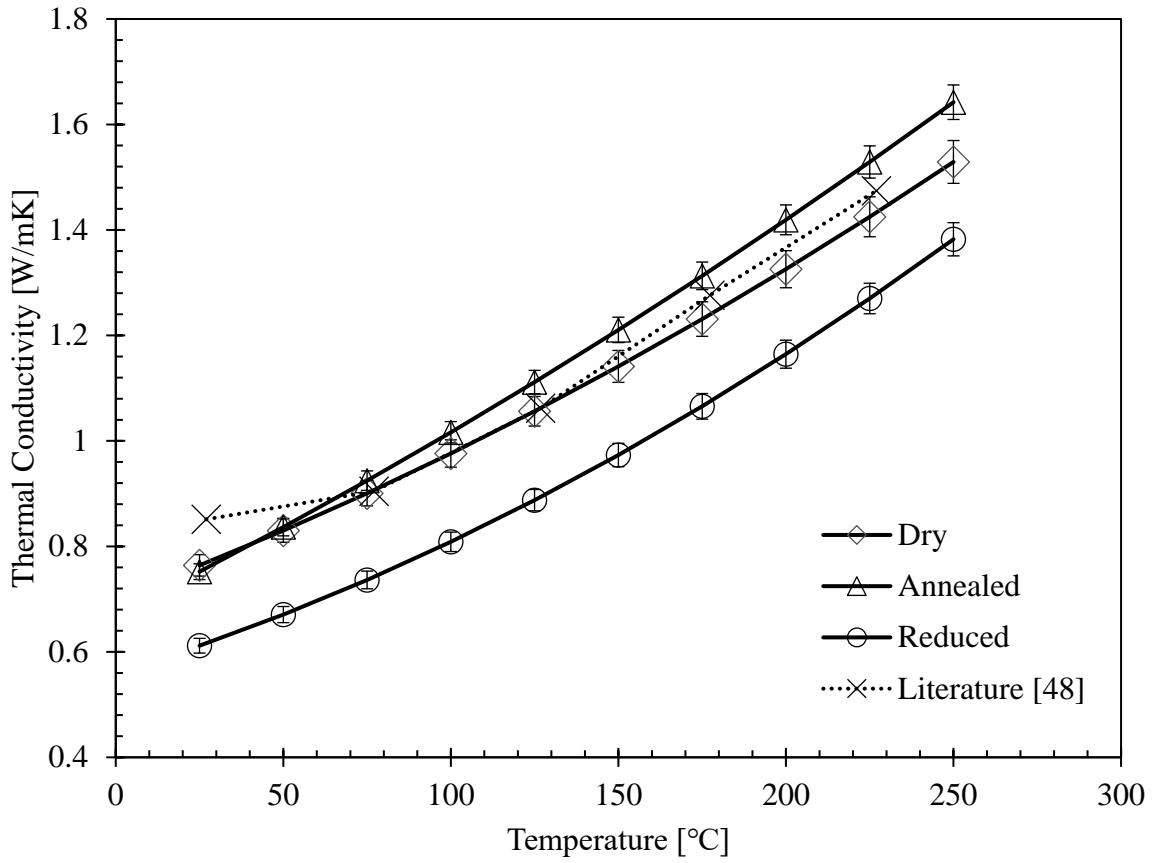


Fig.12. Thermal conductivity vs. temperature for the three powder treatments in the parallel direction only due to limitations in the samples size, and Dharmiah et al. (Literature [48]) with a powder particle size  $< 30 \mu\text{m}$ .

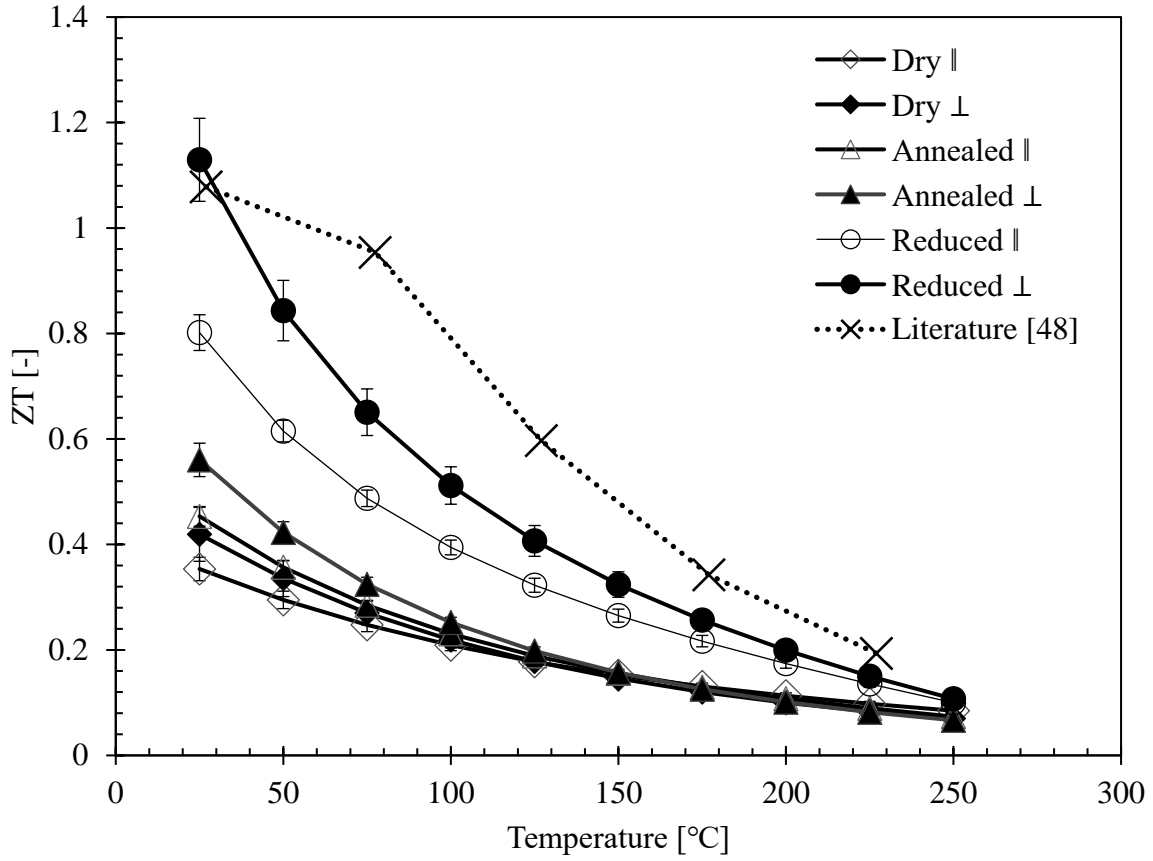


Fig.13. ZT vs. temperature for the three powder treatments in both the parallel and the perpendicular directions, and Dharmiah et al. (Literature [48]) with a powder particle size < 30  $\mu$  m.

Table 1

The average oxygen content and the relative density of spark plasma sintered bodies of P-type  $\text{Bi}_{0.4}\text{Sb}_{1.6}\text{Te}_3$  for the three powder processing routes (dry, annealed and reduced).

Powder Treatment	Oxygen content [wt%]	Relative density [%]
Dry	$0.67 \pm 0.02$	$97.1 \pm 0.3$
Annealed	$0.71 \pm 0.02$	$98.7 \pm 0.1$
Reduced	$0.48 \pm 0.01$	$99.2 \pm 0.1$

Table 2

The average particle directional size of spark plasma sintered bodies of P-type  $\text{Bi}_{0.4}\text{Sb}_{1.6}\text{Te}_3$  for the three powder processing routes (dry, annealed and reduced) in the parallel and perpendicular directions to the sintering applied pressure using high magnification SEM micrographs.

Powder treatment	Average particle size [ $\mu\text{m}$ ]	
	direction	$\perp$ direction
Dry	$1.03 \pm 0.06$	$1.26 \pm 0.09$
Annealed	$0.90 \pm 0.06$	$1.09 \pm 0.07$
Reduced	$0.88 \pm 0.04$	$1.16 \pm 0.06$

Table 3

The average coefficient of thermal expansion ( $CTE_{ave}$ ) of spark plasma sintered bodies of P-type  $Bi_{0.4}Sb_{1.6}Te_3$  for the three powder processing routes (dry, annealed and reduced) in the parallel and perpendicular directions to the sintering applied pressure.

Powder treatment	$CTE_{ave}$ [m/mK]	
	direction	⊥ direction
Dry	$18.2 \pm 0.2$	$17.5 \pm 0.2$
Annealed	$18.2 \pm 0.2$	$17.5 \pm 0.2$
Reduced	$18.4 \pm 0.2$	$17.9 \pm 0.2$

Table 4

Characteristic tensile strength and Weibull modulus for spark plasma sintered P-type  $Bi_{0.4}Sb_{1.6}Te_3$  measured in the parallel and perpendicular directions to the sintering applied pressure.

Powder Treatment	Characteristic tensile strength [MPa]		Weibull modulus [-]	
	Value (upper limit, lower limit)		Value (upper limit, lower limit)	
	direction	⊥ direction	direction	⊥ direction
Dry	16.3 (18.3, 14.6)	16.3 (18.3, 14.6)	5.3 (7.0, 3.2)	4.5 (5.8, 2.8)

Annealed	18.1 (22.3, 14.7)	18.0 (19.9, 16.3)	1.8 (2.3, 1.3)	5.0 (6.4, 3.2)
Reduced	26.3 (28.6, 24.5)	30.6 (34.6, 27.2)	4.9 (6.0, 3.6)	3.2 (3.9, 2.3)

Table 5

Young's modulus Shear Modulus, and Poisson's ratio of spark plasma sintered bodies of P-type  $\text{Bi}_{0.4}\text{Sb}_{1.6}\text{Te}_3$  for the three powder processing routes (dry, annealed and reduced).

Powder Treatment	Young's modulus [GPa]	Shear modulus [GPa]	Poisson's ratio [-]
Dry	$44.3 \pm 0.2$	$17.8 \pm 0.1$	$0.245 \pm 0.003$
Annealed	$48.1 \pm 0.2$	$19.3 \pm 0.1$	$0.248 \pm 0.001$
Reduced	$48.7 \pm 0.1$	$19.5 \pm 0.1$	$0.249 \pm 0.001$

Table 6

Hall effect parameters for the powder treatments

Batch	Carrier concentration ( $10^{18} \text{ cm}^{-3}$ )	Mobility ( $\text{cm}^2/\text{V} \cdot \text{s}$ )
Dry	5.45	163
Annealed	7.54	189
Reduced	9.4	223

## 2.8. References:

- [1] C. Forman, I.K. Muritala, R. Pardemann, B. Meyer, Estimating the global waste heat potential, *Renew. Sustain. Energy Rev.* 57 (2016) 1568–1579.  
<https://doi.org/10.1016/j.rser.2015.12.192>.
- [2] D.M. Rowe, *CRC Handbook of THERMOELECTRICS*, CRC press LLC, 1995.
- [3] A. Massaguer, E. Massaguer, M. Comamala, T. Pujol, J.R. González, M.D. Cardenas, D. Carbonell, A.J. Bueno, A method to assess the fuel economy of automotive thermoelectric generators, *Appl. Energy.* 222 (2018) 42–58.  
<https://doi.org/10.1016/j.apenergy.2018.03.169>.
- [4] Y. Wang, S. Li, X. Xie, Y. Deng, X. Liu, C. Su, Performance evaluation of an automotive thermoelectric generator with inserted fins or dimpled-surface hot heat exchanger, *Appl. Energy.* 218 (2018) 391–401. <https://doi.org/10.1016/j.apenergy.2018.02.176>.
- [5] B. Li, K. Huang, Y. Yan, Y. Li, S. Twaha, J. Zhu, Heat transfer enhancement of a modularised thermoelectric power generator for passenger vehicles, *Appl. Energy.* 205 (2017) 868–879. <https://doi.org/10.1016/j.apenergy.2017.08.092>.
- [6] M.H. Zaher, M.Y. Abdelsalam, J.S. Cotton, Study of the effects of axial conduction on the performance of thermoelectric generators integrated in a heat exchanger for waste heat recovery applications, *Appl. Energy.* 261 (2020) 114434.  
<https://doi.org/10.1016/j.apenergy.2019.114434>.
- [7] E.D.M. Rowe, D. Ph, D. Sc, F. Group, *Thermoelectric Handbook - Macro to Nano*, CRC Press Taylor & Francis Group, 2006.



- [8] H. Bando, K. Koizumi, Y. Oikawa, K. Daikohara, V. a. Kulbachinskii, H. Ozaki, The time-dependent process of oxidation of the surface of  $\text{Bi}_2\text{Te}_3$  studied by X-ray photoelectron spectroscopy, *J. Phys. Condens. Matter.* 12 (2000) 5607. <https://doi.org/10.1088/0953-8984/12/26/307>.
- [9] C.H. Lim, D.C. Cho, Y.S. Lee, C.H. Lee, Effects of Hydrogen Reduction on the Thermoelectric Properties of Spark-Plasma-Sintered  $\text{Bi}_2\text{Te}_3$ -Based Compounds, 46 (2005) 995–1000.
- [10] Y. Horio, A. Inoue, Effect of Oxygen Content on Thermoelectric Properties of n-Type  $(\text{Bi,Sb})_2(\text{Te,Se})_3$  Alloys Prepared by Rapid Solidification and Hot-Pressing Techniques, *Mater. Trans.* 47 (2006) 1412–1416. <https://doi.org/10.2320/matertrans.47.1412>.
- [11] P. Rimal, S.-M. Yoon, E.-B. Kim, C.-H. Lee, S.-J. Hong, Effects of Hydrogen Reduction in Microstructure, Mechanical and Thermoelectric Properties of Gas Atomized n-type  $\text{Bi}_2\text{Te}_{2.7}\text{Se}_{0.3}$  Material, *J. Korean Powder Metall. Inst.* 23 (2016) 126–131. <https://doi.org/10.4150/KPMI.2016.23.2.126>.
- [12] J. Seo, K. Park, D. Lee, C. Lee, Characteristics of p-type  $\text{Bi}_{0.5}\text{Sb}_{1.5}\text{Te}_3$  compounds doped with Te, *Mater. Lett.* 35 (1998) 4–9. [https://doi.org/10.1016/S0167-577X\(97\)00217-6](https://doi.org/10.1016/S0167-577X(97)00217-6).
- [13] S. Seo, Y. Jeong, M.W. Oh, B. Yoo, Effect of hydrogen annealing of ball-milled  $\text{Bi}_{0.5}\text{Sb}_{1.5}\text{Te}_3$  powders on thermoelectric properties, *J. Alloys Compd.* 706 (2017) 576–583. <https://doi.org/10.1016/j.jallcom.2017.02.181>.
- [14] H.S. Shin, H.P. Ha, D. Bin Hyun, J.D. Shim, D.H. Lee, Thermoelectric properties of 25% $\text{Bi}_2\text{Te}_3$ -75% $\text{Sb}_2\text{Te}_3$  solid solution prepared by hot-pressing method, *J. Phys. Chem. Solids.* 58 (1997) 671–678. [https://doi.org/10.1016/S0022-3697\(96\)00049-2](https://doi.org/10.1016/S0022-3697(96)00049-2).

- [15] K. Park, J.H. Seo, D.C. Cho, B.H. Choi, C.H. Lee, Thermoelectric properties of p-type Te doped  $\text{Bi}_{0.5}\text{Sb}_{1.5}\text{Te}_3$  fabricated by powder extrusion, *Mater. Sci. Eng. B Solid-State Mater. Adv. Technol.* 88 (2002) 103–106. [https://doi.org/10.1016/S0921-5107\(01\)00912-6](https://doi.org/10.1016/S0921-5107(01)00912-6).
- [16] S. Yoon, C. Nagarjuna, D. Shin, C. Lee, B. Madavali, S. Hong, K. Lee, Influence of milling atmosphere on thermoelectric properties of p-type Bi-Sb-Te based alloys by mechanical alloying, *J. Korean Powder Metall. Inst.* 24 (2017) 357–363. <https://doi.org/10.4150/KPMI.2017.24.5.357>.
- [17] O.B. Sokolov, S.Y. Skipidarov, N.I. Duvankov, The variation of the equilibrium of chemical reactions in the process of  $(\text{Bi}_2\text{Te}_3)(\text{Sb}_2\text{Te}_3)(\text{Sb}_2\text{Se}_3)$  crystal growth, *J. Cryst. Growth.* 236 (2002) 181–190. [https://doi.org/10.1016/S0022-0248\(01\)01808-5](https://doi.org/10.1016/S0022-0248(01)01808-5).
- [18] O. Yamashita, S. Tomiyoshi, K. Makita, Bismuth telluride compounds with high thermoelectric figures of merit, *J. Appl. Phys.* 93 (2003) 368–374. <https://doi.org/10.1063/1.1525400>.
- [19] G. Kavei, Improving Hardness and Thermoelectric Performance in Pseudo-ternary Thermoelectric Alloys  $(\text{Bi}_2\text{Te}_3)(\text{Bi}_2\text{Se}_3)(\text{Nd}_2\text{Te}_3)$ , *Jpn. J. Appl. Phys.* 45 (2006) 7032–7035. <https://doi.org/10.1143/JJAP.45.7032>.
- [20] J.P. Fleurial, L. Gailliard, R. Triboulet, H. Scherrer, S. Scherrer, Thermal properties of high quality single crystals of bismuth telluride—Part I: Experimental characterization, *J. Phys. Chem. Solids.* 49 (1988) 1237–1247. [https://doi.org/10.1016/0022-3697\(88\)90182-5](https://doi.org/10.1016/0022-3697(88)90182-5).
- [21] Y. Pan, T.-R. Wei, Q. Cao, J.-F. Li, Mechanically enhanced p- and n-type  $\text{Bi}_2\text{Te}_3$ -based

thermoelectric materials reprocessed from commercial ingots by ball milling and spark plasma sintering, *Mater. Sci. Eng. B.* 197 (2015) 75–81.

<https://doi.org/10.1016/j.mseb.2015.03.011>.

- [22] J. Jiang, L. Chen, S. Bai, Q. Yao, Thermoelectric performance of p-type Bi-Sb-Te materials prepared by spark plasma sintering, *J. Alloys Compd.* 390 (2005) 208–211. <https://doi.org/10.1016/j.jallcom.2004.07.056>.
- [23] J. Jiang, L. Chen, S. Bai, Q. Yao, Q. Wang, Fabrication and thermoelectric performance of textured n-type Bi<sub>2</sub>(Te,Se)<sub>3</sub> by spark plasma sintering, *Mater. Sci. Eng. B.* 117 (2005) 334–338. <https://doi.org/10.1016/j.mseb.2005.01.002>.
- [24] L.D. Zhao, B.P. Zhang, J.F. Li, H.L. Zhang, W.S. Liu, Enhanced thermoelectric and mechanical properties in textured n-type Bi<sub>2</sub>Te<sub>3</sub> prepared by spark plasma sintering, *Solid State Sci.* 10 (2008) 651–658. <https://doi.org/10.1016/j.solidstatesciences.2007.10.022>.
- [25] X. a Fan, J.Y. Yang, W. Zhu, S.Q. Bao, X.K. Duan, C.J. Xiao, Q.Q. Zhang, Z. Xie, Effect of nominal Sb<sub>2</sub>Te<sub>3</sub> content on thermoelectric properties of p-type (Bi<sub>2</sub>Te<sub>3</sub>)<sub>x</sub>(Sb<sub>2</sub>Te<sub>3</sub>)<sub>1-x</sub> alloys by MA–HP, *J. Phys. D. Appl. Phys.* 39 (2006) 5069–5073. <https://doi.org/10.1088/0022-3727/39/23/025>.
- [26] X. a Fan, J.Y. Yang, R.G. Chen, H.S. Yun, W. Zhu, S.Q. Bao, X.K. Duan, Characterization and thermoelectric properties of p-type 25%Bi<sub>2</sub>Te<sub>3</sub>–75%Sb<sub>2</sub>Te<sub>3</sub> prepared via mechanical alloying and plasma activated sintering, *J. Phys. D. Appl. Phys.* 39 (2006) 740–745. <https://doi.org/10.1088/0022-3727/39/4/021>.
- [27] J. Yang, R. Chen, X. Fan, W. Zhu, S. Bao, X. Duan, Microstructure control and thermoelectric properties improvement to n-type bismuth telluride based materials by hot

- extrusion, *J. Alloys Compd.* 429 (2007) 156–162.  
<https://doi.org/10.1016/j.jallcom.2006.04.030>.
- [28] K. Park, J.H. Seo, D.C. Cho, B.H. Choi, C.H. Lee, Thermoelectric properties of p-type Te doped  $\text{Bi}_{0.5}\text{Sb}_{1.5}\text{Te}_3$  fabricated by powder extrusion, 88 (2001) 103–106.
- [29] J. Jiang, L. Chen, S. Bai, Q. Yao, Thermoelectric performance of p-type Bi-Sb-Te materials prepared by spark plasma sintering, *J. Alloys Compd.* 390 (2005) 208–211.  
<https://doi.org/10.1016/j.jallcom.2004.07.056>.
- [30] J. Jiang, L. Chen, S. Bai, Q. Yao, Q. Wang, Fabrication and thermoelectric performance of textured n-type  $\text{Bi}_2(\text{Te,Se})_3$  by spark plasma sintering, *Mater. Sci. Eng. B Solid-State Mater. Adv. Technol.* 117 (2005) 334–338. <https://doi.org/10.1016/j.mseb.2005.01.002>.
- [31] Z.J. Xu, L.P. Hu, P.J. Ying, X.B. Zhao, T.J. Zhu, Enhanced thermoelectric and mechanical properties of zone melted p-type  $(\text{Bi,Sb})_2\text{Te}_3$  thermoelectric materials by hot deformation, *Acta Mater.* 84 (2015) 385–392. <https://doi.org/10.1016/j.actamat.2014.10.062>.
- [32] J.H. Son, M.W. Oh, B.S. Kim, S.D. Park, B.K. Min, M.H. Kim, H.W. Lee, Effect of ball milling time on the thermoelectric properties of p-type  $(\text{Bi,Sb})_2\text{Te}_3$ , *J. Alloys Compd.* 566 (2013) 168–174. <https://doi.org/10.1016/j.jallcom.2013.03.062>.
- [33] J. Jiang, L. Chen, Q. Yao, Q. Wang, Preparation and Properties of p-Type  $(\text{Bi}_2\text{Te}_3)_x(\text{Sb}_2\text{Te}_3)_{1-x}$  Thermoelectric Materials, 46 (2005) 959–962.
- [34] C.H. Lim, K.T. Kim, Y.H. Kim, Y.S. Lee, C.H. Lee, D.C. Cho, C.H. Lee, Effect of powder mixing on thermoelectric properties in  $\text{Bi}_2\text{Te}_3$ -based sintered compounds, *Intermetallics.* 14 (2006) 1370–1374. <https://doi.org/10.1016/j.intermet.2005.10.018>.

- [35] D.W. Liu, J.F. Li, C. Chen, B.P. Zhang, Effects of SiC nanodispersion on the thermoelectric properties of p-type and n-Type Bi<sub>2</sub>Te<sub>3</sub>-based alloys, *J. Electron. Mater.* 40 (2011) 992–998. <https://doi.org/10.1007/s11664-010-1476-x>.
- [36] L.D. Zhao, B.P. Zhang, J.F. Li, M. Zhou, W.S. Liu, J. Liu, Thermoelectric and mechanical properties of nano-SiC-dispersed Bi<sub>2</sub>Te<sub>3</sub> fabricated by mechanical alloying and spark plasma sintering, *J. Alloys Compd.* 455 (2008) 259–264. <https://doi.org/10.1016/j.jallcom.2007.01.015>.
- [37] T. Clin, S. Turenne, D. Vasilevskiy, R.A. Masut, Numerical simulation of the thermomechanical behavior of extruded bismuth telluride alloy module, *J. Electron. Mater.* 38 (2009) 994–1001. <https://doi.org/10.1007/s11664-009-0756-9>.
- [38] A.S. Al-Merbati, B.S. Yilbas, A.Z. Sahin, Thermodynamics and thermal stress analysis of thermoelectric power generator: Influence of pin geometry on device performance, *Appl. Therm. Eng.* 50 (2013) 683–692. <https://doi.org/10.1016/j.applthermaleng.2012.07.021>.
- [39] B.S. Yilbas, S.S. Akhtar, A.Z. Sahin, Thermal and stress analyses in thermoelectric generator with tapered and rectangular pin configurations, *Energy.* 114 (2016) 52–63. <https://doi.org/10.1016/j.energy.2016.07.168>.
- [40] S. Shittu, G. Li, X. Zhao, X. Ma, Y.G. Akhlaghi, E. Ayodele, High performance and thermal stress analysis of a segmented annular thermoelectric generator, *Energy Convers. Manag.* 184 (2019) 180–193. <https://doi.org/10.1016/j.enconman.2019.01.064>.
- [41] M. Picard, S. Turenne, D. Vasilevskiy, R.A. Masut, Numerical simulation of performance and thermomechanical behavior of thermoelectric modules with segmented bismuth-telluride-based legs, *J. Electron. Mater.* 42 (2013) 2343–2349.

<https://doi.org/10.1007/s11664-012-2435-5>.

- [42] S. Turenne, T. Clin, D. Vasilevskiy, R.A. Masut, Finite element thermomechanical modeling of large area thermoelectric generators based on bismuth telluride alloys, *J. Electron. Mater.* 39 (2010) 1926–1933. <https://doi.org/10.1007/s11664-009-1049-z>.
- [43] J.L. Gao, Q.G. Du, X.D. Zhang, X.Q. Jiang, Thermal Stress Analysis and Structure Parameter Selection for a Bi<sub>2</sub>Te<sub>3</sub>-Based Thermoelectric Module, *J. Electron. Mater.* 40 (2011) 884–888. [https://doi.org/Doi 10.1007/S11664-011-1611-3](https://doi.org/Doi%2010.1007/S11664-011-1611-3).
- [44] A.S. Al-Merbati, B.S. Yilbas, A.Z. Sahin, Thermodynamics and thermal stress analysis of thermoelectric power generator: Influence of pin geometry on device performance, *Appl. Therm. Eng.* 50 (2013) 683–692. <https://doi.org/10.1016/j.applthermaleng.2012.07.021>.
- [45] Y. Tong, F. Yi, L. Liu, P. Zhai, Q. Zhang, Molecular dynamics study on thermo-mechanical properties of bismuth telluride bulk, *Comput. Mater. Sci.* 48 (2010) 343–348. <https://doi.org/10.1016/j.commatsci.2010.01.019>.
- [46] G. Chen, Y. Mu, P. Zhai, G. Li, Q. Zhang, An investigation on the coupled thermal-mechanical-electrical response of automobile thermoelectric materials and devices, *J. Electron. Mater.* 42 (2013) 1762–1770. <https://doi.org/10.1007/s11664-012-2422-x>.
- [47] U. Erturun, K. Erermis, K. Mossi, Effect of various leg geometries on thermo-mechanical and power generation performance of thermoelectric devices, *Appl. Therm. Eng.* 73 (2014) 128–141. <https://doi.org/10.1016/j.applthermaleng.2014.07.027>.
- [48] S. Fan, Y. Gao, Numerical simulation on thermoelectric and mechanical performance of annular thermoelectric generator, *Energy.* 150 (2018) 38–48.

<https://doi.org/10.1016/j.energy.2018.02.124>.

- [49] S. Shittu, G. Li, X. Zhao, X. Ma, Y.G. Akhlaghi, E. Ayodele, High performance and thermal stress analysis of a segmented annular thermoelectric generator, *Energy Convers. Manag.* 184 (2019) 180–193. <https://doi.org/10.1016/j.enconman.2019.01.064>.
- [50] Z.G. Shen, X. Liu, S. Chen, S.Y. Wu, L. Xiao, Z.X. Chen, Theoretical analysis on a segmented annular thermoelectric generator, *Energy*. 157 (2018) 297–313. <https://doi.org/10.1016/j.energy.2018.05.163>.
- [51] G. Min, D.M. Rowe, Ring-structured thermoelectric module, *Semicond. Sci. Technol.* 22 (2007) 880–883. <https://doi.org/10.1088/0268-1242/22/8/009>.
- [52] A. Schmitz, C. Stiewe, E. Müller, Preparation of ring-shaped thermoelectric legs from PbTe powders for tubular thermoelectric modules, *J. Electron. Mater.* 42 (2013) 1702–1706. <https://doi.org/10.1007/s11664-012-2402-1>.
- [53] A. Sakai, T. Kanno, K. Takahashi, H. Tamaki, Y. Yamada, Power Generation and Peltier Refrigeration by a Tubular Pi-Type Thermoelectric Module, *J. Electron. Mater.* 44 (2015) 4510–4515. <https://doi.org/10.1007/s11664-015-4017-9>.
- [54] N. Mansouri, E.J. Timm, H.J. Schock, D. Sahoo, A. Kotrba, Development of a Circular Thermoelectric Skutterudite Couple Using Compression Technology, *J. Energy Resour. Technol.* 138 (2016) 052003. <https://doi.org/10.1115/1.4032619>.
- [55] M. Morsy, Manufacturing and Characterization of Annular Thermoelectric Generators and Verification of a Novel Design, McMaster University, Hamilton, Canada, 2015.
- [56] N. Mansouri, E.J. Timm, H.J. Schock, D. Sahoo, A. Kotrba, Development of a Circular

- Thermoelectric Skutterudite Couple Using Compression Technology, *J. Energy Resour. Technol.* 138 (2016) 052003. <https://doi.org/10.1115/1.4032619>.
- [57] M. Morsy, Manufacturing and Characterization of Annular Thermoelectric Generators and Verification of a Novel Design, (2015).
- [58] A.U. Tensile, C.A. Force, Standard Test Method for Transthickness Tensile Strength of Continuous Fiber- Reinforced Advanced Ceramics at Ambient Temperature 1, *i* (2012) 1–16. <https://doi.org/10.1520/C1468-06.2>.
- [59] J.M. Simard, D. Vasilevskiy, S. Turenne, Influence of composition and texture on the thermoelectric and mechanical properties of extruded  $(\text{Bi}_{1-x}\text{Sbx})_2(\text{Te}_{1-y}\text{Sey})_3$  alloys, *Int. Conf. Thermoelectr. ICT, Proc. 2003-Janua* (2003) 13–18. <https://doi.org/10.1109/ICT.2003.1287438>.
- [60] O. Yamashita, S. Tomiyoshi, Effect of annealing on thermoelectric properties of bismuth telluride compounds, *Jpn. J. Appl. Phys.* 42 (2003) 492–500. <https://doi.org/10.1143/JJAP.42.492>.
- [61] J.-L. Gao, Q.-G. Du, X.-D. Zhang, X.-Q. Jiang, Thermal Stress Analysis and Structure Parameter Selection for a  $\text{Bi}_2\text{Te}_3$ -Based Thermoelectric Module, *J. Electron. Mater.* 40 (2011) 884–888. <https://doi.org/10.1007/s11664-011-1611-3>.
- [62] X. Jia, Y. Gao, Estimation of thermoelectric and mechanical performances of segmented thermoelectric generators under optimal operating conditions, *Appl. Therm. Eng.* 73 (2014) 333–340. <https://doi.org/10.1016/j.applthermaleng.2014.07.069>.
- [63] S. Fan, Y. Gao, Numerical simulation on thermoelectric and mechanical performance of



annular thermoelectric generator, *Energy*. 150 (2018) 38–48.

<https://doi.org/10.1016/j.energy.2018.02.124>.

- [64] S. St-Laurent, S. Chen, H. Li, Low melting point metal or alloy powders atomization manufacturing processes, US 20190193164 A1, 2018.
- [65] M.M. Stasova, N.H. Abrikosov, *Izv. Akad. Nauk SSSR, Neorg. Mater.*, 6, 1090, 1970.
- [66] V.B. Chernogorenko, K.A. Lynchak, Z.A. Klimak, R.A. Morozova, Kinetics of antimony trioxide reduction by hydrogen. Effect of atomic hydrogen, *Sov. Powder Metall. Met. Ceram.* 17 (1978) 419–421. <https://doi.org/10.1007/BF00795791>.
- [67] Standard Test Methods for Determining Average Grain Size, ASTM Stand. (2020) 1–28. <https://doi.org/10.1520/E0112-13.1.4>.
- [68] Z. Zhang, P.A. Sharma, E.J. Lavernia, N. Yang, Thermoelectric and transport properties of nanostructured Bi<sub>2</sub>Te<sub>3</sub> by spark plasma sintering, *J. Mater. Res.* 26 (2011) 475–484. <https://doi.org/10.1557/jmr.2010.67>.
- [69] H.S. B. Eisenmann, *LANDOLT-BORNSTEIN Numerical Data and Functional Relationships in Science and Technology*, 1985.
- [70] L.M. Pavlova, Y.I. Shtern, R.E. Mironov, Thermal expansion of bismuth telluride, *High Temp.* 49 (2011) 369–379. <https://doi.org/10.1134/S0018151X1103014X>.
- [71] G.D. Quinn, B.T. Sparenberg, P. Koshy, L.K. Ives, S. Jahanmir, D.D. Arola, Flexural Strength of Ceramic and Glass Rods, 37 (2009) 1–23.
- [72] Y. Zheng, H. Xie, S. Shu, Y. Yan, H. Li, X. Tang, High-temperature mechanical and thermoelectric properties of p-type Bi<sub>0.5</sub>Sb<sub>1.5</sub>Te<sub>3</sub> commercial zone melting ingots, *J.*

Electron. Mater. 43 (2014) 2017–2022. <https://doi.org/10.1007/s11664-013-2938-8>.

- [73] L. Ćurković, A. Bakić, J. Kodvanj, T. Haramina, Flexural strength of alumina ceramics: Weibull analysis, *Trans. Famena*. 34 (2010) 13–18.
- [74] Astm, Standard Practice for Reporting Uniaxial Strength Data and Estimating Weibull Distribution Parameters for Advanced Ceramics, *Astm. i* (2000) 1–17.  
<https://doi.org/10.1520/C1239-13.Scope>.
- [75] D.R.L. Ed, *CRC Handbook of Chemistry and Physics*, 84th Edition, 2003-2004, (n.d.).
- [76] T.A.C. Society-discussions, Effect of Porosity on Young's, 45 (n.d.) 94–95.
- [77] K.K. Phani, S.K. Niyogi, Young's modulus of porous brittle solids, *J. Mater. Sci.* 22 (1987) 257–263. <https://doi.org/10.1007/BF01160581>.
- [78] J. Luo, R. Stevens, Porosity-dependence of elastic moduli and hardness of 3Y-TZP ceramics, 25 (1999).
- [79] M. Asmani, C. Kermel, A. Leriche, M. Ourak, Influence of porosity on Young's modulus and poisson's ratio in alumina ceramics, *J. Eur. Ceram. Soc.* 21 (2001) 1081–1086.  
[https://doi.org/10.1016/S0955-2219\(00\)00314-9](https://doi.org/10.1016/S0955-2219(00)00314-9).
- [80] ASTM, *Standard Practice for Measuring Ultrasonic Velocity in Materials*, 2015.  
<https://doi.org/10.1520/E0494-15>.
- [81] M.L. Lwin, P. Dharmaiah, B. Madavali, C.H. Lee, D. won Shin, G. Song, K.H. Lee, S.J. Hong, Oxide formation mechanism and its effect on the microstructure and thermoelectric properties of p-type Bi<sub>0.5</sub>Sb<sub>1.5</sub>Te<sub>3</sub> alloys, *Intermetallics*. 103 (2018) 23–32.  
<https://doi.org/10.1016/j.intermet.2018.09.015>.

- [82] J.M. Schultz, J.P. McHugh, W.A. Tiller, Effects of heavy deformation and annealing on the electrical properties of Bi<sub>2</sub>Te<sub>3</sub>, *J. Appl. Phys.* 33 (1962) 2443–2450.  
<https://doi.org/10.1063/1.1728990>.
- [83] J. Horák, K. Čermák, L. Koudelka, Energy formation of antisite defects in doped Sb<sub>2</sub>Te<sub>3</sub> and Bi<sub>2</sub>Te<sub>3</sub> crystals, *J. Phys. Chem. Solids.* 47 (1986) 805–809.  
[https://doi.org/10.1016/0022-3697\(86\)90010-7](https://doi.org/10.1016/0022-3697(86)90010-7).
- [84] Z. Stary, J. Horák, M. Stordeur, M. Stölzer, Antisite defects in Sb<sub>2-x</sub>Bi<sub>x</sub>Te<sub>3</sub> mixed crystals, *J. Phys. Chem. Solids.* 49 (1988) 29–34. [https://doi.org/10.1016/0022-3697\(88\)90130-8](https://doi.org/10.1016/0022-3697(88)90130-8).
- [85] P. Dharmiah, H.S. Kim, C.H. Lee, S.J. Hong, Influence of powder size on thermoelectric properties of p-type 25%Bi<sub>2</sub>Te<sub>3</sub>-75%Sb<sub>2</sub>Te<sub>3</sub> alloys fabricated using gas-atomization and spark-plasma sintering, *J. Alloys Compd.* 686 (2016) 1–8.  
<https://doi.org/10.1016/j.jallcom.2016.05.340>.
- [86] D.M. Lee, C.H. Lim, S.Y. Shin, D.C. Cho, C.H. Lee, Thermoelectric properties of p-type Bi<sub>0.5</sub>Sb<sub>1.5</sub>Te<sub>3</sub> compounds fabricated by spark plasma sintering, *J. Electroceramics.* 17 (2006) 879–883. <https://doi.org/10.1007/s10832-006-6807-1>.
- [87] D. Hyun, J. Hwang, J. Shim, Thermoelectric properties of (Bi<sub>0.25</sub>Sb<sub>0.75</sub>)<sub>2</sub>Te<sub>3</sub> alloys fabricated by hot-pressing method, *J. Mater. Sci.* 36 (2001) 1285–1291.  
<https://doi.org/10.1023/A:1004862700211>.
- [88] M. Cutler, J.F. Leavy, R.L. Fitzpatrick, Electronic transport in semimetallic cerium sulfide, *Phys. Rev.* 133 (1964). <https://doi.org/10.1103/PhysRev.133.A1143>.

- [89] M. Cutler, R.L. Fitzpatrick, J.F. Leavy, The conduction band of cerium sulfide  $Ce_{3-x}S_4$ , *J. Phys. Chem. Solids.* 24 (1963) 319–327. [https://doi.org/10.1016/0022-3697\(63\)90136-7](https://doi.org/10.1016/0022-3697(63)90136-7).
- [90] G.A.O. Yuanwen, H.E. Yuezhou, Z.H.U. Linli, Impact of grain size on the Seebeck coefficient of bulk polycrystalline thermoelectric materials, (2010). <https://doi.org/10.1007/s11434-009-0705-2>.
- [91] P. Eaksuwanchai, S. Tanusilp, P. Jood, M. Ohta, K. Kurosaki, Increased Seebeck Coefficient and Decreased Lattice Thermal Conductivity in Grain-Size-Controlled p - Type PbTe – MgTe System, (2018). <https://doi.org/10.1021/acsaem.8b01491>.
- [92] D.H. Kim, C. Kim, S.H. Heo, H. Kim, Influence of powder morphology on thermoelectric anisotropy of spark-plasma-sintered Bi-Te-based thermoelectric materials, *Acta Mater.* 59 (2011) 405–411. <https://doi.org/10.1016/j.actamat.2010.09.054>.
- [93] R.J. Moffat, Describing the uncertainties in experimental results, *Exp. Therm. Fluid Sci.* 1 (1988) 3–17. [https://doi.org/10.1016/0894-1777\(88\)90043-X](https://doi.org/10.1016/0894-1777(88)90043-X).
- [94] J. Mackey, F. Dynys, A. Sehirlioglu, Uncertainty analysis for common Seebeck and electrical resistivity measurement systems, *Rev. Sci. Instrum.* 85 (2014). <https://doi.org/10.1063/1.4893652>.

**Chapter 3: The effect of powder pre-treatment on the mechanical and thermoelectric properties of spark plasma sintered N-type bismuth telluride**

*Journal Paper*

# **The effect of powder pre-treatment on the mechanical and thermoelectric properties of spark plasma sintered N-type bismuth telluride**

Ahmed A. Abdelnabi <sup>a</sup>, Vickram Lakhian <sup>a</sup>, Joseph R. McDermid<sup>b</sup>, James S. Cotton <sup>a, \*</sup>

<sup>a</sup> Department of Mechanical Engineering, McMaster University, Hamilton, ON, Canada

<sup>b</sup> Department of Materials Science and Engineering, McMaster University, Hamilton, ON, Canada

\*Corresponding author. Department of Mechanical Engineering, McMaster University, Hamilton, ON, Canada

Email address: cottonjs@mcmaster.ca (James S. Cotton).

## **Highlights:**

- Mechanical and thermoelectric properties were enhanced by reductive powder annealing.
- Powder annealing increases tensile strength from 30.8 to 38.0 MPa in the  $\perp$  direction.
- No anisotropy in the thermoelectric properties was observed.
- The maximum figure of merit ( $ZT_{\max}$ ) increased by 31% to reach 0.63 at 150°C.

**Keywords:** Thermoelectric materials; Mechanical properties; Uniaxial tensile strength;  $(\text{Bi}_{0.95}\text{Sb}_{0.05})_2(\text{Se}_{0.05}\text{Te}_{0.95})_3$ ; Powder pre-treatment; Spark plasma sintering (SPS)

## Abstract

The effect of N-type  $(\text{Bi}_{0.95}\text{Sb}_{0.05})_2(\text{Se}_{0.05}\text{Te}_{0.95})_3$  powder particles pre-treatments, including annealing and surface oxides reduction, was determined in terms of both the mechanical and thermoelectric properties for bodies fabricated using spark plasma sintering (SPS). The uniaxial tensile strength was measured as well as the figure of merit “ZT” is calculated, parallel and perpendicular to the sintering pressure direction. The oxides reduction of the powder particles pre-treatments was carried out using 5%  $\text{H}_2$  - 95% Ar in an in-house built mechanically agitated reduction facility at 380 °C for 24 h, while annealing was carried out at the temperature and holding time using Ar. Both pre-treatments were compared to the manufactured powder sample that was dried under vacuum for 24 h and used as a baseline. The inert gas fusion technique was used to measure the oxide content in the solid sintered samples for the three pre-treatment cases. The oxide content decreased from 0.362 to 0.143 wt.% after  $\text{H}_2$  reduction, while decreased to 0.341 wt.% after annealing. The thermoelectric properties did not show any anisotropic behaviour in the ZT while the uniaxial tensile strength did show due to an anisotropy in the grains shape after SPS. The increase in the mechanical properties is found to be mainly due to annealing that increased the relative density of the sintered samples from 98.0% from 97.0%. Annealing increased the characteristic uniaxial tensile strength from 30.4 to 34.1 MPa and from 30.8 to 38 MPa in the parallel and the perpendicular directions, respectively. The annealing is found to be responsible for the majority of the ZT enhancement while the maximum value of the ZT is archived by the reduction powder pre-treatment. The increase in the ZT is contributed to the increase in the Seebeck coefficient and the decrease in the thermal conductivity despite the increase in the electrical resistivity. The  $\text{ZT}_{\text{max}}$  (150 °C) increased from 0.54 to 0.63 in both parallel and

perpendicular directions due to surface oxide reduction and to 0.58 and 0.62 in the parallel and the perpendicular directions, respectively, due to annealing.

### 3.1.Introduction

Bi<sub>2</sub>Te<sub>3</sub> solution-based compounds are of significant interest in the application of thermoelectric materials (TE) used in low-temperature cooling and power generation applications [1]. The figure of merit:

$$ZT = \frac{\alpha^2 T}{\rho_e k} \quad (1)$$

of the TE material defines the efficiency of thermoelectric generator/cooler (TEG/TEC) materials, in which  $\alpha$  is the Seebeck coefficient,  $\rho_e$  is the electrical resistivity, T is the absolute temperature in Kelvins, and k is the thermal conductivity. Although single crystal N-type (Bi<sub>0.95</sub> Sb<sub>0.05</sub>)<sub>2</sub>(Se<sub>0.05</sub> Te<sub>0.95</sub>)<sub>3</sub> has one of the highest ZT for low-temperature N-type TE materials [2], it suffers from low mechanical strength due to weak cleavage planes along Te(1)-Te(1) layers as they are bonded via Van der Waals forces. SPS is a powder metallurgy sintering technique has shown strong promise in enhancing the mechanical properties of the N-type Bi<sub>2</sub>Te<sub>3</sub> compounds [3,4]. The enhancement in the mechanical strength is due to the small grains and the refinement effect of the microstructure. As reported by Jiang et al. [3], the increase in the bending strength through SPS processing can be as significant as 10 to 80 MPa compared to the zone-melted ingot – i.e. a factor of eight increase. Pan et al. [4] showed that the mechanical strength of the N-type SPSed samples increased from 18.8 to 57.7 MPa compared to the crystal ingot using the modified small punch test. However, despite the increases in mechanical strength, the ZT did not show any enhancement for the N-type SPSed samples [3,4]. An increase in the carrier concentration and a decrease in the mobility was observed for the SPSed samples that leads to a decrease in the Seebeck coefficient and an increase



in the electrical resistivity. Jiang et al. [3] and Pan et al. [4] found that the  $ZT_{\max}$  for the samples sintered using SPS could reach a maximum of 87% of the zone-melted ingots – i.e. a decrease from 0.8 to 0.7.

It is known that the N-type  $\text{Bi}_2\text{Te}_3$  compounds form an oxide layer when exposed to ambient atmosphere [5]. The presence of the oxides in the N-type  $\text{Bi}_2\text{Te}_3$  compound powder affects the thermoelectric properties, where performing a reduction step using  $\text{H}_2$  on the powder results in improved thermoelectric properties of the SPS processed samples [6–8]. Oxide removal was found to increase the carrier concentration and decreases the mobility. The increase in the carrier concentration was the main reason for the Seebeck coefficient increase and the thermal conductivity decrease. The electrical resistivity was found to increase despite the decrease in carrier mobility as the increase in the carrier concentration was the dominant factor. Lim et al. [6] found that the  $ZT$  increased from 0.39 to 0.71 after reducing the powder oxides under  $\text{H}_2$  at 380 °C for 27 h. Rimal et al. [8] found that oxide removal using  $\text{H}_2$  at 360 °C for 4 h enhanced the maximum power factor at 30 °C from  $9.5 \times 10^{-5}$  to  $11.5 \times 10^{-5}$  W/(K<sup>2</sup> m). Although the effect of oxide removal on the thermoelectric properties has been investigated intensively for the N-type  $\text{Bi}_2\text{Te}_3$  compounds, there is a knowledge gap in the literature regarding the effect of the oxide removal on mechanical properties such as uniaxial tensile strength, Young's modulus, shear modulus, Poisson's ratio and the coefficient of thermal expansion for the spark plasma sintered N-type  $(\text{Bi}_{0.95}\text{Sb}_{0.05})_2(\text{Se}_{0.05}\text{Te}_{0.95})_3$  TE materials.

3-point and 4-point bending tests are commonly used to measure the strength of brittle materials, including TE materials [3,9]. However, the bending tests are known to overestimate the tensile strength of brittle materials as a smaller volume of the material is subjected to the maximum stress [10], thereby limiting the chances of encountering the fatal flaw in the material. A more rigorous

determination of the tensile strength and elastic properties of TE materials is critical since the TE legs in TEG modules during operation experience high tensile thermal stresses that could lead to failure [11]. Due to the lack of fully characterized TE materials properties, especially the mechanical properties, researchers use different source of data that are often inconsistent and in some cases just assume properties for their coupled-finite element models to design and study thermoelectric modules during operation [12–15].

The goal of this work is to present a characterization methodology and elaborate on the effect of powder pre-treatment as well as provide consistent and full characterized mechanical and thermoelectric properties of the spark plasma sintered N-type  $(\text{Bi}_{0.95}\text{Sb}_{0.05})_2(\text{Se}_{0.05}\text{Te}_{0.95})_3$ . In this work, the effect of annealing and surface oxide reduction on both the mechanical and thermoelectric properties of is determined. The mechanical properties measured in this study include uniaxial tensile strength, density (including relative density), coefficient of thermal expansion, Young's modulus, Poisson's ratio, and shear modulus. The thermoelectric properties measured include electrical resistivity, Seebeck coefficient and thermal conductivity, which are then used to calculate the ZT via Equation (1). The thermal diffusivity and specific heat capacity values vs. temperature are presented in this study in the Appendix. This work complements the existing body of literature on characterization Abdelnabi et al. [16] in which both contributions provide consistent and full characterized P-type and N-type  $\text{Bi}_2\text{Te}_3$  TE material sintered using SPS.

### **3.2.Experimental methodology**

#### **3.2.1. Sample Preparation**

N-type  $(\text{Bi}_{0.95}\text{Sb}_{0.05})_2(\text{Se}_{0.05}\text{Te}_{0.95})_3$  was provided as powder derived from (5N-Plus, Montréal, Québec). A particle size fraction of 1 to 20  $\mu\text{m}$  was produced by sieving using conventional screens to a particle size range of less than 20  $\mu\text{m}$  and removing all particles less than 1  $\mu\text{m}$  by

sedimentation using methanol. The particle size range was checked by the laser diffraction method (Mastersizer 2000, Malvern Panalytical Ltd). The powder was divided to three equal parts to test the effect of both annealing and powder surface oxide reduction on the resultant sintered body properties. The last third of the powder was dried under vacuum at 100 °C for 24 h and was used as a baseline for comparison to the other two pre-treated powder samples.

All powder pre-treatments were carried out in a mechanically vibrated fluidized bed reactor to ensure even and longer contact of the process gas with the N-type  $(\text{Bi}_{0.95}\text{Sb}_{0.05})_2(\text{Se}_{0.05}\text{Te}_{0.95})_3$  powder. Powder surface oxide reduction was conducted at 380 °C for 24 h using an ultra-pure 5%  $\text{H}_2$  - 95% Ar process atmosphere. Annealing treatments were carried out at 380 °C for 24 h under ultra-pure Ar only to compare the effects of annealing versus the surface oxide reduction treatments. All of the process gases were purified via a molecular sieve to produce a greater than 99.9999% purity process atmosphere. For repeatability, a duplicate of each treatment process was made in the study, for a total of six powder samples.

All further material handling, including the filling of the SPS graphite dies prior to loading into the SPS facility, was done within an  $\text{N}_2$  glovebox to minimize oxidation. The powder was spark plasma sintered using a SPS-211LX (FUJI Electronic Industrial Co., LTD) for 600 s (10 min.), after increasing the temperature from 25 to 420 °C at 8.3 °C/s (50 °C/min.) under 50 MPa of uniaxial pressure. Solid cylindrical samples were produced with dimensions of  $\text{Ø}12.7 \text{ mm} \times 6 \text{ mm}$  and  $\text{Ø}12 \text{ mm} \times 4 \text{ mm}$  for property testing.

### **3.2.2. Sample Analyses**

The phase assemblage of the as-sintered samples for each treatment was obtained by powder X-ray diffraction (XRD, PANalytical X'Pert) using  $\text{Cu-K}\alpha 1$  radiation ( $\lambda = 1.5406 \text{ \AA}$ ). A nitrogen/oxygen analyser (TCH600, Leco) was used to measure the oxygen content in the sintered

samples for each pre-treatment condition using bar-shaped sintered samples with a mass of 1 g. Cross-section micrographs of the sintered samples were taken using a Scanning Electron Microscope (SEM, JEOL JSM-6610LV) using an acceleration voltage of 15 keV and a working distance of 8 mm in backscattered electrons (BSE) mode. No etching step was needed as a 0.25  $\mu\text{m}$  standard colloidal silica (OP-S) was used as the final standard polishing step.

The Archimedes method was used to measure the as-sintered body density for all the solid cylindrical samples under ambient conditions. A quenching dilatometer (L78 RITA Dilatometer, LINSEIS) was used to measure the coefficient of thermal expansion (CTE) through a temperature range of 35 to 250  $^{\circ}\text{C}$  using a 6.7  $^{\circ}\text{C}/\text{s}$  (40  $^{\circ}\text{C}/\text{min}$ ) heating rate. The CTE was measured both parallel ( $\parallel$ ) and perpendicular ( $\perp$ ) to the pressing direction during sintering on  $6 \times 2.5 \times 2.5$  mm samples excised using a precision diamond saw (Struers - MINITOM). The uniaxial tensile strength was measured using a conventional tensile frame (AGS-X, Shimadzu Autograph) using a 500 N load cell with a crosshead speed of 0.1mm/min. The tensile strength was measured using twenty bar-shaped samples with dimensions of  $6 \times 2.5 \times 2.5$  mm from each powder pre-treatment condition, in both parallel and perpendicular directions relative to the sintering pressing direction. The method and the fixture that was used to measure the characteristic uniaxial tensile strength are presented in detail Abdelnabi et al, [16]. Young's modulus, shear modulus and Poisson ratio were determined through measurement of longitudinal and the shear wave velocities in the bulk of the sintered samples. The following relations were to calculate the Young's modulus, shear modulus and the Poisson's ratio:

$$\nu = \frac{1 - 2 \left( \frac{V_T}{V_L} \right)^2}{2 - 2 \left( \frac{V_T}{V_L} \right)^2} \quad (2)$$

$$E = \frac{V_L^2 \rho (1 - \nu)(1 - 2\nu)}{(1 - \nu)} \quad (3)$$

$$G = V_T^2 \rho \quad (4)$$

where  $\nu$  is the Poisson's ratio,  $V_L$  is the longitudinal wave velocity,  $V_T$  is the transverse wave velocity (shear),  $\rho$  is the density,  $E$  is the Young's modulus and  $G$  is the shear modulus. The measurements were only made in the parallel direction due to the ultrasonic transducer size. Both the longitudinal and shear ultrasonic waves were measured using a Pulser/Receiver module (5072PR, OLYMPUS) at 2 kHz pulse repetition frequency (PRF), 104  $\mu$ J pulse energy, 500  $\Omega$  damping, 1 MHz high-pass filter and +5 dB gain using a 100 MHz digital oscilloscope (DSO-X2014A, Agilent Technologies).

A ULVAC ZEM3 system was used to measure both the Seebeck coefficient and the electrical resistivity both parallel and perpendicular to the sintering pressure direction. The average values of both the Seebeck coefficient and the electrical resistivity were calculated using four values from two heating/cooling cycles at 25  $^{\circ}$ C increments between 25 to 250  $^{\circ}$ C with 25  $^{\circ}$ C and 5  $^{\circ}$ C/min for both the heat and the cooling rates. To measure the thermal diffusivity and specific heat capacity, three  $\text{\O}12 \text{ mm} \times 1 \text{ mm}$  solid disks for each pre-treatment condition were tested using the laser flash method (DLF-1200TA, Instruments). The density values measured were used in the laser flash system software to calculate the thermal conductivity.

### 3.3. Results and Discussion

#### 3.3.1. Powder Chemistry and Powder Particle Distribution

Annealing and reduction did not result in any significant change in the phase make-up versus the dried powder, as shown from the XRD patterns in Fig. 1. The XRD patterns for the three pre-treatment spectra matched the standard N-type  $(\text{Bi}_{0.95} \text{Sb}_{0.05})_2(\text{Se}_{0.05} \text{Te}_{0.95})_3$  spectrum [17].

The average oxygen content in weight percent (wt.%) for the three as-sintered pre-treatment conditions (Dried, Annealed, and Reduced) are shown in Table 1. The oxygen content decreased by 61% versus the dried powder, from  $0.362 \pm 0.009$  wt.% to  $0.143 \pm 0.007$  wt.% after reduction. The oxygen content in the reduced sintered samples was higher than the oxygen solubility in  $\text{Bi}_2\text{Te}_3$ , reported to be 0.01 at.% [18], in which transferring the SPS dies from the glovebox to the SPS machine and sintering the powder in non-reducing environment are thought to introduce some oxygen to the samples. It is important to note that the reduction step is believed to only remove surface oxides, not any entrapped oxygen within the powder particles during ball milling step. It should be noted that the annealing pre-treatment did not exhibit any significant difference in oxygen content versus the as-dried powders.

Fig. 3 shows the particle size distribution of the control (dried) powder, as measured using the laser diffraction analyzer. The particle size ranges approximately from 0.7 to 47  $\mu\text{m}$  with a majority of particles less than 10  $\mu\text{m}$  as it is clear that the particle size distribution is non-Gaussian. Additional powder sizes analysis showed that the volume and surface weighted average of the powder particle size distribution were 9.2 and 5.0  $\mu\text{m}$ . The particle size distribution shows that a considerable amount of the particles was agglomerates of small particles subsequent to any powder treatment.

### **3.3.2. Sintered Microstructures**

Low and High magnification SEM cross-section micrographs of as-sintered samples for the three powder pre-treatment (dried, annealed and reduced) are shown in Fig. 3 and Fig. 4, respectively. The images are taken in an orientation where the vertical direction is parallel to the sintering pressing direction. Fig. 3 shows that the powder consists of large grains ranging mostly from 1 to 20  $\mu\text{m}$  in addition to finer grains as well as voids – as is clearer to observe in Fig. 3(a) – and this

agrees with the particles size distribution in Fig. 2. An examination of the high magnification imaging (Fig. 4) reveals that the large grains are agglomerates of sintered finer grains in the range of 1  $\mu\text{m}$  (Table 2) as it was determined by using the linear intercept method (ASTM E112-13 [19]). The disagreement between the particle size ranges determined by the laser diffraction method (Fig. 2) and the linear intercept method (Table 2) is due to the agglomeration of the fine grains to form a larger grains in the control (as-received) powder as this effect is seen in the as-sintered bodies, as it is most apparent in Fig. 3 and Fig. 4.

Table 2 shows a significant microstructure anisotropy in the plate-like fine grains (Fig. 4) as a larger grain size were found along the perpendicular direction. The fine grains morphology (Fig. 4) can be explained as the N-type crystal tend to cleave at  $\text{Te}_{(1)}\text{-Te}_{(2)}$  where the weak van der Waals is the binding force resulting in a plate-like grains after powder milling process. The uniaxial sintering pressure tends to align the plate-like fine grains in which larger grains size is found along the perpendicular direction (Fig. 4). Zhang et al. [20] found that the sintering pressure rotates the plate-like  $\text{Bi}_2\text{Te}_3$  grains resulting in an anisotropic microstructure with the longer grains size perpendicular to the sintering pressing direction which found to be consistent with the presented finding. The anisotropy in the microstructure (Fig. 4) affects the number of grain boundaries per unit length in both directions which, as will be discussed below, influences both the mechanical and the thermoelectric properties. As can also be seen from Table 2, the annealing and the reduction powder pre-treatments before sintering resulted in a slight increase in the grain size in both directions versus the dried powders [21–24]. There was no significant difference in grain size in either direction when comparing the sintered annealed powders versus the reduced powders.

### 3.3.3. As-sintered Relative Density

The theoretical density of the N-type  $(\text{Bi}_{0.95}\text{Sb}_{0.05})_2(\text{Se}_{0.05}\text{Te}_{0.95})_3$  was calculated using the following relation:

$$\rho = 7.86 - 1.32x - 0.12y - 0.4xy \quad (5)$$

where  $\rho$  is in  $[\text{g}/\text{cm}^3]$  and  $x$  and  $y$  are calculated by comparing the general stoichiometry of  $(\text{Bi}_{1-x}\text{Sb}_x)_2(\text{Se}_y\text{Te}_{1-y})_3$  to the composition of the present powder via the XRD spectrum presented in Fig. 2 [25] – i.e.  $(\text{Bi}_{0.95}\cdot\text{Sb}_{0.05})_2(\text{Se}_{0.05}\cdot\text{Te}_{0.95})_3$  were  $x = y = 0.05$  to yield a theoretical density of  $7.79 \text{ g}/\text{cm}^3$ . As is shown in Table 1, the relative density increased significantly versus the dried powders due to the annealing effect, from  $97.0 \pm 0.3 \%$  to  $98.0 \pm 0.3 \%$ , whereas the reduction pre-treatment had no significant effect on the relative density ( $97.9 \pm 0.2 \%$ ) versus the annealing pre-treatment. These results are consistent with those of Zhao et al, [26], who had reported a very close relative density of the reduced samples for N-type bismuth telluride sintered under the same sintering parameters. The increase in the relative density is believed to be a result of the improvement in the diffusion bonding between the particles due to the annealing effects as seen in Fig. 3 and 4.

### 3.3.4. Coefficient of Thermal Expansion and Density of SPS Bodies

The average coefficient of thermal expansion ( $\text{CTE}_{\text{ave}}$ ) was measured in both directions for sintered samples for the three powder pre-treatment conditions, as presented in Table 3. The values of the  $\text{CTE}_{\text{ave}}$  presented in Table 3 are the average of the measured CTE values over a temperature range from 35 to 250 °C in which were measured in the parallel ( $\text{CTE}_{\text{ave}\parallel}$ ) and perpendicular ( $\text{CTE}_{\text{ave}\perp}$ ) of the sintering pressing direction. A slight increase in the  $\text{CTE}_{\text{ave}\parallel}$  due to the reduction pre-treatment versus the dried powders from  $18.5 \pm 0.9$  to  $20.1 \pm 1.0 \mu\text{m}/\text{mK}$  was determined



whereas the reduction pre-treatment had no significant effect in the  $CTE_{ave\perp}$ . There were no significant differences in the average  $CTE_{ave}$  in the between the annealed and dried powder sintered bodies or between the annealed and reduced powder sintered bodies in both directions. The average  $CTE_{ave\parallel}$  was found to be consistently higher for the three pre-treatment conditions due to the higher number of boundaries in the parallel direction than the perpendicular direction [27]. The anisotropy in the  $CTE_{ave}$  is a result of the anisotropy of the as-sintered bodies microstructure shown in Fig. 4.

The average of  $CTE_{ave\parallel}$  and  $CTE_{ave\perp}$  values ( $\overline{CTE}_{ave}$ ) for each pre-treatment condition was used to calculate the density change with temperature, shown in Fig. 5, using the following equation:

$$\rho(T) = \rho(T_o)[1 - (3 * \overline{CTE}_{ave}(T - T_o))] \quad (6)$$

where  $T_o$  is 35°C (the initial temperature in the CTE test). In this analysis, the density at room temperature is assumed to be approximately the same as the density at 35 °C as there were no available CTE data below 35 °C due to limitations in the equipment. Fig. 5 shows that the annealing and the reduction pre-treatment increased the density significantly for the as-sintered bodies as it is a result of the microstructure finding presented Fig. 3 and Fig. 4.

### 3.3.5. Mechanical Properties

Fig. 6 depicts the uniaxial tensile test force vs. displacement curve for a reduced powder pre-treatment sample in the  $\perp$  direction during the uniaxial tensile test. The force vs. displacement curve is linear except for the initial strain portion due to the accommodation of fixture misalignment. As shown in Fig. 6, the sintered N-type  $(Bi_{0.95} Sb_{0.05})_2(Se_{0.05} Te_{0.95})_3$  demonstrated brittle behavior during the uniaxial tensile test as the test showed a linear elastic region followed by fracture with no plastic deformation prior to failure. Weibull analysis was used to determine

the tensile strength for twenty samples per direction and powder pre-treatment condition following ASTM C1239-13 [28]. Fig. 7 shows the effect of the annealing and reduction powder pre-treatments on the characteristic uniaxial tensile strength ( $\sigma_T$ ) in both the parallel ( $\sigma_{T\parallel}$ ) and perpendicular ( $\sigma_{T\perp}$ ) directions to the applied sintering pressure. The annealed samples gave the highest  $\sigma_{T\perp}$  of 38.0 (40.4, 35.7) MPa as well they exhibited the largest degree of anisotropy. It should be noticed that  $\sigma_T$  anisotropy was insignificant for both the dried and reduced powder pre-treatment samples – i.e.  $\sigma_T$  was isotropic for these sintered bodies. The  $\sigma_T$  anisotropy of the annealed pre-treated as-sintered bodies is strongly related to the microstructure anisotropy documented in Fig. 3 and Fig. 4, as stronger bonds are created along the perpendicular direction. Reduction increased the  $\sigma_{T\perp}$  from 30.4 (34.8, 26.6) to 33.8 (36.9, 31.0) MPa however the change in the  $\sigma_{T\parallel}$  was not significant versus the dried powder sintered bodies. This increase in the  $\sigma_T$  for both the reduced and the annealed samples is contributed to the density increase, as reported by Coble and Kingery [29]. The  $\sigma_T$  and the Weibull moduli ( $m$ ) with their upper and lower bounds of 90% confidence interval are presented in Table 4 (ASTM C1239-13) [28]. The “Annealed” and “Reduced” samples demonstrated less flaws in the sintered samples, which led a more consistent pre-treatment condition of samples in both directions, as is demonstrated from the higher Weibull modulus (Table 4).

Table 5 shows the effect of annealing and reduction powder pre-treatment of the as sintered bodies on the Young’s modulus, shear modulus, and Poisson’s ratio. The annealing and reduction pre-treatments found to have the same effect on the as-sintered Young’s modulus and shear modulus. Both pre-treatments increased the Young’s modulus and the shear modulus to the same values of  $47.0 \pm 0.2$  GPa and  $18.6 \pm 0.1$  GPa, respectively. The Poisson’s ratio was not affected by either of the powder pre-treatments, as evidenced by the same value of 0.268 for all three pre-treatment

conditions. The Young's modulus value (46.5 GPa) for the reduction pre-treatment is close to those published by Vasilevskiy et al (47.0 GPa) [30]. The increase in both Young's modulus and the shear modulus are mainly contributed to the decrease in the porosity (the increase in the density) (Table 1) as determined by Wachtman through the following expression [31]:

$$M = M_0(1 - \theta p) \quad (7)$$

where M and M<sub>0</sub> are the elastic modulus (Young's modulus or Shear modulus) at volume porosity p and at zero porosity, respectively, and  $\theta$  is a constant that is experimentally determined.

### 3.3.6. Thermoelectric Properties

The statistical uncertainty of each sample was calculated by repeated sample measurements with 95% confidence interval. All tested samples did not demonstrate any annealing effects during the test cycles of Seebeck coefficient, electrical resistivity and thermal conductivity. The statistical error is only presented in the Fig. 8 to Fig.11 when comparing the three powder pre-treatment samples as the measurements were made under exact conditions. While the total uncertainty values which include the statistical and the propagated error of measurements are presented in the appendix for reference for all the thermoelectric properties following the analysis done by Mackey et al [32]. The reduction powder pre-treatment reduced the surface oxides surrounding the powder particles (Table 1).

As the surface oxides are removed, less barriers are found to oppose the carrier flow. Furthermore, the surface oxide removal results in more of the base powder material to be exposed during powder sintering that increases the weld sites and enhances the diffusional bonding (Fig. 3(c) and Fig. (c)) between the powder particles. As a result, less voids and higher densities are achieved (Table 1 and Fig. 5) as well as higher number of carrier flow paths (Fig. 3 and Fig.4).

Fig. 8 illustrate the Seebeck coefficient ( $\alpha$ ) for the three powder pre-treatment conditions over the temperature range from 25 to 250 °C. The reduction powder pre-treatment demonstrated an increase in  $\alpha$  versus the dried powders; however, the Seebeck coefficient showed a slight increase by the annealing pre-treatment only in the perpendicular direction. No significant anisotropy in the  $\alpha$  values was observed among the three powder pre-treatment conditions. The maximum  $\alpha$  of -144.4  $\mu\text{V/K}$  achieved by the reduced pre-treatment condition in the parallel direction at 250 °C is a 12% increase compared to the dry pre-treatment condition. Subsequently, the oxygen removal in the reduction pre-treatment process found to have the dominant effect on increasing the Seebeck coefficient rather than the annealing effect. This finding is consistent with Lim et al. [6], who reported that the Seebeck coefficient increased by powder pre-treatment of N-type  $\text{Bi}_2\text{Te}_3$  using  $\text{H}_2$  at 380 °C and for 27 h, however Ar annealing powder pre-treatment – at the same conditions - did not show a significant effect. The oxygen in the surface oxide replaces the  $\text{Te}^{(2)}$  and acts like a donor that affects the carrier concentration ( $n$ ) [33,34]. It is possible to express  $\alpha$  for metals or degenerate semiconductors as follows [35]:

$$\alpha = \left( \frac{\pi^2 k_B^2 T}{3e} \right) \left( \frac{8m^*}{h^2} \right) \left( \frac{\pi}{3n} \right)^{\frac{2}{3}} \left( 1 + \left( \frac{d \ln \lambda_s}{d \ln E} \right)_{E_f} \right) \quad (8)$$

where  $k_B$  Boltzmann constant,  $T$  in the temperature,  $e$  is the electron charge,  $m^*$  is the effective mass,  $h$  is Plank's constant,  $n$  is the carrier concentration,  $\lambda_s$  is the scattering distance,  $E$  is the electron average energy. The values of  $\alpha$  at room temperature varies with  $n^{-2/3}$  [36]. Accordingly, it is believed that the increase in  $\alpha$  is due to the surface oxides removal that decreased in the carrier concentration.

Fig. 9 shows a metallic behavior for the electrical resistivity for the three powder pre-treatment conditions as it increases with the temperature from room temperature to 250°C. The reduction

powder pre-treatments increased the electrical resistivity in both directions for temperatures more than 75 °C however, annealing has no significant effect in either directions compared to the dried sample. The difference in the electrical resistivity values between the reduced and dried conditions increases as the temperature increases in both directions. The slope increase in the electrical resistivity trends is believed to be due to the annealing effect as it is seen in both in the reduced and annealed powder pre-treatment conditions (Fig. 9). The electrical resistivity is a function of carrier concentration ( $n$ ) and carrier mobility ( $\mu$ ) as described by [37], where  $e$  is the charge of an electron, is given by:

$$\rho_e = \frac{1}{n e \mu} \quad (8)$$

The decrease in the carrier concentration that led to the increase in the Seebeck coefficient (Fig.8) in the reduction pre-treatment case is believed to be the main reason for the increase in the electrical resistivity. This finding is consistent with, Horio and Inoue [7] and Rimal et al.[8], who reported an increase in the Seebeck coefficient and decrease in the electrical resistivity for a powder oxide reduction pre-treated N-type Bi<sub>2</sub>Te<sub>3</sub> as sintered samples. Their analysis showed that the powder surface oxide removal increases the  $\mu$  and decreases the  $n$ . The oxides at the grain boundaries act like a barrier as well as the oxygen in these oxides at the grain boundaries act like a donor. Although the  $\mu$  increases by oxide reduction, the  $n$  has dominant effect on the increase of the electrical resistivity. The reduction and dried powder pre-treatment conditions showed anisotropic behaviour in the electrical resistivity, as found by Shen et al [38], however annealing did not show significant anisotropy. The anisotropy in the electrical resistivity is due to the sintered grain shape anisotropy (Fig. 3 and Fig. 4), due to the directional alignment and deformation during SPS. Jiang et al. [39] has reported an anisotropy in the electrical conductivity of spark plasma

sintered N-type  $\text{Bi}_2(\text{Te,Se})_3$ . The electrical conductivity in the perpendicular direction to the sintering pressure found to be as twice as the value in the parallel direction as the sintered sample showed lamination of the grains due to sintering pressing direction.

The thermal conductivity was measured only in the parallel direction due to samples size limitations and the values are plotted versus temperature in Fig. 10 for the three powder pre-treatments. The thermal conductivity is the summation of the electronic thermal conductivity  $k_{el}$  and the phonon (lattice) thermal conductivity  $k_{ph}$ :

$$k = k_{ph} + k_{el} \quad (9)$$

The  $k_{ph}$  is a function of phonon scattering but constant with the carrier concentration and as such there was no change with oxide removal [40]. However,  $k_{el}$  is inversely proportional to the electrical resistivity through the Wiedemann-Franz law:

$$k_{el} = \frac{L_0 T}{\rho_e} \quad (10)$$

where  $L_0$  is the Lorenz number. Both the reduction and annealing pre-treatments decreased the thermal conductivity significantly versus the dried powders for the range of temperatures explored. Accordingly, it is thought that the decrease the thermal conductivity is attributed to the increase in the  $\rho_e$  (Fig. 9) as the  $k_{el}$  decreased (Eqn. (10)).

The values of the ZT of the reduced powder pre-treatment condition are higher than those of the dried powder pre-treatment, as shown in Fig. 11. The three powder pre-treatment conditions did not show an anisotropic behavior in their values of ZT. As seen in Fig. 14, the annealing powder pre-treatments treatment is responsible for the majority of the improvement in ZT for all temperatures tested with the reduction powder pre-treatments treatment having a lesser effect, and then only a significant effect at lower temperatures versus annealing. As the ZT reaches its

maximum value at 150 °C, the effect of the reduction treatment versus annealing becomes insignificant. The  $ZT_{\max}$  found to increase by approximately 21% due to annealing and increased another 10% by surface oxide removal versus the dried powders. The  $ZT$  increase is contributed to the increase in the  $\alpha$  (Fig. 8) and the decrease in the  $k$  (Fig. 10), despite the slight increase in the electrical resistivity. The  $ZT_{\max}$  for the reduced powder pre-treatments treatment sample value achieved is 0.63 at 150 °C.

### 3.4. Conclusion

In this work, the effect of three different powder pre-treatments – specifically powder drying under vacuum at 100 °C, powder annealing at 380 °C in flowing high-purity Ar and powder surface oxide reduction in flowing 5% H<sub>2</sub> – 95% Ar (vol%) at 380 °C – on both the mechanical and the thermoelectric properties of spark plasma sintered (SPS) N-type (Bi<sub>0.95</sub> Sb<sub>0.05</sub>)<sub>2</sub>(Se<sub>0.05</sub> Te<sub>0.95</sub>)<sub>3</sub> were determined. In summary, the effect of oxide reduction of the N-type (Bi<sub>0.95</sub> Sb<sub>0.05</sub>)<sub>2</sub>(Se<sub>0.05</sub> Te<sub>0.95</sub>)<sub>3</sub> powder at 380 °C and 24 h in Ar – 5% H<sub>2</sub> before SPS, resulted in an increase in both mechanical and thermoelectric properties. The enhancement in the thermoelectric properties was due to surface oxide removal, however the annealing effect was the dominate in enhancing the mechanical properties. The following are the main findings of the current study:

- 1- Spark plasma sintering N-type (Bi<sub>0.95</sub>Sb<sub>0.05</sub>)<sub>2</sub>(Se<sub>0.05</sub>Te<sub>0.95</sub>)<sub>3</sub> under uniaxial pressure led to anisotropy in the microstructure that had an effect on the directional mechanical properties as assessed parallel and perpendicular to the pressing direction.
- 2- Annealing increased the uniaxial tensile strength by 23% to reach a value of 38.0 MPa from 30.8 MPa in the perpendicular direction compared to the dry pre-treatment condition. The uniaxial tensile strength of the reduced samples increased to a value to 35.5 MPa in

the perpendicular direction, as the annealing effect is the key to the enhancement due to the increase in the relative density.

- 3- Surface oxide reduction using H<sub>2</sub> increased the carrier concentration and decreased the mobility which increased the Seebeck coefficient and the electrical resistivity but decreased the thermal conductivity.
- 4- Despite, the increase of the electrical resistivity due to a decrease in the mobility, the increase in the Seebeck coefficient and the decrease in the thermal conductivity were the key to ZT enhancement
- 5- Reduction of the surface oxide resulted in an increase of ZT<sub>max</sub> by approximately 31% in both directions to a ZT<sub>max</sub> of 0.63 at 150 °C in the parallel direction.

### Acknowledgement

This work was supported by the Natural Sciences and Engineering Research Council of Canada (NSERC CREATE 432242-13, NSERC CRD473500-14) and the Ontario Centre of Excellence (OCE22261).

### 3.5. Appendix

The thermoelectric properties vs. temperature for the reduced spark plasma sintered N-type (Bi<sub>0.95</sub>Sb<sub>0.05</sub>)<sub>2</sub>(Se<sub>0.05</sub>Te<sub>0.95</sub>)<sub>3</sub> were curve-fitted and presented in the temperature range from 35 to 250 °C and presented in the following relationships:

c) In the parallel direction:

$$\alpha_{\parallel} = 0.00057799 T^2 - 0.28062006 T - 110.36637129 \text{ } [\mu\text{V}/\text{K}] \quad (12)$$

$$\rho_{e\parallel} = 0.00000335 T^2 + 0.00214991 T + 0.73814796 \text{ } [\Omega \text{ m} * 10^{-5}] \quad (13)$$

$$k_{\parallel} = 0.00001110 T^2 - 0.00242623 T + 1.28098650 \text{ } [W/m.K] \quad (14)$$



$$ZT_{\parallel} = -0.00001095 T^2 + 0.00353480 T + 0.33487656 \quad [-] \quad (15)$$

$$\alpha_{d\parallel} = 0.00000010 T^2 - 0.00002888 T + 0.01304090 \quad [cm^2/s] \quad (16)$$

$$C_{p\parallel} = 0.00006796 T^2 + 0.07738465 T + 127.36030935 \quad [J/kg.K] \quad (17)$$

d) In the perpendicular direction:

$$\alpha_{\perp} = 0.00059994 T^2 - 0.28207362 T - 107.47269708 \quad [\mu V/K] \quad (18)$$

$$\rho_{e\perp} = 0.0000018057 T^2 + 0.0024302394 T + 0.66504678 \quad [\Omega m * 10^{-5}] \quad (19)$$

$$ZT_{\perp} = -0.00001070 T^2 + 0.00343158 T + 0.35357316 \quad [-] \quad (20)$$

where  $T$  is the temperature in °C. The average uncertainty for the whole temperature range in the Seebeck coefficient is  $\pm 10.3\%$ , the electrical resistivity is  $\pm 4.5\%$ , the thermal conductivity is  $\pm 4.9\%$ , the  $ZT$  is  $\pm 22\%$ , the thermal diffusivity is  $\pm 1.1\%$  and the specific heat capacity is  $\pm 2.5\%$ .

3.6. Figures and Tables:

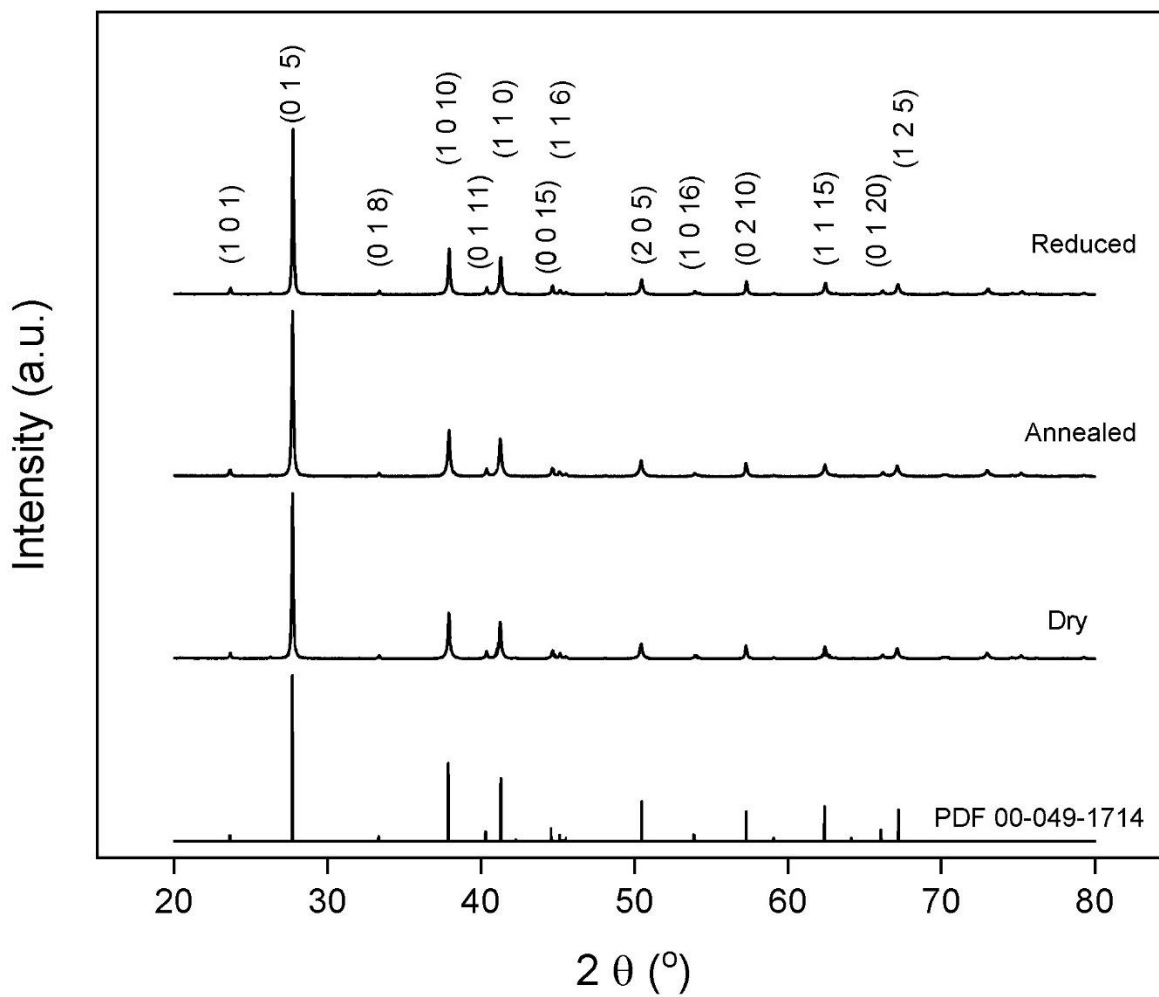


Fig. 1. XRD spectra of the pre-treated N-type  $(\text{Bi}_{0.95}\text{Sb}_{0.05})_2(\text{Se}_{0.05}\text{Te}_{0.95})_3$  powders and a standard spectrum for N-type  $(\text{Bi}_{0.95}\text{Sb}_{0.05})_2(\text{Se}_{0.05}\text{Te}_{0.95})_3$  (PDF 00-049-1714) [17] o.

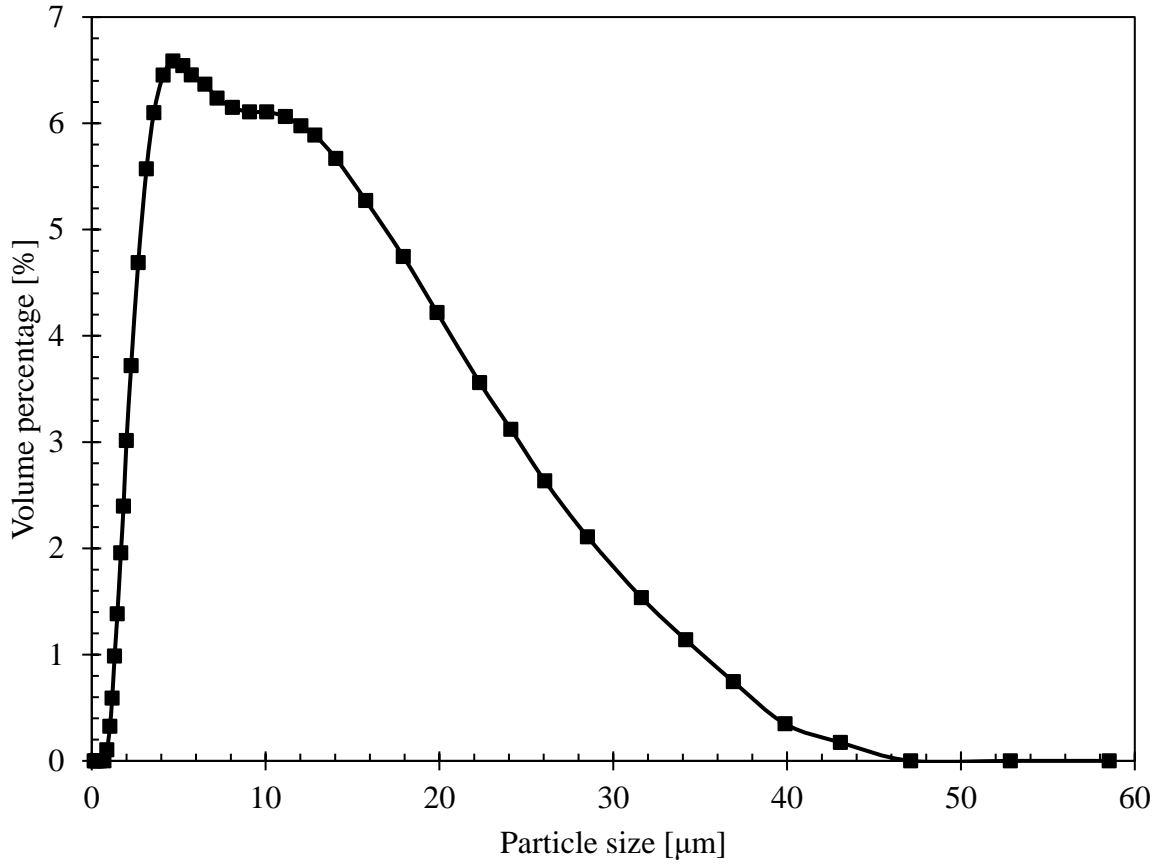


Fig. 2. Particle size distribution measured by laser diffraction particle size analyzer for the starting powder of the N-type  $(\text{Bi}_{0.95}\cdot\text{Sb}_{0.05})_2(\text{Se}_{0.05}\cdot\text{Te}_{0.95})_3$  prior to any power pre-treatment.

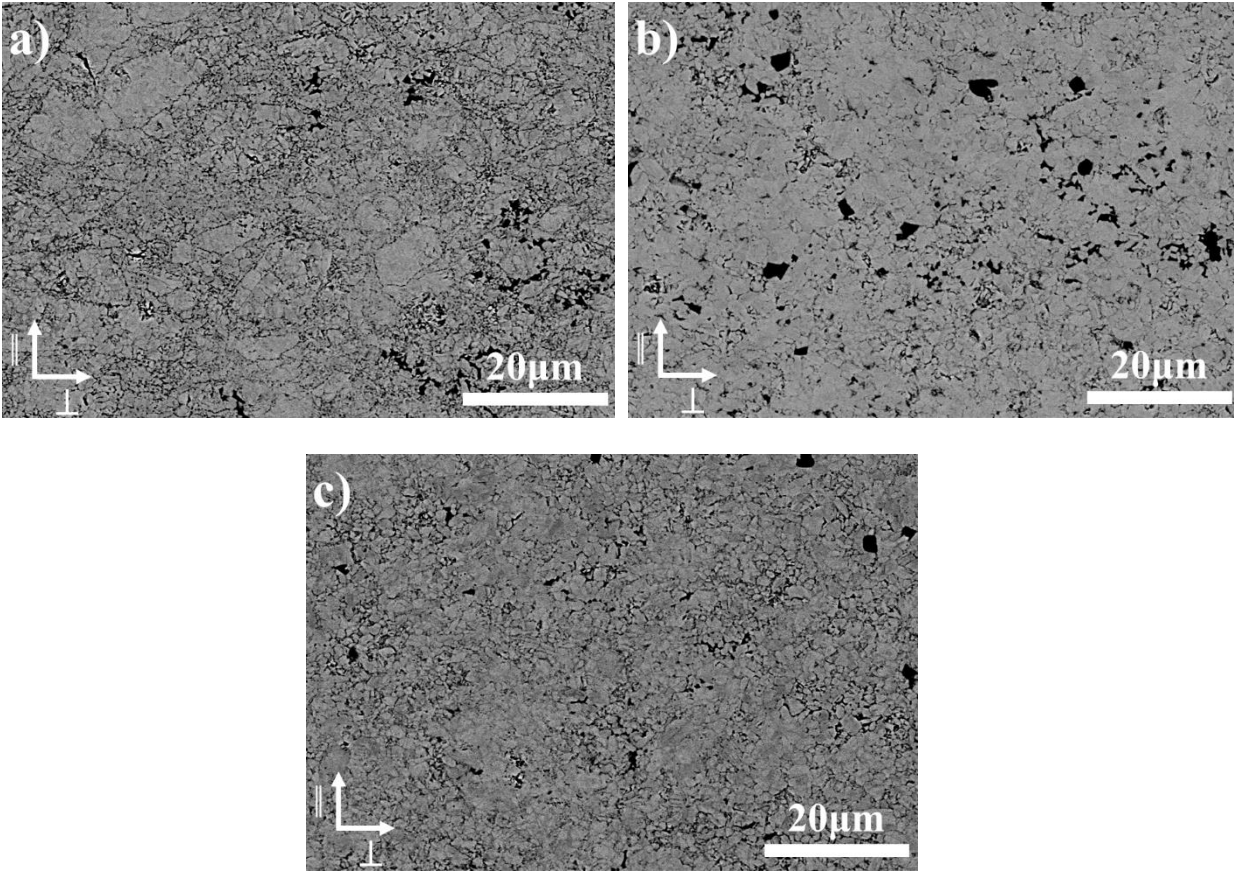


Fig.3. Low magnification SEM cross-section micrographs for the three as-sintered powder pre-treatment conditions (the vertical direction is parallel to the pressing direction). a) Dried, b) Annealed and c) Reduced.

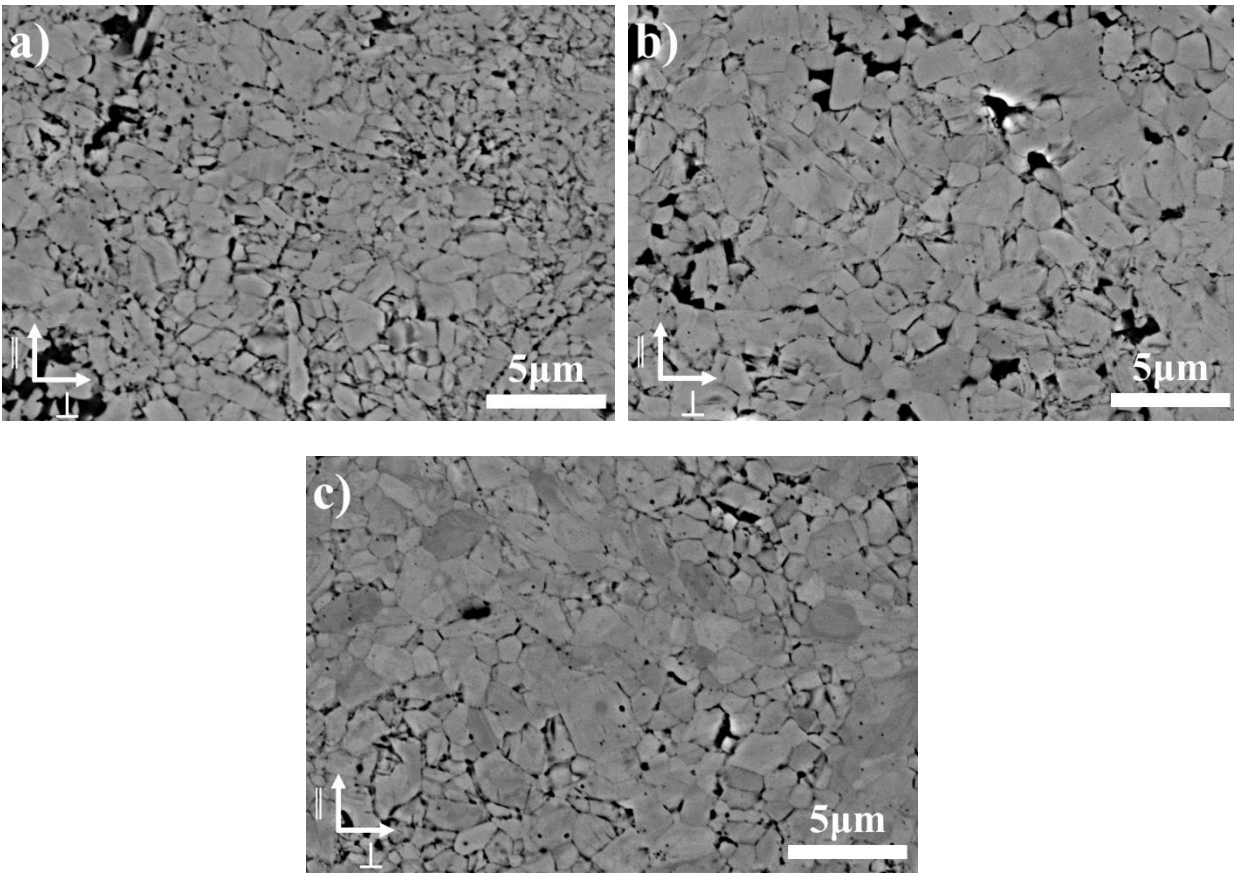


Fig.4. High magnification SEM cross-section micrographs for the three as-sintered powder pre-treatment conditions (the vertical direction is parallel to the pressing direction). a) Dried, b) Annealed and c) Reduced.

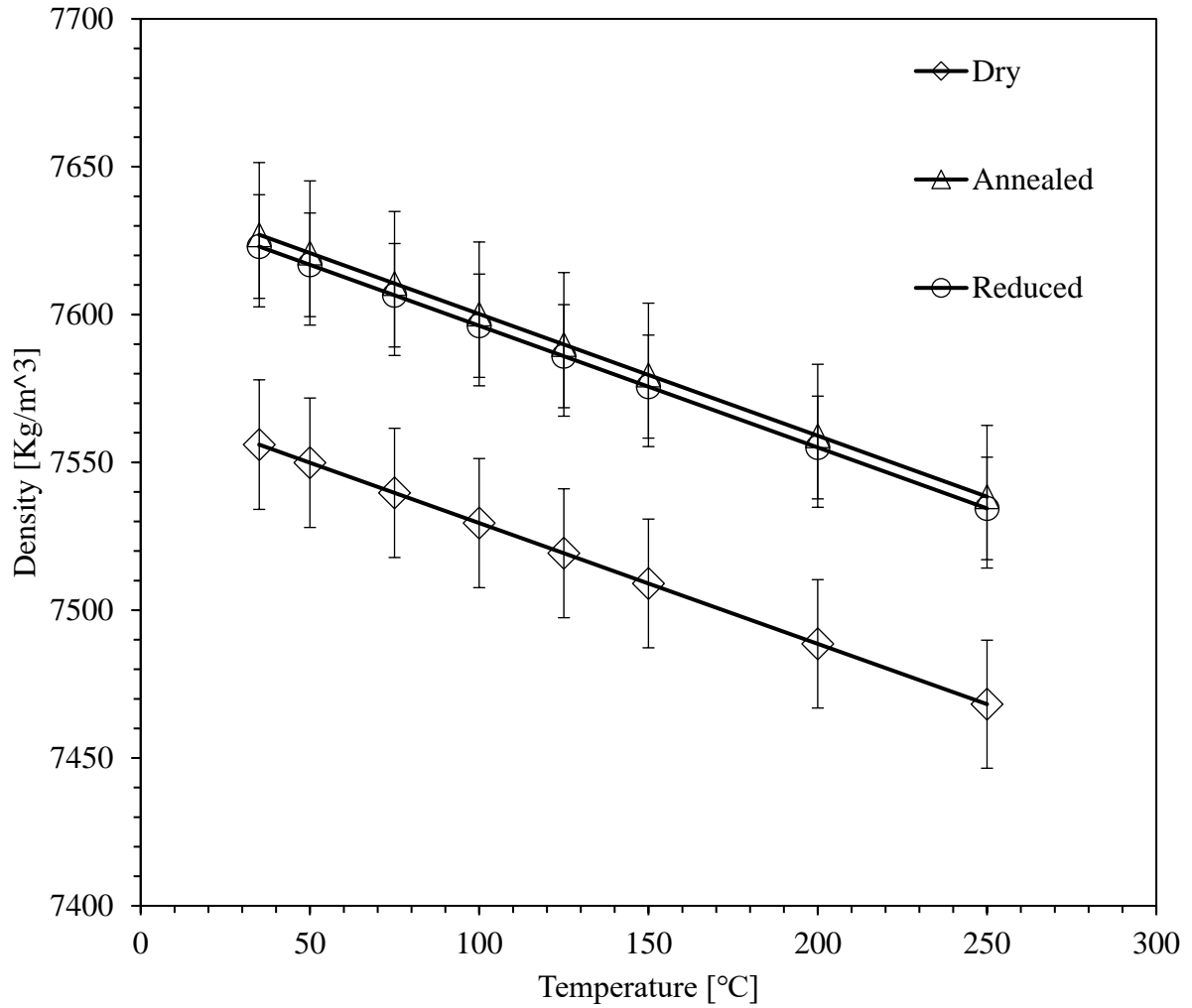


Fig.5. The change of the density with the temperature of the three as-sintered powder pre-treatment conditions corrected using the average CTE.

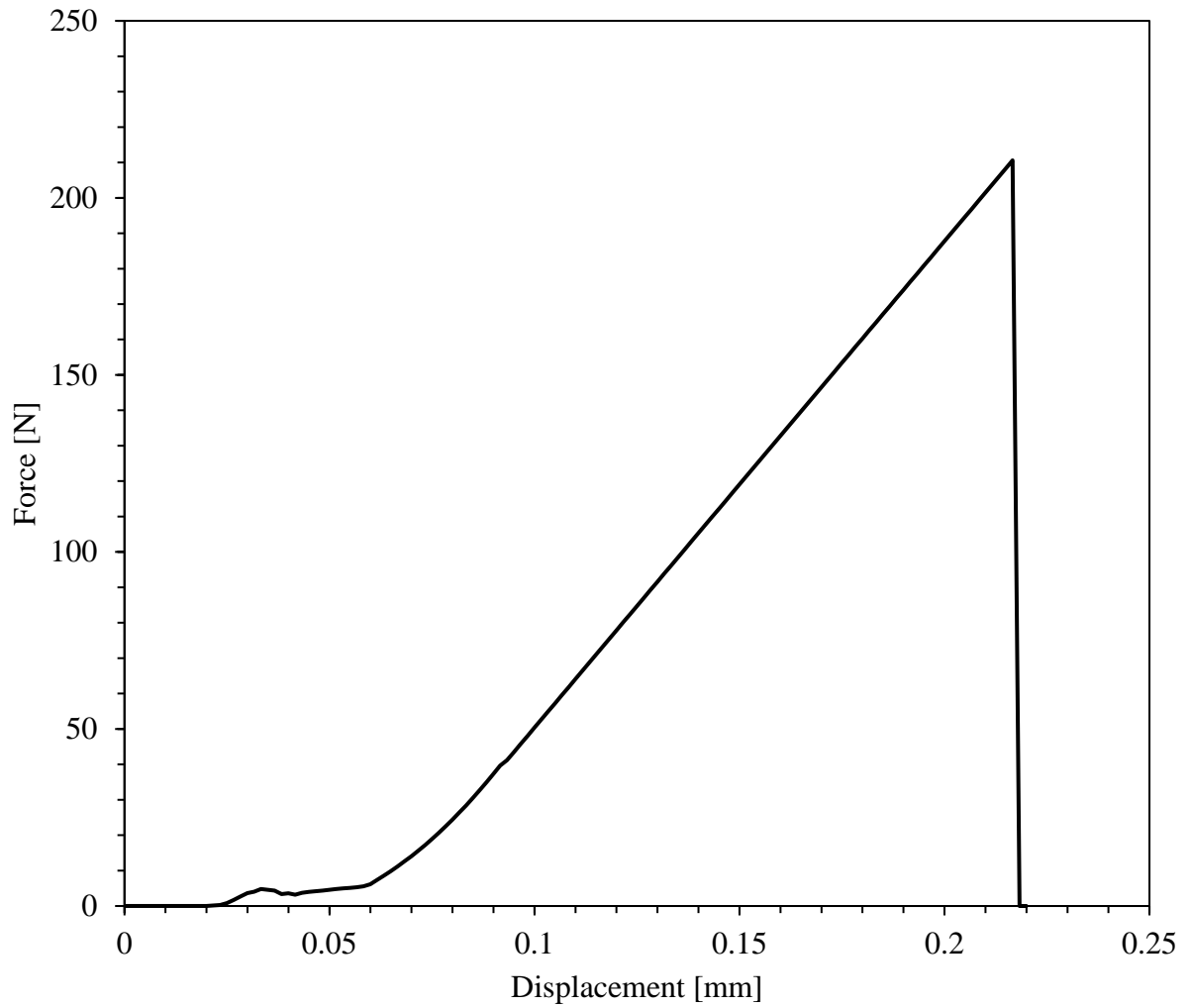


Fig.6. Force vs. displacement for one of the reduced samples of the uniaxial tensile test in the perpendicular direction to the sintering pressing direction.

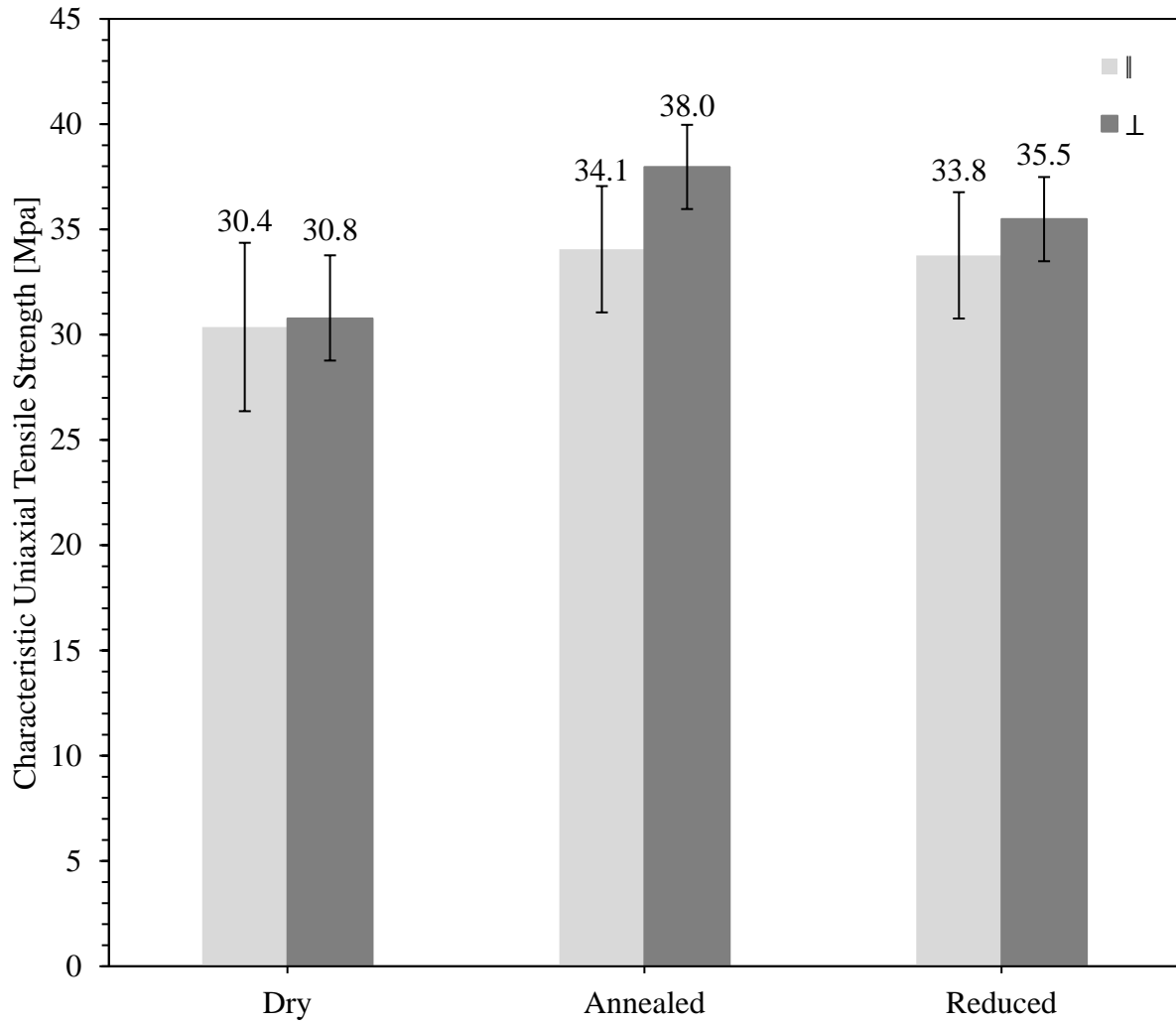


Fig.7. The characteristic uniaxial tensile strength for different as-sintered powder pre-treatment conditions measured in the parallel and the perpendicular direction to the sintering pressing direction.



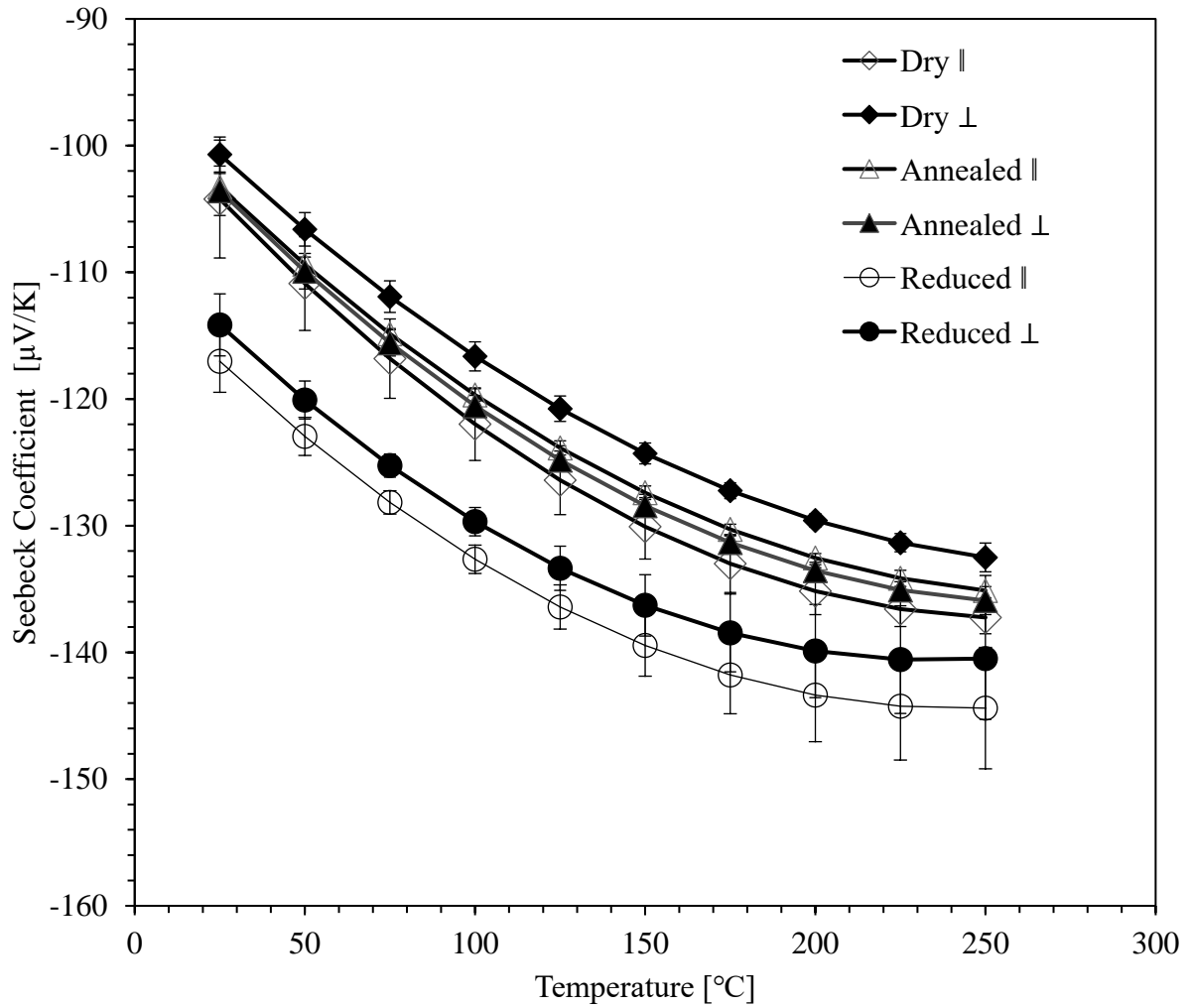


Fig.8. The Seebeck Coefficient ( $\alpha$ ) vs. temperature for the three as-sintered powder pre-treatment conditions in both the parallel and the perpendicular direction to the sintering pressing direction.

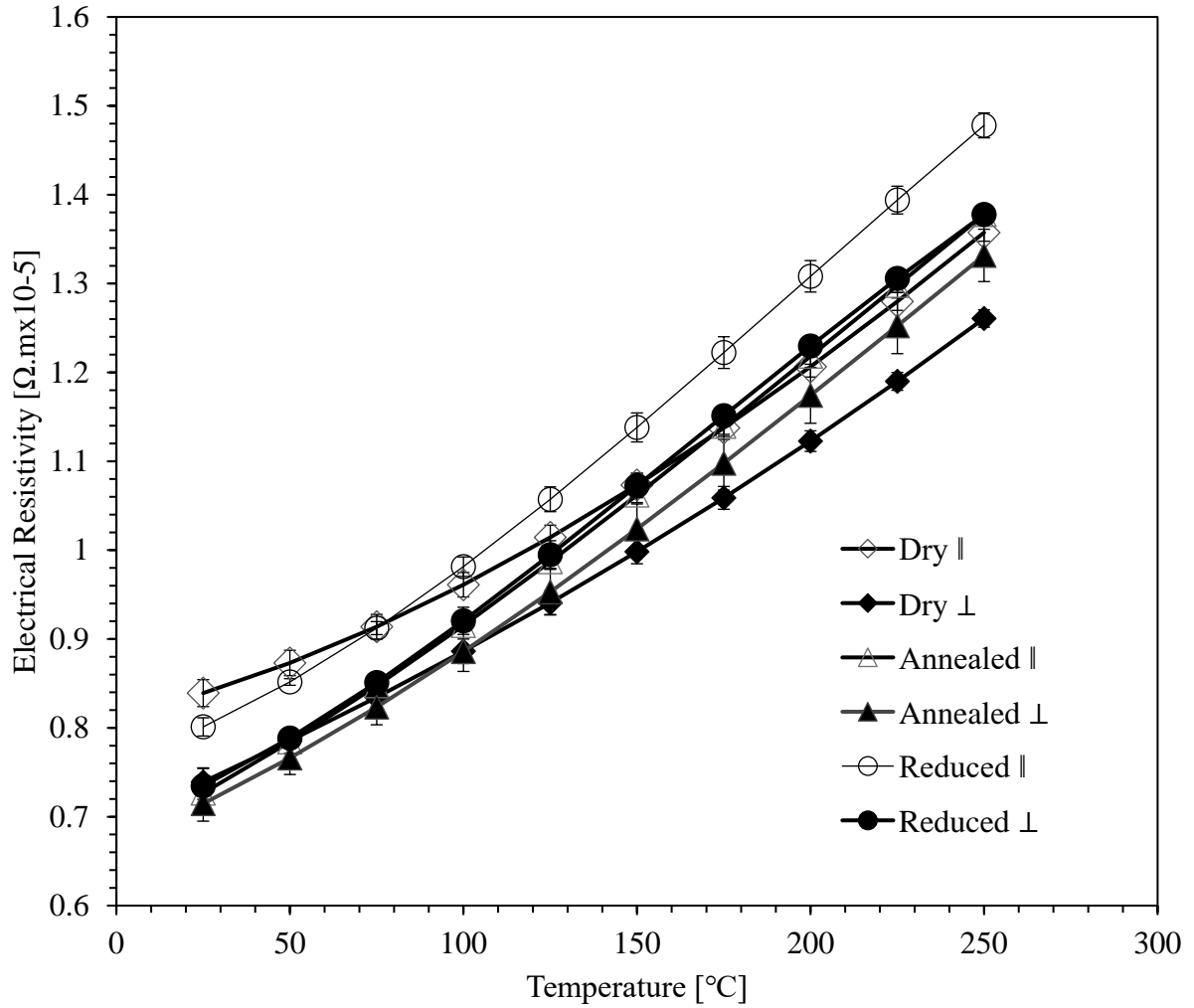


Fig.9. The electrical resistivity ( $\rho_e$ ) vs. temperature for the three as-sintered powder pre-treatment conditions in both the parallel and the perpendicular direction to the sintering pressing direction.

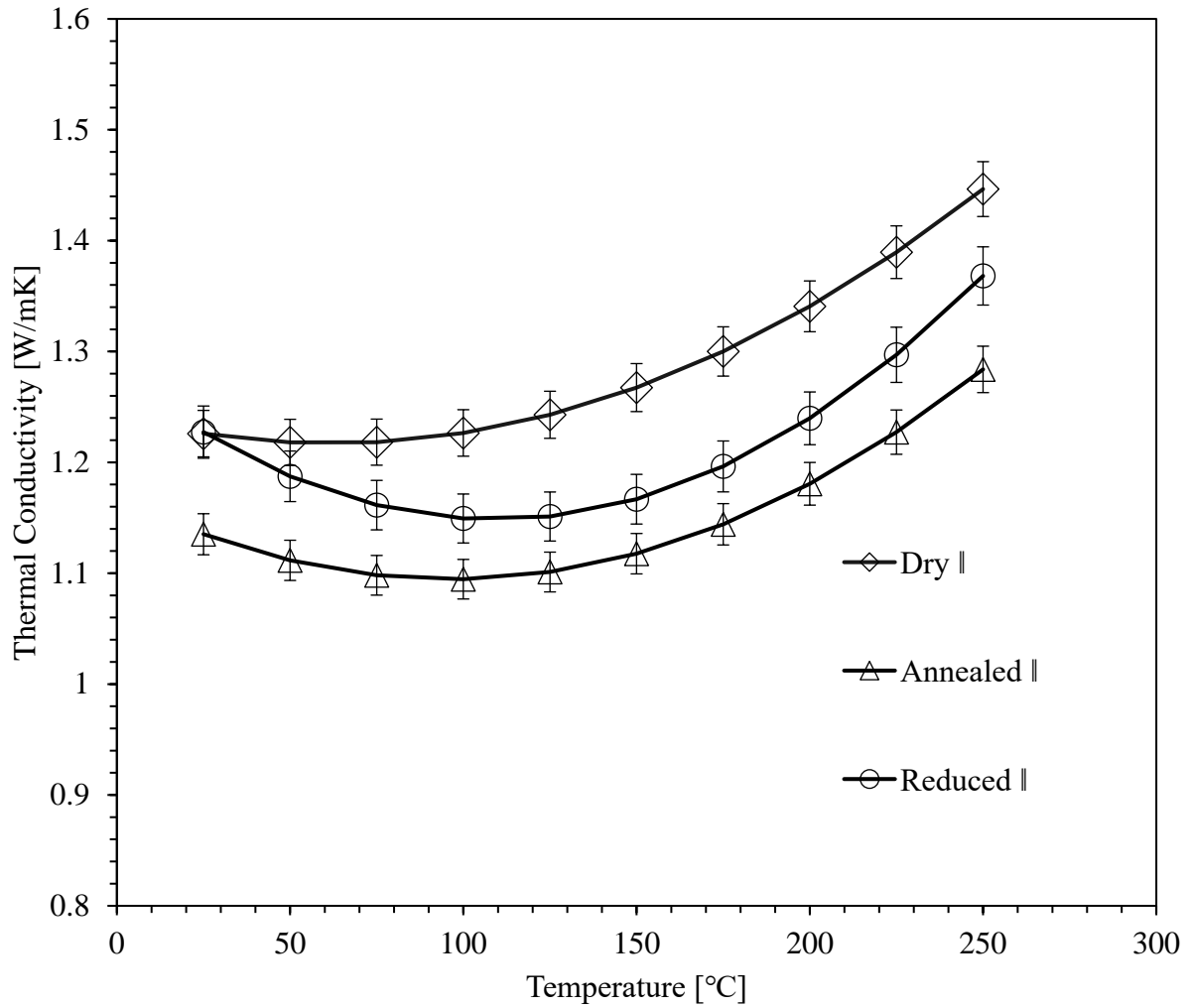


Fig.10. The thermal conductivity of the three as-sintered powder pre-treatment conditions in both the parallel direction to the sintering pressing direction.

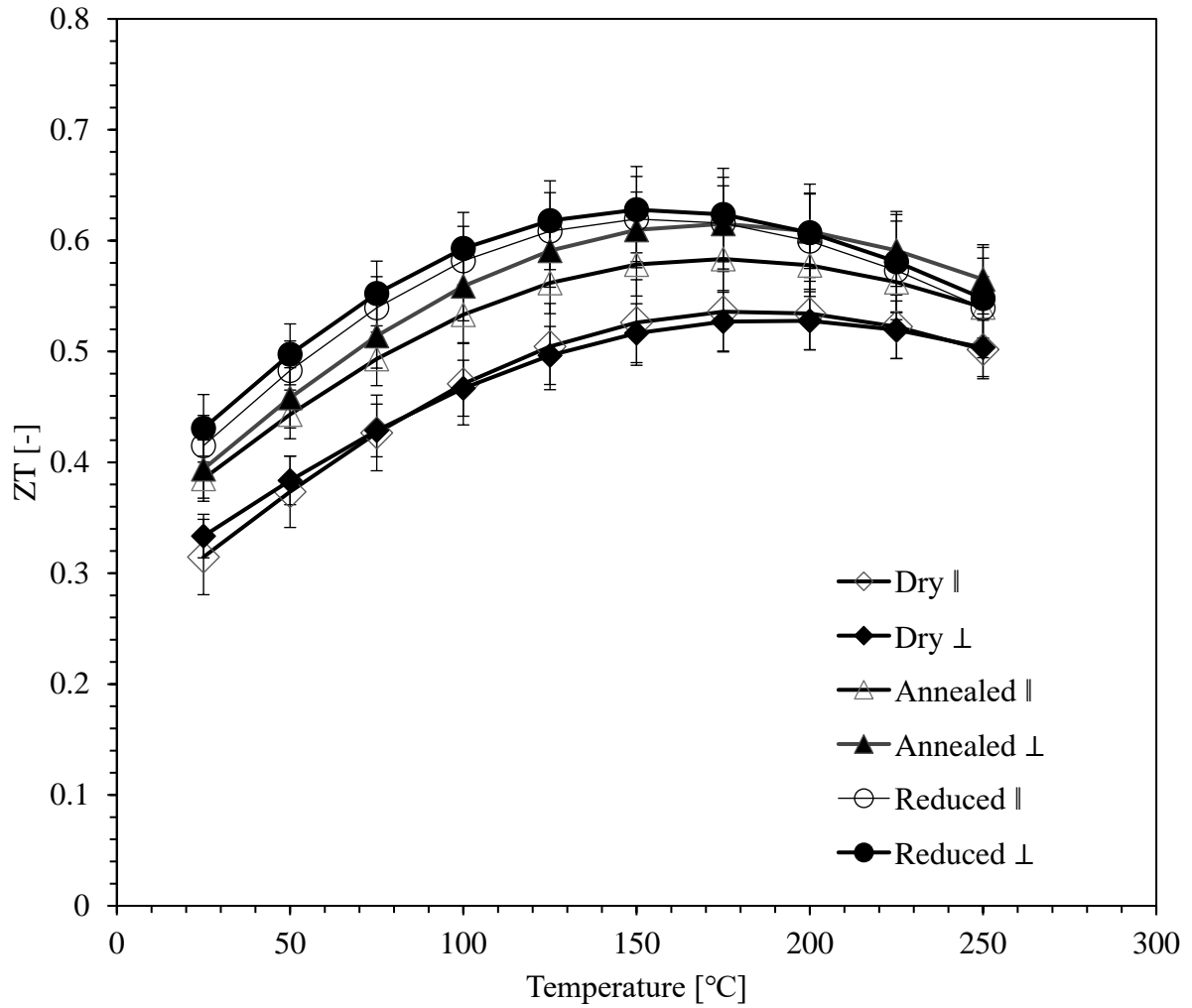


Fig.11. The ZT vs. temperature for the three as-sintered powder pre-treatment conditions in both the parallel and the perpendicular direction to the sintering pressing direction.

Table 1

The average oxygen content and the relative density of spark plasma sintered bodies of N-type  $(\text{Bi}_{0.95}\text{Sb}_{0.05})_2(\text{Se}_{0.05}\text{Te}_{0.95})_3$  for the three powder processing routes (dry, annealed and reduced).

Powder Treatment	Oxygen content [wt%]	Relative density [%]
Dry	$0.362 \pm 0.009$	$97.0 \pm 0.3$
Annealed	$0.341 \pm 0.006$	$98.0 \pm 0.3$
Reduced	$0.143 \pm 0.007$	$97.9 \pm 0.2$

Table 2

The average particle directional size of spark plasma sintered bodies of N-type  $(\text{Bi}_{0.95}\text{Sb}_{0.05})_2(\text{Se}_{0.05}\text{Te}_{0.95})_3$  for the three powder processing routes (dry, annealed and reduced) in the parallel and perpendicular directions to the sintering applied pressure using high magnification SEM micrographs.

Powder treatment	Average particle size [ $\mu\text{m}$ ]	
	direction	$\perp$ direction
Dry	$0.68 \pm 0.03$	$0.79 \pm 0.04$
Annealed	$0.79 \pm 0.03$	$0.91 \pm 0.06$
Reduced	$0.79 \pm 0.04$	$0.95 \pm 0.07$

Table 3

The average coefficient of thermal expansion ( $CTE_{ave}$ ) of spark plasma sintered bodies of N-type  $(Bi_{0.95} Sb_{0.05})_2(Se_{0.05} Te_{0.95})_3$  for the three powder processing routes (dry, annealed and reduced) in the parallel and perpendicular directions to the sintering applied pressure.

Powder treatment	$CTE_{ave}$ [m/mK]	
	direction	⊥ direction
Dry	$18.5 \pm 0.2$	$17.5 \pm 0.2$
Annealed	$19.0 \pm 0.2$	$17.3 \pm 0.2$
Reduced	$20.1 \pm 0.2$	$18.3 \pm 0.2$

Table 4

Characteristic uniaxial tensile strength and Weibull modulus for spark plasma sintered N-type  $(Bi_{0.95} Sb_{0.05})_2(Se_{0.05} Te_{0.95})_3$  measured in the parallel and the perpendicular direction of the pressing direction.

Powder Treatment	Characteristic tensile strength [MPa]		Weibull modulus [-]	
	Value (upper limit, lower limit)	Value (upper limit, lower limit)	Value (upper limit, lower limit)	Value (upper limit, lower limit)
	direction	⊥ direction	direction	⊥ direction
Dry	30.4 (34.8, 26.6)	30.8 (33.3, 28.5)	3.9 (5.1, 2.5)	5.5 (6.9, 3.8)

Annealed	34.3 (37.0, 31.4)	38.0 (40.4, 35.7)	5.2 (6.5, 3.6)	6.9 (8.7,4.8)
Reduced	33.8 (36.9 31.0)	35.5(37.8, 33.4)	4.8 (6.1, 3.3)	6.8 (8.6, 4.7)

---

Table 5

Young's modulus Shear Modulus, and Poisson's ratio of spark plasma sintered bodies of N-type  $(\text{Bi}_{0.95}\text{Sb}_{0.05})_2(\text{Se}_{0.05}\text{Te}_{0.95})_3$  for the three powder processing routes (dry, annealed and reduced).

Powder Treatment	Young's modulus [GPa]	Shear modulus [GPa]	Poisson's ratio [-]
Dry	$45.5 \pm 0.3$	$18.0 \pm 0.1$	$0.268 \pm 0.001$
Annealed	$47.1 \pm 0.1$	$18.6 \pm 0.1$	$0.267 \pm 0.001$
Reduced	$47.0 \pm 0.1$	$18.6 \pm 0.1$	$0.268 \pm 0.001$

### 3.7. References

- [1] E.D.M. Rowe, D. Ph, D. Sc, F. Group, Thermoelectric Handbook - Macro to Nano, CRC Press Taylor & Francis Group, 2006.
- [2] D.A. Wright, Materials for direct-conversion thermoelectric generators, *Metall. Rev.* 15 (1970) 147–160. <https://doi.org/10.1179/mtlr.1970.15.1.147>.
- [3] J. Jiang, L. Chen, S. Bai, Q. Yao, Q. Wang, Fabrication and thermoelectric performance of textured n-type  $\text{Bi}_2(\text{Te,Se})_3$  by spark plasma sintering, *Mater. Sci. Eng. B Solid-State Mater. Adv. Technol.* 117 (2005) 334–338. <https://doi.org/10.1016/j.mseb.2005.01.002>.
- [4] Y. Pan, T.-R. Wei, Q. Cao, J.-F. Li, Mechanically enhanced p- and n-type  $\text{Bi}_2\text{Te}_3$ -based thermoelectric materials reprocessed from commercial ingots by ball milling and spark plasma sintering, *Mater. Sci. Eng. B.* 197 (2015) 75–81. <https://doi.org/10.1016/j.mseb.2015.03.011>.
- [5] H. Bando, K. Koizumi, Y. Oikawa, K. Daikohara, V. a. Kulbachinskii, H. Ozaki, The time-dependent process of oxidation of the surface of  $\text{Bi}_2\text{Te}_3$  studied by X-ray photoelectron spectroscopy, *J. Phys. Condens. Matter.* 12 (2000) 5607. <https://doi.org/10.1088/0953-8984/12/26/307>.
- [6] C.H. Lim, D.C. Cho, Y.S. Lee, C.H. Lee, Effects of Hydrogen Reduction on the Thermoelectric Properties of Spark-Plasma-Sintered  $\text{Bi}_2\text{Te}_3$ -Based Compounds, 46 (2005) 995–1000.
- [7] Y. Horio, A. Inoue, Effect of Oxygen Content on Thermoelectric Properties of n-Type  $(\text{Bi,Sb})_2(\text{Te,Se})_3$  Alloys Prepared by Rapid Solidification and Hot-Pressing Techniques, *Mater. Trans.* 47 (2006) 1412–1416. <https://doi.org/10.2320/matertrans.47.1412>.



- [8] P. Rimal, S.-M. Yoon, E.-B. Kim, C.-H. Lee, S.-J. Hong, Effects of Hydrogen Reduction in Microstructure, Mechanical and Thermoelectric Properties of Gas Atomized n-type Bi<sub>2</sub>Te<sub>2.7</sub>Se<sub>0.3</sub> Material, *J. Korean Powder Metall. Inst.* 23 (2016) 126–131.  
<https://doi.org/10.4150/KPMI.2016.23.2.126>.
- [9] L.D. Zhao, B.P. Zhang, J.F. Li, H.L. Zhang, W.S. Liu, Enhanced thermoelectric and mechanical properties in textured n-type Bi<sub>2</sub>Te<sub>3</sub> prepared by spark plasma sintering, *Solid State Sci.* 10 (2008) 651–658. <https://doi.org/10.1016/j.solidstatesciences.2007.10.022>.
- [10] D. Leguillon, É. Martin, M. Lafarie-frenot, Flexural vs . tensile strength in brittle materials, *Comptes Rendus Mec.* 1 (2015) 3–9.  
<https://doi.org/10.1016/j.crme.2015.02.003>.
- [11] X. Jia, Y. Gao, Estimation of thermoelectric and mechanical performances of segmented thermoelectric generators under optimal operating conditions, *Appl. Therm. Eng.* 73 (2014) 333–340. <https://doi.org/10.1016/j.applthermaleng.2014.07.069>.
- [12] A.S. Al-Merbaty, B.S. Yilbas, A.Z. Sahin, Thermodynamics and thermal stress analysis of thermoelectric power generator: Influence of pin geometry on device performance, *Appl. Therm. Eng.* 50 (2013) 683–692. <https://doi.org/10.1016/j.applthermaleng.2012.07.021>.
- [13] B.S. Yilbas, S.S. Akhtar, A.Z. Sahin, Thermal and stress analyses in thermoelectric generator with tapered and rectangular pin configurations, *Energy.* 114 (2016) 52–63.  
<https://doi.org/10.1016/j.energy.2016.07.168>.
- [14] S. Fan, Y. Gao, Numerical simulation on thermoelectric and mechanical performance of annular thermoelectric generator, *Energy.* 150 (2018) 38–48.  
<https://doi.org/10.1016/j.energy.2018.02.124>.

- [15] S. Shittu, G. Li, X. Zhao, X. Ma, Y.G. Akhlaghi, E. Ayodele, High performance and thermal stress analysis of a segmented annular thermoelectric generator, *Energy Convers. Manag.* 184 (2019) 180–193. <https://doi.org/10.1016/j.enconman.2019.01.064>.
- [16] A.A. Abdelnabi, V. Lakhian, Y. Tseng, J.R. Mcdermid, J.S. Cotton, Enhancement of mechanical properties and thermoelectric performance of spark plasma sintered P-type Bismuth Telluride by powder surface oxide reduction, (n.d.) 1–42.
- [17] J. Ritter, P. Maruthamuthu, *Inorg. Chem.*, 36, 260, Gaithersburg, MD, USA, 1997.
- [18] M.I. TSIPIN, L.T. EVDOKIMENKO, Oxygen effect on structure and properties of Bi<sub>2</sub>Te<sub>3</sub> base alloys, *Izv. Akad. Nauk SSSR, Neorg. Mater.* 19 (1973) 1973. [https://inis.iaea.org/search/search.aspx?orig\\_q=RN:4090901](https://inis.iaea.org/search/search.aspx?orig_q=RN:4090901).
- [19] Standard Test Methods for Determining Average Grain Size, ASTM Stand. (2020) 1–28. <https://doi.org/10.1520/E0112-13.1.4>.
- [20] Z. Zhang, P.A. Sharma, E.J. Lavernia, N. Yang, Thermoelectric and transport properties of nanostructured Bi<sub>2</sub>Te<sub>3</sub> by spark plasma sintering, *J. Mater. Res.* 26 (2011) 475–484. <https://doi.org/10.1557/jmr.2010.67>.
- [21] J.M. Schultz, J.P. McHugh, W.A. Tiller, Effects of heavy deformation and annealing on the electrical properties of Bi<sub>2</sub>Te<sub>3</sub>, *J. Appl. Phys.* 33 (1962) 2443–2450. <https://doi.org/10.1063/1.1728990>.
- [22] O. Yamashita, S. Tomiyoshi, Effect of annealing on thermoelectric properties of bismuth telluride compounds doped with various additives, *J. Appl. Phys.* 95 (2004) 161–169. <https://doi.org/10.1063/1.1630363>.

- [23] P. Zou, G.Y. Xu, S. Wang, P.L. Chen, F.Z. Huang, Effect of high pressure sintering and annealing on microstructure and thermoelectric properties of nanocrystalline Bi<sub>2</sub>Te<sub>2.7</sub>Se<sub>0.3</sub> doped with Gd, *Prog. Nat. Sci. Mater. Int.* 24 (2014) 210–217. <https://doi.org/10.1016/j.pnsc.2014.05.009>.
- [24] S. Seo, Y. Jeong, M.W. Oh, B. Yoo, Effect of hydrogen annealing of ball-milled Bi<sub>0.5</sub>Sb<sub>1.5</sub>Te<sub>3</sub> powders on thermoelectric properties, *J. Alloys Compd.* 706 (2017) 576–583. <https://doi.org/10.1016/j.jallcom.2017.02.181>.
- [25] H.S. B. Eisenmann, *LANDOLT-BORNSTEIN Numerical Data and Functional Relationships in Science and Technology*, 1985.
- [26] L.D. Zhao, B.P. Zhang, J.F. Li, M. Zhou, W.S. Liu, Effects of process parameters on electrical properties of n-type Bi<sub>2</sub>Te<sub>3</sub> prepared by mechanical alloying and spark plasma sintering, *Phys. B Condens. Matter.* 400 (2007) 11–15. <https://doi.org/10.1016/j.physb.2007.06.009>.
- [27] H.J. Klam, H. Hahn, H. Gleiter, The thermal expansion of grain boundaries, *Acta Metall.* 35 (1987) 2101–2104. [https://doi.org/10.1016/0001-6160\(87\)90038-1](https://doi.org/10.1016/0001-6160(87)90038-1).
- [28] Astm, Standard Practice for Reporting Uniaxial Strength Data and Estimating Weibull Distribution Parameters for Advanced Ceramics, *Astm. i* (2000) 1–17. <https://doi.org/10.1520/C1239-13.Scope>.
- [29] C. and Kingery, Effect of Porosity on Physical Properties of Sintered Alumina, 39 (1956) 377–385.
- [30] D. Vasilevskiy, S. Turenne, R. a. Masut, Application of mechanical spectroscopy to the

study of high performance  $(\text{Bi}_{1-x}\text{Sb}_x)_2(\text{Te}_{1-y}\text{Se}_y)_3$  extruded thermoelectric alloys, 2007 26th Int. Conf. Thermoelectr. 2 (2007) 3–6.

<https://doi.org/10.1109/ICT.2007.4569420>.

- [31] J.B. Wachtman, Mechanical and Thermal Properties of Ceramics, NBS Spec. Publ. 303 (1969) 139.  
[https://books.googleusercontent.com/books/content?req=AKW5QaeZb8cCzWl4I5L5LPrBClSJJgAXxJxciOie9Nj7iGbkyHgkrSKm9\\_f\\_eQZBmoPJ-LQQeri7eZdQbiBrACMUvmaq8k5jh-CyOT97vEdjCbC9lZkltWgy565ZnSag8m-cDJYIEGvgQupUrfpQ872PWSk2UuDKmw2c-wbLtqk2HWF2IP\\_ywlLi4L6KmLa7khGsKsla](https://books.googleusercontent.com/books/content?req=AKW5QaeZb8cCzWl4I5L5LPrBClSJJgAXxJxciOie9Nj7iGbkyHgkrSKm9_f_eQZBmoPJ-LQQeri7eZdQbiBrACMUvmaq8k5jh-CyOT97vEdjCbC9lZkltWgy565ZnSag8m-cDJYIEGvgQupUrfpQ872PWSk2UuDKmw2c-wbLtqk2HWF2IP_ywlLi4L6KmLa7khGsKsla).
- [32] J. Mackey, F. Dynys, A. Sehirlioglu, Uncertainty analysis for common Seebeck and electrical resistivity measurement systems, Rev. Sci. Instrum. 85 (2014).  
<https://doi.org/10.1063/1.4893652>.
- [33] J.M. Schultz, J.P. McHugh, W. a. Tiller, Effects of heavy deformation and annealing on the electrical properties of  $\text{Bi}_2\text{Te}_3$ , J. Appl. Phys. 33 (1962) 2443–2450.  
<https://doi.org/10.1063/1.1728990>.
- [34] D. Bin Hyun, T.S. Oh, J.S. Hwang, J.D. Shim, Effect of excess Te addition on the thermoelectric properties of the 20%  $\text{Bi}_2\text{Te}_3$ -80%  $\text{Sb}_2\text{Te}_3$  single crystal and hot-pressed alloy, Scr. Mater. 44 (2001) 455–460. [https://doi.org/10.1016/S1359-6462\(00\)00631-X](https://doi.org/10.1016/S1359-6462(00)00631-X).
- [35] M. Cutler, J.F. Leavy, R.L. Fitzpatrick, Electronic transport in semimetallic cerium sulfide, Phys. Rev. 133 (1964). <https://doi.org/10.1103/PhysRev.133.A1143>.
- [36] M. Cutler, R.L. Fitzpatrick, J.F. Leavy, The conduction band of cerium sulfide  $\text{Ce}_{3-x}\text{S}_4$ ,

- J. Phys. Chem. Solids. 24 (1963) 319–327. [https://doi.org/10.1016/0022-3697\(63\)90136-7](https://doi.org/10.1016/0022-3697(63)90136-7).
- [37] G.J. Snyder, E.S. Toberer, Complex thermoelectric materials, *Nat. Mater.* 7 (2008) 105–114. <https://doi.org/10.1038/nmat2090>.
- [38] J.J. Shen, L.P. Hu, T.J. Zhu, X.B. Zhao, J.J. Shen, L.P. Hu, T.J. Zhu, X.B. Zhao, The texture related anisotropy of thermoelectric properties in bismuth telluride based polycrystalline alloys The texture related anisotropy of thermoelectric properties in bismuth telluride based polycrystalline alloys, 124102 (2012). <https://doi.org/10.1063/1.3643051>.
- [39] J. Jiang, L. Chen, S. Bai, Q. Yao, Q. Wang, Fabrication and thermoelectric performance of textured n-type  $\text{Bi}_2(\text{Te,Se})_3$  by spark plasma sintering, *Mater. Sci. Eng. B.* 117 (2005) 334–338. <https://doi.org/10.1016/j.mseb.2005.01.002>.
- [40] S. Choi, S. Maruyama, Evaluation of the Phonon Mean Free Path in Thin Films by Using Classical Molecular Dynamics Evaluation of the Phonon Mean Free Path in Thin Films by Using Classical Molecular Dynamics, (2003). <https://doi.org/10.3938/jkps.43.747>.

**Chapter 4: A parametric study aimed at selecting dimensions for a new annular TEG module design that will yield maximum power density and minimum thermal stress**

*Journal Paper*

A parametric study aimed at selecting dimensions for a new annular TEG module design that will yield maximum power density and minimum thermal stress

Ahmed A. Abdelnabi, Joseph R. McDermid, James S. Cotton \*

<sup>a</sup> Department of Mechanical Engineering, McMaster University, Hamilton, ON, Canada

\*Corresponding author. Department of Mechanical Engineering, McMaster University, Hamilton, ON, Canada

Email address: cottonjs@mcmaster.ca (James S. Cotton).

Keywords:

Annular thermoelectric generator; ring-shaped TE legs; axial heat flow; radial heat flow; contact resistance; thermal interface material; coupled finite element model; thermal stress;

Highlights:

- The heat flow direction in an ATEG couple affects power output and thermal stresses
- The increase in  $\Delta T$  across the ATEG increases both power output and thermal stresses
- The radial ATEG design generates more power but with higher thermal stresses
- The axial ATEG design has lower thermal stresses even when generating the same power
- The solder plastic deformation releases the thermal stresses in the ATEG couple

**Abstract:**

In this paper, two annular thermoelectric generator (ATEG) couple configurations with ring-shaped thermoelectric legs (TE) are compared with respect to their thermoelectric performance and mechanical reliability integrated between hot- and cold-side heat exchangers. In one design, the couple is configured to allow heat/electrical current to flow radially; in the other design, the couple is configured to allow for axial flow. An analytical model and a 3D thermoelectric/thermal stress coupled finite element model were constructed to examine how changes to the diameter ratio ( $D_o/D_i$ ), thickness ratio ( $t/D_i$ ), and the hot-side thermal resistance affected the performance and thermal stress of the two configurations. The accuracy and validity of the finite element model were verified against the analytical model and previous work. The analytical model provided efficiency maps for a broad dimensional range to compare the two ATEG configurations, which were then used to select points of interest for the finite element model, thereby saving computational time. The importance of the ATEG thermal resistance to heat exchanger thermal resistance ratio ( $R_{TEG}/R_{HX}$ ) is critical to the performance of the ATEG couple. The results indicated that, as the thermal resistance of the hot-side heat exchanger decreases due to an increase in the convective heat transfer coefficient, the radial couple configuration generates more power than the axial couple configuration for the tested range of  $D_o/D_i$  and  $t/D_i$ . The increase in  $\Delta T$  lead to increases in both power and thermal stresses across both ATEG couple configurations. The radial configuration was found to have thermal stresses that were as much as 67 MPa higher than those in the axial configuration when both were generating the same power at  $\Delta T = 105^\circ\text{C}$  due to the formation of additional tensile hoop stresses. The axial couple configuration had the lowest  $\sigma$  at 67.8 MPa, with a  $D_o$  of 16 mm, a  $t$  of 1 mm, a  $\Delta T$  of  $14.8^\circ\text{C}$ , and power generation of 10.4 mW



per couple. The maximum thermal stress values were located at the corners of the interface between the solder and the TE rings due to mismatched CTE.

#### **4.1.Introduction**

Approximately 70% of the world's energy is lost as heat waste from industrial and power plants. Thermoelectric generators (TEG) are one technology that can be used to recover some of this heat waste, thereby enhancing fuel efficiency and lowering greenhouse gas emissions [1]. TEG modules are solid-state heat engines that are connected to a heat source and a heat sink; the module functions as heat flows through it, which allows it to generate electricity commensurate with its efficiency. The building block of a TEG module is a TEG couple. Typically, each TEG module consists of multiple TEG couples, which are connected electrically in series and thermally in parallel. Since TEG couples contain no moving parts, TEG modules produce no noise or vibration during operation. Notably, TEG modules are also able to operate at low-temperature differences, which makes them ideal for a wide range of heat waste recovery applications, such as in automobile [2–4] and commercial pizza oven energy recovery systems [5].

There are two main approaches to improving the performance of a TEG module. The first approach involves improving the thermoelectric properties of the used in the module, which is achieved by improving the ZT, as well as the thermoelectric (TE) materials mechanical properties. The efficiency of a TEG module is a function of the TE material's figure of merit,  $ZT = \alpha^2 T / \rho_e k$ , where  $\alpha$  is the Seebeck coefficient, T is the temperature in Kelvins,  $\rho_e$  is the electrical resistivity, and k is the thermal conductivity. Researchers have attempted to increase ZT by increasing the Seebeck coefficient and decreasing the electrical resistivity and thermal conductivity via ball milling and powder sintering techniques [6–11]. The mechanical strength of the TE material is also an important determinant of TE module performance. Consequently, researchers have

explored a number of approaches for improving the strength of TE materials, including powder pre-treatment [12,13], additives [14,15], sintering [11], and hot forging [16]. Abdelnabi et al. [12,13] have developed a method that enables the measurement of the uniaxial tensile strength of small-sized samples. They found that introducing an H<sub>2</sub> gas reduction pre-treatment step to both the P- and N-type Bi<sub>2</sub>Te<sub>3</sub> increased the tensile strength of the spark plasma sintered samples to 31 and 35.5 MPa, respectively. Furthermore, Abdelnabi et al.'s approach enabled the ZT<sub>max</sub> of P- and N-type Bi<sub>2</sub>Te<sub>3</sub> to be increased to 1.13 and 0.63, respectively. Similarly, Zhao et al.'s [16] use of spark plasma sintering hot forging with N-type Bi<sub>2</sub>Te<sub>3</sub> resulted in a ZT<sub>max</sub> value of 1.18 and a bending strength value of 120 MPa. The second approach to improving the performance of TEG modules focuses on selecting the optimum material and optimizing the geometry of the TEG couple to fit the application. For instance, findings have shown that, at a temperature difference of 200 K, segmented annular TEG couples comprised of both Bi<sub>2</sub>Te<sub>3</sub> and skutterudite are more efficient than couples comprised of only Bi<sub>2</sub>Te<sub>3</sub> or skutterudite by 21.7% and 82.9%, respectively [17].

Flat TEG (FTEG) modules require flat interfaces to be integrated into power generation systems. In contrast, ATEG modules are optimal in applications where either the heat source or sink are round in shape. Min et al. [18] fabricated a novel ring-shaped ATEG module made up of two couples that was able to produce 33 mW at a temperature difference of 70 K. Min et al.'s [18] ring-shaped ATEG module offers comparable performance to an FTEG, with the added advantage of a geometry that can be used in applications with radial heat flow. In this ATEG design, the P- and N-type legs were arranged axially in an alternating pattern, so as to fully surround the inside tube and were linked by metallic connectors. Despite these advantages, subsequent research on ring-shaped ATEGs has revealed a number of challenges, such as high contact resistance due to

assembly [19,20] and the cracking of ring-shaped TE legs during manufacturing and testing [21,22]. The successfully manufactured modules were tested at temperature difference of  $<100^{\circ}\text{C}$ , as this temperature range is thought to mitigate the chance of failure during operation due to excessive thermal stresses [18,20]. Mansouri et al. [21] have made several attempts to manufacture a ring-shaped P-type module by sintering skutterudite directly between two titanium rings to act as metallic conductors. Finite element analysis revealed the possibility of cracking due to thermal stresses caused by the mismatch between the P-type skutterudite and the titanium rings. They were able to eliminate this problem by using multiple legs between brass rings in place of the previous full ring-shaped approach. Morsy [22] was also unable to obtain reproducible performance results for his ring-shaped ATEG modules, which were manufactured using bismuth telluride ( $\text{Bi}_2\text{Te}_3$ ) for both P- and N-type rings, as the rings cracks after each test at a temperature difference of 160 K.

ATEG couple performance has been investigated using analytical modelling that focuses on the leg geometry effect, especially the annular shape parameter,  $S_r$  which is the ratio of the outer to the inner radius of the TE legs in ATEG couple [23–28]. In one such study, Shen et al. [29] examined how couple performance is affected by  $S_r$  under a constant heat flux boundary condition compared to a constant temperature boundary condition. Their results showed that performance increases as  $S_r$  deviates from 1, and leg length increases as power output increases. Electrical and thermal contact resistances have been neglected in many ATEG analytical models, which is important to predict the actual ATEG couple performance [23,28,30]. Indeed, Shen et al. [30] observed a sharp 7.5% decrease in power when they employed an electrical contact resistance of  $10^{-10} \Omega\text{m}^2$  in their model. Thomson effect is inherently neglected if temperature-independent thermoelectric properties are considered in theoretical ATEG modelling [24,27,28] it is nevertheless an accurate predictor of power output [23,25,31,32]. As Sun et al. [33] reported, it is

important to account for the Thomson effect with respect to high-temperature differences across ATEG couples, as it produces a 6.62% deviation in output power at  $\Delta T=500$  K.

Thermoelectric/structural 3D coupled finite elements have been used to investigate how leg geometry, leg dimensions, and the solder used to connect the legs to the metallic electric conductors influence thermoelectric performance and thermal stress fields in both flat [34–41] and annular [17,42–44] TEG modules. The findings of these investigations indicated that decreasing the TE leg length increases the performance of the ATEG couple. However, these findings also showed that decreasing the TE leg length leads to an increase in thermal stress, though this effect decreases at a specific leg angle range [17,43]. Therefore, ATEG performance can be optimized based on the geometry of the ATEG couple and the yield strength of the TE material. A review of the literature reveals that, compared to flat TEGs, little attention has been paid to thermal stress fields in relation to ATEGs. In fact, only one ATEG couple design configuration similar to the one patented by Markman et al. was studied [45]. In this ATEG couple design, alternating P- and N-type TE tapered legs are connected with metallic conductors and wrapped around the peripheral of a cylinder, acting as either the hot or cold side of the power generation system. The ring-shaped ATEG design was investigated only for the thermoelectric performance by Bauknecht et al. [45]. They simulated the non-uniform temperature distribution around the outer surface of the ring-shaped ATEG module due to the flow of the exhaust gases which resulted in an efficiency decrease by 10%.

The above critical literature review has focused on current research in TEG and ATEG modules with respect to both thermoelectric performance and thermal stress. As the examined studies demonstrate, the optimization of module geometry requires a trade-off between performance and mechanical reliability. The literature review also exposed three key research

gaps, which will be addressed by the current work. 1) To the best of our knowledge, no prior research has examined the mechanical reliability of ATEG couples with ring-shaped legs. 2) Prior studies have only considered the heat and electric current flows in the ATEG in the radial direction. And 3) prior ATEG thermal stress analyses have neglected to consider the effects of the hot-side and cold-side heat exchangers; rather, these effects have only been considered in performance studies.

The current work evaluates the thermoelectric performance and thermal stresses of a ring-shaped ATEG couple integrated between hot-side and cold-side heat exchangers. To this end, two configurations are compared with respect to their heat/electrical current flow paths: one that allow for radial flow (radial configuration), and one that allows for axial flow (axial configuration). A simplified analytical model was constructed to compare the thermoelectric performance of the two configurations under three different hot-side thermal resistances, and a 3D coupled finite element ANSYS model was constructed to study and compare the thermal stresses of the two configurations at different dimensions. The dimensions of interest used in the thermal stress evaluations were selected based on the analytical model results. All results are presented using 2D maps and graphs, as these formats are optimal for studying the effects of the different parameters and identifying the optimum design.

The remainder of this paper is organized as follows: Section 2 explains the two ATEG configurations geometry details; Section 3 describes the analytical model that was used to study and compare the performance of the two ATEG configuration, including the material properties and boundary conditions that were used in its construction; Section 4 describes the 3D coupled thermoelectric/thermal stresses finite element ANSYS model, including its material properties, boundary conditions, and computational procedure, as well as the model verification method that

was used; Section 5 presents and discusses the results for both the analytical and 3D coupled finite element models; and finally, Section 6 presents the conclusions of the current work.

#### **4.2. Geometric model description**

In this study, two ATEG couples with different heat/electrical current flow configurations are investigated. In an ATEG couple, heat and electrical current typically either flows radially or axially with respect to the couple's axis. All of the ATEG couples investigated in this study were comprised of the same components, regardless of configuration. Fig. 1 shows the two design configurations; note that the ring-shaped P- and N-type TE legs in both designs were made from directly sintered TE material in order to save on materials. In the radial design (Fig. 1a), both heat and electrical current were made to flow radially by soldering the P- and N-type rings to inner and outer copper cylindrical conductors from the inside and outside, respectively. These copper cylinders act as electrical conductors the TE rings and thermal interface between the couple and the heat exchanger. This configuration is similar to the one proposed by Schmitz et al. [19]. In contrast, the copper conductors in the axial design (Fig. 1b) have a "T" shaped cross-section, which redirects heat flow along the axial direction and enhances the thermal contacts with both the aluminum block and the copper cooling pipe. The stem parts of this "T" shaped configuration are soldered to the sides of both the P- and N-type TE rings to allow electrical current to pass through axially. A similar conductor configuration was proposed for an ATEG module by Morsy [46], and for an FTEG module by Crane et al. [47]. To reduce thermal contact resistance between the ATEG couple and both the aluminum block and the copper cooling pipe, thermal interface material was applied.

In the current investigation, and for both the analytical and finite element models, P- and N-type TE rings with an inner diameter ( $D_i$ ) of 7.9 mm were used for both configurations in order

to ensure consistency. As shown in Fig. 1, “ $t$ ” is the thickness in the axial direction and the “ $D_o$ ” is the outer diameter of the P- and the N-type rings; these variables were assumed to be equal, despite being varied for the comparisons of the axial and radial configurations. The two annular TEG couple configurations were simulated to be working between hot-side and cold-side heat exchangers. For the simulations, the aluminum block that acts as the base of the fin was only used as the hot-side heat exchanger, and the fin thermal equivalent resistance was considered in the convective thermal boundary condition for the sake of model simplicity and saving computational time. The cold-side heat exchanger for both configurations was a standard 1/8 inch copper pipe with an inner diameter of 4.72 mm and an outer diameter of 6.35 mm, and both configurations were outfitted with 0.1mm thick electrically insulative thermal interface material (TIM) between the couple and both the aluminum block and the copper cooling water pipe. In addition, the solder between the copper conductors and the P- and N-type rings had a thickness of 0.1 mm. The dimensions for both ATEG couple configurations were changed by altering either the  $t$  or the  $D_o$ , with the TIM and the solder thicknesses remaining constant throughout. The gap between the P- and the N-type rings in the radial configuration, as well as the stem of the T-shaped conductor in the axial configuration, is a function of  $t$ , as they are equal to  $1/2 t$ . All copper conductor thicknesses and gaps in the radial were kept constant, and not as a function of  $D_o$ . The aluminum block was thick enough to account for changes in  $D_o$  such changes to the hot side’s thermal resistance will not be as significant as changes to  $D_o$ , as aluminum offers relatively high thermal conductivity compared to the gas convective coefficient ( $h_g$ ). On the other hand, as  $t$  changes, the dimensions of both the aluminum block and the copper cooling pipe change in the axial direction, which changes the area in which  $h_g$  and  $h_w$  are applied, respectively.

### 4.3. Analytical model

#### 4.3.1. Thermoelectric governing equations

The analytical TEG couple model used in this work was similar to Ioffe's constant property model (CPM) [48], but was also axisymmetric in order to account for the ATEG module's cylindrical shape and its effect on both electrical resistance and thermal conductance. A similar modelling approach was used to find the optimum radial configuration for ATEG couples in the multi-row TEG Pizza Oven Energy Recovery System (POWER) [49]. In the proposed analytical model, the coupling between Peltier heat, thermal conductance, and joule heating was modelled using constant temperature-average thermoelectric properties, an approach which inherently neglects the Thomson effect [28]. The model accounted for the additional electrical contact resistance of the solder between the P and N legs, as well as the thermal contact resistance between the annular TEG couple and both the hot-side and cold-side heat exchangers. The model was extended to capture the effect of the hot-side and the cold-side heat exchangers in order to establish constant hot gases ( $T_g$ ) and constant cooling water ( $T_w$ ) temperatures as the thermal boundary conditions. An ATEG couple is simply a heat engine that works between a heat source ( $T_g$ ), which supplies hot-side heat flow ( $Q_H$ ), and a heat sink ( $T_w$ ), which dissipates cold-side heat flow ( $Q_C$ ). The produced electrical power ( $P$ ) is the difference between the  $Q_H$  and  $Q_C$ . Fig. 2 shows an enlarged schematic of the TEG couple (heat engine) thermal circuit that explains the different effects in the ATEG couple that were considered, and the direction of heat flow. The thermal conductance through the couple is represented as  $((T_h - T_c)/R_{TEG})$ , the Peltier heat is represented as  $(\alpha I T_h)$  for the hot side and  $(\alpha I T_c)$  for the cold side, and the joule heating ( $I^2 r_{total}$ ) is split equally between the hot and cold sides [24]. The analytical model has eight equations for the eight



unknowns ( $Q_H$ ,  $Q_C$ ,  $P$ ,  $T_h$ ,  $T_c$ ,  $I$ ,  $V$  and  $\eta$ ), and  $Q_H$  is calculated through the hot side heat exchanger as follows:

$$Q_H = \frac{T_g - T_h}{R_H} \quad (1)$$

where  $T_h$  is the TEG couple hot-side temperature and  $R_H$  is the total hot-side thermal resistance, which is comprised of the fins thermal resistance ( $R_{fins}$ ), the aluminum fin base (aluminum block) thermal resistance ( $R_{Al \text{ block}}$ ), and the thermal contact resistance between the TEG couple and the hot-side heat exchanger ( $R_{th \text{ cont}}$ ). The  $Q_H$  is also calculated from the TEG couple side as,

$$Q_H = (T_h - T_c)/R_{TEG \text{ th}} + \alpha I T_h - \frac{1}{2} I^2 R_{TEG \text{ ele}} \quad (2)$$

where  $I$  is the electrical current,  $T_c$  is the ATEG couple cold-side temperature, and  $R_{TEG \text{ th}}$  is the total thermal resistance of the ATEG couple. The thermal resistances of the P- and N-type rings in parallel,  $\frac{1}{R_{TEG \text{ th}}} = \frac{1}{R_P} + \frac{1}{R_N}$ .  $\alpha = |\alpha_P| + |\alpha_N|$ , give the ATEG couple's total Seebeck coefficient, which is also the P- and N-type rings' absolute Seebeck coefficient values.  $R_{TEG \text{ ele}} = r_{TEG} + R_{cont \text{ ele}}$  is the total couple electrical resistance, where ( $r_{TEG} = r_P + r_N$ ) is the electrical resistance and ( $R_{cont \text{ ele}}$ ) is the electrical contact resistance between the TE rings and the metallic conductors.  $Q_C$  is calculated from the ATEG couple-side and cold-side heat exchanger as:

$$Q_C = (T_h - T_c)/R_{TEG \text{ th}} + \alpha I T_c + \frac{1}{2} I^2 R_{TEG \text{ ele}} \quad (3)$$

$$Q_C = \frac{T_c - T_w}{R_C} \quad (4)$$

where  $T_w$  is the temperature of the water flowing through the copper cooling pipe. The cold-side total thermal resistances,  $R_C = R_{conv} + R_{pipe} + R_{th \text{ cont}}$ , are comprised of the cooling water convection,

copper pipe, and contact thermal resistances, respectively. As P is the difference between the  $Q_H$  and  $Q_C$  values,

$$P = \alpha I (T_h - T_c) - I^2 R_{TEG\ ele} \quad (5)$$

For the external electrical load,  $R_L$ , which is powered by the ATEG couple, P is also calculated as:

$$P = I^2 R_L \quad (6)$$

Both the voltage across the ATEG couple and the couple's thermal efficiency are calculated as follows:

$$V = IR_L \quad (7)$$

$$\eta = \frac{P}{Q_H} \quad (8)$$

The couple's thermal resistance and the Peltier effect are joined when an electrical current is flowing through the couple. The starting point is the couple's thermal resistance, which is its main thermal component and is a function of its dimensions and heat path (i.e., the couple's configuration). The couple's performance is also affected by its electrical resistance, which, like thermal resistance, is a function of the couple's configuration. However, the thermal and electrical resistance of the TE rings are functions of the resistivity values of the geometrical parts through which heat or the electrical current flow. For a given set of ATEG couple dimensions, the resistance of either heat or electrical current along the radial and axial paths will be different. The radial ( $R_{TEG\ (th/ele)R}$ ) and the axial ( $R_{TEG\ (th/ele)A}$ ) resistances (thermal or electrical) of any of the P- or the N-type rings are found by,

$$R_{TEG\ (th/ele)R} = \frac{1}{k_{th/ele}} \frac{\ln(D_o/D_i)}{2 \cdot \pi \cdot t} = \frac{1}{2 \cdot \pi \cdot D_i \cdot k_{th/ele}} \left( \frac{D_i}{t} \right) \left( \ln \left( \frac{D_o}{D_i} \right) \right) \quad (9)$$

$$R_{TEG(th/ele)A} = \frac{4 \cdot t}{\pi \cdot k_{th/ele}} \left( \frac{1}{(D_o^2 - D_i^2)} \right) = \frac{4}{D_i \cdot \pi \cdot k_{th/ele}} \left( \frac{D_i}{t} \right) \left( \frac{1}{\left( \frac{D_o}{D_i} \right)^2 - 1} \right) \quad (10)$$

where  $k_{th/ele}$  is either the thermal or electrical conductivity,  $D_o$  and  $D_i$  are the outer and inner diameters of the P- or the N-type rings, respectively,  $t$  is the axial thickness of the P- or N-type rings, and  $D_o/D_i$  and  $t/D_i$  are the diameter and thickness ratios, as  $D_i$  is kept constant throughout the current work. The resistance of the radial configuration is directly proportional to  $\ln(D_o/D_i)$  and inversely proportional to  $t/D_i$ ; conversely, the axial configuration is directly proportional to  $t/D_i$  and inversely proportional to  $(D_o/D_i)^2$ . The internal resistance (thermal or electrical) of the radial and axial direction flows can be compared by calculating the ratio of  $R_{(th/ele)R}$  to  $R_{(th/ele)A}$ . This can be achieved by dividing equation (9) by equation (10), which produces equation (11):

$$\frac{R_{TEGR}}{R_{TEGA}} = \frac{1}{8} \cdot \left( \frac{D_i}{t} \right)^2 \cdot \ln \frac{D_o}{D_i} \cdot \left( \left( \frac{D_o}{D_i} \right)^2 - 1 \right) \quad (11)$$

### 4.3.2. Material properties and boundary conditions

The analytical model uses constant temperature-averaged thermoelectric properties of spark-plasma-sintered P- and N-type bismuth telluride, which has been measured within a temperature range of 25 to 250 °C in a previous work [12,13]. Bismuth telluride was selected for this research, as its thermoelectric properties were optimal for the temperature range that would be used. The hot-side convective heat transfer coefficient ( $h_g$ ) included both the exhaust-gas convection and the fins thermal resistance without the aluminum base. Table 1 lists all of the property values for the materials used in the analytical model, with the exception of the thermal and electrical conductivity of the copper electrical conductors. The following assumptions and boundary conditions were used in the analytical model:

- 1) The exhaust gas and cooling water temperatures were set to  $T_g = 270$  °C and  $T_c = 25$  °C, respectively.
- 2) Three hot-side convective heat transfer coefficients ( $h_g = 40, 80, \text{ and } 160$  W/m<sup>2</sup>K) were used for the outer surface of the aluminum block, while the cold-side convection heat transfer coefficient was a constant value of  $h_w = 20,000$  W/m<sup>2</sup>K at the inner surface of the copper cooling pipe (Appendix A).
- 3) A thermal contact resistance of  $\rho_{th\_cont} = 8 \times 10^{-4}$  K.m<sup>2</sup>/W was considered for the connections between the ATEG couple and both the aluminum block and the copper cooling pipe [3].
- 4) An electrical contact resistivity of  $\rho_{ele\_cont} = 5 \times 10^{-9}$   $\Omega$ .m<sup>2</sup> was used for the four contacts between the solder and the P- and N-type rings [50].
- 5) The thermal and electrical conductivity of the metallic conductors connecting the TE rings was assumed to be high; hence, these values were neglected.
- 6) Convection and radiation heat transfer was neglected for all other surfaces and was set to be adiabatic.
- 7) A Maximum Power Point Tracking (MPPT) chip was assumed to be connected to the ATEG couple that changes  $R_L$ , accordingly the ATEG couple is operating at maximum power.

#### **4.4.Finite element model**

The coupled finite element analysis of both the axial and the radial configurations contains two main analysis systems which are: thermoelectric analysis module and thermal stresses analysis module. The coupled finite element model is one-way model in which the thermoelectric analysis

provides the temperature fields as well as the generated power and the thermal stresses analysis uses the temperature field as an input to provide the thermal stresses field.

#### 4.4.1. Thermoelectric analysis' governing equations

The thermoelectric governing equations for both the axial and radial couple configurations were solved using ANSYS workbench 19.2. The thermoelectric analysis module accounts for the Fourier heat conduction effect, Peltier effect, Joule heating effect and Thomson effect.

The equation of heat flow in the thermoelectric analysis could be written as [51]:

$$\rho C_P \frac{\partial T}{\partial t} + \nabla \cdot \vec{q} = \dot{q} \quad (12)$$

and the equations of the electric charge continuity as:

$$\nabla \cdot \left( \vec{J} + \frac{\partial \vec{D}}{\partial t} \right) = 0 \quad (13)$$

where  $\rho$  is the density,  $C_P$  is the specific heat,  $\vec{q}$  is the heat flux,  $\dot{q}$  is the heat generation,  $\vec{J}$  is the electric current density and  $\vec{D}$  is the electric flux density. The above Eqs (12) and (13) are coupled by the following thermoelectric constitutive equations [52]:

$$\vec{q} = T[\alpha] \cdot \vec{J} - [k] \cdot \nabla T \quad (14)$$

$$\vec{J} = [k_{ele}] \cdot (\vec{E} - [\alpha] \cdot \nabla T) \quad (15)$$

where  $[\alpha]$ ,  $[k]$  and  $[k_{ele}]$  are the matrices of the Seebeck coefficient, thermal conductivity, and electrical conductivity, respectively. The electric field intensity  $\vec{E}$  is defined in terms of the electric scalar potential  $\phi$  as:

$$\vec{E} = -\nabla \phi \quad (16)$$

The steady state coupled thermoelectric equations can be acquired by substituting Eqs (14)-(16) into Eqs (12),(13):

$$\nabla \cdot (T[\alpha] \cdot \vec{j}) - \nabla \cdot ([\alpha] \cdot \nabla T) = \dot{q} \quad (17)$$

$$\nabla \cdot ([k_{ele}] \cdot [\alpha] \cdot \nabla T) + \nabla \cdot ([k_{ele}] \cdot \nabla \phi) = 0 \quad (18)$$

#### 4.4.2. Thermal stress analysis' governing equations

The steady state thermal differential equation from the thermoelectric analysis as it provide the temperature field that is used in the thermal stress analysis can be expresses as [17]:

$$\frac{\partial}{\partial x} \left[ k \frac{\partial T}{\partial x} \right] + \frac{\partial}{\partial y} \left[ k \frac{\partial T}{\partial y} \right] + \frac{\partial}{\partial z} \left[ k \frac{\partial T}{\partial z} \right] = 0 \quad (19)$$

The thermal stresses are created due to the mismatch in the coefficient of thermal expansion (CTE) between different TEG couple components as well as the uneven expansion in the same component due to temperature gradient. The displacement-strain relations are [53]:

$$\bar{\epsilon}_{XX} = \frac{\partial \bar{u}}{\partial \bar{x}}, \bar{\epsilon}_{YY} = \frac{\partial \bar{v}}{\partial \bar{y}}, \bar{\epsilon}_{ZZ} = \frac{\partial \bar{w}}{\partial \bar{z}} \quad (20)$$

$$\bar{\epsilon}_{XY} = 0.5 \left( \frac{\partial \bar{u}}{\partial \bar{y}} + \frac{\partial \bar{v}}{\partial \bar{x}} \right), \bar{\epsilon}_{YZ} = 0.5 \left( \frac{\partial \bar{w}}{\partial \bar{y}} + \frac{\partial \bar{v}}{\partial \bar{z}} \right), \bar{\epsilon}_{ZX} = 0.5 \left( \frac{\partial \bar{w}}{\partial \bar{x}} + \frac{\partial \bar{u}}{\partial \bar{z}} \right) \quad (21)$$

The dimensionless form of a non-symmetrical Jacobian matrix expresses stress-strain relation:

$$\begin{pmatrix} \bar{\sigma}_{XX} \\ \bar{\sigma}_{YY} \\ \bar{\sigma}_{ZZ} \\ \bar{\sigma}_{YZ} \\ \bar{\sigma}_{ZX} \\ \bar{\sigma}_{XY} \end{pmatrix} = \frac{\bar{E}}{(1+\nu)(1-2\nu)} \begin{bmatrix} 1-\nu & \nu & \nu & 0 & 0 & 0 \\ \nu & 1-\nu & \nu & 0 & 0 & 0 \\ \nu & \nu & 1-\nu & 0 & 0 & 0 \\ 0 & 0 & 0 & 1-2\nu & 0 & 0 \\ 0 & 0 & 0 & 0 & 1-2\nu & 0 \\ 0 & 0 & 0 & 0 & 0 & 1-2\nu \end{bmatrix} \times \begin{pmatrix} \bar{\epsilon}_{XX} \\ \bar{\epsilon}_{YY} \\ \bar{\epsilon}_{ZZ} \\ \bar{\epsilon}_{YZ} \\ \bar{\epsilon}_{ZX} \\ \bar{\epsilon}_{XY} \end{pmatrix} \quad (22)$$

$$- \begin{pmatrix} 1 \\ 1 \\ 1 \\ 0 \\ 0 \\ 0 \end{pmatrix} \frac{\bar{\alpha}\bar{E}T}{1-2\nu}$$

The Maximum Normal Stress Theory was adopted in the current analysis as the P and N-type Bi2Te3 rings have a brittle behavior [12,13]. In case of non-zero principle stress values, they are marked as  $\sigma_1$ ,  $\sigma_2$  and  $\sigma_3$  (assuming  $\sigma_1 \geq \sigma_2 \geq \sigma_3$ ). The maximum normal (principle) stress  $\sigma_{max}$  and the minimum normal (principle) stress  $\sigma_{min}$  are expresses as:

$$\sigma_{max} = \sigma_1, \sigma_{min} = \sigma_3 \quad (23)$$

#### 4.4.3. Material properties

The P- and N-type TE materials were chosen based on the operational temperature range (< 270°C) of the current study with the aim of achieving optimal TEG couple performance. Accordingly, spark plasma sintered bismuth telluride was selected for the P- and N-type rings, as it is known for its higher mechanical strength compared to zone-melted bismuth telluride [54,55]. The isotropic and anisotropic temperature-dependent thermoelectric properties and the mechanical properties of the spark plasma sintered bismuth telluride were measured in a previous work [12,13] and are listed in Table 2. The thermal conductivity, electrical resistivity, and mechanical properties of the aluminum block, solder, thermal interface material, and copper used for the conductors and the cooling pipe are listed in Table 1. A bilinear model was assumed for the copper and solder, as they were treated as elastoplastic materials; all other materials were assumed to be linear elastic

materials. The yield stresses of the copper and solder were 70 MPa and 26 MPa, respectively, while their respective tangential moduli were 24 GPa and 8.9 GPa.

#### 4.4.4. Computational procedure

ANSYS Workbench was used to build a 3D thermoelectric/static structure finite element coupled model. The model enabled the thermoelectric performance and the thermal stress fields of the two couple design configurations to be simulated, and the effects of altering their dimensions to be observed. Specifically, the model first solves the couple's thermoelectric field at the maximum power point based on its configuration and dimensions, and then feeds this result to the static structure module in order to solve for the thermal stresses. Since both couple design configurations were axisymmetric, only the wedge-shaped section was simulated in order to reduce computational time (Fig. 3).

The ANSYS model also made use of quadratic mesh elements (Fig. 3), with different sized elements being tested to ensure mesh independent model performance. The model contains multiple element types to insure accurate prediction of both the thermoelectric performance and the thermal stresses field. The thermoelectric analysis includes: SOLID226, SOLID90 and CONTA174, while the thermal stress analysis includes: SOLID186, CONTA174 and TARGE170. A mesh independence test was carried out on both the radial and axial configurations, with a ring outside diameter ( $D_o$ ) and thickness ( $t$ ) of 10 mm and 1 mm, respectively. The smallest dimensions were chosen for this test to ensure that the chosen element size could capture the large thermal and stresses gradient. First, wedge-shaped models with angles of  $1^\circ$ ,  $2^\circ$ , and  $4^\circ$  were tested with different element sizes to identify the smallest angle at which the performance of the TEG couple could be simulated. Fig. 4a shows the maximum stress values for the P- and N-type rings with respect to the maximum principal stresses of deferent wedge angels versus element size for both



configurations. The results showed that changing the wedge angle did not affect the model; thus, 1° wedge angle was selected for use in ANSYS model. To show the effect of the element size on the model's performance, changes in both the maximum stress value of the maximum principal stresses in the TE rings versus the total number of elements were plotted (Fig. 4b). An element of 0.035 mm was chosen for both configurations, as this element size provided 5% error at 1/16 the computational time of the smallest element tested.

#### 4.4.5. Boundary conditions

The 3D annular TEG couple finite element model was simulated using the following assumptions and boundary conditions:

- 1) An exhaust gas temperature of  $T_g = 270$  °C and a convective heat transfer coefficient of  $h_g = 80$  W/m<sup>2</sup>K were taken as the thermal boundary conditions for the hot side located on the outer surface of the aluminum block (Appendix A).
- 2) A cooling water temperature of  $T_c = 25$  °C and a convective heat transfer coefficient of  $h_c = 20,000$  W/m<sup>2</sup>K were taken as the thermal boundary conditions for the cold side located on the inner side of the copper cooling pipe (Appendix A).
- 3) Convection and radiation heat transfer was neglected for all other surfaces and was set to be adiabatic.
- 4) The thermal and electrical contact resistivities are assumed to be  $\rho_{th\_cont} = 8 \times 10^{-4}$  K.m<sup>2</sup>/W and  $\rho_{ele\_cont} = 5 \times 10^{-9}$  Ω.m<sup>2</sup> as in the analytical model [3,50].
- 5) The voltage on the outer side of the N-type copper conductor was grounded, while the outer side of the P-type copper conductor was set to the half the open circuit voltage value of the specific couple dimensions to ensure maximum power point operation.

- 6) The cross-sectional area of the copper cooling pipe was given displacement boundary conditions and only fixed in the axial direction, while all other parts were assumed to be free and connected via bonded-type contacts.
- 7) To set the cyclic symmetry effect for the  $1^\circ$  angle wedge-shaped model, the frictionless support boundary condition was set for both wedge sides for all the parts.

#### **4.4.6. Model verification**

The thermoelectric component of the 3D coupled model was verified against the analytical model. This verification consisted of a comparison that included the effects of the hot- and cold-side heat exchangers, the electrical and thermal contact resistances, except the electrical and thermal resistances of the metallic conductors, the thermal interface materials, and the solder. A comparison of the output voltage and the output power (Fig. 5) reveals that the 3D coupled model's thermoelectric predictions are in agreement with those of the analytical model. In order to verify the 3D coupled modelling thermal stresses analysis system, the study conducted by [56] was used, and the segmented TEG couple geometry, material properties, and boundary conditions were input to the current coupled model. As shown in Figs. 6a and 6b, the von-Mises stresses and the voltages along L1 were nearly identical between the previous study and current model, which verifies the predictive reliability of the current 3D coupled model.

#### **4.5. Results and discussion**

The maps generated (Fig. 7, 8, 9, and 10) by the analytical model compare the two couple configurations at different TE ring dimensions, with  $t/D_i$  being changed from 0.01 to 1, and  $D_o/D_i$  being changed from 1.02 to 3. Accordingly, the axial thickness and outer diameter values range from 0.079 mm to 7.9 mm and 8.058 mm to 23.7 mm, respectively. To help make the analytical

model results easier to grasp, the power output ratio maps have been divided into four square areas (A, B, D, and C), starting from the bottom left corner moving to the right, and then from the top left corner moving to the right (Fig. 10). The  $t/D_i$  range for areas A and B spans from 0.01 to 0.5, while C and D span from 0.5 to 1; the  $D_o/D_i$  range for areas A and C spans from 1.02 to 2, while the range for B and D spans from 2 to 3. The grey areas in the resistance and power output maps present a ratio of the radial-to-axial configuration values and are located where the radial couple values are higher than those of the axial design.

#### **4.5.1. The effect of the ATEG couple configuration on performance**

Internal resistance (thermal or electrical) is critical to the performance of an ATEG couple that has been integrated into a heat exchanger with given constant hot-side gas ( $T_g$ ) and cold-side water ( $T_w$ ) temperatures and heat exchanger thermal resistances. The couple's thermal resistance determines the temperature difference across it ( $T_h$  and  $T_c$ ), hence the heat flow and power output. However, thermal resistance does not only depend on the resistivity and geometry of the TE material; rather, it also depends on the Peltier heat flow—which is partly a function of the Seebeck coefficient—the current, and the  $T_h$  and  $T_c$  across the couple. As seen in Fig. 2a, the Peltier effect acts as a parallel resistance to the couple's actual thermal resistance and can account for up to 20% of the couple's actual thermal resistance effect. This gives the couple a total effective thermal resistance of less than its actual thermal resistance while in operation. The joule heating component has a very small effect on the heat flow; however, it must not be neglected when considering electrical power, as it accounts around 50% of the produced electrical power. Fig. 7 shows the internal ATEG couple resistance ratio,  $R_{TEG R}/R_{TEG A}$  (Equation 11), of the radial-to-axial configuration for different diameter (X-axis) and thickness ratios (Y-axis). The two ATEG couple configurations were found to have the same internal resistance along a diagonal line (unity line),

which splits the map into two areas. In the area under the unity line (the bottom right of the map, coloured grey), the radial configuration has a higher internal resistance, which yields a small thickness ratio and a high diameter ratio. That is, the  $R_{TEG R}/R_{TEG A}$  ratio increases as the  $t/D_i$  decreases for all  $D_o/D_i$ . Conversely, in the area above the unity line (the top left area of the map), the internal resistance of the axial couple configuration is higher than the radial configuration.

The ATEG couple Fig. 2a, is a thermal resistance in a thermal circuit formed between hot-side and cold-side heat exchangers. The  $T_h$  and  $T_c$  across the ATEG couple are affected by the ratio of the couple's thermal resistance ( $R_{TEG}$ ) to the total thermal resistance of the heat exchanger ( $R_{HX}$ ) hence, the module's power output. For a given ATEG couple configuration, it has been reported that the  $P_{max}$  reaches its maximum value when  $R_{TEG}/R_{HX} = 1$  as the ATEG dimensions change [49]. Figs. 8b and 9b respectively map the  $R_{TEG}/R_{HX}$  and the  $\Delta T$  for the radial (dash lines) and axial (solid lines) couple configurations for different diameter (X-axis) and thickness ratios (Y-axis), with  $h_g = 80 \text{ W/m}^2\text{K}$ . As these maps show, the  $R_{TEG}/R_{HX}$  significantly affect the couple's performance, as the trends for temperature differences across both ATEG couple configurations match the trends for the  $R_{TEG}/R_{HX}$ .

Fig.10b maps the radial/axial configuration electrical maximum power output ratio ( $P_{R max}/P_{A max}$ ), with  $h_g = 80\text{W/m}^2\text{K}$  for different diameter ratios (X-axis) and thickness ratios (Y-axis). The hatched regions are those where the electrical current produced by the ATEG exceeds 10 A; the borders of these regions are labelled with 10 A. The hatched region on the top right corner is the current generated by the axial couple configuration, while the other hatched part is the current generated by the radial couple configuration. 10 A is assumed as an upper limit for being able to efficiently handle the power generated by the ATEG module. Both configurations were found to generate the same power along the diagonal line as where the internal thermal, electrical

resistances and the temperature difference across both configurations are the same. In squares A and B, the  $P_{R \max}/P_{A \max}$  ratio follows the  $R_{TEG R}/R_{TEG A}$  ratio. The only part of the map in which the axial couple configuration generates more power is above the unity line in square A. In this region, the axial couple is capable of generating 5 times more power than the radial couple configuration due to having a higher  $\Delta T$  throughout. As the  $t/D_i$  decreases in square B, the  $P_{R \max}/P_{A \max}$  ratio increases until it reaches 32; this trend follows the  $R_{TEG R}/R_{TEG A}$  ratio, as the  $\Delta T$  increases across the radial couple configuration, but decreases across the axial couple configuration. In square D, both configurations generate the same power, as they have a  $\Delta T$  that is similar that shown in Fig. 9b. However, the  $\Delta T$  across the axial couple configuration is higher at the top part of square C. Here, the radial couple configuration generates nearly twice as much power as the axial couple configuration because the  $R_{TEG R}/R_{HX}$  ratio is closer to 1 than the  $R_{TEG A}/R_{HX}$  ratio (Fig. 8b).

#### **4.5.2. The effect of hot-side thermal resistance on the performance of the two couple configurations**

The increase in the  $h_g$  value translates to a decrease in the total thermal resistances of the hot-side and the cold-side, as the thermal resistance of the hot-side heat exchanger is dominant. Figs. 10a, 10b, and 10c map the  $P_{R \max}/P_{A \max}$  as the  $D_o/D_i$  (X-axis) and the  $t/D_i$  (Y-axis) is changed to  $h_g = 40, 80,$  and  $160 \text{ W/m}^2\text{K}$ , respectively. The  $P_{R \max}/P_{A \max}$  remains unaffected by the changes to  $h_g$  in squares A and B, with the trends following the  $R_{TEG R}/R_{TEG A}$  ratio as shown in Fig. 8. The radial configuration begins to generate more power than the axial configuration as the  $h_g$  increases from 40 to  $160 \text{ W/m}^2\text{K}$  at the top part of square C, while the  $P_{R \max}/P_{A \max}$  is close to 1 in square D. The results for the three  $h_g$  values in Fig. 8 show that the  $R_{TEG R}/R_{HX}$  ratio moves closer to 1; in contrast, the  $R_{TEG A}/R_{HX}$  ratio deviates from 1 in square C, which is not the case for the three other

squares. Accordingly, as the  $h_g$  increases, the radial couple configuration generates more power than the axial couple configuration for most of the tested range for  $D_o/D_i$  and  $t/D_i$ .

#### 4.5.3. Thermal stresses vs performance:

Fig. 11 shows the 16 points of interest that were selected to be modelled using the 3D coupled finite element model and compared for maximum thermal stresses. Of these 16 points, six points where the radial configuration generates more power than the axial configuration, four points fall along the line where both configurations generate the same power, and six points where the axial configuration generates more power than the radial configuration. All of the selected points produce an electrical current of less than 10 A for both configurations when operating at maximum power. The convection heat transfer coefficient for this comparison was  $h_g = 80 \text{ W/m}^2\text{K}$ .

Figs. 12a and 12b respectively map the  $\Delta T$  across the axial and radial couple configurations for the different  $D_o/D_i$  and  $t/D_i$  obtained using the 16 selected points. Both maps show the same trends and values as the  $\Delta T$  map produced by the analytical model (Fig. 9b). As shown in Fig. 12a, the  $\Delta T$  of the axial configuration decreases when the  $D_o/D_i$  increases, and increases in response to increases in  $t/D_i$ . Additionally, the couple thermal resistance in the axial direction decreases as the  $D_o/D_i$  increases, but decreases alongside the  $t/D_i$ . However, increases in  $t$  result in decreased thermal resistance in both heat exchangers due to a greater increase in resistance along the axial direction, which in turn results in an increase in  $\Delta T$ . As a result, a wide range of  $\Delta T$  values were obtained for the axial configuration, with a maximum  $\Delta T$  of  $189.2 \text{ }^\circ\text{C}$  being obtained when  $D_o = 10 \text{ mm}$  and  $t = 4 \text{ mm}$ , and a minimum  $\Delta T$  of  $14.8 \text{ }^\circ\text{C}$  being obtained when  $D_o = 16 \text{ mm}$  and  $t = 1 \text{ mm}$ . In the case of the radial couple configuration, increases in the  $D_o/D_i$  resulted in increases in  $\Delta T$ ; however, the  $t/D_i$  did not affect the  $\Delta T$ , as the thermal resistances of the heat exchangers

changed in proportion to the resistance along the radial direction when  $t$  was changed (Fig. 12b). Accordingly, changes in dimensions resulted in a narrower range of  $\Delta T$  values for the radial couple configuration, with a maximum  $\Delta T$  of 111.2 °C being obtained when  $D_o = 16$  mm and  $t = 1$  mm, and a minimum  $\Delta T$  of 49.7 °C being obtained when  $D_o = 10$  mm and  $t = 4$  mm.

Figs. 13a and 13b respectively map the maximum principal stress,  $\sigma$ , for the axial and radial configurations in response to changes in the  $D_o/D_i$  (X-axis) and the  $t/D_i$  (Y-axis). Since the small difference in the thermal expansion (CTE) coefficient between the N- and the P-type rings resulted in nearly identical  $\sigma$  values for both, only the N-type ring results are presented. Across both ATEG couple configurations, the increases in the  $\sigma$  were the result of increases in the  $\Delta T$  (Fig. 12). In addition, the trends of the  $\sigma$  generally followed those of the  $\Delta T$ , with some deviation occurring due to the effect of other couple components and the mismatches in their coefficients of thermal expansion (CTE). Although the axial configuration had wider and higher  $\Delta T$  values (Fig. 12), the radial configuration had higher  $\sigma$  values. Whereas the maximum  $\sigma$  in the axial couple configuration was 146.7 MPa at a  $\Delta T = 117.8$  °C, the radial configuration had a maximum  $\sigma$  of 190.2 MPa at a  $\Delta T = 104.8$  °C. This result was largely attributable to the radial-wise direction of the temperature gradient in the TE rings in the radial couple configuration, which produced additional tensile hoop stresses due to the rings' closed geometry in addition to the thermal stresses due to the CTE mismatch. Figs. 14a and 14b respectively map the maximum power generated for the axial and radial configurations in response to changes in the  $D_o/D_i$  (X-axis) and the  $t/D_i$  (Y-axis). As can be seen, the amount of power generated increased as couple volume increased for both configurations. The axial couple configuration had the lowest  $\sigma$ , at 67.8 MPa for a  $D_o$  and  $t$  of 16 mm and 1 mm, respectively, with a  $\Delta T = 14.8$  °C and 10.4 mW of power generated per couple. The radial couple configuration produced 5.2 times more power ( $P_{\max R} = 54.4$  mW) than the axial configuration at

the same dimensions, but it also had an  $\sigma$  of 180.8 MPa, which was 2.6 times the maximum principal stress. Table 3 presents the values of  $\Delta T$ , the electrical current, the maximum power, and the maximum principal stress where the axial and radial couple configurations produce the same power. At each point, both configurations have almost the same  $\Delta T$ , electrical current, and maximum power, though the  $\sigma$  is always lower in the axial couple configuration. In addition, the increase in power generated is accompanied by an increase in  $\sigma$  due to an increase in  $\Delta T$  across the ATEG couple.

Figs. 15a and 15b map the temperature contours of the axial and the radial couple configurations, respectively, when  $D_o = 16$  mm and  $t = 1$  mm. The copper conductors connected to the aluminum block in the axial couple configuration deliver heat flow to the sides of the P- and the N-type rings, where it flows axially to the middle conductor to be conducted to the cooling pipe. In the radial configuration, the copper conductors on the outer and inner diameters respectively deliver and dissipate the heat in a radial direction. Figs. 16a and 16b map the maximum principal stress contours in the axial and the radial couple configurations, respectively, when  $D_o = 16$  mm and  $t = 1$  mm. As reported by Turenne et al. [34], all of the maximum principal stress values were located at the corners of the interface between the solder and the TE rings due to the CTE mismatch between them. The solder underwent plastic deformation as the stresses at the interface exceeded its yield strength (26 MPa), which helped to release the maximum amount of thermal stresses at these locations. The maximum and minimum thermal stress values in the radial couple configuration occurred at the inside and the outside diameters of the TE rings, respectively, which was largely due to the additional tensile hoop stresses caused by the closed ring geometry of the TE rings. The maximum thermal stress value could result in cracking along the TE ring's axial thickness at the inside diameter, causing it to separate from the cold side copper



conductors. However, there are two spots at which maximum thermal stress values may lead to diagonal cracking in the TE rings used in the axial couple configuration.

#### **4.6. Conclusion**

This paper investigated how heat flow/electrical current paths affect the performance and thermal stress fields in ATEG couples. To this end, radial and axial ATEG couple configurations using P- and N-Type Bi<sub>2</sub>Te<sub>3</sub> rings with a wide range of thickness-to-outer-diameter ratios were compared. An analytical model was used to compare the thermoelectric performances of both configurations at different dimensions, as well as how the thermal resistance of the hot-side heat exchanger - by changing the exhaust gas convective coefficient ( $h_g = 40, 80, \text{ and } 160 \text{ W/m}^2\text{K}$ )- affects their performance. ANSYS workbench was then used to build a 3D coupled finite element model, which provided detailed temperature and thermal stress fields for both ATEG couple configurations. Thermal and electrical contact resistance was considered in both models, while the thermal interface material, solder, and their mechanical behaviours were considered in the finite element model to obtain a more accurate understanding of the ATEG couples' behaviour. The current investigation produced the following key findings:

- 1- The heat flow and electrical current paths determine the couple's internal resistance, which in turn determines its  $\Delta T$  and the temperature field hence the couple's power output and thermal stresses.
- 2- The  $R_{TEG}$  values and  $R_{TEG}/R_{HX}$  ratio are critical for ATEG couples installed between hot- and cold-side heat exchangers, as they determine the temperature difference across the couple, and thus, its power output.

- 3- As the thermal resistance of the hot-side heat exchanger decreases due to an increase in the convective heat transfer coefficient, the radial couple configuration generates more power than the axial couple configuration for the tested range of  $D_o/D_i$  and  $t/D_i$ .
- 4- The increase in  $\Delta T$  lead to increases in both power and thermal stresses across both ATEG couple configurations.
- 5- The thermal stress values in the radial couple configuration decreased alongside the  $D_o/D_i$  and the  $t/D_i$ ; in contrast, the thermal stresses in the axial design decreased when the  $D_o/D_i$  increased, and the  $t/D_i$  decreased.
- 6- The formation of tensile hoop stresses caused the radial configuration to have thermal stresses that were as much as 67 MPa higher than those in the axial configuration when both were generating the same power at  $\Delta T = 105\text{ }^\circ\text{C}$ .
- 7- The axial couple configuration had the lowest  $\sigma$  at 67.8 MPa, with a  $D_o$  of 16 mm, a  $t$  of 1 mm, a  $\Delta T$  of 14.8  $^\circ\text{C}$ , and power generation of 10.4 mW per couple.
- 8- The maximum thermal stress values were located at the corners of the interface between the solder and the TE rings due to mismatched CTE; at these points, the solder layer undergoes plastic deformation, which releases some of the thermal stresses.

#### 4.7. Appendix A. – Analytical and finite element models details

Hot-side heat transfer coefficient ( $h_g$ ):

The heat transfer coefficient values for the hot-side heat exchanger that was used a boundary condition in both the analytical and the 3D ANSYS finite element model are effective values. These values include only the thermal resistance of the fin array and its efficiency used to increase the surface area facing the hot-side exhaust gases while the fin base thermal resistances were calculated in the models as it changes with changing the ATEG couple outer diameter ( $D_o$ ). The hot-side heat exchanger design, dimensions and exhaust gas flow rate values are chosen following the design found in previous work Zaher [49]. Fig. 17 show a CAD drawing for the hot-side fin array including the dimensions of the aluminum fins, fin spacing and fin aluminum base. The exhaust flow rate used is 0.06 kg/s as it is considered to be coming form a commercial pizza oven. The fin spacing was changed in a range from 0.5 to 5 mm to determine and calculate the different effective hot-side heat transfer coefficients. The exhaust gas temperature is 270 °C and convective fin tip condition was assumed. The fin thermal resistance could be calculated as follows:

$$R_{th\ fin} = \frac{1}{\eta_{fin} A_{fins} h_{gas}} + \frac{1}{A_{base} h_{gas}} \quad (24)$$

$$\eta_{fin} = \frac{\tanh(m L_{cr})}{m L_{cr}} \quad (25)$$

where  $\eta_{fin}$  is the fin efficiency,  $A_{fins}$  is the total surface area of fins,  $A_{base}$  is the un-fined portion of the aluminum fin base area,  $h_{gas}$  is the calculated exhaust gas heat transfer coefficient,  $L_{cr}$  is the fin corrected length that includes the added tip area and  $m^2 = (h_{gas} p) / (k A_c)$ ,  $p$  and  $A_c$  are the fin perimeter and cross sectional area, respectively. The flow is found to be laminar for the given exhaust gas flow rate and range of fin spacing by calculating the Reynolds number as follows:

$$Re = \frac{\rho_{air} v_{air} D_h}{\mu_{air}} \quad (26)$$

$$D_h = \frac{4 A_c}{p} \quad (28)$$

The entrance length was considered in calculated the Nusselt number ( $Nu_g$ ) for the laminar flow between two parallel plates and corrected for the channel aspect ratio ( $\alpha^*$ ) [] for uniform surface temperature as follows:

$$Nu_g = 7.541 \times (1 - 2.610 \alpha^* + 4.970 \alpha^{*2} - 5.119 \alpha^{*3} + 2.702 \alpha^{*4} - 0.548 \alpha^{*5}) \quad (29)$$

Then the Nusselt number was corrected to consider the combined thermal and velocity entry length for uniform surface temperature using Baehr and Stephan [] correlation using Graetz number ( $Gz_{Dh}$ ) as follows:

$$\overline{Nu}_{D_h} = \frac{\frac{Nu}{\tanh [2.264 (Gz_{D_h})^{-\frac{1}{3}} + 1.7(Gz_{D_h})^{-\frac{2}{3}}]} + 0.0499 Gz_{D_h} \tanh(Gz_{D_h})^{-1}}{\tanh(2.432 Pr^{\frac{1}{6}} Gz_{D_h}^{-\frac{1}{6}})} \quad (30)$$

$$Gz_{D_h} = \left(\frac{D_h}{x}\right) Re Pr \quad (31)$$

$$\overline{Nu}_{D_h} = \frac{h_{gas} D_h}{k_{gas}} \quad (32)$$

The effective heat transfer coefficient for the hot side ( $h_g$ ) equals to the reciprocal of the product of the fin thermal resistance and the surface area of the aluminum fin base ( $A_{fin\ base}$ ) as follows:

$$h_g = \frac{1}{A_{fin\ base} R_{th\ fins}} \quad (33)$$

Cold-side heat transfer coefficient ( $h_w$ ):

The cooling copper pipe is a round tube with an inner diameter ( $D_{i \text{ pipe}}$ ) of 4.72 mm and was kept as a constant value in the current work. The flow is turbulent as the flow rate is 10 LPM and water temperature of 25 °C [49]. The heat transfer coefficient of the cooling water was calculated using Dittus-Boelter equation with  $n = 0.4$  for heating condition as the heat is transferred to the cooling water as follows:

$$Nu_w = 0.023 Re^{0.8} Pr^{0.4} \quad (34)$$

$$Re = \frac{\rho_{water} v_{water} D_{i \text{ pipe}}}{\mu_{water}} \quad (35)$$

$$Nu_w = \frac{h_w D_{i \text{ pipe}}}{k_{water}}$$

#### 4.8. Figures and Tables

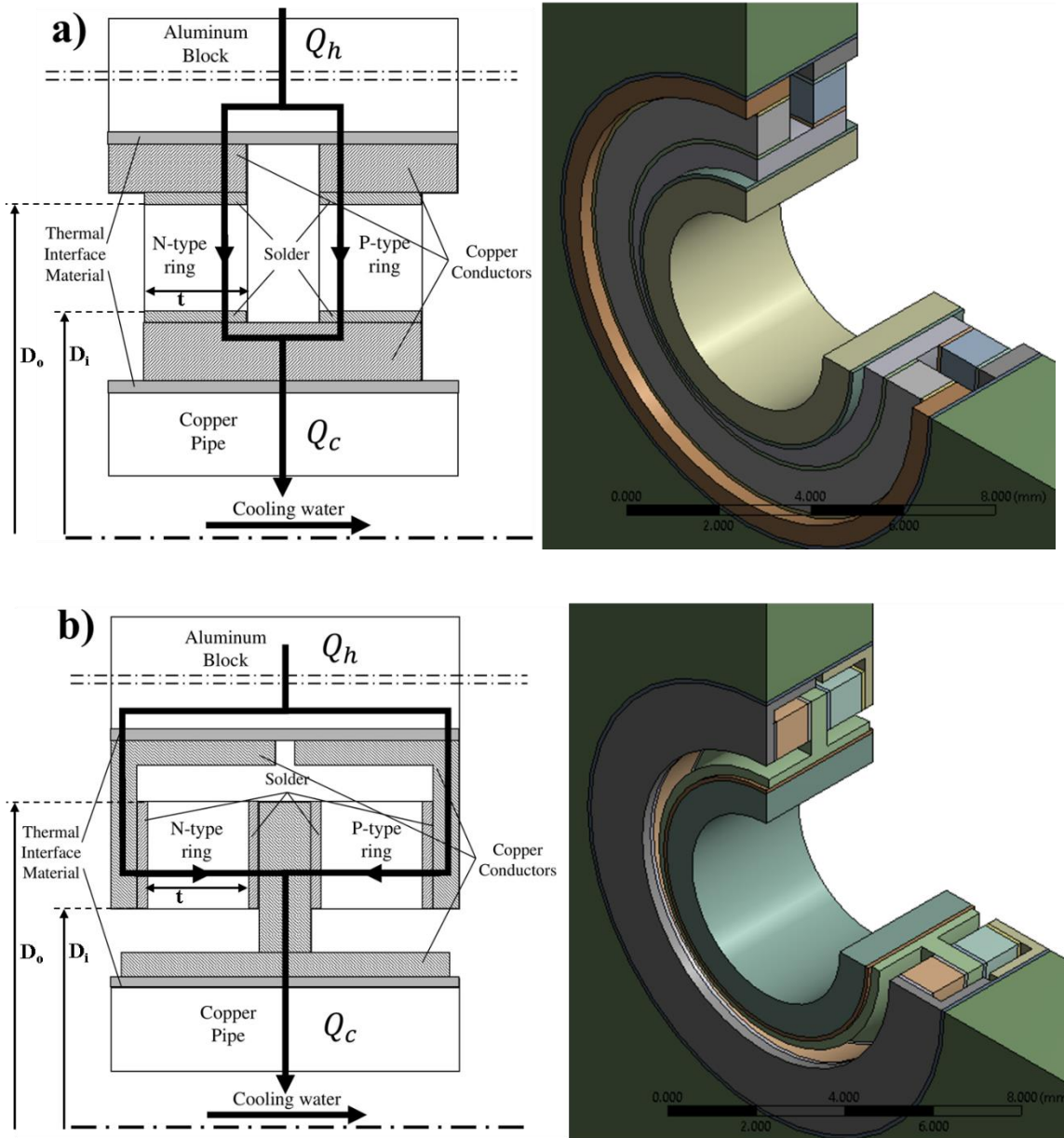


Fig. 1. The two ring-shaped ATEG couple configurations, a) Radial configuration b) Axial configuration.

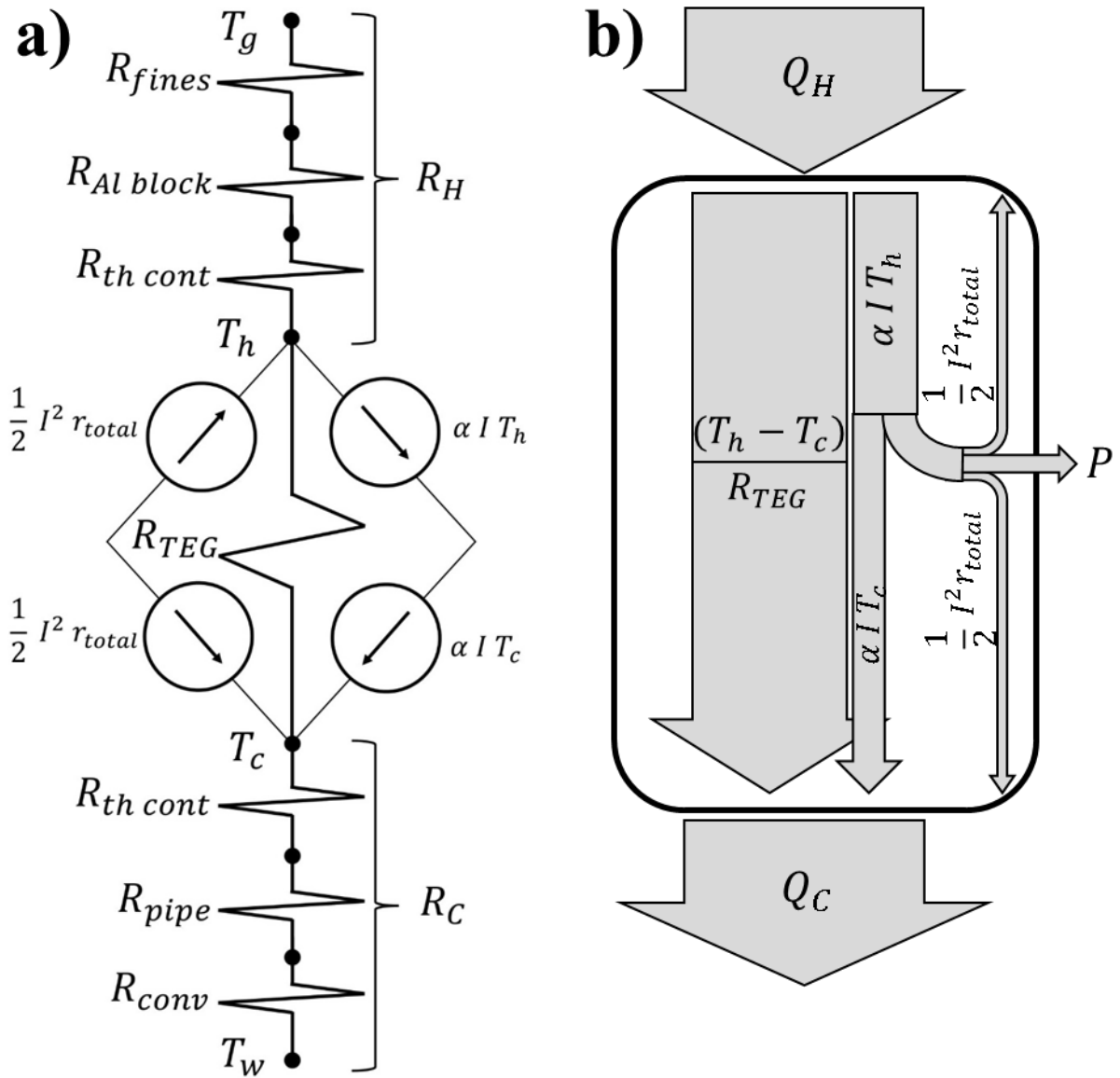


Fig. 2. a) Schematic of the ATEG couple in the thermal circuit including the hot-side and cold-side thermal resistances, b) Schematic of the different effects in the ATEG couple including; Fourier conduction, Peltier effect, and Joule heating.

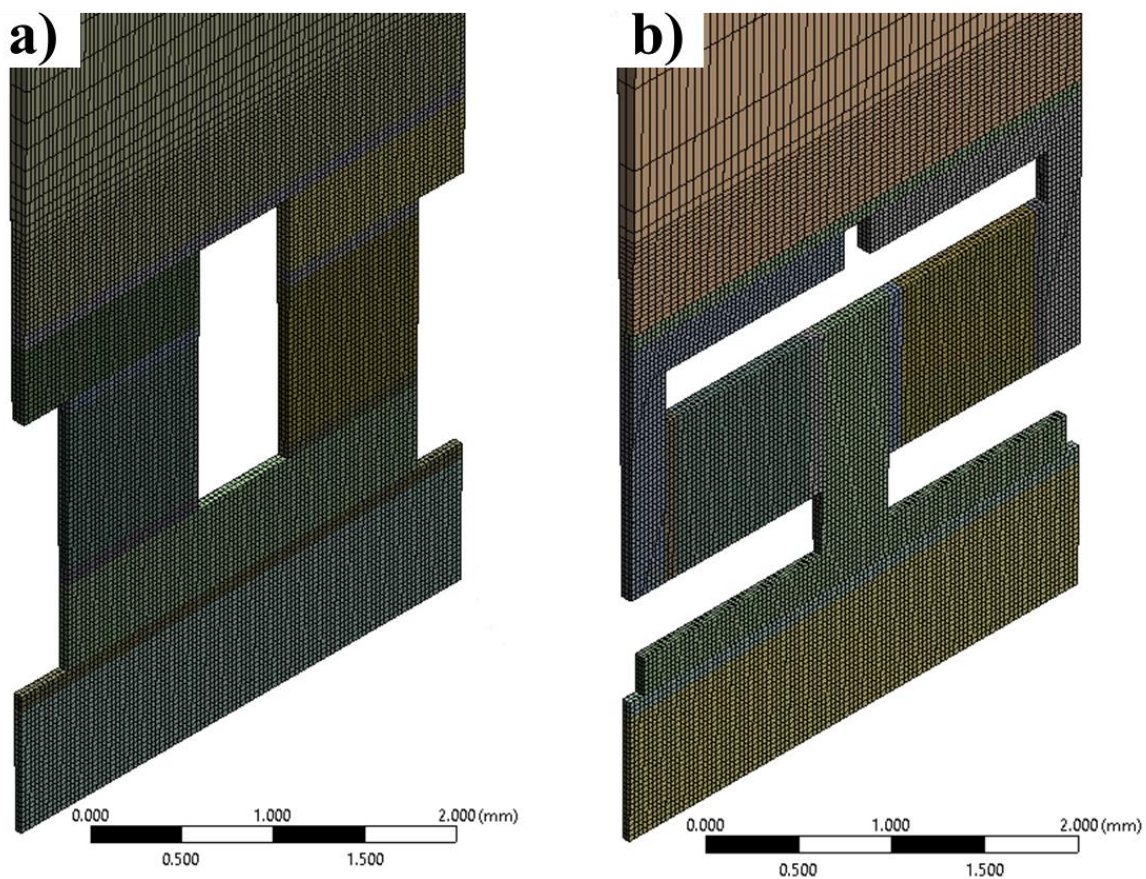


Fig. 3. The 1° wedge-shaped finite element module geometry with the quadratic mesh, a) Radial configuration b) Axial configuration.



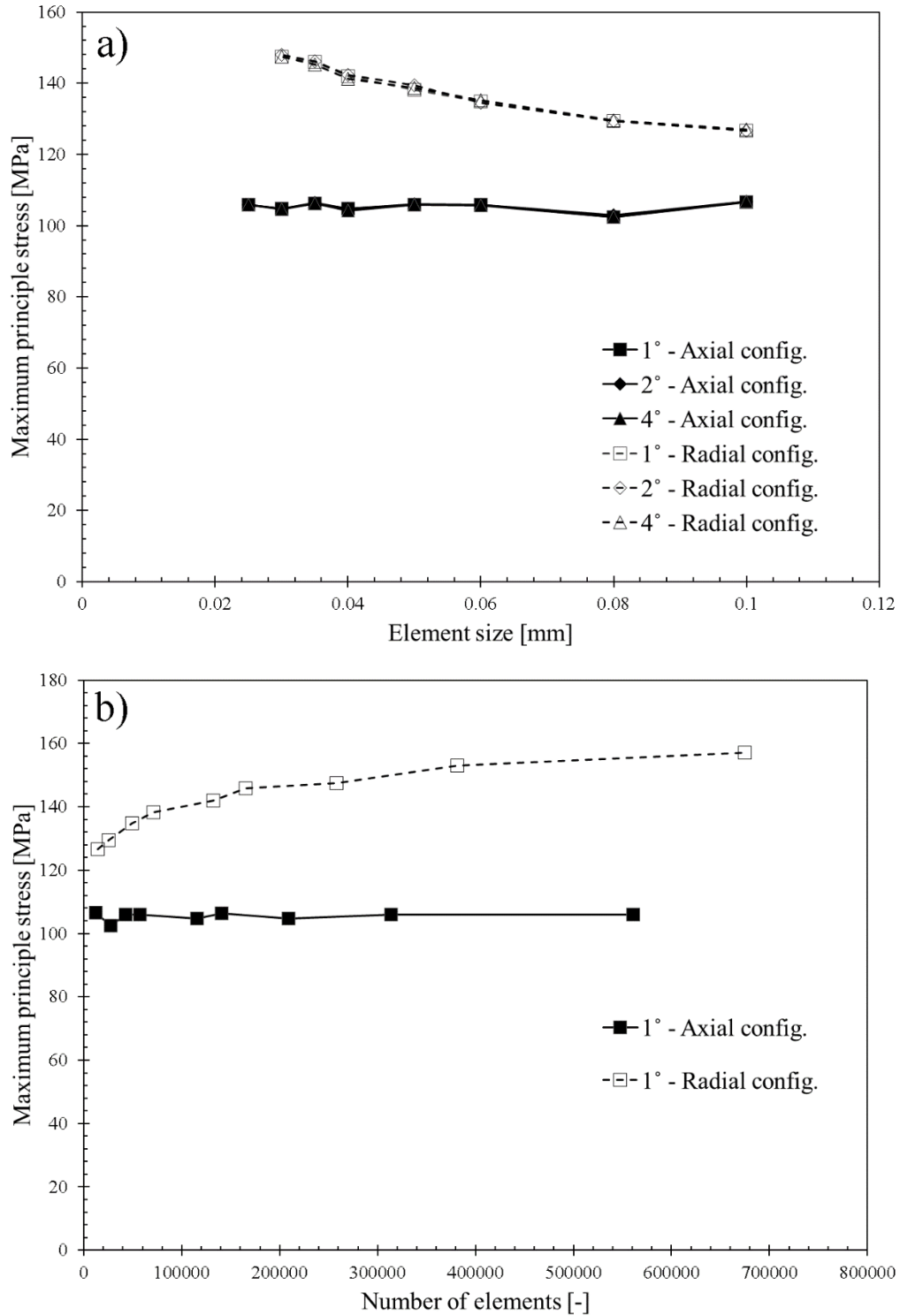


Fig. 4. Mesh independency test a) The maximum stress value of the maximum principal stress N-type TE ring of different wedge angles versus element size for the radial and axial configurations. b) The maximum stress value of the maximum principal stress N-type TE ring versus the total number of elements.

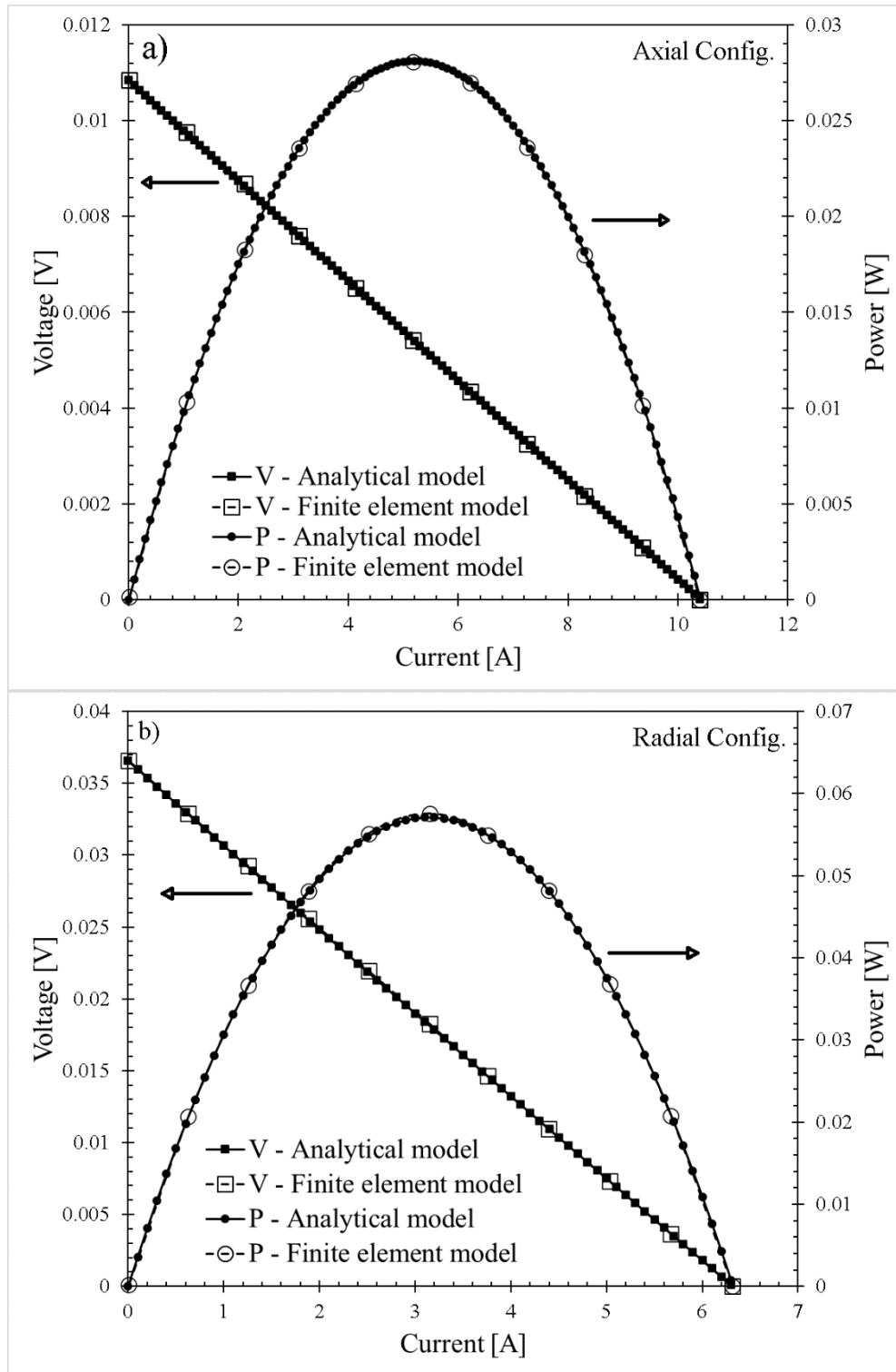


Fig. 5. The output power and the voltage of both the analytical and 3D finite element model, a) Axial configuration b) Radial configuration.

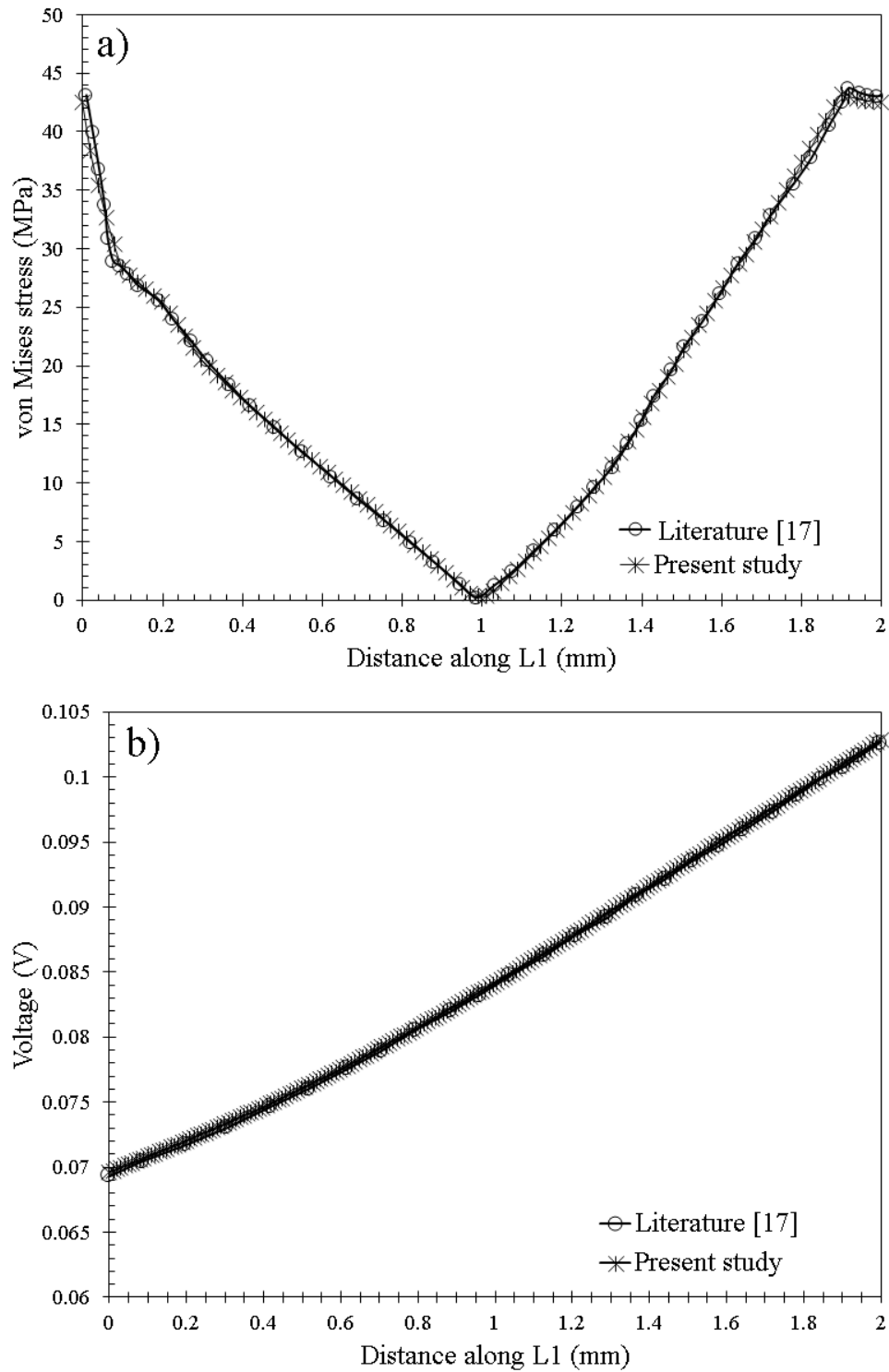


Fig. 6. Verification of present study's finite element model with literature [17]. a) The von-Mesis stress and b) the voltage along L1.

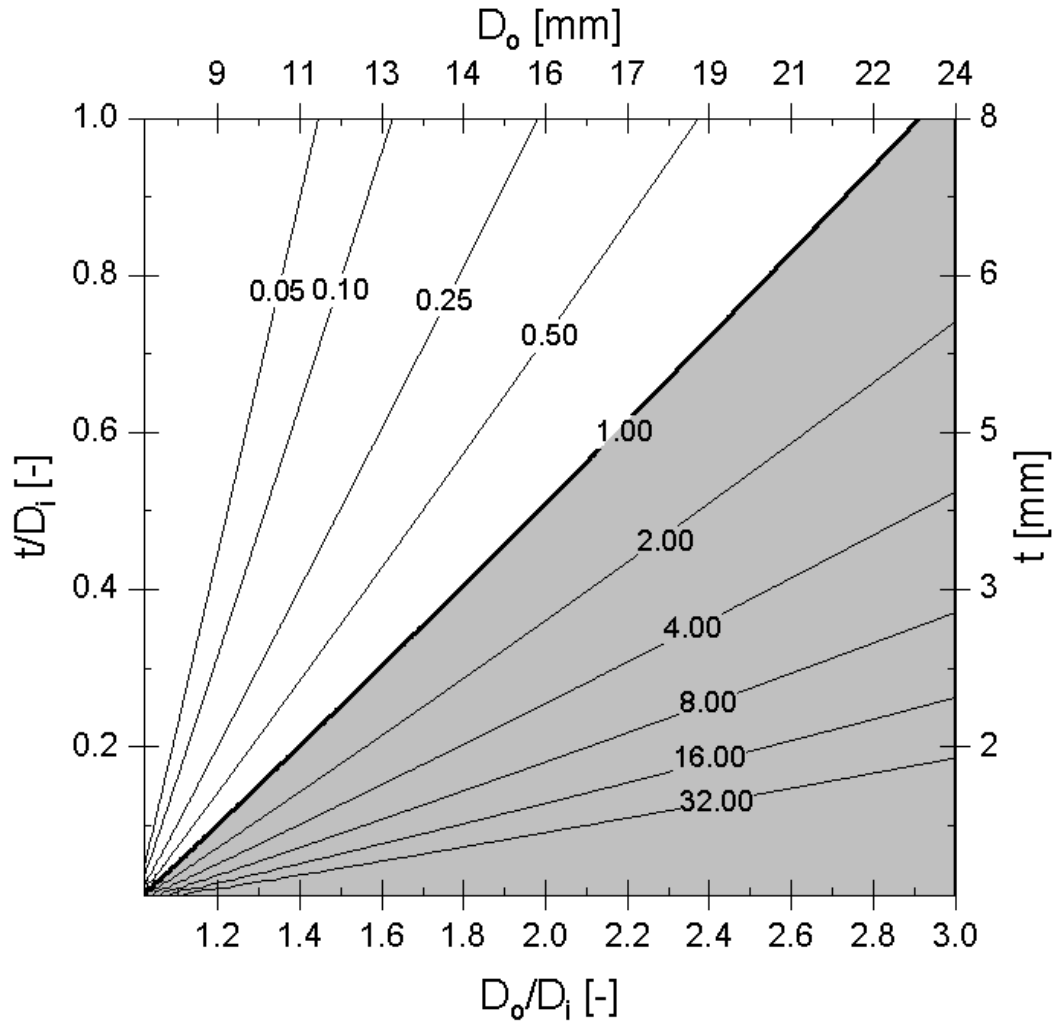


Fig. 7. The internal ATEG couple resistance ratio,  $R_{TEG R}/R_{TEG A}$ , of the radial-to-axial configuration for different diameter (X-axis) and thickness ratios (Y-axis).

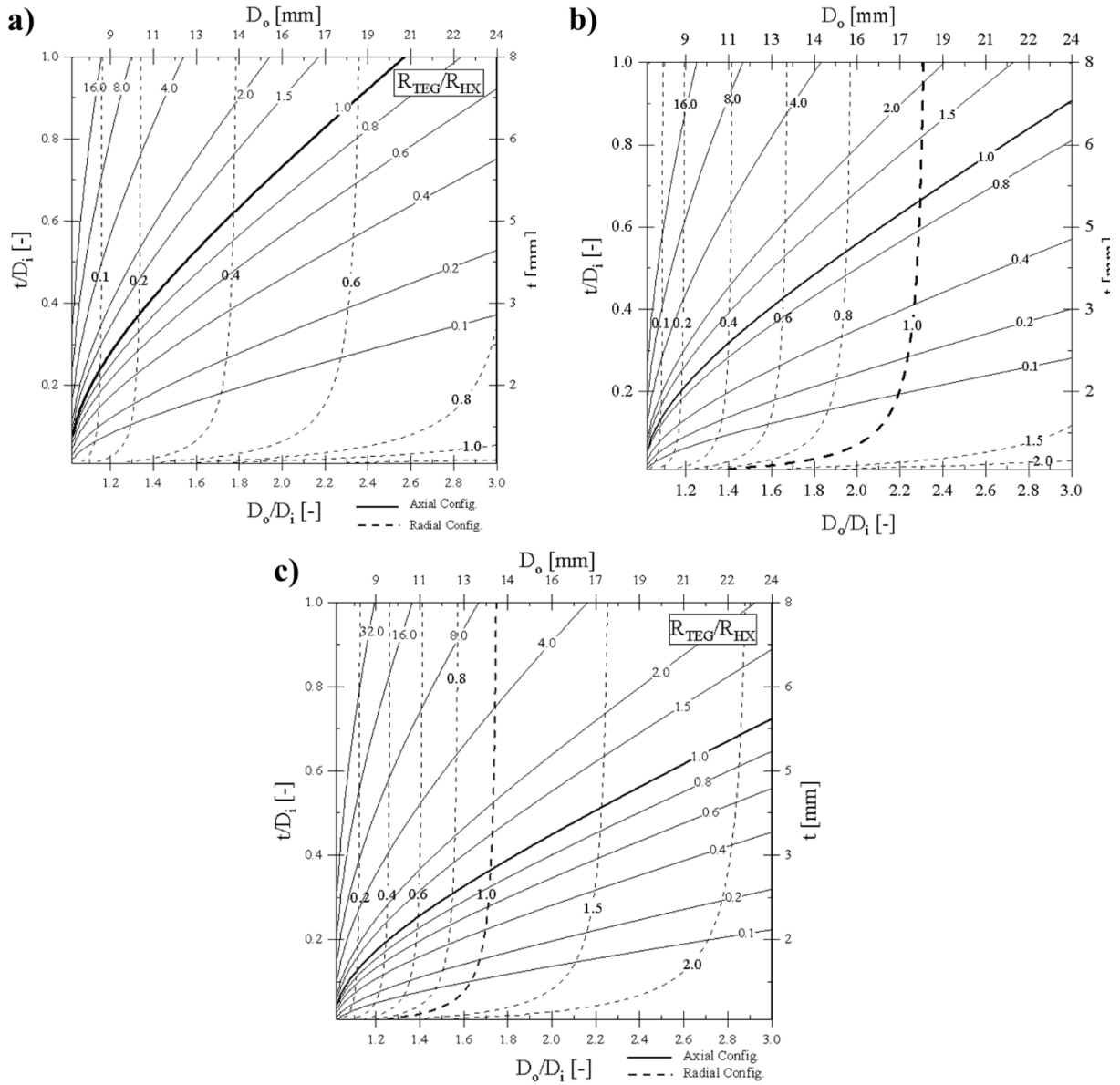


Fig. 8. The couple thermal resistance to the total heat exchanger resistance ratio,  $R_{TEG}/R_{HX}$ , for the radial (dash lines) and axial (solid lines) couple configurations for different diameter (X-axis) and thickness ratios (Y-axis), at a)  $h_g = 40 \text{ W/m}^2\text{K}$ , b)  $h_g = 80 \text{ W/m}^2\text{K}$ , and c)  $h_g = 160 \text{ W/m}^2\text{K}$ .

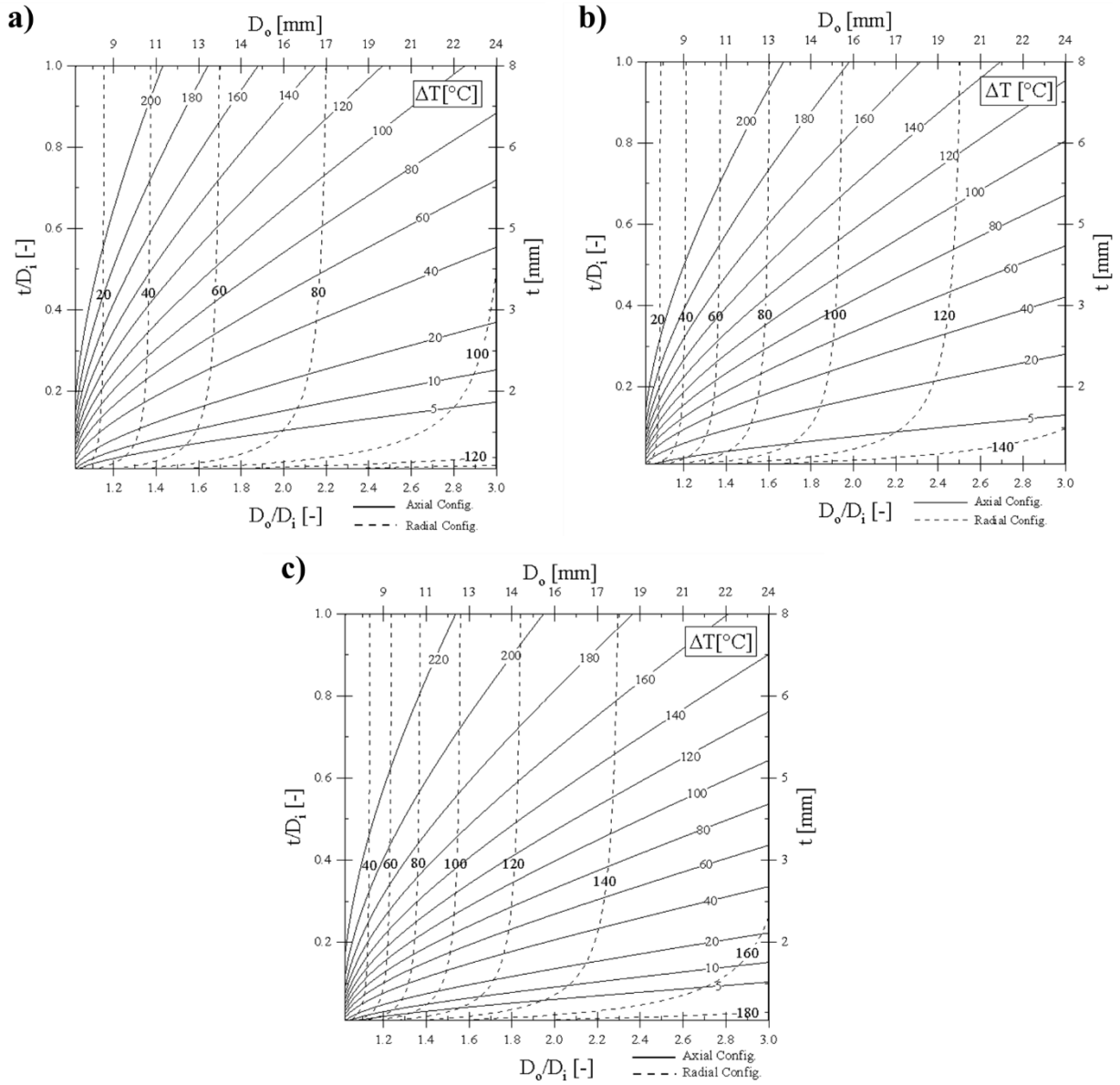


Fig. 9. The temperature difference across the ATEG couple,  $\Delta T$ , for the radial (dash lines) and axial (solid lines) couple configurations for different diameter (X-axis) and thickness ratios (Y-axis), at a)  $h_g = 40 \text{ W/m}^2\text{K}$ , b)  $h_g = 80 \text{ W/m}^2\text{K}$ , and c)  $h_g = 160 \text{ W/m}^2\text{K}$ .

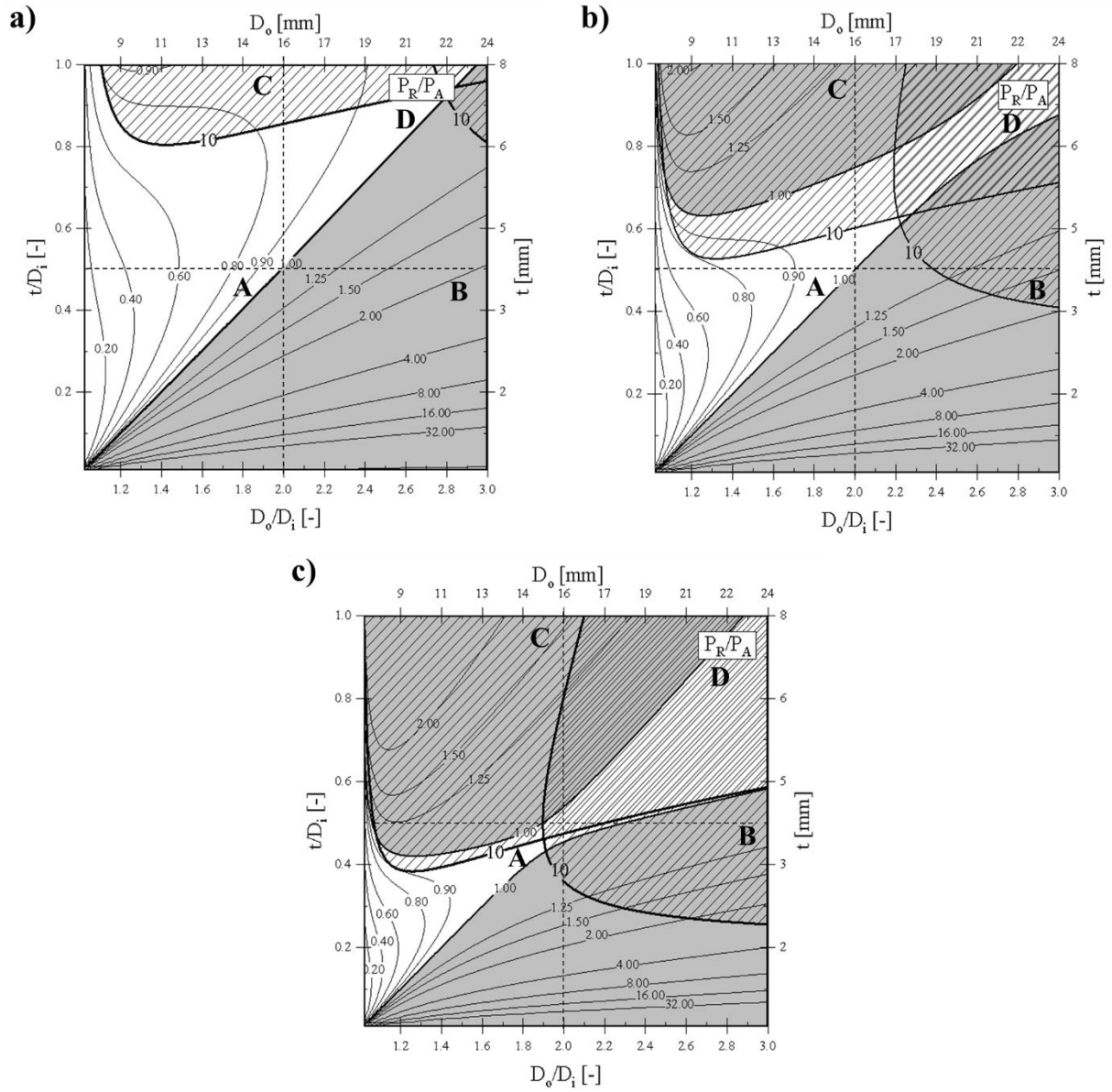


Fig. 10. The radial-to-axial couple configurations' output power ratio,  $P_R/P_A$ , of for different diameter (X-axis) and thickness ratios (Y-axis), at a)  $h_g = 40 \text{ W/m}^2\text{K}$ , b)  $h_g = 80 \text{ W/m}^2\text{K}$ , and c)  $h_g = 160 \text{ W/m}^2\text{K}$ .

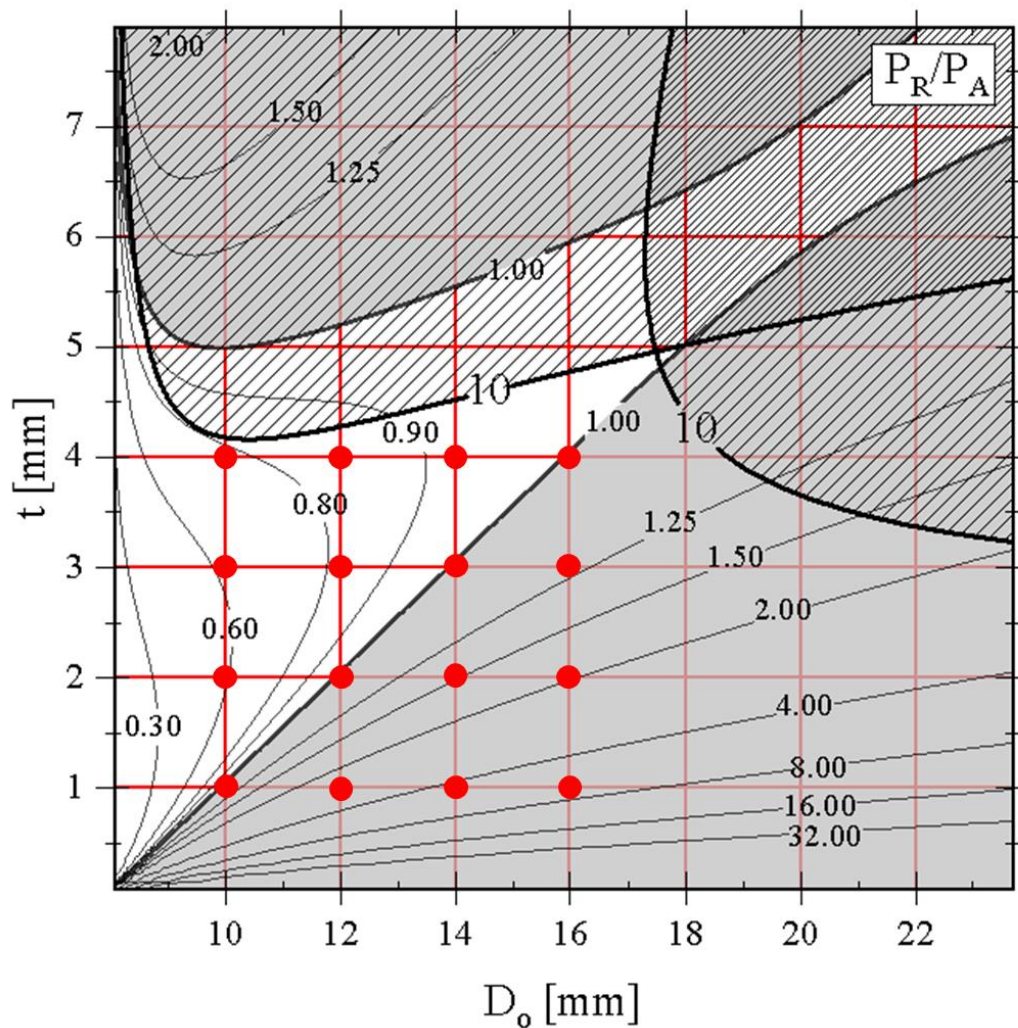


Fig. 11. The radial-to-axial couple configurations' output power ratio,  $P_R/P_A$ , of for different diameter (X-axis) and thickness ratios (Y-axis), at  $h_g = 80 \text{ W/m}^2\text{K}$ .



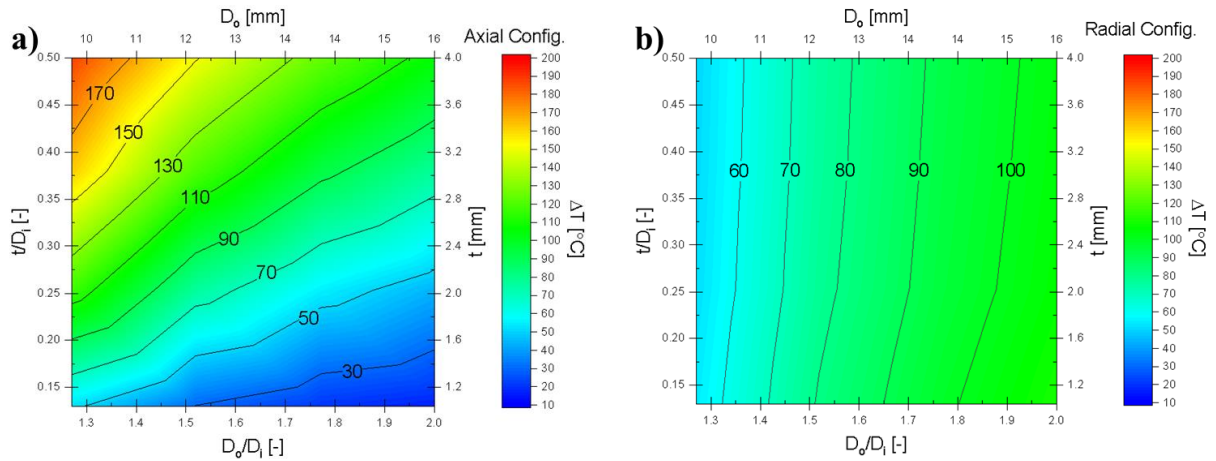


Fig. 12. The temperature difference across the ATEG couple,  $\Delta T$ , for a) the axial and b) the radial couple configurations of for different diameter (X-axis) and thickness ratios (Y-axis), at  $h_g = 80 \text{ W/m}^2\text{K}$ .

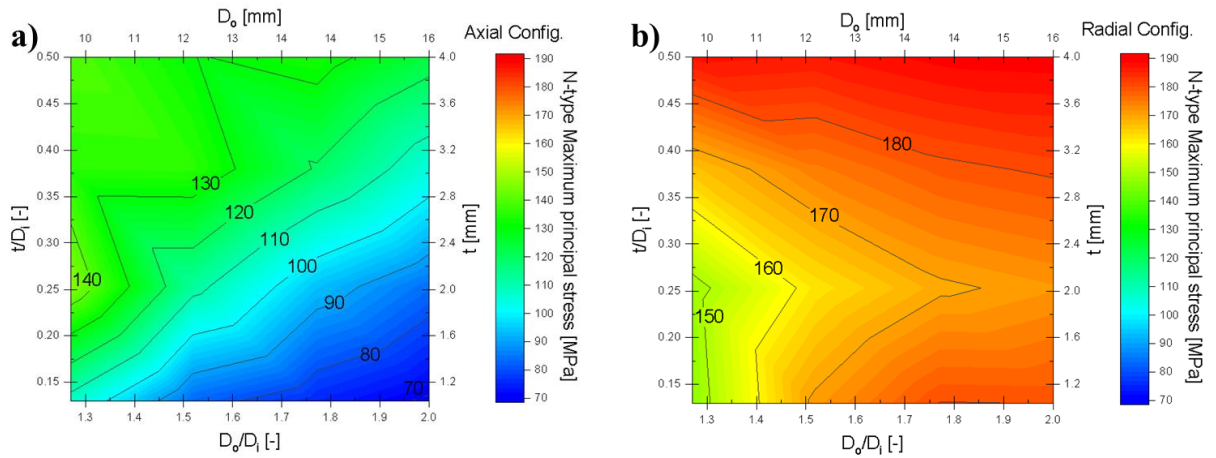


Fig. 13. The maximum principle stress in the N-type ring for a) the axial and b) the radial couple configurations of for different diameter (X-axis) and thickness ratios (Y-axis), at  $h_g = 80 \text{ W/m}^2\text{K}$ .

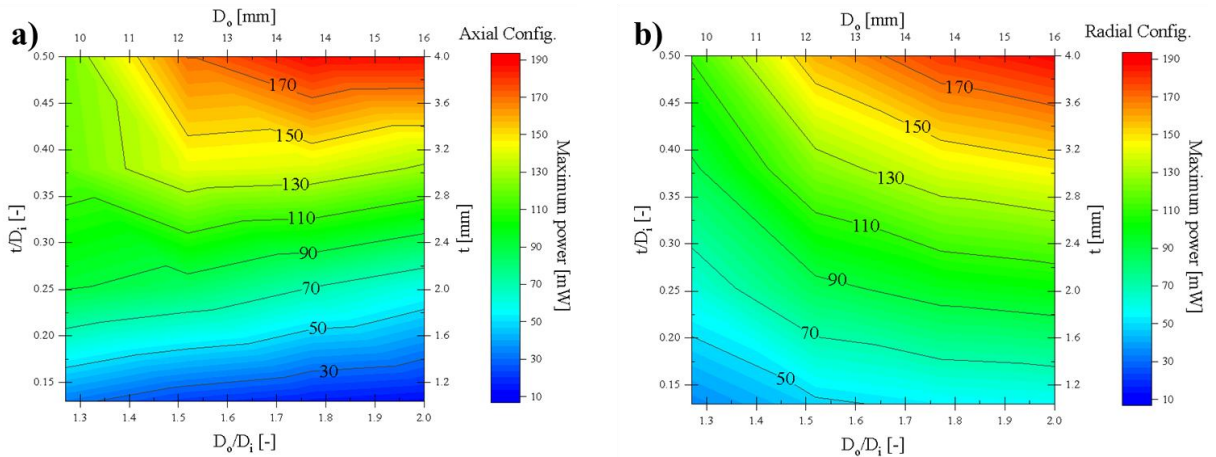


Fig. 14. The maximum output power for a) the axial and b) the radial couple configurations of for different diameter (X-axis) and thickness ratios (Y-axis), at  $h_g = 80 \text{ W/m}^2\text{K}$ .

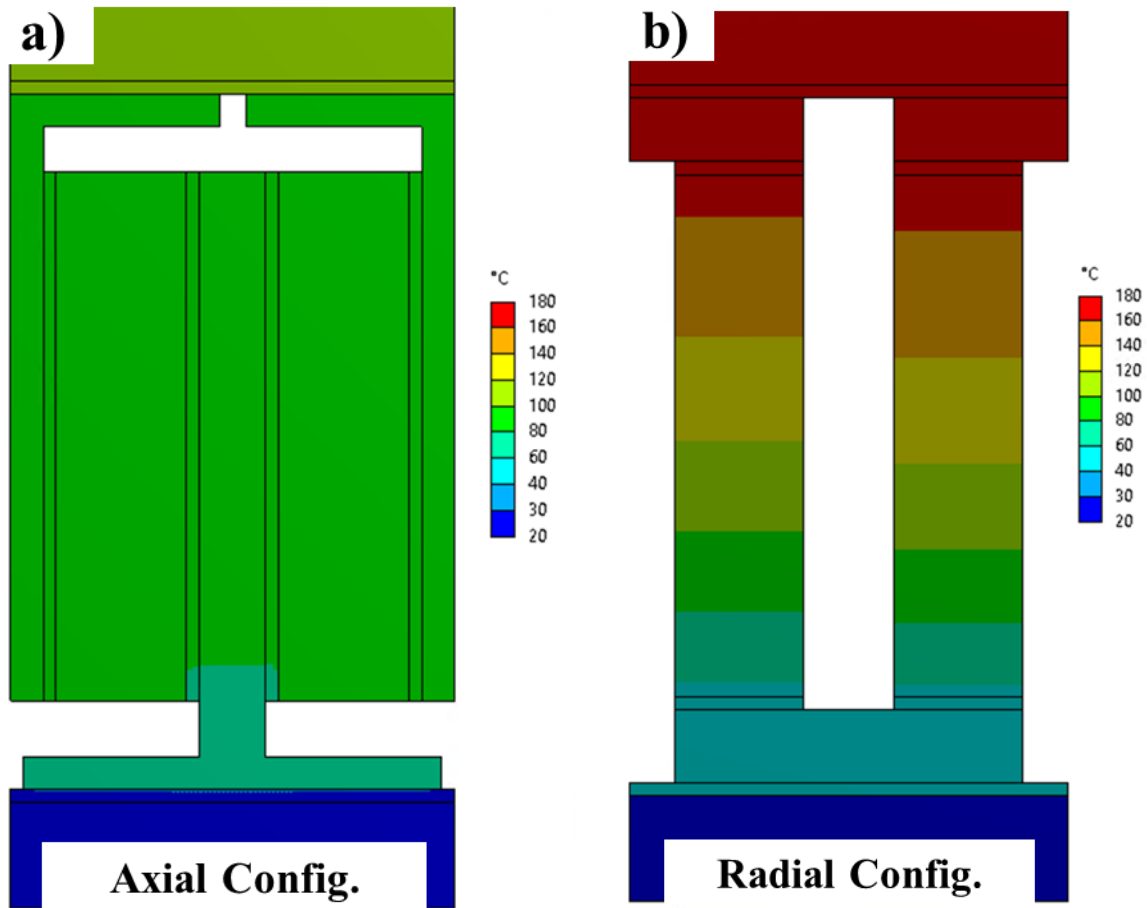


Fig. 15. The temperature contours of a) the axial and b) the radial couple configurations, respectively, when  $D_o = 16 \text{ mm}$  and  $t = 1 \text{ mm}$ .

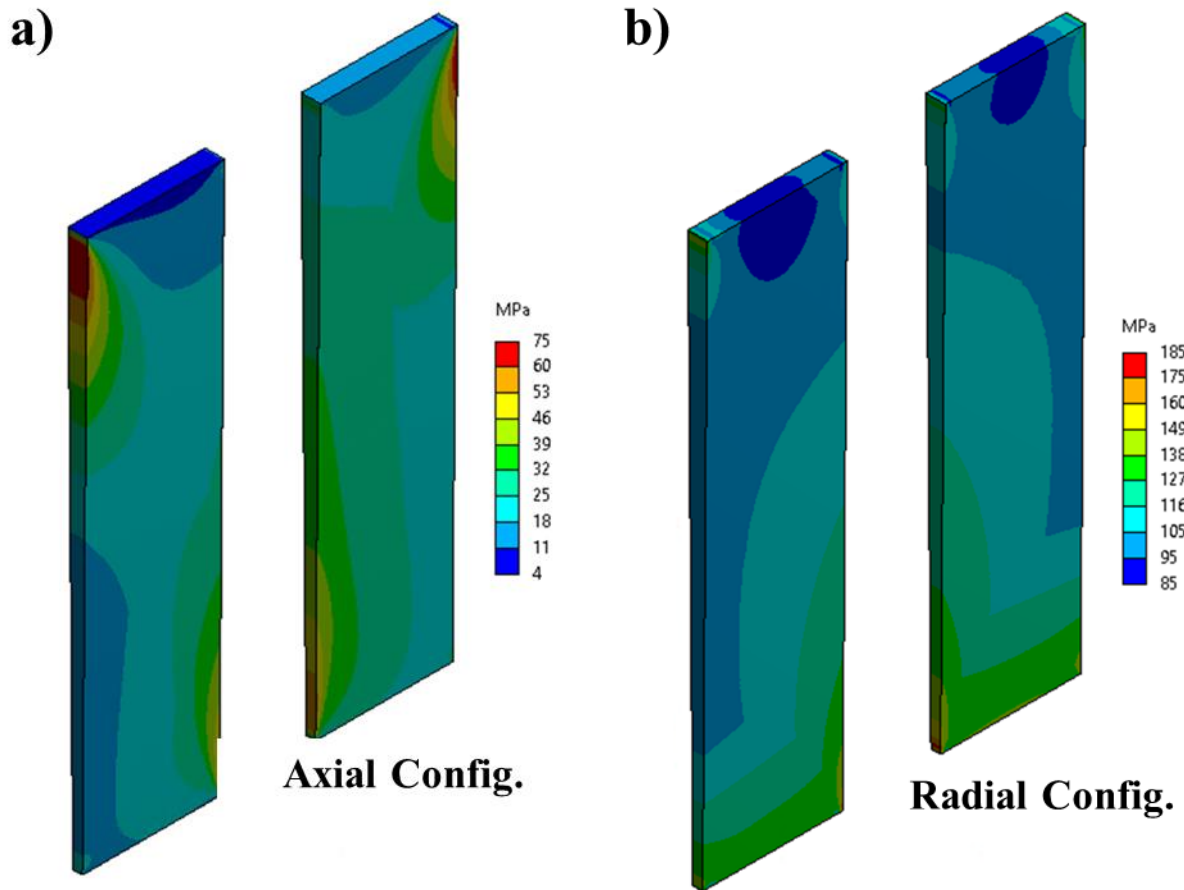


Fig. 16. The maximum principle stress contours of a) the axial and b) the radial couple configurations, respectively, when  $D_o = 16$  mm and  $t = 1$  mm.

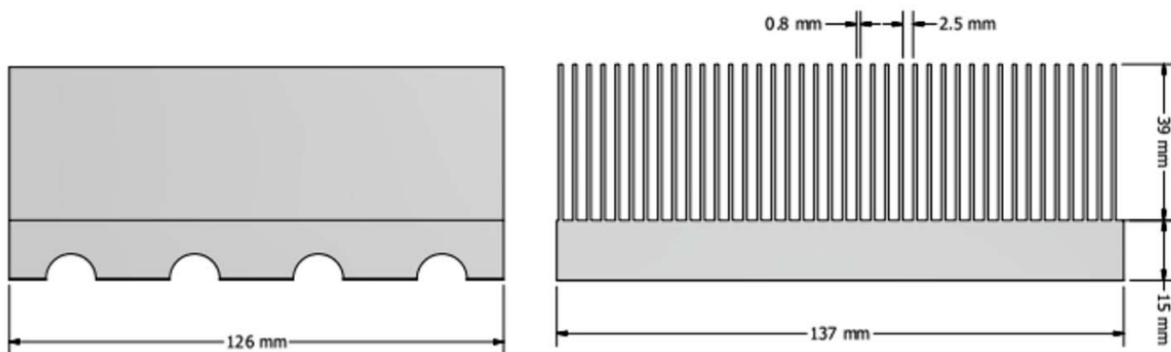


Fig. 17. The fin array of the hot-side heat exchanger [49].

Table 1

The material property values used in the analytical model.

Materials	Electrical resistivity $\rho_e$ [ $\Omega m$ ]	Thermal conductivity [ $W/mK$ ]	Seebeck coefficient [ $\mu V/K$ ]
P- type Bi <sub>2</sub> Te <sub>3</sub> [12]	5.49e-5	0.96	211.50
N- type Bi <sub>2</sub> Te <sub>3</sub> [13]	1.08e-5	1.22	-133.43
Aluminum	-	167	-
Copper	-	385	-

Table. 2 a)

The material property values for P-and N-type Bi<sub>2</sub>Te<sub>3</sub> used in the 3D coupled finite element model [12,13].

$\alpha_{PA}$ [ $\mu\text{V/K}$ ]	$0.00082635 T^2 - 1.19253647 T - 361.38672353$		
$\alpha_{PR}$ [ $\mu\text{V/K}$ ]	$0.00115230 T^2 - 1.33136475 T - 360.96732450$		
$\alpha_{NA}$ [ $\mu\text{V/K}$ ]	$0.00057799 T^2 - 0.28062006 T - 110.36637129$		
$\alpha_{NR}$ [ $\mu\text{V/K}$ ]	$0.00059994 T^2 - 0.28207362 T - 107.47269708$		
$\rho_{PA}$ [ $\Omega \text{ m}$ ]	$0.01145339 T^3 - 0.23843639 T^2 + 1.16237225 T + 5.76676682$		
$\rho_{PR}$ [ $\Omega \text{ m}$ ]	$0.00783850 T^3 - 0.16657315 T^2 + 0.83857866 T + 3.97280280$		
$\rho_{NA}$ [ $\Omega \text{ m}$ ]	$0.00000335 T^2 + 0.00214991 T + 0.73814796$		
$\rho_{NR}$ [ $\Omega \text{ m}$ ]	$0.0000018057 T^2 + 0.0024302394 T + 0.66504678$		
$k_P$ [ $\text{W/mK}$ ]	$0.00000532 T^2 - 0.00196080 T + 0.55932397$		
$k_N$ [ $\text{W/mK}$ ]	$0.00001110 T^2 - 0.00242623 T + 1.28098650$		
$\text{CTE}_{PA}$ [ $\text{m/mK}$ ]	1.79e-5	$E_P$ [GPa]	48.7
$\text{CTE}_{PR}$ [ $\text{m/mK}$ ]	1.84e-5	$E_N$ [GPa]	47
$\text{CTE}_{NA}$ [ $\text{m/mK}$ ]	1.83e-5	$\nu_P$ [-]	0.249
$\text{CTE}_{NR}$ [ $\text{m/mK}$ ]	2.01e-5	$\nu_N$ [-]	0.268

Table 2 b)

The material property values for the aluminum block, copper conductors and cooling pipe, thermal interface material and solder used in the 3D coupled finite element model [17].

Material	Electrical resistivity [ $\Omega$ m]	Thermal conductivity [W/mK]	Coefficient of thermal expansion [m/mK]	Young's modulus [GPa]	Poisson's ratio [-]
Aluminum	-	167	2.52e-5	68.9	0.33
Copper	1.7e-8	385	1.7e-5	120	0.3
Thermal interface material	-	5	2.7e-6	21	0.2
Solder	5e-8	55	2.7e-5	45	0.33

Table 3

The  $\Delta T$ , the electrical current, the maximum output power and the maximum value of the thermal stresses values for dimensions that produces the same output power for both the axial and radial couple configurations.

Dimensions at same power	$D_o = 10$ mm		$D_o = 12$ mm		$D_o = 14$ mm		$D_o = 16$ mm	
	$t = 1$ mm		$t = 2$ mm		$t = 3$ mm		$t = 4$ mm	
ATEG couple configuration	Axial	Radial	Axial	Radial	Axial	Radial	Axial	Radial
$\Delta T$ [°C]	50.7	54.0	76.4	77.5	93.3	93.4	105.4	104.8
Electrical Current [A]	3.0	3.0	5.6	5.4	7.8	7.5	9.7	9.4
Maximum power [mW]	31.3	33.7	83.9	86.1	139.0	140.0	190.6	192.2
Maximum principle stress [MPa]	106.3	145.9	112.5	162.2	119.3	178.9	123.2	190.1

#### 4.9. References

- [1] D.M. Rowe, CRC Handbook of THERMOELECTRICS, CRC press LLC, 1995.
- [2] A. Massaguer, E. Massaguer, M. Comamala, T. Pujol, J.R. González, M.D. Cardenas, D. Carbonell, A.J. Bueno, A method to assess the fuel economy of automotive thermoelectric generators, *Appl. Energy*. 222 (2018) 42–58.  
<https://doi.org/10.1016/j.apenergy.2018.03.169>.
- [3] Y. Wang, S. Li, X. Xie, Y. Deng, X. Liu, C. Su, Performance evaluation of an automotive thermoelectric generator with inserted fins or dimpled-surface hot heat exchanger, *Appl. Energy*. 218 (2018) 391–401. <https://doi.org/10.1016/j.apenergy.2018.02.176>.
- [4] B. Li, K. Huang, Y. Yan, Y. Li, S. Twaha, J. Zhu, Heat transfer enhancement of a modularised thermoelectric power generator for passenger vehicles, *Appl. Energy*. 205 (2017) 868–879. <https://doi.org/10.1016/j.apenergy.2017.08.092>.
- [5] M.H. Zaher, M.Y. Abdelsalam, J.S. Cotton, Study of the effects of axial conduction on the performance of thermoelectric generators integrated in a heat exchanger for waste heat recovery applications, *Appl. Energy*. 261 (2020) 114434.  
<https://doi.org/10.1016/j.apenergy.2019.114434>.
- [6] J.H. Son, M.W. Oh, B.S. Kim, S.D. Park, B.K. Min, M.H. Kim, H.W. Lee, Effect of ball milling time on the thermoelectric properties of p-type (Bi,Sb)<sub>2</sub>Te<sub>3</sub>, *J. Alloys Compd.* 566 (2013) 168–174. <https://doi.org/10.1016/j.jallcom.2013.03.062>.
- [7] J. Jiang, L. Chen, S. Bai, Q. Yao, Thermoelectric performance of p-type Bi-Sb-Te materials prepared by spark plasma sintering, *J. Alloys Compd.* 390 (2005) 208–211.  
<https://doi.org/10.1016/j.jallcom.2004.07.056>.
- [8] J. Jiang, L. Chen, Q. Yao, Q. Wang, Preparation and Properties of p-Type



- (Bi<sub>2</sub>Te<sub>3</sub>)<sub>x</sub>(Sb<sub>2</sub>Te<sub>3</sub>)<sub>1-x</sub> Thermoelectric Materials, 46 (2005) 959–962.
- [9] C.H. Lim, K.T. Kim, Y.H. Kim, Y.S. Lee, C.H. Lee, D.C. Cho, C.H. Lee, Effect of powder mixing on thermoelectric properties in Bi<sub>2</sub>Te<sub>3</sub>-based sintered compounds, *Intermetallics*. 14 (2006) 1370–1374. <https://doi.org/10.1016/j.intermet.2005.10.018>.
- [10] S. Seo, Y. Jeong, M.W. Oh, B. Yoo, Effect of hydrogen annealing of ball-milled Bi<sub>0.5</sub>Sb<sub>1.5</sub>Te<sub>3</sub> powders on thermoelectric properties, *J. Alloys Compd.* 706 (2017) 576–583. <https://doi.org/10.1016/j.jallcom.2017.02.181>.
- [11] Y. Pan, T.-R. Wei, Q. Cao, J.-F. Li, Mechanically enhanced p- and n-type Bi<sub>2</sub>Te<sub>3</sub>-based thermoelectric materials reprocessed from commercial ingots by ball milling and spark plasma sintering, *Mater. Sci. Eng. B*. 197 (2015) 75–81. <https://doi.org/10.1016/j.mseb.2015.03.011>.
- [12] A.A. Abdelnabi, V. Lakhian, Y. Tseng, J.R. Mcdermid, J.S. Cotton, Enhancement of mechanical properties and thermoelectric performance of spark plasma sintered P-type Bismuth Telluride by powder surface oxide reduction, (n.d.) 1–42.
- [13] A.A. Abdelnabi, V. Lakhian, J.R. Mcdermid, J.S. Cotton, The effect of powder pre-treatment on both mechanical and thermoelectric performance properties of spark plasma sintered N-type bismuth telluride, (n.d.) 1–37.
- [14] D.W. Liu, J.F. Li, C. Chen, B.P. Zhang, Effects of SiC nanodispersion on the thermoelectric properties of p-type and n-Type Bi<sub>2</sub>Te<sub>3</sub>-based alloys, *J. Electron. Mater.* 40 (2011) 992–998. <https://doi.org/10.1007/s11664-010-1476-x>.
- [15] L.D. Zhao, B.P. Zhang, J.F. Li, M. Zhou, W.S. Liu, J. Liu, Thermoelectric and mechanical properties of nano-SiC-dispersed Bi<sub>2</sub>Te<sub>3</sub> fabricated by mechanical alloying and spark plasma sintering, *J. Alloys Compd.* 455 (2008) 259–264.

<https://doi.org/10.1016/j.jallcom.2007.01.015>.

- [16] L.D. Zhao, B.P. Zhang, J.F. Li, H.L. Zhang, W.S. Liu, Enhanced thermoelectric and mechanical properties in textured n-type Bi<sub>2</sub>Te<sub>3</sub> prepared by spark plasma sintering, *Solid State Sci.* 10 (2008) 651–658. <https://doi.org/10.1016/j.solidstatesciences.2007.10.022>.
- [17] S. Shittu, G. Li, X. Zhao, X. Ma, Y.G. Akhlaghi, E. Ayodele, High performance and thermal stress analysis of a segmented annular thermoelectric generator, *Energy Convers. Manag.* 184 (2019) 180–193. <https://doi.org/10.1016/j.enconman.2019.01.064>.
- [18] G. Min, D.M. Rowe, Ring-structured thermoelectric module, *Semicond. Sci. Technol.* 22 (2007) 880–883. <https://doi.org/10.1088/0268-1242/22/8/009>.
- [19] A. Schmitz, C. Stiewe, E. Müller, Preparation of ring-shaped thermoelectric legs from PbTe powders for tubular thermoelectric modules, *J. Electron. Mater.* 42 (2013) 1702–1706. <https://doi.org/10.1007/s11664-012-2402-1>.
- [20] A. Sakai, T. Kanno, K. Takahashi, H. Tamaki, Y. Yamada, Power Generation and Peltier Refrigeration by a Tubular Pi-Type Thermoelectric Module, *J. Electron. Mater.* 44 (2015) 4510–4515. <https://doi.org/10.1007/s11664-015-4017-9>.
- [21] N. Mansouri, E.J. Timm, H.J. Schock, D. Sahoo, A. Kotrba, Development of a Circular Thermoelectric Skutterudite Couple Using Compression Technology, *J. Energy Resour. Technol.* 138 (2016) 052003. <https://doi.org/10.1115/1.4032619>.
- [22] M. Morsy, Manufacturing and Characterization of Annular Thermoelectric Generators and Verification of a Novel Design, McMaster University, Hamilton, Canada, 2015.
- [23] S.C. Kaushik, S. Manikandan, The influence of Thomson effect in the energy and exergy efficiency of an annular thermoelectric generator, *Energy Convers. Manag.* 103 (2015) 200–207. <https://doi.org/10.1016/j.enconman.2015.06.037>.

- [24] Z. Shen, S. Wu, L. Xiao, Theoretical analysis on the performance of annular thermoelectric couple, *Energy Convers. Manag.* 89 (2015) 244–250.  
<https://doi.org/10.1016/j.enconman.2014.09.071>.
- [25] Z.G. Shen, S.Y. Wu, L. Xiao, Assessment of the performance of annular thermoelectric couples under constant heat flux condition, *Energy Convers. Manag.* 150 (2017) 704–713.  
<https://doi.org/10.1016/j.enconman.2017.08.058>.
- [26] Z.G. Shen, X. Liu, S. Chen, S.Y. Wu, L. Xiao, Z.X. Chen, Theoretical analysis on a segmented annular thermoelectric generator, *Energy.* 157 (2018) 297–313.  
<https://doi.org/10.1016/j.energy.2018.05.163>.
- [27] Q. Tan, G. Chen, Y. Sun, B. Duan, G. Li, P. Zhai, Performance of annular thermoelectric couples by simultaneously considering interface layers and boundary conditions, *Appl. Therm. Eng.* 174 (2020) 115301. <https://doi.org/10.1016/j.applthermaleng.2020.115301>.
- [28] A.B. Zhang, B.L. Wang, D.D. Pang, J.B. Chen, J. Wang, J.K. Du, Influence of leg geometry configuration and contact resistance on the performance of annular thermoelectric generators, *Energy Convers. Manag.* 166 (2018) 337–342.  
<https://doi.org/10.1016/j.enconman.2018.04.042>.
- [29] Z.G. Shen, S.Y. Wu, L. Xiao, Assessment of the performance of annular thermoelectric couples under constant heat flux condition, *Energy Convers. Manag.* 150 (2017) 704–713.  
<https://doi.org/10.1016/j.enconman.2017.08.058>.
- [30] Z.G. Shen, X. Liu, S. Chen, S.Y. Wu, L. Xiao, Z.X. Chen, Theoretical analysis on a segmented annular thermoelectric generator, *Energy.* 157 (2018) 297–313.  
<https://doi.org/10.1016/j.energy.2018.05.163>.
- [31] S. Manikandan, S.C. Kaushik, Energy and exergy analysis of solar heat pipe based annular

- thermoelectric generator system, *Sol. Energy*. 135 (2016) 569–577.  
<https://doi.org/10.1016/j.solener.2016.06.031>.
- [32] R. Lamba, S.C. Kaushik, Thermodynamic analysis of thermoelectric generator including influence of Thomson effect and leg geometry configuration, *Energy Convers. Manag.* 144 (2017) 388–398. <https://doi.org/10.1016/j.enconman.2017.04.069>.
- [33] Y. Sun, G. Chen, B. Duan, G. Li, P. Zhai, An annular thermoelectric couple analytical model by considering temperature-dependent material properties and Thomson effect, *Energy*. 187 (2019). <https://doi.org/10.1016/j.energy.2019.115922>.
- [34] T. Clin, S. Turenne, D. Vasilevskiy, R.A. Masut, Numerical simulation of the thermomechanical behavior of extruded bismuth telluride alloy module, *J. Electron. Mater.* 38 (2009) 994–1001. <https://doi.org/10.1007/s11664-009-0756-9>.
- [35] S. Turenne, T. Clin, D. Vasilevskiy, R.A. Masut, Finite element thermomechanical modeling of large area thermoelectric generators based on bismuth telluride alloys, *J. Electron. Mater.* 39 (2010) 1926–1933. <https://doi.org/10.1007/s11664-009-1049-z>.
- [36] J.L. Gao, Q.G. Du, X.D. Zhang, X.Q. Jiang, Thermal Stress Analysis and Structure Parameter Selection for a Bi<sub>2</sub>Te<sub>3</sub>-Based Thermoelectric Module, *J. Electron. Mater.* 40 (2011) 884–888. <https://doi.org/10.1007/S11664-011-1611-3>.
- [37] M. Picard, S. Turenne, D. Vasilevskiy, R.A. Masut, Numerical simulation of performance and thermomechanical behavior of thermoelectric modules with segmented bismuth-telluride-based legs, *J. Electron. Mater.* 42 (2013) 2343–2349.  
<https://doi.org/10.1007/s11664-012-2435-5>.
- [38] A.S. Al-Merbati, B.S. Yilbas, A.Z. Sahin, Thermodynamics and thermal stress analysis of thermoelectric power generator: Influence of pin geometry on device performance, *Appl.*

- Therm. Eng. 50 (2013) 683–692. <https://doi.org/10.1016/j.applthermaleng.2012.07.021>.
- [39] X. Jia, Y. Gao, Estimation of thermoelectric and mechanical performances of segmented thermoelectric generators under optimal operating conditions, *Appl. Therm. Eng.* 73 (2014) 333–340. <https://doi.org/10.1016/j.applthermaleng.2014.07.069>.
- [40] U. Erturun, K. Erermis, K. Mossi, Effect of various leg geometries on thermo-mechanical and power generation performance of thermoelectric devices, *Appl. Therm. Eng.* 73 (2014) 126–139. <https://doi.org/10.1016/j.applthermaleng.2014.07.027>.
- [41] B.S. Yilbas, S.S. Akhtar, A.Z. Sahin, Thermal and stress analyses in thermoelectric generator with tapered and rectangular pin configurations, *Energy*. 114 (2016) 52–63. <https://doi.org/10.1016/j.energy.2016.07.168>.
- [42] S. Asaadi, S. Khalilarya, S. Jafarmadar, Numerical study on the thermal and electrical performance of an annular thermoelectric generator under pulsed heat power with different types of input functions, *Energy Convers. Manag.* 167 (2018) 102–112. <https://doi.org/10.1016/j.enconman.2018.04.085>.
- [43] S. Fan, Y. Gao, Numerical simulation on thermoelectric and mechanical performance of annular thermoelectric generator, *Energy*. 150 (2018) 38–48. <https://doi.org/10.1016/j.energy.2018.02.124>.
- [44] S. Fan, Y. Gao, Numerical analysis on the segmented annular thermoelectric generator for waste heat recovery, *Energy*. 183 (2019) 35–47. <https://doi.org/10.1016/j.energy.2019.06.103>.
- [45] M.A. Markman, I.R. Jurkevich, N.V. Kolomoets, T. Kamensky, M. Matskov, P.E.R. Wilbur, A.E.E. Berger, United States Patent (19), 45 (1977).
- [46] M. Morsy, Manufacturing and Characterization of Annular Thermoelectric Generators and

Verification of a Novel Design, (2015).

- [47] D.T. Crane, D. Kossakovski, L.E. Bell, Modeling the building blocks of a 10% efficient segmented thermoelectric power generator, *J. Electron. Mater.* 38 (2009) 1382–1386. <https://doi.org/10.1007/s11664-009-0673-y>.
- [48] A.F. Ioffe, *Semiconductor thermoelements and thermo-electric cooling*, 1959. [https://doi.org/10.1016/0038-092X\(60\)90073-6](https://doi.org/10.1016/0038-092X(60)90073-6).
- [49] M. ZAHER, *The Integration of Annular Thermoelectric Generators in a Heat Exchanger for Waste Heat Recovery Applications*, McMaster University, 2017.
- [50] D.E. Wesolowski, R.S. Goeke, A.M. Morales, S.H. Goods, P.A. Sharma, M.P. Saavedra, K.R. Reyes-Gil, W.C.G. Neel, N.Y.C. Yang, C.A. Applett, Development of a Bi<sub>2</sub>Te<sub>3</sub>-based thermoelectric generator with high-aspect ratio, free-standing legs, *J. Mater. Res.* 27 (2012) 1149–1156. <https://doi.org/10.1557/jmr.2012.27>.
- [51] E.E. Antonova, D.C. Looman, Finite elements for thermoelectric device analysis in ANSYS, *Int. Conf. Thermoelectr. ICT, Proc.* 2005 (2005) 200–203. <https://doi.org/10.1109/ICT.2005.1519922>.
- [52] L.D. LANDAU, E.M. LIFSHITZ, *Electrodynamics of Continuous Media*, Pergamon Press, 1963.
- [53] T. Ming, W. Yang, Y. Wu, Y. Xiang, X. Huang, J. Cheng, X. Li, J. Zhao, Numerical analysis on the thermal behavior of a segmented thermoelectric generator, *Int. J. Hydrogen Energy.* 42 (2017) 3521–3535. <https://doi.org/10.1016/j.ijhydene.2016.11.021>.
- [54] J. Jiang, L. Chen, S. Bai, Q. Yao, Thermoelectric performance of p-type Bi-Sb-Te materials prepared by spark plasma sintering, *J. Alloys Compd.* 390 (2005) 208–211. <https://doi.org/10.1016/j.jallcom.2004.07.056>.

- [55] J. Jiang, L. Chen, S. Bai, Q. Yao, Q. Wang, Fabrication and thermoelectric performance of textured n-type Bi<sub>2</sub>(Te,Se)<sub>3</sub> by spark plasma sintering, *Mater. Sci. Eng. B.* 117 (2005) 334–338. <https://doi.org/10.1016/j.mseb.2005.01.002>.
- [56] S. Shittu, G. Li, X. Zhao, X. Ma, Y.G. Akhlaghi, E. Ayodele, High performance and thermal stress analysis of a segmented annular thermoelectric generator, *Energy Convers. Manag.* 184 (2019) 180–193. <https://doi.org/10.1016/j.enconman.2019.01.064>.
- [57] S. Kakac, R.K. Shah, W. Aung, *Handbook of single-phase convective heat transfer*, Wiley, New York, 1987.
- [58] H.D. Baehr, K. Stephan, *Heat and mass transfer*, 2nd ed., Springer, 2006.
- [59] R.H.S. Winterton, Where did the Dittus and Boelter equation come from?, *Int. J. Heat Mass Transf.* 41 (1998) 809–810. [https://doi.org/10.1016/S0017-9310\(97\)00177-4](https://doi.org/10.1016/S0017-9310(97)00177-4).

## Chapter 5: Conclusions and Future Work

This chapter presents conclusions based on of the main findings of the thesis and offers recommendations for future work to advance this research.

### 5.1. Conclusions

This thesis provides state-of-the-art methodologies for designing a ring-shaped ATEG module that offers reliable, robust, and predictable thermoelectric and mechanical performance for low-temperature waste heat recovery applications. To this end, this work utilized optimum high-performance P- and N-type bismuth telluride at low-temperate chemical compositions, as well as state-of-the-art powder preparation, pre-treatment, and sintering techniques. The current work addresses a number of challenges and key literature gaps, including those related to TE material mechanical and thermoelectric performance, and the configuration and dimensions of the ATEG module design.

The main contributions of this work relate to two main aspects of high-performance ATEG modules. The first aspect relates to the methodologies used to characterize and prepare TE materials. The state-of-the-art literature contains no prior studies measuring the uniaxial tensile strength values for spark plasma sintered P-type  $\text{Bi}_{0.4}\text{Sb}_{1.6}\text{Te}_3$  and N-type  $(\text{Bi}_{0.95}\text{Sb}_{0.05})_2(\text{Se}_{0.05}\text{Te}_{0.95})_3$  both parallel and perpendicular to the applied sintering pressure. Additionally, the literature contains no prior studies examining how powder pre-treatment affects the mechanical properties of these materials, nor does it contain consistent and full characterizations of these materials' mechanical and thermoelectric properties. With respect to these gaps, this thesis makes the following key contributions: i) it provides accurate and precise measurements of the uniaxial tensile strength of spark plasma sintered P-type  $\text{Bi}_{0.4}\text{Sb}_{1.6}\text{Te}_3$  and N-type  $(\text{Bi}_{0.95}\text{Sb}_{0.05})_2(\text{Se}_{0.05}\text{Te}_{0.95})_3$  both parallel and perpendicular to the applied sintering pressure; ii) it determines and



documents the effect of powder surface oxide reduction and powder annealing on the mechanical and thermoelectric properties of these materials; and iii) it provides a full characterization of the mechanical and thermoelectric properties of spark plasma sintered P-type  $\text{Bi}_{0.4}\text{Sb}_{1.6}\text{Te}_3$  and N-type  $(\text{Bi}_{0.95}\text{Sb}_{0.05})_2(\text{Se}_{0.05}\text{Te}_{0.95})_3$  both parallel and perpendicular to the applied sintering pressure. The above contributions are detailed in the journal papers presented in Chapters 2 and 3.

The second set of contributions made by this thesis relates to the effects of the configuration and dimensions of a ring-shaped ATEG module integrated into a low-temperature waste heat recovery system that contains hot- and cold-side heat exchangers. The literature contains no prior studies examining how heat flow path directions—either radially or axially in relation to the ATEG geometrical axis—affect ATEG couple performance, or studies investigating how a couple's dimensions influence its thermoelectric performance and thermal stresses during operation. The research in this thesis addresses these gaps as follows: i) it creates full-dimensional 2D maps of thermoelectric performance under an electrical current of 10 A in order to compare radial and axial heat flow in ring-shaped ATEG couple configurations; and ii) it constructs 2D thermal stress maps for dimension ranges selected based on the thermoelectric performance of the two configurations in order to determine the optimum configuration and dimensions for a ring-shaped ATEG couple. These contributions are discussed in detail in the journal paper presented in Chapter 4.

The findings of the research in this thesis are presented next. The findings presented in Chapters 2 and 3 relate to the contributions regarding the first aspect of this research. Specifically, these chapters investigate how three different powder pre-treatments—namely, powder drying under a vacuum at 100 °C, powder annealing at 380 °C in flowing high-purity Ar, and powder surface oxide reduction in flowing 5%  $\text{H}_2$  – 95% Ar (vol%) at 380 °C—affect both the mechanical and the thermoelectric properties of spark plasma sintered P-type  $\text{Bi}_{0.4}\text{Sb}_{1.6}\text{Te}_3$  and N-type  $(\text{Bi}_{0.95}$

$\text{Sb}_{0.05}\text{Te}_{0.95}$ )<sub>2</sub>( $\text{Se}_{0.05}\text{Te}_{0.95}$ )<sub>3</sub>. As was shown, the oxide reduction pre-treatment caused the P-type telluride's characteristic uniaxial tensile strength to increase to 26.3 MPa and 30.6 MPa in the parallel and perpendicular directions, respectively; similarly, this pre-treatment step caused the values of the N-type telluride to increase to 33.8 MPa and 35.5 MPa in the parallel and perpendicular directions, respectively. In addition, the oxide reduction pre-treatment caused the  $ZT_{\max}$  values of the P-type telluride to increase to 0.8 and 1.1 at 25 °C in the parallel and perpendicular directions, respectively, and the  $ZT_{\max}$  values of the N-type telluride to increase to 0.63 at 150 °C in both directions.

The two contributions related to the second aspect of this research were presented in Chapter 4, which investigated the effect of heat flow/electrical current paths on the performance and thermal stress fields in ATEG couples. To this end, radial and axial ATEG couple configurations using P- and N-Type  $\text{Bi}_2\text{Te}_3$  rings with a wide range of thickness-to-outer-diameter ratios were compared. The formation of tensile hoop stresses caused thermal stresses in the radial configuration that were as much as 67 MPa higher than those in the axial configuration when both were generating the same power at  $\Delta T = 105$  °C. The axial couple configuration had the lowest  $\sigma$  at 67.8 MPa, with a  $D_o$  of 16 mm, a  $t$  of 1 mm, a  $\Delta T$  of 14.8 °C, and power generation of 10.4 mW per couple.

This research also made secondary contributions in the form of the tools that were used to achieve the main contributions. These tools included: an in-house-built powder pre-treatment facility with mechanical agitation to increase the powder-gas contact time; a special in-house fixture that ensured the uniaxial tensile failure of small brittle P- and N-type bismuth telluride as sintered bodies; an accurate analytical thermoelectric performance model for ring-shaped ATEG

modules; and a verified 3D coupled thermoelectric/thermal stresses finite element model of a ring-shaped ATEG module.

In conclusion, in order to design and build a ring-shaped ATEG module that offers reliable, robust, and predictable performance for low temperature waste heat recovery applications, the following recommendations are provided: i) P-type  $\text{Bi}_{0.4}\text{Sb}_{1.6}\text{Te}_3$  and N-type  $(\text{Bi}_{0.95}\text{Sb}_{0.05})_2(\text{Se}_{0.05}\text{Te}_{0.95})_3$  powder surface oxides should be reduced prior to spark plasma sintering using a 5% $\text{H}_2$ -95% $\text{Ar}$  process atmosphere at 380 °C for 24 h, as these parameters provided the maximum enhancement effect on both the mechanical and thermoelectric properties; and ii) given its superior performance, an axial ring-shaped ATEG couple configuration should be used in conjunction with a lower operation exhaust gas temperature to ensure safe operation. operation exhaust gas temperature for a safe operation.

## 5.2. Recommendations for Future Work

Designing a high-performance and reliable ring-shaped ATEG module for low-temperature applications is challenging. Although the contributions made by the research in this thesis address many of these challenges, there remain a number of avenues for future research to build upon this work, including:

- Investigating the effect of particle size on the mechanical properties of P- and N-type  $\text{Bi}_2\text{Te}_3$ .
- Using higher  $\text{H}_2$  reduction gas percentage in the oxide reduction pre-treatment processes, as well as using reducing sintering environment.
- Investigating how additives to  $\text{Bi}_2\text{Te}_3$  powder (e.g., silicon carbide) affect uniaxial tensile strength.
- Optimizing the sintering temperature of the SPS for both the P- and N-type  $\text{Bi}_2\text{Te}_3$ .
- Importing the solder layer alloy type and thickness effect into the 3D coupled finite element model for further investigation, as the maximum thermal stresses occur at the interface between the TE rings and the solder layer.
- Exploring the effect of the type and thickness of the thermal interface material. Such research would be valuable, as the thermal interface material is responsible for transferring the stresses between the hot- and cold-side heat exchangers and the ATEG couple.
- Investigating and comparing a half ring-shaped radial ATEG couple configuration to a full ring-shaped ATEG couple configuration, as the half-ring configuration is thought to be free of hoop stresses due to temperature gradient in the radial direction.
- Optimizing the copper conductor geometry of the axial ATEG couple configuration for heat spreading and thermal stresses.

- Investigating a segmented ring-shaped ATEG module, especially one with an axial couple configuration.

## Appendix:

### Uncertainty analysis of the measured material properties:

All the measured properties for P- and N-type Bi<sub>2</sub>Te<sub>3</sub> including the mechanical and thermoelectric properties associated with two types of errors. The first is the statistical random error that includes the repetition of the same measurement, the multiple samples measured from the same batch and the multiple batches for the same powder pre-treatment condition. This random statistical error is considered in all the graphs of Chapter 2 and 3 when comparing between different powder pre-treatment conditions. The second is the random propagated error associated with the measuring device. The propagated error of the thermoelectric properties is found to be comparable to the statistical error in which the two were added and the total is included in Chapter 2 and 3 below the properties table in the appendix of each Chapter for reference. However, the propagated error of the mechanical properties found to be negligible with respect to the sample statistical error. The following is detailed description of the different sources of errors.

### The statistical random error:

The statistical random error of each powder pre-treatment condition was calculated with 95% confidence interval as follow:

$$\varepsilon = \pm t_{95\%} \frac{S}{\sqrt{N-1}} \quad (1)$$

where  $t_{95\%}$  is the 95% confidence interval t-student, S is the sample standard deviation and N is the total number of measurements performed for each powder pre-treatment condition for specific property.

The device propagated random error:

Most of the measured properties  $R$  are not directly measured but calculated from independent directly measured values  $(x_1, x_2, \dots, x_N)$ . The error in each independent directly measured value  $\varepsilon_{x_i}$  are added using the root-sum-square method according to Moffat [93] to give the device propagated error:

$$\varepsilon_p = \pm \sqrt{\sum_{i=1}^N \left( \frac{\partial R}{\partial x_i} \varepsilon_{x_i} \right)^2} \quad (2)$$

The total error of a measured property is the root-sum-square of both the statistical random error and the device propagated random error:

$$\varepsilon_T = \pm \sqrt{\varepsilon^2 + \varepsilon_p^2} \quad (3)$$

Error associated with electrical resistivity and Seebeck coefficient measurements:

The error values of the independent sources in the measurement of the electrical resistivity and the Seebeck coefficient are presented following the analysis performed by Mackey et al [94] as they used the same machine model used in the current work. The electrical resistivity and the Seebeck coefficient were calculated from the following formulas:

$$\rho_e = \frac{\sum V_i \sum I_i - N \sum V_i I_i w l}{(\sum V_i)^2 - N \sum V_i^2} \frac{l}{z} \quad (4)$$

$$\alpha = -\frac{\Delta V}{\Delta T} + \alpha_{wire}(T) \quad (5)$$

where  $V$  is the voltage,  $I$  is the current,  $N$  is the sampling size,  $w$ ,  $l$  and  $z$  are the sample width, length and height, respectively,  $T$  is the temperature and  $\alpha_{wire}$  is the Seebeck wire.

The following Table 1 and 2 list the different error source values in the electrical resistivity and the Seebeck coefficient measurement, respectively:

Table 1

Electrical resistivity sources of error:

Source of error	Value	Uncertainty
Prop radius [m]	1.25E-04	1.00E-05
Prop distance [m]	3.50E-03	1.25E-04
Voltage reading [V]	5.20E-05	1.20E-06
Current reading [A]	5.00E-04	1.05E-06
Caliper resolution [m]	1.00E-03	1.00E-05
Sample width [m]	2.20E-03	1.00E-05
Sample length [m]	2.20E-03	1.00E-05

Table 2

Seebeck coefficient sources of error:

Source of error	Value	Uncertainty
Prop radius [m]	1.25E-04	1.00E-05
Prop distance [m]	3.50E-03	1.25E-04
Voltage reading [V]	1.76E-03	1.29E-06
Current reading [A]	5.00E-04	1.05E-06
$\Delta T$ [K]	3.00E+00	1.00E-01
Seebeck wire [V]	2.20E-03	1.00E-05
Caliper resolution [m]	1.00E-03	1.00E-05
Sample width [m]	2.20E-03	1.00E-05
Sample length [m]	2.20E-03	1.00E-05



Error associated with thermal diffusivity, specific heat capacity and thermal conductivity measurements:

The thermal diffusivity was measured using the flash laser method which calculated from the following formula:

$$\alpha_d = 0.1388 \frac{l}{t_{50}} \quad (6)$$

where  $t_{50}$  is half the temperature rise time. The sample specific heat could be calculated by a comparative method using a reference sample under the same conditions as:

$$C_p^{sample} = \frac{T_{max}^{ref}}{T_{max}^{sample}} \cdot \frac{(\rho \cdot l)^{ref}}{(\rho \cdot l)^{sample}} \cdot C_p^{ref} \quad (7)$$

where  $T_{max}$  is the maximum temperature recorded, and  $\rho$  is the density. The thermal conductivity could be calculated as:

$$k = \alpha_d \cdot C_p \cdot \rho \quad (8)$$

Table 3 list the different error source values:

Table 3

Laser flash method sources of error:

Source of error	Value	Uncertainty
Sample radius [m]	6.00E-03	1.00E-05
Reference radius [m]	6.35E-03	1.00E-05
Sample thickness [m]	1.50E-03	1.00E-05
Reference thickness [m]	3.17E-03	1.00E-05
$\Delta T$ [K]	5.00E+00	1.00E-02
Sample density [kg/m <sup>3</sup> ]	6750	67

Reference density [kg/m <sup>3</sup> ]	10212	102
Reference specific heat [J/kg K]	266	16

---